UNIVERSITY OF
Southampton

University of Southampton Research Repository
ePrints Soton

Copyright © and Moral Rights for this thesis are retained by the author and/or other copyright owners. A copy can be downloaded for personal non-commercial research or study, without prior permission or charge. This thesis cannot be reproduced or quoted extensively from without first obtaining permission in writing from the copyright holder/s. The content must not be changed in any way or sold commercially in any format or medium without the formal permission of the copyright holders.

When referring to this work, full bibliographic details including the author, title, awarding institution and date of the thesis must be given e.g.

AUTHOR (year of submission) "Full thesis title", University of Southampton, name of the University School or Department, PhD Thesis, pagination

http://eprints.soton.ac.uk

UNIVERSITY OF SOUTHAMPTON

Chalcogenide Thin Film Materials for Next Generation Data Storage

by

Robert E. Simpson

A thesis submitted in partial fulfillment for the degree of Doctor of Philosophy

in the
Faculty of Engineering, Science and Mathematics
Optoelectronics Research Centre

January 2008

UNIVERSITY OF SOUTHAMPTON

ABSTRACT

FACULTY OF ENGINEERING, SCIENCE AND MATHEMATICS
OPTOELECTONICS RESEARCH CENTRE

Doctor of Philosophy

Chalcogenide Thin Film Materials for Next Generation Data Storage

by Robert E. Simpson

Data can be stored in the form of amorphous and crystalline marks within a chalcogenide thin film. Commonly $Ge_2Sb_2Te_5$ is used as the active data storage material to record these two different phases. Changes in phase are induced by controlled heating and cooling with laser radiation or an electric current. The research reported here shows, for the first time, that phase changes are possible in two new materials: BiSbTe and GaLaS. A further, known, phase change system, GeSbTe, has been used to test combinatorial deposition techniques and high throughput characterisation methodologies. An optical system, the static tester, was developed to test the time necessary for phase transitions. The system, capable of automated operation, can sequentially characterise the phase change kinetics of composition spread, thin film, samples. The GeSbTe system was investigated, as a function of composition, using combinatorial deposition methods. This showed that combinatorial methods can be applied to phase change materials and allowed new material characterisation over the whole ternary system. Using combinatorial methods, the electrical sheet resistance of the amorphous material is shown to be correlated to the tellurium concentration and is thought to be due to correlated increases in lone-pair defect charge trapping centres. The material's resistivity can change by more than an order of magnitude by increasing the Te content from 20 at.% to 50 at.%. Conversely, in the amorphous phase, the refractive index was shown to decrease with increasing Te proportion and this has been related to a decrease in the material's polarizability. The Sb:Te binary system has been doped with Bi using two different methods; sputter deposition from a composite target and using combinatorial, thermal evaporation deposition of elemental targets. New results have shown that Sb_8Te_2 can be doped with up to 13at.% Bi and still exist in a stable amorphous state. A novel chalcogenide material consisting of gallium, lanthanum and sulphur was shown, for the first time, to phase change. The crystallisation time of Ga:La:S:Cu material was found to be 150ns and dependent on the Cu proportion. Increasing the Cu by 30 at.% increased the crystallisation time to 350ns. The electrical resistivity of these materials was approximately $4\Omega m$. This allows efficient Joule heating and electrical switching was demonstrated. A finite element analysis has shown that this material can be amorphised with a current of just $0.4\mu A$ in comparison to $2.5mA$ required for a similar volume of $Ge_2Sb_2Te_5$. Therefore Ga:La:S:Cu shows potential as a future electrical phase change data storage material.

Statement of Authorship

Declaration of Authorship I, Robert Edward Simpson, declare that the thesis entitled 'Chalcogenide Thin Film Materials for Next Generation Data Storage' and the work presented in it are my own. I confirm that:

- this work was done wholly while in candidature for a research degree at this University;
- where any part of this thesis has previously been submitted for a degree or any other qualification at this University or any other institution, this has been clearly stated;
- where I have consulted the published work of others, this is always clearly attributed;
- where I have quoted from the work of others, the source is always given;
- With the exception of such quotation, this thesis is entirely my own work;
- I have acknowledged all main sources of help;
- where the thesis is based on work done by myself jointly with others, I have made clear exactly what was done by others and what I have contributed myself;
- parts of this work have been published as shown in the List of Publications;

Signed: .... Date: ....

Contributions of Others

In modern day science collaboration between groups of common research interest allows the sharing of ideas, equipment and knowledge. During the course of my PhD research such collaborations have proven enjoyable and extremely fruitful. I would like to take this opportunity to thank all those who i have had the fortune of working with during the last 4 years. I have prepared a list to show the contributions that these collaborators have made to the research documented here.

Daniel Hewak	ORC	PhD supervision and direction
Arshad Mairaj	ORC	supervision and direction during the first 12-months of my research and thermal data on GLS used in chapter 6
Brian Hayden	Chemistry	Combinatorial and high throughput methodology
Samuel Guerin	Chemistry/Ilika	Deposition spread deposition of GeSbTe and BiSbTe samples used chapter 4 and 5
Bob Greef	Chemistry	Training on Imaging Ellipsometer
Thiery Le Gall	Ilika	XRD Training
John Tetteh	Ilika	Paradise toolbox used to generate figures 4.22, 4.23, 4.25-4.29, 5.18, A1 and A10
Jonathan Fitzmaurice	Ilika	Measurements for Figures 4.10, 4.16 and A10
Mark Derby	ORC	PLD collaboration, EDX analysis used for figure 6.14-6.16, nanosecond PLD measurement
Francesco Mezzapesa	ORC	Assistance with the measurement of bulk GaLaS conductivity, figure 6.9

Costantino Corbari	ORC	Assistance with the measurement of bulk GaLaS conductivity, figure 6.9
James Withnall	Ilika	Static tester software development
Jan Ricter	Ilika	Help with the incorporation of the autofocus system into the static tester hardware, development of the static tester software and many fruitful (mainly off topic) discussions
Neil Sessions	ORC	Assistance with sputtering of GaLaS and general help in the planar clean room
Dave Sager	ORC	General help in the planar clean room
Kenton Knight	ORC	Practical help with GaLaS fabrication
Kevin Huang	ORC	SEM image included for figure 7.1
Tominaga-san	CAN-FOR, AIST	Supervision and direction during JSPS summer project, training on helicon wave sputtering system.
Paul Fons	CAN-FOR, AIST	Supervision and direction during JSPS summer project, XRD analysis of BiSbTe spectra, idea to use mote carlo simulation to model x-ray generation during EDX (Cpt 2)
Shima-san	CAN-FOR, AIST	Training on ellipsometer, Shibura sputtering system, 633nm ellipsometer, Linkam heating stage
Eleanor Tarbox	ORC	Proof reading of thesis

List of Publications

R.E. Simpson, A. Mairaj, R.J. Curry , C.C. Huang; K. Knight; N. Sessions; M. Hassan; D.W. Hewak, Electrical phase change of Ga:La:S:Cu films, *Electronics Letters* 43 (15), 830 - 831, July, 2007

R E Simpson, A Mairaj, R J Curry, D W Hewak., "Phase Change Memory Materials, Devices and Methods" UK Patent No. GB2433647, 27 June 2007 (Patent Publication)

R.E.Simpson, C.C.Huang, C.J.Liu, C.Y.Tai, D.W.Hewak, "Nano-scale sulphide phase change materials and applications", *Nanoscale Physics and Technology IoP*, Southampton, 26-27 March, 2007 (Conference Publication)

S.Guerin, B.Hayden, D.W.Hewak, G.Purdy, R.Simpson, High throughput synthesis and screening of chalcogenide materials for data storage, *Singapore International Chemistry Conference*, 8-10 December, 2005 (Conference Publication)

S.Guerin, B.Hayden, D.W.Hewak, G.Purdy, R.E.Simpson, "Combinatorial synthesis and screening of chalcogenide materials for data storage", *PCOS 17th Symposium*, Japan 17-18, November, 2005 (Conference Publication)

S.Guerin, M.Hassan, B.Hayden, D.W.Hewak, G.Purdy, R.E.Simpson, "Material optimisation for optical data storage", *OSA Frontiers in Optics Arizona*, October, 2005 (POST DEADLINE Conference Publication)

R.E.Simpson, D.W.Hewak, S.Guerin, B.Hayden, G.Purdy, "High throughput synthesis and screening of chalcogenide materials for data storage", *EPCOS '05*, Cambridge, September, 2005 (Conference Publication)

R.J.Curry, C.C.Huang, A.K.Mairaj, R.E.Simpson, D.Hewak, "Advancing the application of planar chalcogenides", *ACerS. Glass & Optical Materials Div.*, Florida, November 2004 (Conference Publication)

A.K.Mairaj, R.J.Curry, M.Hughes, R.Simpson, K.Knight, D.W.Hewak, "Towards a compact optical waveguide device for active infrared applications", *SPIE Symposium on Optics and Photonics in Security and Defence*, London, pp. 5618-07, Oct 2004 (Conference Publication)

Publications Submitted

MSB Darby, R E Simpson, T May-Smith, DW Hewak, RW Eason, "Influence of Deposition Parameters on composition and refractive index of femtosecond and nanosecond pulsed laser deposited gallium lanthanum oxysulphide", *Journal of Non-Crystalline Solids*

M S B Darby, R E Simpson, T May-Smith, DW Hewak, RW Eason, "Femtosecond Pulsed Laser Deposition of Amorphous Gallium Lanthanum Oxysulphide Films", *9th International Conference on Laser Ablation (COLA)*, Tenerife, 24-28 September 2007 (Accepted)

Contents

Statement of Authorship ii

Contributions of Collaborators iii

List of Publications vi

Nomenclature xix

Acronyms xxi

Acknowledgements xxiii

1 Introduction **2**
- 1.1 Motivation . . . 2
- 1.2 Project Aim . . . 6
- 1.3 Thesis Synopsis . . . 6

2 Background **9**
- 2.1 Chalcogenide Glasses and Thin Films . . . 9
- 2.2 Chalcogenides . . . 10
- 2.3 Optical Properties . . . 12
  - 2.3.1 Photo-Induced Effects . . . 12
  - 2.3.2 Electrical Properties . . . 14
- 2.4 Data Storage . . . 19
- 2.5 Phase Change Data Storage . . . 21
  - 2.5.1 Optical Phase Change Media . . . 25
  - 2.5.2 Electrical Phase Change Devices . . . 29
- 2.6 Deposition of Chalcogenides . . . 31
  - 2.6.1 Thermal Evaporation . . . 32
  - 2.6.2 Sputtering . . . 32
  - 2.6.3 Pulsed Laser Deposition . . . 33
  - 2.6.4 Chemical Vapour Deposition . . . 34
- 2.7 High Throughput Methodology . . . 35
- 2.8 Characterisation Methodologies . . . 37
  - 2.8.1 Composition Measurements . . . 37
  - 2.8.2 Optical Characterisation . . . 40

2.8.3 Electrical Characterisation 41
2.8.4 Thermal Characterisation 42
2.8.5 Activation Energy Measurements 44
2.8.6 X Ray Diffraction 47
2.9 Summary 47

3 High Throughput Static Tester 49
3.1 Introduction 49
3.2 Set-up 52
3.2.1 Laser Selection 52
3.2.2 Filters 54
3.2.3 Lens Selection 55
3.2.4 Auto-Focus System 57
3.3 Development of the Static Tester 58
3.4 Initialisation Steps 60
3.4.1 Alignment 60
3.4.2 Manual Focussing 60
3.4.3 Misalignment Effects 62
3.4.4 Effects of Over Power 65
3.5 Application of Static Tester to a Graded Composition Film 67
3.5.1 Control Software 68
3.5.2 Phase Transform Kinetics Plots 71
3.6 Potential Development of the Static Tester 73
3.7 Summary 78

4 Ge:Sb:Te High Throughput Deposition and Screening 80
4.1 Introduction 80
4.1.1 Modification of $Ge_2Sb_2Te_5$ 84
4.1.2 Structure of Ge:Sb:Te 84
4.1.3 Electrical Properties 86
4.1.4 Optimisation of Ge:Sb:Te 87
4.2 Sputtered $Ge_2Sb_2Te_5$ Films -fabrication and characterisation 88
4.2.1 Composition Spread Trials 88
4.2.2 Crystallisation Temperature 89
4.2.3 Electrical Properties 89
4.2.4 X-Ray Diffraction 91
4.2.5 Crystallisation Time 91
4.2.6 Amorphisation Phase Change Kinetics 92
4.3 Compositional Spread Films 95
4.3.1 Composition Ge:Sb:Te Ternary 95
4.3.2 Crystallisation Temperature as a Function of Composition 95
4.3.3 Electrical resistivity as a function of composition 97
4.3.4 Refractive index as a function of composition 98
4.3.5 XRD as a function of composition 103
4.3.6 Crystallisation time as a function of composition 106

4.4 Discussion . . . 109
4.5 Summary . . . 119

5 BiSbTe System 121
5.1 Introduction . . . 121
5.2 Sputtered BiSbTe Films . . . 124
5.2.1 Crystallisation Properties . . . 124
5.2.2 Optical Properties . . . 127
5.2.3 Electrical Properties . . . 128
5.2.4 Crystallisation Time . . . 128
5.2.5 XRD . . . 132
5.3 Compositional Spread Results . . . 133
5.3.1 Electrical Resistivity as a Function of Composition . . . 133
5.3.2 Refractive Index as a Function of Composition . . . 135
5.3.3 XRD as a function of composition . . . 138
5.3.4 Crystallisation Time as a function of composition . . . 140
5.4 Discussion . . . 142
5.4.1 Sputtered BiSbTe Films . . . 142
5.4.2 Composition Spread BiSbTe Films . . . 146
5.5 Summary . . . 150

6 Ga:La:S phase Change Materials 151
6.1 Introduction . . . 151
6.2 Bulk Ga:La:S Glasses . . . 155
6.2.1 Synthesis . . . 155
6.2.2 Thermal Properties of Ga:La:S Bulk Samples . . . 156
6.2.3 Electrical Properties of Bulk Ga:La:S Glasses . . . 159
6.3 Ga:La:S Thin Film Deposition . . . 164
6.3.1 Ga:La:S Pulsed Laser Deposition . . . 164
6.3.2 Ga:La:S Sputtering . . . 173
6.4 Phase Change of Ga:La:S Thin Films . . . 177
6.5 Discussion . . . 178
6.6 Summary . . . 185

7 Conclusions and Future Work 186
7.1 Conclusion . . . 186
7.2 GaLaS Phase Change Materials . . . 187
7.3 BiSbTe Phase Change Materials . . . 188
7.4 Static Tester . . . 189
7.5 High Throughput Deposition and Analysis of the GeSbTe Phase Change System . . . 190
7.6 Further Work . . . 191

A Ge:Sb:Te Ternary Maps 198
A.1 Electrical Resistivity . . . 198
A.2 Refractive Index . . . 201

A.3 XRD Maps 204

B High Temperature Four Point Probe Fabrication 206

Bibliography 207

List of Figures

1.1 Number of publications cited in Inspec with the search terms 'Phase Change Memory' and 'Electrical Properties' as a function of time 5

2.1 Band Levels in a chalcogenide semiconductor 16
2.2 Typical I-V characteristics of threshold and memory switches 18
2.3 Filament forms after field exceeds V_{th} 18
2.4 Structure of a compact disk 20
2.5 Phase Transition energy schematic 25
2.6 Phase Transition energy schematic 25
2.7 The core components of a CD-RW [63] 26
2.8 Depiction of the two possible crystallisation mechanisms in phase change recording [63] 27
2.9 Crystallisation pulse (Red), Amorphising pulses (Blue) and Read pulse (Green) shown on axes of electrical current and pulse duration. 31
2.10 Schematic of a sputtering system showing atoms accelerated from a target to a substrate [73]. 33
2.11 A schematic showing how composition varying thin films have been synthesised 36
2.12 Transmitted X-ray intensity from a silicon substrate as a function of a Ge film layer depth. 39
2.13 Monte Carlo simulation of electron trajectories in a film and substrate accelerated at (a)5keV and (b)20keV) 40
2.14 Schematic of the in-line Four Point Probe used to measure the sheet resistance of chalcogenide thin films 41
2.15 The hotplate and CCD camera arrangement used to map reflected intensity as a function of sample and position. 43
2.16 A schematic of a typical Differential Thermal Analysis thermogram 44

3.1 Schematic of the semi-automatic static tester 52
3.2 Schematic of the automatic static tester 53
3.3 Schematic of the hardware connections for the automatic static tester . . 53
3.4 FEM model to demonstrate the quenching time as a function of spot size 56
3.5 Schematic of the focussing of a Gaussian Beam 56
3.6 An early measurement of the reflection change as a function of pulse duration for a $Ge_2Sb_2Te_5$ film. 59
3.7 An early single laser measurement of the reflection change as a function of pulse duration for a $Ge_2Sb_2Te_5$ film. 59

3.8 Detector voltage as a function of z) 61
3.9 A schematic of how an off axis beam could lead to large changes of incident angle 62
3.10 A model which shows the effect of incident angle and spot displacement as a function of the radial displacement from the objective's optical axis . 63
3.11 (a)The reflectance of a 300nm GST film as a function of incidence angle (b) The percentage increase in reflectivity between the crystalline and amorphous marks as a function of incidence angle. 64
3.12 (a) The amorphous and crystalline P, S and mean reflectivities of the plasmon stack (b) the amorphous and crystalline P, S and mean increase in reflectivity between the amorphous and crystalline states 64
3.13 Modulation as a function of z position. 66
3.14 Marks showing ablation as the sample is moved through the laser spot's focus. 66
3.15 The affect of power on the modulation as a function of z-position 66
3.16 The main control flow for compositional mapping of PTK data 69
3.17 The control flow for focussing. 70
3.18 The control flow for collecting PTK data. 71
3.19 PTK plot for crystallisation of as-deposited $Ge_2Sb_2Te_5$ 72
3.20 Reflectivity increase plotted as a function of time(a) and optical power(b) for an as-deposited $Ge_2Sb_2Te_5$ film 72
3.21 PTK plots as a function of relative substrate position 73
3.22 Mean reflection as a function of time plots as a function of relative substrate position 74
3.23 Crystallisation times for a 15% change in reflection, the colorbar shows the pulse time in nanoseconds 75
3.24 A schematic to show how the optical fibre components could be implemented in the static tester 77

4.1 Ge-Te Crystallisation time as a function of composition [113] 81
4.2 Phase Diagram for Ge-Te [114] 81
4.3 Phase Diagram for Sb-Te [116] 82
4.4 Phase Diagram for pseudo-binary system $Sb_2Te_3 - GeTe$ [118] 83
4.5 Ternary of Ge:Sb:Te. The pseudo binary line, the amorphous bulk and the fast growth compositional areas are indicated 84
4.6 Stacking models for the three congruent compounds along the $GeTe - Sb_2Te_3$ pseudobinary system 85
4.7 Compositions deposited by helicon sputtering of a $Ge_2Sb_2Te_5$ target and a an Sb Target. The compositions were measured by XRF spectroscopy. . 89
4.8 Reflected intensity of a broadband visible source from a sputtered $Ge_2Sb_2Te_5$ film as a function of temperature. 90
4.9 Sheet Resistance of a 200nm ±20nm $Ge_2Sb_2Te_5$ film as a function of temperature 90
4.10 XRD spectra of $Ge_2Sb_2Te_5$ thin films and target 91
4.11 Phase Change Kinetics Plots; (a) linear scale (b) Logarithmic scale 92
4.12 (a) Reflectivity as a function of time (b) Reflectivity as a function of power 93

4.13 Phase Change Kinetics plot for the amorphisation of $Ge_2Sb_2Te_5$ thin film 94
4.14 Phase Change Kinetics plot for the amorphisation of $Ge_2Sb_2Te_5$ thin film 94
4.15 GeSbTe Compositions synthesised 95
4.16 Ge:Sb:Te map of crystalline areas at $273°C$. The red area denotes compositions which have phase changed. 96
4.17 Ge:Sb:Te transition temperature map (sample 1310) 96
4.18 Ge:Sb:Te reflected intensity along the pseudobinary tie line. Where x represents the fraction of $GeTe$ to Sb_2Te_3 $((GeTe)_x(Sb_2Te_3)_{x-1})$ 97
4.19 Ge:Sb:Te crystallisation transition temperature along the pseudo-binary tie line. Where x is defined by $((GeTe)_x(Sb_2Te_3)_{x-1})$ 97
4.20 Sample 1309 sheet resistance; (a) as-deposited (b) annealed at $272°C$ . . . 98
4.21 Sheet Resistance of sample 1309 after annealing at $273°C$; where x is defined by $GeTe$ to Sb_2Te_3 $((GeTe)_x(Sb_2Te_3)_{x-1})$ 99
4.22 Sample 1310 as-deposited refractive index and extinction coefficient (assuming infinitely thick film) 100
4.23 Sample 1310 refractive index and extinction coefficient after annealing at $272°C$ (assuming infinitely thick film) 101
4.24 Sample 1310 assuming infinitely thick; where x is defined by $GeTe$ to Sb_2Te_3 $((GeTe)_x(Sb_2Te_3)_{x-1})$ 102
4.25 Ternary plot indication compositional coverage of the amorphous spectra shown in (b) 103
4.26 Ternary plot (a) showing the areas which have the as-deposited crystalline phase shown by the diffractogram of (b) 104
4.27 Ternary plot (a) showing the location of spectra (b) for sample annealed at $270°C$ 104
4.28 Compositional coverage and associated diffraction pattern of a third crystal phase as deposited 104
4.29 Compositional coverage and associated diffraction pattern of a fourth crystal phase after annealing at $270°C$ 105
4.30 Reflectance as a function of $ZnS{-}SiO_2$ film depth for a SiO_2/GST/$ZnS{-}SiO_2$ structure. The green line shows the percentage change in reflectance as a function of $ZnS - SiO_2$ layer depth. 106
4.31 Crystallisation time as a function of Ge, Sb and Te. The color bar indicates time in nanoseconds. 108
4.32 The influence of tellurium on the Sheet Resistance of Ge:Sb:Te 112
4.33 Change in sheet Resistance, R_s, as a function of composition. 113
4.34 The influence of tellurium on (a) refractive index, n, and (b) extinction coefficient, k, of Ge:Sb:Te 115
4.35 Reflectance change at, 532nm normal incidence, as a function of composition 116
4.36 The power-pulse duration threshold for crystal growth 116
4.37 The deterioration of increase in reflection as a function of cycle 117

5.1 Complete Erasure Time (CET) as a function of mark size for Ge doped Sb-Te phase change materials with various Sb/Te ratios [147] 122
5.2 $Bi - Te$ Phase Diagram 123

5.3 Sputtered BiSbTe compositions measured by X-Ray Fluorescence (XRF) spectroscopy . . . 124
5.4 Increase in reflectivity at 633nm for $(SbTe)Bi$, $(Sb_2Te_3)Bi$ and $(Sb_8Te_2)Bi$ films as a function heating rate . . . 125
5.5 (a)Reflectivity as a function of temperature for $(Sb_8Te_2)_{97}Bi_3$ films heated at 5, 10 ,15, 20 and 25°$Cmin^{-1}$, (b) Differential of reflectivity as a function of temperature for $(Sb_8Te_2)_{97}Bi_3$ films heated at 5, 10, 15, 20 and 25°$Cmin^{-1}$ . . . 126
5.6 The Arrhenius plots used in the non-isothermal Kissinger analysis of $(Sb_8Te_2)Bi$ films . . . 126
5.7 Refractive index, n, and extinction coefficient, k, before and after annealing at 532nm. (Lines linking the data points have been included to aid the reader. . . . 127
5.8 $(Sb_8Te_2)_{x-1}Bi_x$ electrical resistivity as a function of Bi content . . . 128
5.9 Phase Transform Kinetics (PTK) plots of a Sb_8Te2 as-deposited films doped increasing proportions of bismuth . . . 129
5.10 $(Sb_8Te_2)_{x-1}Bi_x$ crystallisation time . . . 130
5.11 Crystallisation time as a function of Bi concentration $SbTe$ and Sb_8Te_2 based phase change films . . . 131
5.12 X-ray diffraction spectra as a function of Bi content. (a) as-deposited (b) annealed . . . 132
5.13 BiSbTe compositions synthesised and measured by EDX . . . 133
5.14 Electrical sheet resistance, R_s as a function of composition (a) as-deposited state, (b) annealed state and (c) factor decrease . . . 134
5.15 Electrical sheet Resistance, $R_{,s}$ of BiSbTe films . . . 135
5.16 Refractive index, n, and extinction coefficient, k, for as-deposited Bi doped Sb-Te compositions at 532nm . . . 136
5.17 Refractive index, n, and extinction coefficient, k, for Bi doped Sb-Te compositions annealed at 200°C at 532nm . . . 137
5.18 (a) Compositions of observed spectra in the as-deposited state (b)Compositions of observed spectra in the as-deposited state (c) Corresponding observed spectra. KEY: Spectra 1: red, Spectra 2: blue, Spectra 3: green, Spectra 4: yellow, Spectra 5: cyan, Spectra 6: magenta. . . . 139
5.19 The static tester (a) crystallisation time (ns), (b) the nucleation time (ns) and (c) pulse energy for crystallisation . . . 141
5.20 The A7-type which has been assigned to the crystallised Sb_8Te_2:Bi compositions. The atomic positions are marked by the red circles. The black and blue lines represent, respectively, the long and short atomic bonds of the R$\bar{3}$m space group. . . . 143
5.21 Increase in reflectivity factor as a function of composition for 532nm light at normal incidence . . . 148
5.22 The refractive index as a function of tellurium for $< 1\%$ Bi and approximately 10% bismuth . . . 149

6.1 The covalent Ga_2S_3 crystalline network [28] . . . 153
6.2 Effect of La_2S_3 on Ga_2S_3[28] . . . 154

6.3 Phase Diagram for (a) Ga_2S_3-La_2S_3 and (b) Ga_2S_3-La_2O_2S systems. The shaded area shows bulk glass forming compositions. (Redrawn from Flahaut et al.[162]). . . . 155
6.4 Glass transition (T_g), crystallisation (T_p) and Melting (T_m) temperature ($°C$) as a function of composition. . . . 157
6.5 Glass transition (T_g), crystallisation (T_p) and Melting (T_m) temperature as a function of Ga:La ratio. . . . 158
6.6 Arrhenius plot used in Kissinger analysis to calculate the crystallisation activation energy of GaLaS glass . . . 158
6.7 Viscosity as a function of Ga/S and S/O at 640$°C$ . . . 159
6.8 The experimental setup used to measure the current as a function of voltage 160
6.9 Samples 1, 2 and 3 glass and crystalline current for 500V increments at 30s intervals. Blue shapes- glassy discs, red and green shapes- crystalline discs. For multiple measurements; circles- 1st measurement, triangles- 2nd measurement . . . 161
6.10 Average resistance of GaLaS glasses and crystalline samples for 3 different Ag concentrations. The resistivity was measured over a 30s period for each 500V increase. . . . 162
6.11 Absorption spectra of Ag doped GaLaS at the electron band edge. . . . 162
6.12 Tauc analysis to calculate the electronic band-gap of Ga:La:S glass. For dashed line use left y-axis for solid line use right y-axis. . . . 163
6.13 Tauc analysis of (a) glassy and (b) crystalline Ga:La:S bulk materials . . 164
6.14 Ternary diagrams showing the effect of fluence, material path length and deposition pressure on the resultant films' composition for films deposited by nano-second pulsed laser deposition. . . . 166
6.15 Ternary diagrams showing the effect of fluence, material path length and deposition pressure on the resultant films composition for films' deposited by femto-second pulsed laser deposition. . . . 167
6.16 Composition spread across a single silicon substrate for an off axis deposition from a Ga:La:S target. . . . 168
6.17 Tauc Analysis of GaLaS films prepared by femto-second pulsed laser deposition under different conditions . . . 170
6.18 Optical band-gap, E_g, of Ga:La:S thin films deposited by femto-second and nano-second pulsed laser deposition . . . 171
6.19 Refractive index at 1.5μm of Ga:La:S thin films deposited by femto-second and nano-second pulsed laser deposition . . . 171
6.20 GLS PLD electrical test structure . . . 172
6.21 Electrical resistivity of GLS prepared by nanosecond PLD as a function of position on the substrate. Circles indicate compositions that switched. The graph legend shows the measured values of electrical resistivity (Ωm). 172
6.22 XRD spectrum of a Ga:La:S:Cu film in its as-deposited state . . . 174
6.23 (a) Tauc analysis curves used to calculate the (b) energy gap, E_g of the Ga:La:S:Cu films as a function of oxygen fraction to argon background sputtering gas. . . . 175

6.24 (a) A typical measurement of transmission of 633nm laser through GaLaS thins films fabricated by pulsed laser deposition and on the right hand side, XRD spectra for asdeposited (top) and annealed (bottom) states. Figure (b): Ternary showing the crystallisation temperature as a function of composition. 176
6.25 The set-up used to measure the Ga:La:S:Cu I-V characteristics 177
6.26 Current Voltage of a 200nm thick GaLaSCu sputtered film 178
6.27 PTK plot of Ga:La:S:Cu sample. 178
6.28 (a) Schematic of the cell structure used for the Finite Element Modelling and (b) an example of a large cell heat distribution 183
6.29 Temperature of crystalline cell as a function of pulse duration for (a) Ga:La:S:Cu and (b) $Ge_2Sb_2Te_5$ 184

7.1 Scanning Electron Microscope image of a nanowire test structure for sulphide based phase change memory materials (developed in collaboration with the University of Taiwan) 187
7.2 Absorption as a function of depth simulation for GLS at 405nm and 658nm and $Ge_2Sb_2Te_5$ at 658nm 193
7.3 First generation high throughput electrical chip 193
7.4 Thermogram modelled using Finite Element simulation of the non-isothermal heating stage 196
7.5 Heating rates on the surface of a silicon substrate atop of the non-isothermal heating stage 196

A.1 Sample 781 Sheet Resistance 199
A.2 Sample 768 Sheet Resistance 200
A.3 Sample 792 as-deposited Sheet Resistance 200
A.4 Sample 792 after heating to 150°C 200
A.5 Sample 781 refractive index, n, (532nm) and extinction coefficient, k, as a function of temperature 202
A.6 Sample 792 refractive index, n, (532nm) and extinction coefficient, k, as a function of temperature 203
A.7 Sample 1306 refractive index, n, (532nm) and extinction coefficient, k, as a function of temperature assuming infinitely thick HEATED(633nm) . . 203
A.8 Observed as-deposited XRD Spectrum 1 204
A.9 Observed as-deposited XRD Spectrum 2 204
A.10 Observed as-deposited XRD Spectrum 3 204
A.11 Observed as-deposited XRD Spectrum 4 205
A.12 Observed as-deposited XRD Spectrum 5 205
A.13 Observed as-deposited XRD Spectrum 6 205

B.1 Schematic of the high temperature four point probe 206

List of Tables

1.1 Comparison of data storage technologies based on 180nm lithography. Data taken from manuscript prepared by Stefan Lai (Intel) and Lowery Tyler (Ovonyx) [4] . . . 4

2.1 Amorphous chalcogenide systems grouped by class [21] . . . 12
2.2 The advantages and disadvantages of various thin film deposition techniques [73] . . . 35
2.3 Compositional spread characterisation techniques . . . 37

3.1 Computer controlled static tester hardware . . . 69
3.2 Specification of Static Tester . . . 79

4.1 Influence of common dopants on Ge:Sb:Te . . . 85

5.1 Summary of crystallisation temperature, refractive index and electrical resistivity measurements. . . . 132

6.1 Composition of Ga:La:S:Cu films deposited by RF sputtering with and without a Dark Space Shield (DSS) . . . 173
6.2 Energy Gap, E_g, and, where measurable, electrical resistivity as a function of O:Ar ratio during sputter deposition . . . 174

Nomenclature

α	Heating Rate
α	Polarizability
D^0	Neutral, Dangling Bond, Point Defect
D^+	Positively Charged Dangling Bond, Point Defect
D^-	Negatively Charged Dangling Bond, Point Defect
Δ	In ellipsometry, the difference in phase difference of the parallel and perpendicular component of an electromagnetic wave after a reflection.
E_a	Activation Energy
E_c	Activation Energy for Crystallisation
E_f	Fermi Energy Level
E_g	Energy Gap
γ	Interface Energy
d	Separation of atomic layers
D	Diameter (of a lens for the diffraction limit)
ΔG	Gibbs Free Energy
dof	Depth of Field
I	Electric Current
I_v	Crystal Nucleation Frequency (per unit volume)
k	Extinction Coefficient
k_b	Boltzmann Constant
λ	Wavelength
n	Refractive Index
N_A	Avogadro's Number
$N(r)$	Number of nuclei with critical radius
NA	Numerical Aperture
Ψ	In ellipsometry, the angle whose tangent is the ratio of the magnitudes of the total reflection coefficients
P	Power
ρ	Particle Density
r_c	Critical Radius for crystal nucleation

R	Resistance
R	Reflection
ΔR	Fractional Increase in Reflection
R	Gas constant, $R = \frac{k_b}{N_A}$
R_s	Sheet Resistance
σ	Electrical Conductivity
s	Refractive Index of Substrate
t	Time
θ	Angle of ray relative to normal
T_g	Temperature of Glass Transition
T_m	Temperature of Melting
T_m	Minimum Value of Transmission
T_M	Maximum Value of Transmission
T_p	Temperature of Peak Crystallisation Rate
T_s	Transmission of Substrate
V	Electric Voltage
w	Beam waist radius
W	Polaron Energy
u	Crystal Growth Rate
x	Fraction of volume crystallised

Acronyms

4PP	Four Point Probe
ADC	Analogue to Digital Convertor
AF	Auto Focus
AFS	Auto Focuss System
AOS	All Optical Switch
BD	Blue-ray Disk
CD	Compact Disk
CCD	Charge Coupled Device
CET	Complete Erasure Time
CMOS	Complementary Metal Oxide Semiconductor
CVD	Chemical Vapour Deposition
DAQ	Data Acquisition
DRAM	Dynamic Random Access Memory
DSC	Differential Scanning Calorimeter
DSS	Dark Space Shield
DTA	Differential Thermal Analyser
DVD	Digital Versatile Disk
EDX	Energy Dispersive X-ray analysis
EDS	Energy Dispersive Spectrometry
EEPROM	Electrically Erasable Programable Read Only Memory
EPROM	Erasable Programable Read Only Memory
EXAFS	Extended X-ray Absorption Fine Structure
FBG	Fibre Brag Grating
FCC	Face Centred Cubic
FEM	Finite Element Model
FeRAM	Ferroelectric Random Access Memory
FWHM	Full Width Half Maximum
fs	Femto Second
GLS	Ga:La:S
GST	$Ge_2Sb_2Te_5$

GPIB	General Purpose Interface Bus
HCP	Hexagonal Close Packed
HD-DVD	High Density Digital Versatile Disk
HWP	Helicon Wave Plasma
MRAM	Magnetoresistive Random Access Memory
ns	Nanosecond
PCM	Phase Change Material
PLD	Pulsed Laser Deposition
PRAM	Phase Change Random Access Memory
PROM	Programmable Read Only Memory
PTE	Power Time Effect
PTK	Phase Transform Kinetics
PVD	Physical Vapor Deposition
RAM	Random Access Memory
RF	Radio Frequency
RIBE	Reactive Ion Beam Etcher
ROM	Read Only Memory
RS232	Recommended Standard 232, serial transmission
SNR	Signal to Noise Ratio
TMA	Thermal Mechanical Analyser
TEM	Transmission Electron Microscope
WORM	Write Once Read Many
UHV	Ultra High Vacuum
XANES	X-ray Absorption Near Edge Structure
XRD	X-Ray Diffraction
XRF	X-Ray Fluorescence Spectroscopy

Acknowledgements

I am indebted to my colleagues in the Optoelectronics Research Centre, School of Chemistry, Ilika Technologies and the Center applied Near-Field Optical Research who were encouraging and helpful throughout my PhD research. I am particularly grateful to Dan Hewak whose supervising style allowed me sufficient freedom to make the project my own but was always available for discussion throughout past four yeas.

The weekly meetings between Ilika technologies, the School of Chemistry and the ORC provided many interesting and often enlightening discussions during the latter half of this research; I would therefore like to thank Brian Hayden, Samuel Guerin, Brian Webb, Jan Richter, Jonathan Fitzmaurice and James Withnall. I am also grateful to Graeme Purdy for Ilika's funding of the static tester.

During the third year of my PhD I spent ten extremely enjoyable weeks in Japan as part of a JSPS summer scholarship. I am specially appreciative of this opportunity which allowed me to make so many new friends and colleagues. I would particularly like to thank Tominaga san and Paul Fons for their guidance, enthusiasm and stimulation throughout the time at CAN-FOR and Shima-san for training me on much the equipment which I used during the placement.

Studying at Southampton has allowed me to make many new colleagues and friends from across the world. I am sure they have all contributed, often unwittingly, to the research conducted for this thesis and for that and their support i am grateful. I would like to give a special thank you to Adriana Salgado whose has been enthusiastic, understanding and supportive throughout the latter stages of the research and during the writing of this thesis. My final thanks must go to my family. In particular, my dad, gran & grandad and brother for all of their encouragement throughout my education and my grandad for reading the thesis and encouraging me to consider a career in science.

Chapter 1

Introduction

1.1 Motivation

The world has become dependant on the storage of information. A visionary talk in 1959, entitled 'There's plenty of room at the bottom', by Richard Feynman postulated that the entire history of printed text could be stored in a volume of material which measured $100\mu m$ by $100\mu m$ by $100\mu m$ [1]; he allowed 125 atoms to store each bit. In modern times, binary data is stored through a multitude of technologies spanning many disciplines of science. Historically, nonvolatile optical and electrical data storage technologies exploit very different physical principles. Electrical storage is achieved by trapping electrons on a conductor and isolating them with oxide material[2]. In contrast, rewritable optical storage media rely on crystal-amorphous phase transitions of a thin bi-stable chalcogenide film; materials which exhibit this property are known as 'Phase Change Materials' (PCM).

The astounding energy and investment, over the past two and half decades, into optical data storage devices and media has resulted in a mature industry worth billions of dollars. Despite this wide commercialisation, the first demonstration of the switching phenomena of these materials actually focussed on the electrical properties [3]. The chosen materials for rewritable optical data storage are based on compounds of tellurium, with $AgInSbTe$ and $Ge_2Sb_2Te_5$ being two well researched examples. In recent years, with the increased scaling to smaller feature sizes, conventional electrical storage technologies, such as Flash, are anticipated to become impractical. This has allowed renewed vigor for alternative technologies such as Magnetoresistive Random Access Memory (MRAM), Ferroelectric (FeRAM) and Phase Change RAM (PRAM) which is the topic of this thesis. S. Lai of Intel produced a useful table to review these technologies. Some of its relevant data is presented in table 1.1 [4]. The table compares a $Ge_2Sb_2Te_5$ PRAM cell

with the well developed Dynamic Random Access Memory (DRAM) and Flash technologies, as well as the novel competing technologies MRAM and FERAM. The potential of PRAM is clear, it has competitive read/write times, comparatively low energy operation and good potential for scaling to reduced dimensions. The data storage principle for PRAM is also conceptually clear (phase change mechanism is discussed in chapter 2); this is another advantage over other storage technologies.

Much of the research reported for PRAM concentrates on the well known optical storage materials but their applicability to electrical storage is not straight-forward. One of their major drawbacks is their inherent high electrical conductivity which results in high power consumption [5]. However, their efficiency is improved with decreasing device dimensions[6]; this is an appealing feature to prospective chip manufacturers.

New optical data storage technologies concentrate on the near-field operation[7]. Material suitability for near-field media is an extremely active area of study[8, 9, 10]. As the size of the optically induced mark is reduced beyond the diffraction limit, materials which were before unsuitable, because their crystal growth time was long, become increasingly attractive. This is especially true if their crystals required a comparatively short nucleation time. The aforementioned antimony-tellurium based materials may not be the most suitable when writing to much smaller scales.

A statistical analysis of over 500 patent documents, by Savransky and Wei [11], has been performed for the PCM field. It revealed that the semiconductor PCM technology is currently in a period of extreme growth. Generally speaking, according the analysis employed by Savransky, the number of patents generated increases until the latter stages of a technologies maturity. The analysis also indicates that much of the generated inventions concentrate on only 10% of the available spectrum of problems that need to be solved. However, the paper did not continue to specify possible PCM areas which have not yet been fully targeted. Patent generation is a clear indication of novel research and thus this is a further, quantative, indication that phase change memory research is valid and that novel ideas and important results are possible for many years to come.

It is also interesting to look at the number of publications as a function of time, to establish if a technological field is yielding fruitful research. To check this, the Inspec database has been used to search for all of the documents with the terms ‘electrical properties’ and ‘phase change memory’. A bar chart is displayed in figure 1.1. It is clear that the number of papers published increases rapidly from the year 1994, until the time of writing, with the number increasing on average by approximate 30% every two years. This is consistent with the patent literature, statistical, analysis by Savransky, which also identified a transition of the technology into a growth stage between the years of 1991-1994.

	DRAM	**FLASH**	**PCRAM**	**MRAM**	**FERAM**
Volatile/Non-Volatile	Volatile	Non-volatile	Non-volatile	Non-volatile	Non-Volatile
Endurance/Read	∞/∞	10^6 $/\infty$	10^{12} $/\infty$	10^{12} $/\infty$	$10^{12}/10^{12}$
Direct Overwrite	yes	no	yes	yes	yes
Bit/Byte Write Erase	yes	block	yes	yes	yes
Dynamic Range	100-200mV	Δ Current	$10\times-100\times$R	20-40%R	100-200mV
Programming Energy	medium	high	low	medium	medium
Write/Erase/Rad time	50ns/50ns/50ns	$1\mu s$/1-$100ms$(block)/60ns	$10ns/50ns/20ns$	$30ns/30ns/30ns$	$80ns/80ns/80ns$
Transistors	low performance	high voltage	high performance	high performance	low performance
CMOS Compatible	bad	ok, high voltage	good	?	ok, high voltage
Scaling limit	capacitor	tunnel oxide	lithography	current density	polarizable capacitor
Multi-bit storage	no	yes	yes	no	no
3D potential	no	no	yes	no	no
Cost per a bit	low	high	low	?	high

Table 1.1: Comparison of data storage technologies based on 180nm lithography. Data taken from manuscript prepared by Stefan Lai (Intel) and Lowery Tyler (Ovonyx) [4]

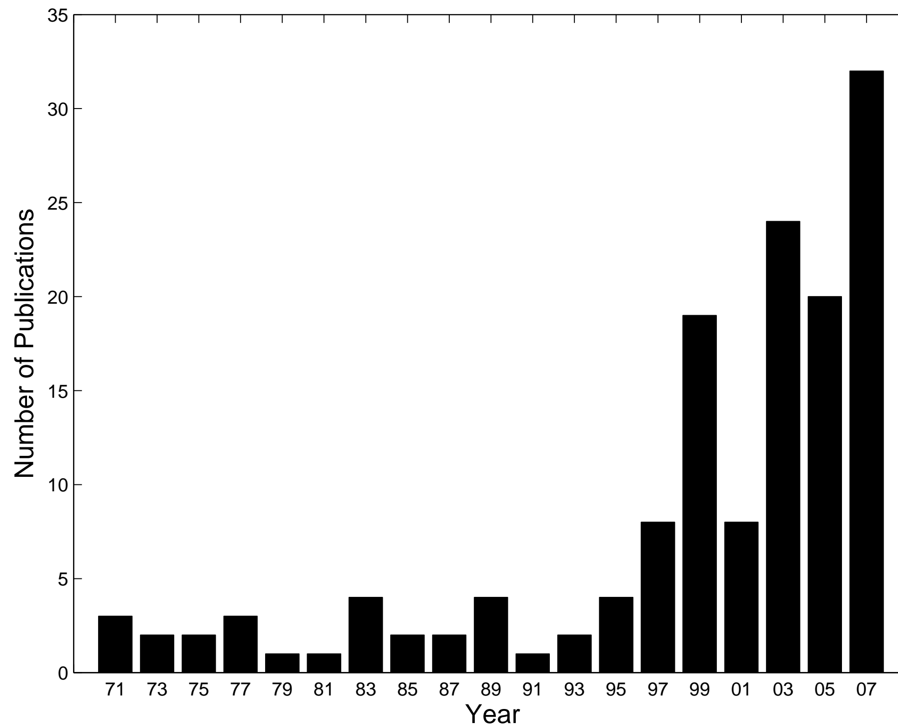

FIGURE 1.1: Number of publications cited in Inspec with the search terms 'Phase Change Memory' and 'Electrical Properties' as a function of time

Despite the many years of research, there still remain some important physical phenomena to be understood. Possibly the most important of which, for the PRAM, is the origin of threshold switching whereby the phase change material shows a high conductivity on application of an applied electrical potential without undergoing a phase transition. Similarly for optical data storage, controversy still surrounds the understanding of the actual phase switching dynamics in $Ge_2Sb_2Te_5$ [12, 13]; resulting in intense modelling and optical pump, X-ray synchrotron probe experiments by a number of groups[14, 12].

To summarise, the key areas motivating, world wide, research into phase change data storage materials are:

- New materials which outperform current phase change materials upon scaling to smaller dimesions.
- Scaling also enforces engineering of novel device and media structure which in-turn invokes material performance questions.
- Novel, high performance, materials for electrical phase change materials.
- Compositional effects on switching and threshold voltage.
- Full understanding of the phase change mechanism on an atomic scale.

1.2 Project Aim

> *"The advancement of phase change data storage materials for both optical and electrical applications."*

Much of the phase change data storage material research has been focussed on the tellurium based materials because it is a good glass former [15] and its glasses tend to have a lower glass transition temperature than Se and S [16]. However, with the increase in data storage densities, corresponding reduced optically written mark and electrically addressed cell dimensions, novel materials which operate at higher temperatures are becoming increasingly feasible. Further, the crystallisation time of $Ge_2Sb_2Te_5$ is known to be dominated by the time taken for crystal nucleation; thus its crystallisation time is independent of mark or cell dimensions. However the crystallisation time for other, novel, materials is known to be dependent on the time taken for the crystal to grow, thus the crystallisation time reduces with the mark dimensions. Therefore these materials have great potential for future PCM devices and media.

Material discovery and optimisation is a time consuming task. For this reason, combinatorial and high throughput methodologies are appealing for efficient evaluation of phase change memory materials. Therefore one of the targets of this project was to employ, where possible, combinatorial and high throughput techniques. Further objectives are summarised below:

- Design, build and characterise a high throughput static tester to analyse the crystallisation dependence on compositions.
- Characterise the optical, electrical and crystallisation of GeSbTe phase change films, deposited by combinatorial techniques.
- Analysis of the effect of Bi on SbTe films through single composition deposition and combinatorial techniques. Compare with Bi effect on $Ge_2Sb_2Te_5$ films.
- Assess the potential of GaLaS based films for optical and electrical data storage.
- Assess pulsed laser deposition for combinatorial deposition of Ga:La:S materials.

1.3 Thesis Synopsis

The aims of this project have been described in this chapter. This thesis details original research aimed at fulfilling the objectives outlined in section 1.2. Chapter 3 describes

the design and development of a 'static tester' system to examine the crystallisation properties of phase change films. Two of the four experimental chapters (4 and 5) examine samples of ternary systems, which were prepared by the School of Chemistry and Ilika Technologies LTD; though the choice of ternary system, the composition range and the substrate was my own. Chapter 6 describes a novel high throughput approach to deposition of Ga:La:S films and the phase change properties of such films.

The thesis has been organised such that when a new material system is introduced the background research relevant to the material is given at the beginning of the chapter. In order to guide the reader, a detailed overview of each succeeding chapter is now presented.

Chapter 2 gives a general background to chalcogenide glasses. It goes on to focus on some of the interesting optical and electrical properties of such glasses, before giving a detailed description of the phase change mechanism of chalcogenides. The chapter aims to review what has been done in the area of chalcogenide phase change and discusses methodologies of deposition and characterisation. Most of these methodologies have been employed at some point throughout the course of this project. The concept of high throughput and combinatorial methodology is also introduced and particular emphasis is given to the approach used to achieve the composition spread samples, analysed in chapters 4 and 5.

Chapter 3 discusses a means of measuring the crystallisation time of phase change films using an optical pump probe system called a static tester. A static tester was implemented for this research thus the design choices are stated and reasoned. The principles used during the set-up of the system are also discussed and the effects of a poorly set-up system are shown such that system and measurement errors can be identified. The software developed for this research is described and its operation outlined. The chapter ends by showing some typical measurements achieved by both manual and fully automated operation. The design of a novel optical fibre based system is also introduced as a future project. The advantages of such a system are discussed.

Chapter 4 is the first of two chapters which take advantage of the composition spread approach. The main aim of this chapter is to show that such an approach is a viable means of material optimisation for phase change applications. The compositionally spread, thermally evaporated, films are compared against both sputtered $Ge_2Sb_2Te_5$ standards and results in the available literature. Several characterisation methodologies including, ellipsometry, four-point probe analysis, X-ray diffraction, minimum crystallisation time and temperature have been mapped against composition, such that compositional trends can be analysed.

Chapter 6 aims to assess the phase change capability of GaLaS based films. Sputtering and Pulsed Laser Deposition (PLD) have been used to deposit thin films of the material. The deposition parameters are optimised such that amorphous films can be realised. For the first time, PLD of GaLaS is deliberately used to achieve compositionally spread samples and a possible alternative high throughput deposition technique is suggested. Both the electrical and optical phase change properties of the films are examined and the system is critically examined as a potential phase change memory material.

Chapter 5 introduces the Bi doped, Sb:Te system. The affect of Bi on the phase change properties of Sb:Te films is discussed. The chapter can be thought of in two parts. The first half discusses films, which were deposited during a summer research secondment to the Center of Applied Near-Field Optical Research (CAN-FOR) at the Japanese National Institute of Advanced Industrial Science and Technology (AIST). The phase change characteristics and physical film properties are presented. The second half of the chapter employs high throughput methods to examine a compositional area surrounding one of the interesting sputtered samples. A novel, fast-crystallising, composition is identified to show the potential for, high data transfer speed, future, chips and media. The effect of Bi on this system is compared to published data of its effect on $Ge_2Sb_2Te_5$

The final chapter summarises the results of this work and suggests areas of possible advancement and work generated as a result of this research.

The principal highlights of this thesis which contributed to fulfilling the outlined objectives are:

- Design and development of a fully automated tool for efficiently assessing the crystallisation dynamics of compositionally spread, phase change films.
- A combinatorial study of Ge:Sb:Te phase change films over the widest ever reported compositional range.
- Demonstration of reduced crystallisation time of Sb:Te based films through the incorporation of Bi.
- The discovery and characterisation of a novel sulphur based phase change materials highly suited for future nanoscale electrical PRAM (UK Patent No. GB2433647).

Chapter 2

Background

2.1 Chalcogenide Glasses and Thin Films

The term glass usually refers to the product resulting from inorganic materials which have been fused together at temperatures above their individual melting points and cooled at a rate which prevents crystallisation occurring. Commonly "glass" is used to describe silica, SiO_2, based materials but many other materials can also exist in a glassy[1] state [18].

Some oxides are known to exist in a glassy state without addition of further chemicals. These are known as glass network formers. They generally have cation-oxygen bonds with high ($> 50\%$) covalent behavior. Conversely, at the other extreme are materials in which more than 70% of the cation-oxygen bonds have an ionic character; these are not natural glass formers. Intermediate glass formers lie between these two extremes. They are known to form glasses when melted with at least one other oxide of sufficient proportion[18].

Electrical conduction in glasses has been studied for more than 100 years and, essentially, there are two chief mechanisms through which electrical conduction is possible: ion transport and electron conduction. Electron conduction can be described by consideration of an energy band model. In good conductors, like metals, the electrons in the outer shells of the atoms are only loosely bound to the nucleus. At low temperatures most of the electrons have energies below the Fermi-level, E_f. If an electric field is applied to the metal, electrons with energies close to E_f only require a small amount

[1] This report will follow definitions used in Malcolm D. Ingram's review of the electrical properties of glasses [17]. That is "glasses" are taken to mean bulk solids quenched from a melt, and exhibit a glass transition temperature, whereas "amorphous" materials include thin films deposited by sputtering or evaporation.

of additional energy from the electric field to reach nearby empty energy states. Thus, under a small electric field the electrons within a metallic conductor are free to move because there are many empty unoccupied energy states available close to the occupied energy levels.

Conventional glasses, like silica, are poor electrical conductors. The unoccupied energy level (conduction band) is not close to the occupied level (valence band). In fact, for silica the energy gap between these two levels is approximately $10eV$. At room temperature the energy given to the electrons is $k_B T = 0.025eV$. Thus the proportion of electrons thermally excited to the conduction band is very low. The overall electrical conductivity is small resulting in a high value for its resistivity.

Materials which have a band-gap of a few eV are classed as semiconductors. Since the energy gap is small an appreciable number of electrons can be thermally excited from the valance band into the conduction band. There are many empty states in the conduction band, thus a small applied electric field can promote the electrons resulting in a moderate current. At higher temperatures more electrons are thermally excited and the conductivity rises rapidly. The chalcogenide glasses investigated for this report can be regarded as amorphous semiconductors, their band-gap can range between 1 and 3eV [19].

Ionic conduction arises from the movement of negative (cations) or positive (anions) ions when an electric field is applied across an ionic material. The cations or ions are effectively placed in gaps within a glassy structure. The gaps allow the ions an extent of freedom to move under the influence of an electric field. In a typical vitreous material, below the glass transition temperature the ionic conduction tends to be thermally activated and it is possible to calculate an activation energy. At temperatures greater than the glass transition temperature this fitting to an Arrhenius plot is not observed[17].

2.2 Chalcogenides

The name chalcogenide originates from the Greek word chalcos - 'ore' and gen - 'formation'. Thus the term chalcogenide is generally considered to mean 'ore former' [20]. Chalcogenides can exist naturally as minerals; two of the most well known being FeS_2 (pyrite) and $AuTe_2$. In fact $AuTe_2$ was the chief reason for the name given to the gold-rush town 'Telluride' in Southwest Colorado. The elements of group six of the periodic table are known as the chalcogens. The group consists of oxygen, sulphur, selenium, tellurium, polonium and ununquadium (although the existence of this element is still to be confirmed). Often oxygen is not included in the chalcogenide category. There is a

historic and scientific reason for this division. Historically, oxide materials are the oldest-known glass forming systems, especially in silica; it has thus become tradition to treat them separately from more recently discovered chalcogenide compounds. Scientifically oxide materials behave rather differently from other chalcogenides. This difference is present in the form of band-gap energies. As previously discussed, SiO_2 has a band-gap around 10eV, yet other chalcogenides have band-gaps between 1eV and 3eV; they are semiconductors[21].

Chalcogenide glasses have many interesting properties; optically they are often transparent from the visible spectrum up into the infrared, they can readily be deposited in the form of thin and thick films, they can exist as glasses over a wide composition range with other varying physical properties and they can be applied to many different applications, from optical transmission to electronic taste sensors [22]. Some tellurium based glasses can be transparent out to 20μm [23]. This long wavelength transmission is in part due to the material's low phonon energy which is a characteristic of materials with heavy ions and weak bond-strengths[24] . They also have a high nonlinear refractive index and hence could be useful as the active element in an All Optical Switch (AOS)[25]. This has been demonstrated in an As_2S_3 material [26].

Although chalcogenides can exist over a wide range of compositions, not all of them exist in a glassy form. It is often possible to find materials with which these non-glass forming compositions can be alloyed in order to form a glass. The model of a binary glass-forming chalcogenide is considered to be analogous to silica; there are two chalcogen (group 6) elements bonded to a single group 4 element. Another common class of chalcogenides have glass forming regions where three chalcogens are bonded to two group 5 elements [21]. Most stable binary chalcogenide glasses are compounds of a chalcogen and a group 4 or 5 element. This allows a wide range of atomic ratios. Ternary glasses allow a larger variety of atoms to be incorporated into the glass structure; thus giving even greater engineering capacity [27].

Amorphous chalcogenide materials can be broadly classed by the type of atoms to which they bond to form amorphous systems [21]. Table 2.1 lists the chalcogenide classification and gives some common examples of the type of chalcogenide which falls into the category. A review by Elliott compares the typical properties of these different chalcogenide classes. It should be noted that Ga_2S_3 is not listed as an amorphous chalcogenide compound, this particular compound occurs as a crystal [28]. The relevance of this is discussed in chapter 6.

As_2S_3, also termed orpiment, is an example of a stable binary glass, it preferentially exists as a glass whereas tellurium based materials are more likely to exist as a crystal [27]. Looking down the chalcogen group of the periodic table from oxygen to polonium,

Class	Examples
Pure chalcogenide	S, Se, Te, S_xSe_{1-x}
Pnictogen-chalcogen (V-VI)	As_2S_3, P_2Se
Tetragen-chalcogen (IV-VI)	$SiSe_2$, GeS_2
III-VI	B_2S_3, $In_xSe_1 - x$
Metal chalcogenide	MoS_3, WS_3, Ag_2S-GeS_2
Chalco-halides	As-Se-I, Ge-S-Br, Te-Cl

Table 2.1: Amorphous chalcogenide systems grouped by class [21]

the atomic bonds become more metallic and isotropic, the energy gap decreases and electronegativities decrease. As a result, the electronic conductivity increases [27].

Some chalcogenides are stable in both amorphous and crystalline phases[3][29]. These materials are of particular interest for phase change data storage applications. Phase change data storage materials will be discussed in section 2.5.

2.3 Optical Properties

2.3.1 Photo-Induced Effects

It is possible to photo-induce changes in chalcogenide materials. There are at least seven mechanisms through which this is possible in amorphous chalcogenides[25] which can result in materials that are optically, electrically, chemically, structurally and physically different after irradiation. These changes can be broadly classed into irreversible and reversible alterations. Clearly reversible changes are most desirable for re-writable data storage applications. Some of the most common and useful forms of photo-induced changes in chalcogenides are now described.

Photocrystallisation [21]

A chalcogenide film crystallises upon optical irradiation due to a heating effect. This is particularly common for chalcogenides with a low glass transition temperature, T_g. This process can be reversed by heating the crystallised volume to the glass melting temperature, T_m, and quenching.

Photopolymerisation [30, 31, 32]

Polymerisation is the process of two or more molecules combining to form a more complex continuously bound molecule. Such processes can be thermally and photo-induced in some chalcogenides. In the case of the well studied As_2S_3, a polymerisation model has been suggested whereby As_4S_4 polymers are created in the material after thermal annealing at the glass transition temperature, T_g.

Photodissolution of Metals [21]

A layer of metal in contact with the chalcogenide dissolves into it upon irradiation with light of similar energy to the chalcogenide's band-gap, E_g. The requirements for this process is a near band-gap radiation source and a deposited metal film. This process is not easily reversed.

Photocompaction and Contraction [24, 33, 34, 35]

Photo-induced compaction has been reported in Ga:La:S, under illumination from ultra-violet radiation. The locally compacted region showed a change in its chemical composition to higher concentrations of lanthanum. Large compaction depths were measured in the range of 0.2 to $1.3\mu m$. The densification led to a maximum refractive index change of $\Delta n = 10^{-3}$. Photo or radiation compaction has been observed in other chalcogenides and reversal via thermal annealing has also been reported. Densification and compaction has also been observed in conventional oxide glasses (SiO_2). These effects are useful for optical waveguide, laser and holographic grating applications.

Photodarkening [21]

The optical absorption of the chalcogenide increases at a particular wavelength after irradiation from some other source. This results from a shift in the Urbach absorption edge to lower energies. The effect is largest at low temperatures. At higher temperatures, close to T_g, the effect is not measured since the glass is annealed as fast as the effect is induced.

Photodarkening is sometimes associated with other structural alterations in the chalcogenide. Hamanaka et al.[36] have observed macroscopic photoexpansion in As_2S_3 glasses upon illumination with near band-gap radiation. However, the requirement of band-gap radiation is not a necessity, Hisakuni et al.[37] observed an order of magnitude volumetric change after illuminating As_2S_3 with below band-gap light.

Photobleaching

Photobleaching involves the optical absorption edge shifting to shorter wavelengths. It is a common effect in chalcogenide films and has been observed in GaLaS[38]. Again, this bleaching is due to a structural change in the glass network.

The direction of the shift in the absorption edge can be dependant on the film deposition method and its parameters. For instance, thermally evaporated arsenic sulphide based films can be either photobleached or darkened depending on the deposition conditions[39].

Photoinduced Anisotropy [21]

Dichroism and birefringence have been experimentally observed in some amorphous chalcogenides through illumination of linearly polarised light. Various theoretical models involving bond breaking and twisting have been proposed to explain this effect.

The abundance of processes through which optical changes can be induced in chalcogenides lends them to applications including integrated waveguide circuits, diffraction gratings, surface and potential volume data storage.

2.3.2 Electrical Properties

As previously mentioned, chalcogenide glasses can be considered as semiconductors with an energy gap up to 3eV. It was originally believed that semiconducting materials must have a long range order and periodicity such that a quantum band energy level could be used to describe the band structure of the semiconductor. However the chemical nature of the atoms which form the material was neglected. This was to change in the nineteen fifties when it was found that the chemical behaviour between the constituent atoms, not a periodic structure, is key to understanding the band structure of amorphous solids[40].

On the whole chalcogenide materials obey the '8-N' bonding rule whereby all electrons are taken up in bonds so that the electrical conductivity is not sensitive to small changes in composition or the addition of elements such as Ge or Si with four (or more) outer electrons. Adding elements to the glass with less than four outer s and p electrons often has a major effect on the conductivity [41]. Thus Kolomeits [42] found that the addition of Cu, Ag, In, and Tl to As_3Se_2 and As_3S_2 causes a significant increase in conductivity.

An ideal continuous random network with an entropy related to its disorder is the first approximation of a glass. However, in reality there are point defects which are either 'frozen in' during the quench from a molten state or grown during deposition. These defects contribute to the material's entropy and are responsible for 'states in the gap'. These gap states have a number of implications, the most important of which for this thesis are (1) change in the space charge distribution at the defect and (2) pinning of the Fermi energy, E_f [41, 42].

The Anderson model [43] assumes there are more bonding states than pairs of electrons and all states are either doubly occupied by electrons or empty. The suggested reason

for this is that the polaron energy, gained by bond contraction, more than compensates for electron repulsion forcing both electrons to occupy the same defect site, D, and causing a negative correlation energy [44, 43]. Sir Nevill Mott applied this analysis to chalcogenides, proposing that a large number of dangling bonds are present in the form of point defects in the amorphous network. The dangling bonds arise when normal coordination of the atom cannot be satisfied because of its surrounding configuration. The dangling bond/point defect is neutral, D^0, but contains an unpaired electron. If no electrons were present, it would have a positive charge, D^+. If there were two electrons present it would have a negative charge, D^-. Mott's model, in agreement with that of Anderson, assumed that a local lattice distortion occurs upon a change in the defect electron occupation. The distortion is such that the reaction $2D_0 \rightarrow D^+ + D^-$ is preferential and that electrons can only occupy the D^0 as a result of excitation.

In chalcogenides lone pair electrons form the upper edge of the valance band whilst, higher energy, antibonding states form the conduction band. Since in bonding atoms the electrons are effectively screened by the bonded atoms, the D^+ defects are strongly attracted to lone pair atoms where the electrons are somewhat more exposed. This attraction causes a bond and distorts the local environment. This bond also liberates a large amount of electronic energy because the lone pair electrons are now transformed into deep bonding states thus creating energy level B in figure 2.1. The D^+ defect is influenced by this extra electron which is in its vicinity. It has the effect to slightly reduce the charge around the defect and a shallow donor level is achieved (energy level A). The assumption is that the electron doesn't enter the D^+ defect (it remains unoccupied); it is merely attracted to it because of its charge. However, the act of this attraction/bond reduces its energy slightly and forms the shallow donor level. This energy separation is typically 0.1eV[44, 43].

Similarly, the defects which contain 2 electrons with a negative charge, D^-, feel an attraction to lone-pair-like atoms which have a positive charge. Since there is a negative charge on D^-, an acceptor-like energy level is formed above the valance band[44].

Energy levels W^+ and W^- are equal to the polaron energy of each defect. U is the correlation energy which represents the effective electrostatic attraction when two electrons (one of each spin) are simultaneously present in the vicinity of the same defect [45]. As electrons are injected into the gap they populate energy level B.

In the situation described where D^0 centres are not naturally stable, the minimum energy of optical absorption occurs between the valance band and D^+ centres at level A and for transitions from D^- centres to the conduction band. Photon energies greater than these two minima will also be absorbed leading to a shallow absorption tail near the band edge [44, 43]; this is known as an Urbach tail.

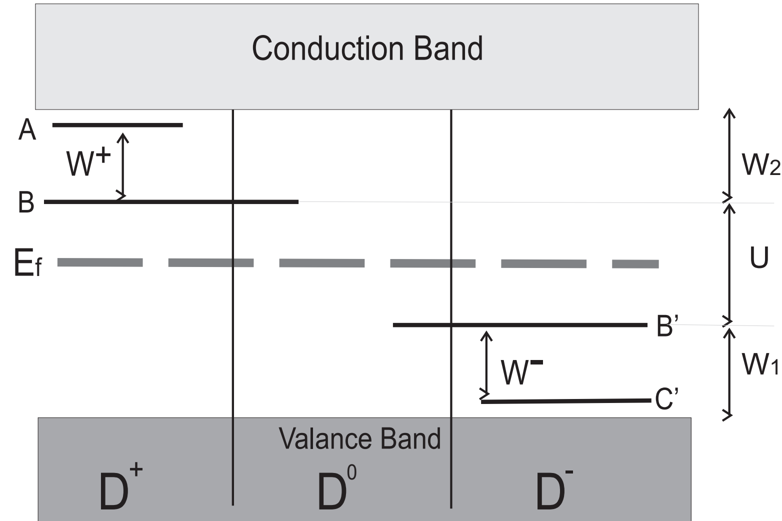

FIGURE 2.1: Band Levels in a chalcogenide semiconductor

When an electron is promoted from the valance band it enters the defect and becomes trapped and sits in level B, as shown in figure 2.1. The state of the defect changes to that of D^0. In order to escape, an activation energy is required which is equal to W_2. For a hole in the valance band, the coulomb attraction of a D^- defect can trap it, the activation energy required for its release is equal to W_1. In these materials there can also be a large number of lone pair chalcogen atoms thus there will be a large number of, D^- type, hole traps. This considerably limits the hole mobility and deems the material highly resistive, unless the activation energy for conduction, W_1, is exceeded.

It is assumed that the polaron energy associated with a distortion to form D^- and D^+ is approximately the same, thus $W_1 - W_2$, this has the effect of pinning the Fermi level at the same energy $\pm\frac{1}{2}U$ from levels B and B'. So it is now possible to form a semiconductor energy level diagram, this is given in figure 2.1.

In summary, there are three possible charged defect states D^+, D^- and D^0 resulting from the addition and removal of a dangling bond. These D^+ and D^- states act as shallow acceptors and donors. Once they have trapped either the hole or electron they distort to become neutral D^0 states with an associated activation energy for the electron to escape.

If there is a high density of electrons, the Fermi energy, E_f, lies above energy of the conduction band, E_c, and the conductivity is similar to that of a metal and shows no increase with temperature. However, as the density of electrons is lowered, the Fermi energy falls until it is equal to E_c and the conductivity is equal to the minimum metallic conductivity. In chalcogenide amorphous materials the density falls still further, the

material cannot be considered to be a metallic conductor and conduction is only possible by the two mechanisms: (1) at low temperatures by thermally activated 'hopping' from one localised state to another and (2) at high temperatures, current is carried by holes excited to the mobility edge[46]. Thermally activated hole hopping leads to a conductivity, σ, given by equation 2.1 whilst at higher temperatures electrons gain enough energy to be thermally activated to the hole edge and equation 2.2 gives the conductivity [46]. Where σ is the electrical conductivity, σ_{min} is the minimum metallic conductivity, E_g is the energy difference between the conduction band and valance band, B is dependant on the density of states and on the extent of the trapped holes' wavefunctions.

$$\sigma = \sigma_{min}\{\exp \frac{E_g}{kT}\} \tag{2.1}$$

$$\sigma = A\exp\{\frac{-B}{T^{1/4}}\} \tag{2.2}$$

A unique characteristic of some chalcogenides is their ability to threshold switch. S. Ovshinsky first observed the switching nature of chalcogenides back in 1968 [3]. The paper reported a threshold switching effect whereby the electrical resistance of an amorphous chalcogenide thin film may switch from a highly resistive state to a conducting state along a load line. This occurs at a threshold voltage, V_{th}. Once in the conducting state the current can be increased or decreased without affecting the voltage drop across the film, known as the holding voltage, V_h. If the current is reduced below a critical value, known as the holding current, I_h, the chalcogenide film switches back to the non-conducting, highly resistive, state. The switching process is highly repeatable [3] with evidence of certain chalcogenide compositions cycling between states more than 10^{12} times [47]. Figure 2.2 (a) shows the I-V characteristic of such a threshold switch. This type of switch is volatile, since current must be supplied to keep it in the conducting state. Non-volatile 'memory switches' are able to maintain a high or low conduction state without drawing any current; figure 2.2(b) gives the I-V characteristic for such a device. Once the material is in the conductive state ($V > V_{th}$), the current is increased to the point where enough thermal energy is supplied to the chalcogenide, through Joule heating, to create a crystallised filament. The voltage can be reduced below the holding voltage, V_h, without switching back to the highly resistive state. Outside the crystallised filament the material remains amorphous.

The true nature of threshold switching is still unclear but the basic model is as follows: as the voltage is increased the vacancies in the amorphous network, and consequently, the gap states in the band-gap of the material become filled. Since there is a high density of these states, usually the conductivity is very low since holes are trapped by these states [40, 48, 49, 46]. However, once the gap states are filled, there is nothing else to prevent

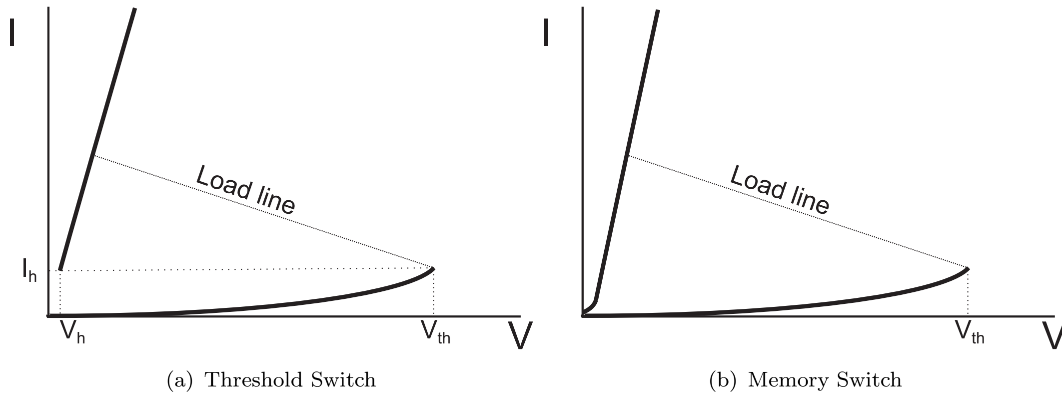

(a) Threshold Switch (b) Memory Switch

FIGURE 2.2: Typical I-V characteristics of threshold and memory switches

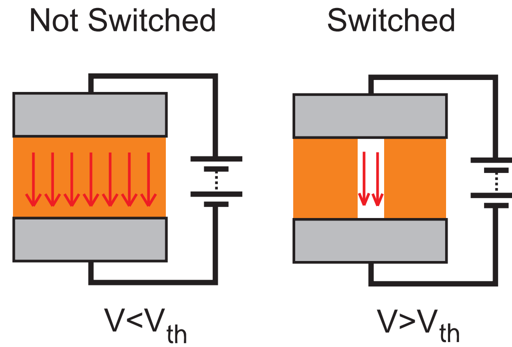

FIGURE 2.3: Filament forms after field exceeds V_{th}

the charge carriers from crossing the band-gap. At this point the conductivity becomes very sensitive to voltage and the device is switched to the 'on' state [3, 40]. The gap states will remain filled as long as the current remains high but when the current falls below a holding current, the generation of carriers is not high enough to keep the gap states filled. The empty states are free, once again, to capture carriers thus reducing the current.

In the resistive, 'off state', the current flows through the whole volume of chalcogenide film enclosed by the two electrodes but in the conductive, 'on state', the current flow is through a much smaller diameter, local area, between the electrodes. This has become known as the current filament[50, 49, 51] (see figure 2.3) .

Recently Pirovano[40] established a model which postulated that since the conduction is dependant on carrier concentration, it is probably an impact ionisation process whereby, in a large electric field, a hole can lose energy through the creation of further holes; thus creating an avalanche effect. At V_{th} the hole and electron recombination, whose energy is usually spent through the creation of a phonon, are no longer balanced since more holes are being created, and the conductivity sharply increases [40].

An alternative theory [52] for the threshold switching effect initially postulates a rather different mechanism for the conduction. Arhenius type experiments to measure the activation energy for conduction in the amorphous phase found that the activation energy actually decreased with applied voltage. This led to the hypothesis that the applied field reduces the potential barrier which the trapped electrons must overcome in order to move through the material thus allowing a reduction in the activation energy. At fields close to those that induce threshold switching, the potential barrier is reduced to the extent that field driven emission of electrons through the potential barrier overcomes thermally activated conduction. The electrons are allowed to access empty trap sites with larger kinetic energies, this excess energy can then be exchanged to lower energy electrons thus increasing the conductivity further. From this rather qualative explanation, an analytical model was developped which seemed to fit experimental data well.

Chalcogenide materials, annealed above the crystallisation temperature, structurally transform leading to different atomic arrangements which can enhance the energy of electronic states in the vicinity of the Fermi level [13]. Thus, in the crystalline state, the materials tend to have a higher carrier mobility and greater carrier concentration than in the amorphous state [15].

2.4 Data Storage

Mass storage is the concept of non-volatile storage of large volumes of data. Mass storage devices usually consist of a head which is used to write or read to or from a storage medium. The storage medium is usually addressed by positioning it relative to the read/ write head. Data can be exchanged by transferring mechanical, optical, magnetic or electrical energy to the media. In contrast Random Access Memory (RAM) devices usually consist of a matrix of addressable conducting lines. An individual memory cell is electronically addressed by linking the corresponding column and row conducting lines via the cell. Thus the principal difference between mass storage devices and RAM devices is the method by which the data is accessed [2].

Storage media can be classed by their ability to record as well as read: pre-written media, Write Once, Read Many (WORM) media and read write media. The compact disk media comes in all forms of the above. They are sold either, prefabricated with data encoded as modulated pits on a metalised layer in a structure (similar to that depicted in figure 2.4), as write once CD-R media whereby a photo-sensitive polymer is written to by a modulated laser. And finally CR-R/W which can be re-written up to the order of 100 000 times by changing the phase of a chalcogenide active layer [2]. Dimensionality

of the media is clearly of importance since encoding data across different dimensions will increase the media's capacity. Magnetic tape has a low storage density, since data is encoded in 1-D along the length of the tape, CD's have a higher density since data is recorded in a 2-D plane, radially and angularly. Finally 3D storage has the highest potential capacity since data is stored in the media volume; holographic storage is an example of this [2].

The compact disk introduced digital audio to the commercial world in the early 1980s. It, and its derivatives; the Digital Versatile Disk (DVD) and more recently, the Blue Ray Disk (BD) and the High Density-DVD, have allowed ever increasing storage densities by increasing the objective lens' refractive index and reducing the operating wavelengths from 780nm to 650nm and now to 405nm for the CD, DVD and BD or HD-DVD respectively; thus allowing smaller marks to be written and distinguished[2]. The pre-recorded CD is formed by injection molding a polycarbonate substrate onto a metal master. A reflective metallic layer is then deposited on the molded polycarbonate. The data is stored in the form of indentations on the surface of the metal. The bit depth is a quarter of the reading laser's wavelength. The spot size is bigger than the pit so there is destructive interference between the light reflected from the depth of the pit and light reflected from the area surrounding the pit. A photo-detector measures the intensity of the reflected light; if the beam scans over a pit, the destructive interference causes the reflected intensity to be modulated thus allowing the data on the disk to be read[2]. The linear velocity of the read area is kept constant at $1.3ms^{-1}$, which means that the angular velocity of the disk is reduced from 500rpm at the centre of the disk to 200rpm at the edge of the disk[2].

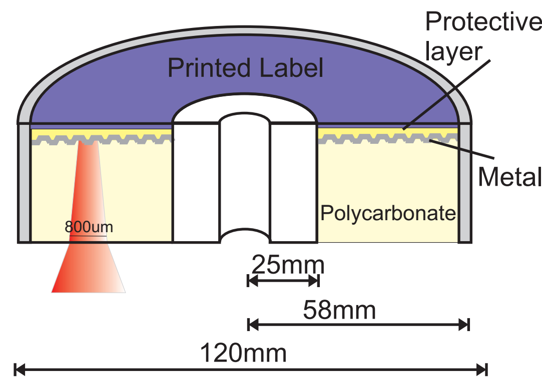

Figure 2.4: Structure of a compact disk

Read Only Memory (ROM) is an example of an electrical non-volatile memory; it is used in most electronic items. The essential technology behind ROM is a diode positioned at the intersection of an addressable column and row conducting lines. These chips, however, cannot be programmed. Programmable- ROM (PROM), on the other hand, can; small fuses are broken at the relevant intersection to disconnect and, thus, program the

chip. However these chips are write once and they cannot be re-programmed. Erasable Programmable ROM (EPROM) can be written to many times. In an EPROM chip, two transistors are separated from one another by a thin oxide layer. Electrons can tunnel through onto the oxide layer, where they are then trapped. If there are no electrons on the oxide layer, the two transistors are essentially connected (this represents a 1), if there are electrons on the layer, the two transistors can be thought of as disconnected (representing 0). The EPROM can be erased by removing all the electrons from the oxide layer. This is usually done by illuminating with ultraviolet light, allowing the electrons to gain enough energy to break out of the oxide layer. The next advancement in ROM is the Electrical Erasable Programable ROM (EEPROM). Rather than UV radiation to remove the electrons, an electric field is applied to the junction which allows the electrons to escape the oxide layer. This has the advantage that each intersection can be re-written to individually. Flash memory is a type of EEPROM, it is wired such that either the whole chip can be erased or segments of the chip, containing many intersections, can be erased at once[2]; this reduces the erasing time. A distinct disadvantage of Flash memory is its write speed, which is at least one microsecond[53]. There are a number of emerging technologies which write data using various mechanisms. Most of these technologies not only outperform Flash, with respect to their write time, but also their read/write cycle endurance [53], see table 1.1.

2.5 Phase Change Data Storage

Phase change data storage has been introduced as a possible replacement for magnetic media. The CD has replaced the audio cassette and, in-turn, the DVD has replaced the video cassette. The advantages are well known: higher transfer rates, faster access times, improved endurance; all of which contribute to a higher standard of audio and video respectively. However, at present, optical phase change media are not able to compete with the write and erase times and cycle endurance of the magnetic hard disk [15].

The concept of phase change memory is relatively straightforward. It relies on a material which maintains either the amorphous or crystalline phase until switched. In order to switch between the two phases, energy must be put into the system. Electromagnetic or electrical energy is usually supplied to the phase change film where it is transformed into heat. If sufficient energy is acquired by the material to overcome that required to break the atomic bonds, the material will be excited to a high mobility state [54]. It is then possible for the atoms to settle into different structures, either crystalline or amorphous depending on the rate of cooling. Quenching at a high cooling rate prevents the atoms migrating from their random, liquid-like, arrangement; thus an amorphous structure is

formed. A lower cooling rate, with a gradual reduction of heat allows the atoms to form a more ordered, energetically stable, crystalline arrangement [55].

Changing the phase of a material affects the structural, optical and electrical properties [3, 54] of the chalcogenide material. The crystalline materials have a small electronic band-gap thus allowing electrical conduction at room temperatures. The amorphous phase have a larger band-gap and hence their intrinsic absorption is lower and electrical conductivity is reduced. Materials which exhibit such contrast in electrical and optical properties are of interest for data storage[15]. In most cases crystalline materials have a higher refractive index (at visible wavelengths) and a lower electrical resistance, in comparison with amorphous materials of the same chemical composition[3, 56, 53].

Chalcogenides typically exhibit this aforementioned phase change property. They, in particular, are chosen since they can be switched between phases relatively easily, yet may be thermally stable well beyond the anticipated storage and usage environments [57]. This ease of switching and thermal suitability is what separates chalcogenides from other types of glasses like silica (SiO_2), where bond strengths are much greater. However, phase change is a material property which is not exclusive to chalcogenide material. Phase change storage has been reported in other non-chalcogenide materials including vanadium oxide[58] and gallium [59]. An amorphous area can be formed in a predominantly crystalline film by heating the material to its melting point, T_m, and cooling quickly. The amorphous mark can be erased by applying enough heat for a sufficient duration to raise the mark's temperature to that required for crystallisation[60] allowing the atoms within the mark to relax to their preferred crystalline state.

During crystallisation the phases of the amorphous material can separate, this is accompanied by diffusion of atomic species. The atoms clearly need to move such that they can bond to other available atoms to form a crystal[57]. This diffusion process limits the crystallisation speed[61]. Crystal nucleation centres can be added in the form of dopants in an effort to decrease the crystallisation time. Diffusion-less crystallisation growth is also possible. This class of material is designed such that the chemical composition for both crystalline and amorphous states are identical[61]. The interatomic rearrangement necessary for this process involves minor changes to bond angles and lengths[57]. Since the atoms do not diffuse in this process, the crystallisation speed can be quicker.

To achieve high writing transfer rates, materials which show fast crystallisation are of interest. Phase transitions are only possible if the Gibbs free energy is reduced after the transformation. There are essentially two classes of materials: nucleation dominated and growth dominated. The crystallisation time of nucleation dominated materials are heavily dependant on crystal nucleation whereas growth dominated materials are heavily dependant on the time taken for the crystal to grow. Following the analysis performed

by Wuttig [15]; the total Gibbs free energy for crystallisation has contributions from the energy required to form a phase boundary enclosing the nucleated phase, ΔG_{IF}, and the elastic energy, ΔG_E, hence equation 2.3:

$$\Delta G_{total} = \Delta G + \Delta G_{IF} + \Delta G_E \tag{2.3}$$

If the elastic contribution is ignored and spherical nuclei are assumed, the Gibbs free energy as a function of radius is then given by the Gibbs free enthalpy per a unit volume (ΔG_V), multiplied by the volume and the interface energy per unit area (γ,) multiplied by the spherical area of the crystal nucleus ($\Delta G_{total} = \Delta G_V V + \gamma A$), hence:

$$\Delta G(r) = \Delta G_V \frac{4\pi}{3} r^3 + \gamma 4\pi r^2 \tag{2.4}$$

Equation 2.4 is plotted in figure 2.5. For nuclei smaller than the critical radius, r_c, further nucleus growth is required which, in turn, requires more energy and hence it is unfavourable. Nuclei with radii greater than r_c promote a reduction in the total Gibbs free energy hence their formation is favourable. Differentiating equation 2.4 to find its peak, where $r = r_c$, the critical radius criteria is found:

$$r_c = -\frac{2\gamma}{\Delta G_v} \tag{2.5}$$

such that the critical total Gibbs free energy is:

$$\Delta G_C = \frac{16\pi}{3} \frac{\gamma^3}{\Delta G_V^2} \tag{2.6}$$

It can be seen from the negative sign in equation 2.5 that negative values of ΔG_V can lead to a phase transition, since nuclei can only form if there is a reduction of the free enthalpy. ΔG_C is the free enthalpy that must be overcome for nuclei to form. Since some nuclei form, but their size is below r_c, hence they are energetically unfavourable and decay; Wuttig was able to take this analysis further and analyse the size distribution of nuclei resulting from thermal fluctuations:

$$N(r) = N_0 e^{-\frac{\Delta G_{total}}{k_B T}} \tag{2.7}$$

Where $N(r)$ is the number of nuclei with radius, r and N_0 is the total number of nucleation sites.

The number of nuclei with a critical radius is of great importance, since if one of the nuclei captures a single atom it becomes stable. The number of critical nuclei is then given by:

$$N_C = e^{-\frac{\Delta G_C}{k_B T}} \tag{2.8}$$

For such a nucleus to catch an additional atom, the atom must overcome an interface activation barrier, W_K. ΔG is dependent on temperature and decreases with temperature[15] whilst, as can be seen, the number of critical nuclei increase with temperature. This leads to a spike in the curve of nucleation rate as a function of temperature. The width and position of the spike is dependant on the material's melting temperature, latent heat of melting, interface energy γ and activation energy W_k. After nucleation, the two phases co-exist, separated by the interface energy. The transfer of atoms to the nucleated crystal is dependant on the activation energy and the difference in enthalpy.

The growth rate of the crystal is proportional to the product of the attempt frequency, ν, the probability of an atom overcoming an energy barrier to join the nucleated crystal (described by $exp(\frac{-W_K}{KT}))$ [15] and $(1 - e - \frac{\Delta G_{atom}}{KT})$ where ΔG is the free enthalpy difference per atom between the two phases. This leads to another maximum in the growth rate as a function of temperature, but this time the maximum occurs at a higher temperature. The expression $exp(\frac{-W_K}{KT})$ is inversely proportional to viscosity, this means that the growth rate is also dependent on viscosity[15].

To measure the crystallisation temperature of a material Differential Thermal Analysis (DTA) is typically used; this is discussed in section 2.8.4. However, it is sufficient to note here that it gives a peak associated with the net effect of nucleation rate and growth rate. Since only the nucleation growth is dependant on the activation energy, it is possible to measure the activation energy by the knowledge that maximum nucleation rate will always occur at the same temperature irrespective of heating rate. However the crystal growth has some time dependence associated with the frequency, ν (rate at which atoms attempt to overcome the energy barrier and join the nucleated crystal site). Since only the term associated with the activation energy shows a time dependence, the activation energy can be found by conducting a series of DTA measurements, at different heating rates, and then measuring the difference in the temperature of crystallisation. The activation energy is of great importance since it gives a measure of the amorphous phase stability.

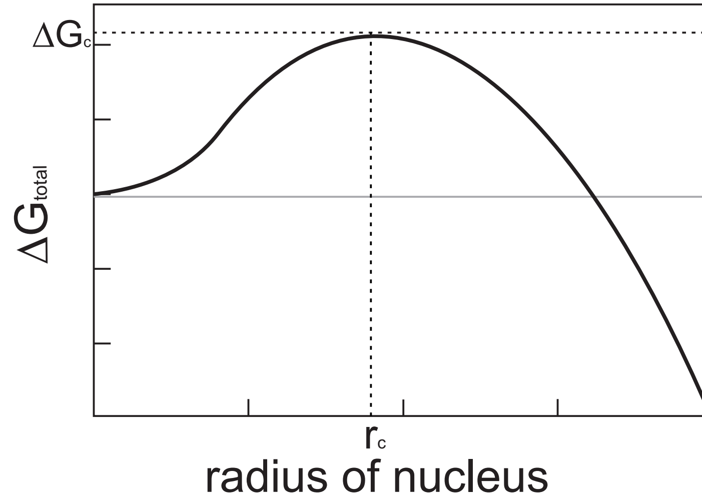

FIGURE 2.5: Phase Transition energy schematic

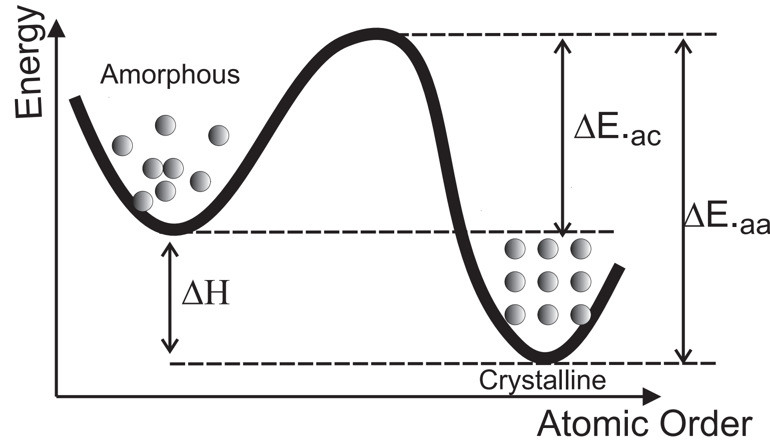

FIGURE 2.6: Phase Transition energy schematic

2.5.1 Optical Phase Change Media

CD-RWs and DVD-RWs take advantage of the phase change nature of chalcogenide materials. The active layer of the CD-RW consists of a mix of silver, indium, antimony and telluride ($Ag_8In_{13}Sb_{48}Te_{30}$) [62]. When the layer is heated to T_p and cooled slowly it becomes crystalline, if it is heated to the melting temperature, T_m, it becomes amorphous when quenched at a rate greater than 10^9 $°Cs^{-1}$ [15] and the phase of the material is changed. Writing and reading the phase change layer is achieved via the same laser as the reading process but during reading its power is reduced to a level which prevents the phase change layer reaching its glass transition temperature. Erasure of amorphous marks occurs at a power level which causes the phase change film's temperature to reach T_p and writing to T_m. The reading laser is reflected from the surface of the disk and the reflected signal is modulated by the amorphous marks with low reflectivity and higher

intrinsic absorption in comparison with the crystalline state. A diagram is given to show the cross section of a conventional CD-RW; see Figure 2.7. If the writing power is too high the phase change layer can be ablated, resulting in permanent damage to the disk.

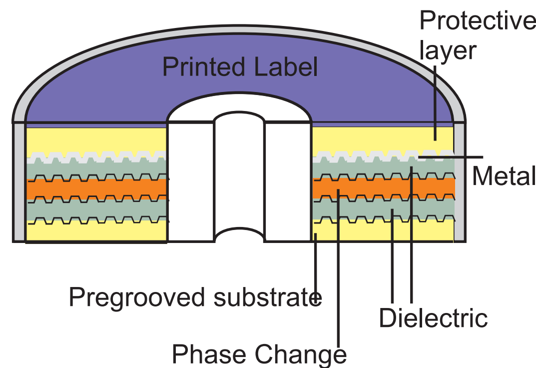

FIGURE 2.7: The core components of a CD-RW [63]

For fast crystallisation, and hence short erase times, it is necessary to incubate the chalcogenide film for a specific time and temperature. This allows nucleation seeds to form in the chalcogenide layer and is referred to as 'priming'. Once the nucleation sites have formed, the crystallisation time is only limited by the time taken for the crystal to grow. The temperature required for priming is the same as that for crystallisation [64] thus, if the material is held at this temperature for a long enough time, the nucleation sites will form and eventually crystal growth will occur. After priming, the optical properties of the material are slightly different to those of the as-deposited state; measurements made by the Philips laboratory on a Ge:Sb:Te:Se film found an increase of 0.2 in the extinction coefficient and a depth change of about 1% [63].

As previously mentioned, since the nucleation time can be orders of magnitude longer than the crystallisation time [64], phase change materials can be broadly classed as nucleation dominated and growth dominated. In the nucleation dominated material, the majority of the crystallisation time is taken by the nucleation of crystallites, whereas growth dominated materials tend to nucleate in a very short time but their growth rate is comparably long and hence the majority of the crystallisation time is dominated by growth [63, 29]. Even within the same material system there can exist both classes of material. For example in the Ge:Sb:Te system, materials along the $GeTe - Sb_2Te_3$ tie line are nucleation dominated whereas materials close to the $Sb - Te$ binary are growth dominated [29].

Identification of the dominating mechanism can be achieved by analysing where the crystallisation starts. If it starts at the centre of an amorphous mark, where the temperature is highest and the stresses are large, it is a predominantly nucleation driven. In contrast,

if the crystal growth starts at the interface between the amorphous area and the crystalline background, it is a growth dominated process[63]. This is depicted in figure 2.8. Distinguishing growth dominated crystallisation from nucleation driven is based on the knowledge that if the crystal must grow from the interface, it will be strongly dependent on the size of the amorphous mark. Whereas, a nucleation dominated process will be independent of the amorphous mark size. Thus for growth dominated crystallisation the crystallisation time will increase with mark radius but for nucleation driven, the crystallisation duration will be constant.

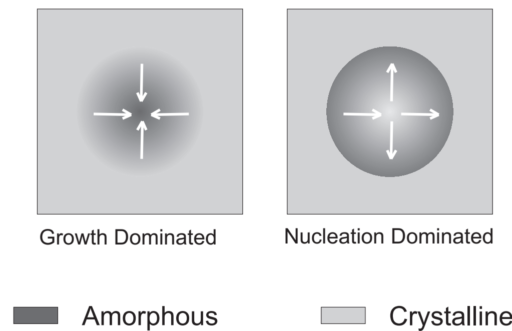

FIGURE 2.8: Depiction of the two possible crystallisation mechanisms in phase change recording [63]

The ability to write amorphous marks on the disk relies on the material being a good glass former [15]. The disk must be easily heated to its melting temperature but should also dissipate heat quickly such that the necessary high quench rates are possible. If the surrounding dielectric layers have a large thermal capacity, large amounts of heat energy will still be present in the disk once the laser is switched off, this means that the heated mark cannot dissipate its energy to its surroundings and cools slowly from the molten state resulting in a melt-crystallised state[15]. It is clear that the thermal and optical design of a disk is crucial to enable high data writing rates with the maximum amount of incident light reaching the active layer. The layer stack should also increase the conversion efficiency of incident optical energy to heat.

The data transfer rate of phase change media is directly dependant on the crystallisation rate which is in turn dependant on the phase change layer composition, its thickness and its interface [63]. At high temperatures the crystallisation rate should be great thus enabling high data transfer rates. In phase change media the limitation in recording occurs due to the time taken for previously recorded data to be overwritten with new data. This time is dictated by the speed at which the amorphous marks of the previous data can be erased. Conversely at low temperature or storage temperature, the crystallisation rate should be infinitesimally small to increase the time taken for the amorphous mark to be naturally made crystalline. The media should be stable against spontaneous

re-crystallisation for several years; the length of time for which the material can be considered stable is known as the archival lifetime. To summarise, the crystallisation rate should be high at high temperatures and practically zero at low temperatures. This conflict complicates phase change media development [16].

For an optical phase change disk there are a number of phase change material properties which should be optimised:

1. Ability to form a glass; easy glass former.
2. Rapid crystallisation to ensure short erase times.
3. High crystallisation activation energy to ensure amorphous mark stability.
4. Good optical contrast between phases.
5. Read/Write endurance; low stresses encountered due to thermal expansions and different phase densities.

In the case of archival data storage the cycle endurance is not necessarily of such high importance as conventional re-writable disks. In this case, longevity and stability of the data are of utmost importance and even the read endurance could be reduced in comparison to the high specification of an everyday data disk. In the words of BBC archivists Dr Richard Wright *'if large volumes of data storage can be achieved, we would settle for write once, read every now and again'*[65] a comment made in response to the erasure problems often encountered with holographic memory materials upon accessing the data.

Optical phase change recording is already a mature technology for re-writable CDs and DVDs. Increasing the capacity of phase change discs thus far seems to have followed the trend of decreasing the write beam spot size. Plasmon and Sony both have products that use short wavelength violet and blue lasers. This allows for smaller marks to be made on the film and thus a higher density of marks on a disk. The Sony product boasts a capacity of 23.3GB and later generations of the disc could allow up to 100GB storage on a standard size 5.25"/12cm disc. Plasmon's product should deliver a capacity of 120GB by 2008 but currently holds 30Gb [66].

Increasing the capacity of phase change optical disks is, at present, the subject of much research. Conventional far-field optics restricts the size of a mark to the diffraction limit, $1.22\frac{\lambda}{NA}$, where λ is the wavelength and NA is the numerical aperture of the objective lens [67]. To overcome the diffraction limit, new approaches involving negative index lenses [68] or ideas borrowed from the Scanning Near-Field Optical Microscope (SNOM)

[69] are researched. In such a SNOM device, light is guided through a tapered optical fibre to its tip, which can be just 50nm diameter. As the fibre diameter is reduced, the intensity in the fibre becomes very high. The tip is coated with a metal, thus trapping the electromagnetic field inside the fibre even at such small dimensions. Below the diffraction limit, the intense electromagnetic field is evanescent and decays in a short distance. If the tip is brought to within a few 10s of nanometers above the phase change layer, some of the field can be used to heat a phase change data storage film, thus allowing sub-wavelength marks to be written on it. The marks can also be resolved by the same device [70]. However, data storage devices based around SNOMs have a number of limitations. The amount of energy transmitted by the SNOM tip is very low, thus high laser energies are required to overcome the attenuation of the evanescent field. The necessary laser powers can cause damage to the SNOM tip including melting of the metallic coating. Another big problem is the ability to position the removable media consistently within the evanescent field emanating from the tip. A possible solution to both of these problems is the Super-Resolution Near-field Structure(Super-Rens) Disk, suggested by J. Tominaga [7]. The idea is: instead of coating a tapered fibre with a metal, to actually put a heat sensitive, metallic layer on top of a phase change layer. When a laser is focussed through a 0.6NA lens onto Sb it heats non-linearly and a sub-wavelength aperture is opened at the centre of the laser's Gaussian mode. The laser's electric field in the vicinity of the aperture is evanescent and extends to the phase change layer. This allows sub-wavelength marks on the phase change layer to be both written and read. Since the disk structure can be easily controlled with nanometer accuracy and the metallic layers are very thin (20nm), the positioning and high optical intensity problems associated with SNOM data storage are overcome[7]. Such a disk structure shows great potential for the next generation of optical storage media.

2.5.2 Electrical Phase Change Devices

Electrical phase change data storage uses the same principles as optical storage but rather than optical heating, it is possible to heat electrically such that both the crystallisation and melting temperatures can be reached within the film [3]. Heat generation in the chalcogenide film is possible by passing an electric current through it. The power dissipated into the material, due to an electric current passing through it, is given by equation 2.9, for power dissipation.

$$P = VI = I^2R \tag{2.9}$$

Where P is the power dissipated, V is the electric potential applied to the film, I is the electric current and R is the resistance of the film. As mentioned earlier, the high

density of charge carrier traps in a chalcogenide's amorphous state means that it has a high intrinsic electrical resistivity; thus R is large. Since R is large, only a small current is necessary to generate enough power for the material to crystallise. However, this requires a high voltage. Creating short pulses of high voltage using circuitry with nanometer scale features is currently one of the problems with conventional Flash devices[16].

The volatile nature of the threshold switch deems it unsuitable for non-volatile data storage but the threshold switching materials are still extremely useful. The threshold voltage provides a unique mechanism through which the chalcogenide's amorphous resistance can be reduced such that a higher current may pass that is capable of crystallising the material at lower voltages. Figure 2.2 shows the I-V curve of a device operating with a threshold voltage. Initially the voltage across the material is increased and it shows a high resistance. At V_{th} it switches to a highly conductive state and the voltage across the material drops considerably. The current passing through the material is now very sensitive to changes in voltage. Increasing the voltage eventually leads to a current capable of generating sufficient heat to cause the chalcogenide material to generate a crystalline filament [50, 49]. The electrical resistivity of the material is now low, even below the holding voltage. A suitable electrically switchable chalcogenide memory material will remain crystalline until heated above its melting temperature; therefore these materials are non-volatile.

To make the crystalline filament amorphous again, a greater current pulse with shorter duration is required. The crystalline filament's temperature must be increased to the chalcogenide's melting point and cooled quickly such that it is quenched in an amorphous state. Conversely a lower current pulse, longer in duration, raises the chalcogenides temperature above the crystallisation onset temperature. The long pulse allows the film to relax from an amorphous state into a crystalline form. A short, low power, pulse which has little heating effect on the chalcogenide is used to read the state of the material; this is depicted in figure 2.9.

One of the most important criteria for an optical disc is the optical contrast between phases, similarly in electrical storage a large resistivity contrast is required. Orders of magnitude change in sheet resistance of Te based films are possible [71, 72, 15]. However, in order to obtain high cooling rates, the phase change layer should have a high ratio of surface area to volume [15] such that the heat can be conducted away and cooling rates of the phase change as high as 10^9 $°C^{-1}$ are possible. However this causes a reduction in the resistance change of the phase change cell.

The main challenges facing electrical phase change research is to create a material which reliably has orders of magnitude change in resistance between the two phases whilst minimizing the energy necessary to read and write to the material. In a practical electrically

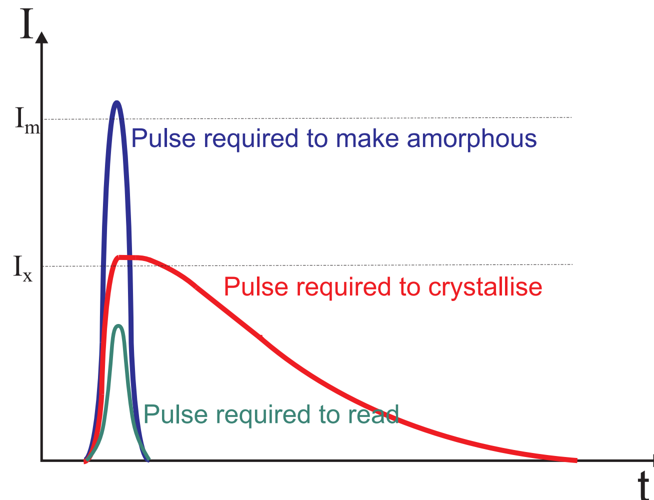

FIGURE 2.9: Crystallisation pulse (Red), Amorphising pulses (Blue) and Read pulse (Green) shown on axes of electrical current and pulse duration.

switchable device, each cell will require a transistor to access the relevant chalcogenide cell. The transistor size will be on the scale of the chalcogenide cell itself. This puts strict current limitations on the maximum current which can be supplied to switch the chalcogenide cell. Some research groups are concentrating on the cell design to increase its resistance. By fabricating chalcogenide cells with a high aspect ratio (small area and long length), the resistance can be increased[6]. However another approach, is to optimise the phase change materials themselves, perhaps by introducing dopants or through the discovery and optimisation of novel chalcogenide compositions which show a relatively high intrinsic resistivity in the crystalline phase. Another important consideration is the reduction of atomic diffusion and stresses at the electrodes induced after repeated read/write cycling. Again, to a certain extent, this can be limited by appropriate cell design such that only small areas are in contact with the electrodes thus the electrodes act as large heat sinks [6]. Stresses can be reduced at a materials level by choosing materials which show little volume change between phases. Growth dominated materials are likely to show the greatest potential for phase change electrical storage since the crystallisation duration and switching time will decrease with cell area.

2.6 Deposition of Chalcogenides

There are a number of techniques that could be employed to create the necessary thin films of chalcogenide materials. These techniques are described in this section. A table is presented (2.2) to allow comparisons between the described techniques.

2.6.1 Thermal Evaporation

Thermal evaporation is perhaps the simplest method for creating thin films. The source material and substrate are under vacuum and in direct line of sight. Usually they are separated by a few tens of centimetres. The source material is heated until it is sometimes sublimated or evaporated. When the evaporated material comes into contact with the substrate it condenses and forms a film. The rate of evaporation and depth of film deposited can be measured indirectly by analysing the frequency change of a quartz crystal.

There are, in principle, two common ways to heat the source material: (1) By passing a large electric current through a resistive holder or filament, thus Joule heating it, or (2) by directing a beam of electrons (e-beam) onto the source material. The beam causes highly localised heating of the source material due to the bombardment of the electrons on the source's surface. E-beams are principally used to vaporise materials with a high melting temperature[73]. In cases of simultaneous deposition from several sources, accurate control is required over the temperature of each source such that evaporation source dependent fluxes are possible. In such cases a Knudsen cell is employed, this consist of a crucible in thermal contact with a Joule heating element, a thermocouple, radiative heat shielding, and a cover to prevent out-gassing of contaminants [73].

2.6.2 Sputtering

The sputtering technique allows very thin films to be deposited onto a wide variety of substrates. The process involves applying a high voltage across a low pressure gas, usually argon (Ar). The atoms within the gas become ionised due to the large electric field and are excited into a high energy state, thus creating a plasma[74].

The energised ions within the plasma come into contact with the coating material (target). Some of the ions' energy is exchanged to the atoms within the target. If sufficient energy is supplied, the atoms can escape from the target and bond to materials within the plasma chamber, including any substrates which maybe present. A diagram showing atoms being ejected from the target and bonding to a substrate is shown in figure 2.10. Powerful magnets are used to control the location and volume of the plasma. This enables a higher density of ions to be moved close to the target, thus increasing the deposition efficiency[73].

Since the ejection depth of the target can be just a few 10s of nanometers, the deposition is stoichiometric [73]. This is because, if a multi-component target is used, the different components may well have different sputtering rates but once the component with the

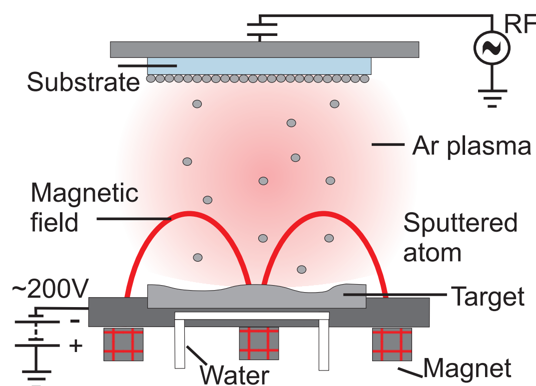

FIGURE 2.10: Schematic of a sputtering system showing atoms accelerated from a target to a substrate [73].

highest rate has been ejected from the surface, only the lower deposition rate component is visible to the plasma thus forcing it to be ejected. In reality the situation is much more balanced and both components are sputtered simultaneously. Sputtering locks the deposited atoms together at the molecular level forming a very strong bond. It can be used to create very thin, uniform and the most cost effective films possible. It can be also used to apply both conductive and insulating materials to any type of substrate, including heat sensitive plastics (sputtering is a cold momentum transfer technique), which is useful for optical disks[74]. Introduction of a further gas into the chamber can result in reactive sputtering whereby the resultant film's composition is altered to include the additional gas.

The effect of argon pressure on the sputter deposition rate has been predicted by Keller and Simmons. Increasing the argon pressure decreases the ballistic sputtering flux and increases the ratio of diffusively scattered atoms reaching the substrate, with respect to direct bombardment from the target [75]. Therefore increasing pressure of the Ar will result in a film with increased depth uniformity; however the deposition rate is decreased and it can be detrimental to the film quality.

2.6.3 Pulsed Laser Deposition

Pulsed Laser Deposition (PLD) uses a short pulse of laser radiation to ablate the surface of a target thus creating a plasma plume of the target material. If the plume comes into contact with a substrate, it is possible to coat the substrate with the contents of the plume.

PLD of the GaLaS materials, discussed in chapter 6 of this thesis, has been reported [38, 76, 77, 78]. However, it proved very difficult to create large areas of uniform depth and compositional accuracy. By performing quantitative energy dispersive x-ray analysis

on the sample, the sulphur and gallium content was shown to increase as a function of radial distance from the central area of the deposited film. Conversely the lanthanum was found to decrease as a function of radial distance [76]. The deposited films also had flaws in the form of sub-micrometer particulates [38].

The properties of the resultant film can be altered through careful control of the background gas pressure, pulse energy, laser wavelength, pulse duration, substrate temperature and target-substrate distance. This alteration of film properties is noticed on the atomic scale. In GaLaS films it has been found that the local environment of the Ga atom is significantly changed by altering the deposition energy density but the bond lengths were found to be independent[78].

2.6.4 Chemical Vapour Deposition

Chemical Vapour Deposition (CVD) is a process of reacting gasses on the surface of a heated substrate. The heat from the substrate supplies energy which can activate a chemical reaction to form a solid film of products within the chemical composition of the gasses. The principle advantage of this technique is its ability to uniformly and conformally coat non-planar surfaces. In electrical phase change chips, holes, tens of nanometers diameter with high aspect ratios must be completely filled, thus CVD is a desirable technique for such problematic devices [79].

CVD can be a complicated deposition process since there are several factors occurring simultaneously and non-uniformly whilst in the gas phase. These factors include: forced convection (flow due to pressure gradients), free convection (flow due to buoyancy of hot gas), homogeneous reactions and diffusion.

Table 2.2 has summarised all four deposition techniques discussed. Each has its merits, but the chosen deposition method is dependent on the film properties which are to be achieved. For routine deposition of a known material with good uniformity, sputtering is probably the most suitable, but the resultant film is usually non-epitaxial and voids are often unavoidable. PLD and thermal evaporation processes are a little bit more involved and are not as suitable as sputtering for a manufacturing process. In this thesis all four methodologies have been employed to deposit chalcogenide materials. The choice of deposition technique was dependent on the desired outcome. In some cases the composition of the deposited film was deliberately varied across the substrate; in such cases, an evaporation technique was used (discussed in section 2.7). In another case, a specific composition was doped with different amounts of another element; the sputtering technique was used. The ability to control the composition of a film deposited from a multi-component target was also explored and PLD was chosen as the desired deposition technique.

Technique	Advantages	Disadvantages
Sputtering	Good uniformity possible, cost-effective, bonding at molecular level allows for good strength, good control possible, any type of material for substrate, compounds volatilised stoichiometrically, kinetic energy of sputtered atoms falls largely within the energy window for displacing surface atoms on film without causing sub-surface damage	Vacuum required, large sputtering target discs need to be created, expensive to perform trials over a wide range of compositions
Evaporation	Simple method, good uniformity can be achieved	High vacuum required, stoichiometry lost, difficult to evaporate compounds due to vapour component ratios drifting with time and changing source composition
Chemical Vapour Deposition (CVD)	Possible to create shapes and designs of the deposited material, high pressure of fluid flow decreases the need for pumping, conformal coating or large areas possible	Complex, difficult to ensure homogeneous reactions, high temp required limit imposing substrate restrictions
Pulsed Laser Deposition (PLD)	Multilayered structures possible, many parameters can be controlled to achieve films with different properties.	Stoichiometry change, problems with particulates, often poor surface quality

Table 2.2: The advantages and disadvantages of various thin film deposition techniques [73]

2.7 High Throughput Methodology

Historically, material experimentation and characterisation has been on a sample by sample basis. This is a very expensive and time consuming process. However, in recent times, component miniaturisation has allowed a high-tech solution to this process thus, combinatorial experimentation is becoming an increasingly popular and powerful tool for efficient material synthesis and characterisation[80]. The concept of high throughput is simple: systematically vary the material composition of a large number of samples and measure the change in properties as a function of composition. Ideally, the whole material system is covered by the compositions synthesised.

Spatially varying thin film synthesis is sometimes performed such that the films composition is spread over the substrates area [80, 81].

In chapters 4 and 5 measurements are made on samples fabricated using a compositional spread Physical Vapour Deposition (PVD) technique [81]. The method consists of evaporation of the elemental samples in a Ultra High Vacuum (UHV) by either Knudsen cell or e-beam heating. Simultaneous evaporation was possible from six different elemental sources but for this work only three sources were used; allowing fabrication of ternary systems. Each source was positioned off-axis from the substrate and separated by an angle of 60°. The silicon and quartz square substrates were 32mm by 32mm. Shutters in the vapour beam allow masking, thus the vapour beam casts a shadow onto the substrate allowing a deposition rate change as a function of position on the substrate and growth of a wedge. Therefore deposition from multiple sources at different angles allows the atoms to have an opposing component to their velocity. This is clearly maximised when the sources are separated by 180°. Since each source produces a wedge, the composition of the film changes as a function of position, this can be seen in figure 2.11.

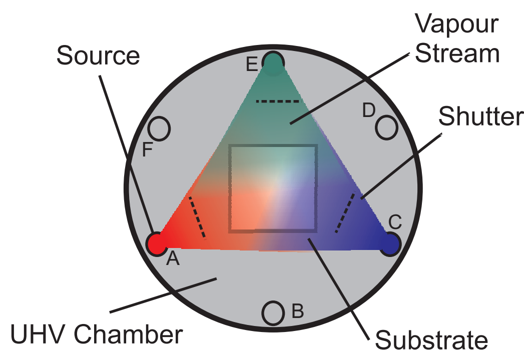

FIGURE 2.11: A schematic showing how composition varying thin films have been synthesised

Characterisation of the synthesised materials is also performed in a high throughput manner; ideally the characterisation of the whole system is performed in parallel. Thus the individual compositions are treated exactly the same and the characterisation of all samples is performed at the same time. This increases reliability by ensuring elimination of measurement differences due to a variable sample history.

In order to map the data from a Cartesian co-ordinate system on the substrate to a ternary plot, it is necessary to measure the composition at the points where measurements are made. Energy Dispersive X-Ray (EDX) analysis is used to measure the composition as a function of position. Further measurements and characterisations are also made as a function of position on the substrate thus they can then be linked and mapped with the EDX data and plotted in compositional space.

A number of characterisation methodologies were adopted to characterise the data storage properties of the chalcogenide thin-films. Table 2.3 lists the measurements which have been adapted to either high throughput, parallel or sequential, characterisations. The details of these measurements are discussed in detail in section 2.8.

Technique	Measures	Type
EDX	Composition as a function of position	Sequential
XRD	Crystalline areas and crystal structure	Sequential
Hot plate	Crystallisation temperature	Parallel
Ellipsometry	n and k	Sequential
4PP	Sheet Resistance	Sequential
Profilometry	Film depth	Sequential
Static Tester	Crystallisation time	Sequential

TABLE 2.3: Compositional spread characterisation techniques

The above techniques are also valid analyses for constant composition films and bulk pieces of the material. In addition, measurements of crystallisation activation energy and ultraviolet-visible transmission spectra have been made on single composition samples.

2.8 Characterisation Methodologies

In this section the characterisation methods, listed in table 2.3, are described and the conditions used for experiments conducted for this thesis given.

2.8.1 Composition Measurements

Two non-destructive methods of composition measurement were used in this thesis; X-Ray Fluorescence (XRF) and more frequently, Energy Dispersive X-Rays (EDX) spectroscopy. Both methods are based on the analysis of the X-rays ejected from a sample illuminated with either X-rays or an electron beam.

In XRF analysis, high energy X-ray photons from a X-ray tube are projected onto a sample at a specific angle. The absorbed photons give rise to either X-ray photons or Auger electrons. If the incident photons have sufficient energy to ionise atomic inner electrons, the atom is rendered unstable and an electron from a higher energy orbital must fall into its place. In doing so a photon with energy equal to the difference of the two orbital electron levels is ejected; this is fluorescence. Every element has electron orbitals of characteristic energy. By using the broadband Bremsstrahlung radiation, the electrons from a range of energy levels can be excited. A diffracting crystal is used to select a specific wavelength from the X-ray photons emitted from the sample. These

monochromatic photons are then projected onto the detector. Since the wavelength and relative intensity of the photons are known, an accurate measurement of the film's chemical composition can be made.

For the measurements carried out in this thesis, thin film samples were prepared on top of silicon substrates. A Rigaku RIX 2100 XRF system was used to measure 10mm diameter samples, with film thicknesses of typically 300nm. Measurements were usually made with the following system settings:

- Generator acceleration voltage = 50kV
- Generator current = 50mA
- LiF diffraction crystal
- Slit = fine
- aperture = 30mm
- Chamber Pressure $<$ 10Pa

The EDX analysis is similar to the XRF, only accelerated electrons are used to excite X-rays in the sample. The electron beam of a Scanning Electron Microscope, (SEM) is projected onto the sample and similarly, to XRF, electrons from the sample can be ionised resulting in instability and the falling of a higher energy electron to fill the place of the ionised electron, thus emitting a photon. The energy of the emitted photon is characteristic for each element. Thus, to identify the composition of a material it is necessary to, initially, know the photon energies generated and, secondly, the relative intensities of each photon energy. By comparing the intensities it is possible to measure the relative composition of each atom.

Composition measurements of thin film samples on top of Si substrates were performed in this thesis. The films were prepared by PVD and they were typically between 70nm and 150nm in depth. For thin film samples the penetration depth of the electrons into the sample becomes very important. If too many X-rays are generated in the substrate, the X-ray signal from the film under test will become very weak and therefore reducing measurement accuracy. Thus it is desirable to make measurements at lower accelerating voltages, such that the electron's kinetic energy is reduced so that a larger fraction is absorbed by the film; thus increasing the X-ray generation from the film. However, the acceleration voltage should be greater than the excitation edge of the atoms which are present in the sample. For materials studied in this thesis an acceleration voltage of 7keV was sufficient. At 7KeV the absorption of electrons occurs within a few hundred nanometers. Figure 2.12 shows the X-ray generation from the silicon substrate

as a function of Ge film depth. The Monte Carlo simulation was performed using the NISTmonte[82] java program. Ge was chosen since it is the lightest atom deposited by PVD and therefore has the lowest electron stopping power [83]. The simulation parameters were: 10000 electrons, 7keV electrons, 33° detector angle.

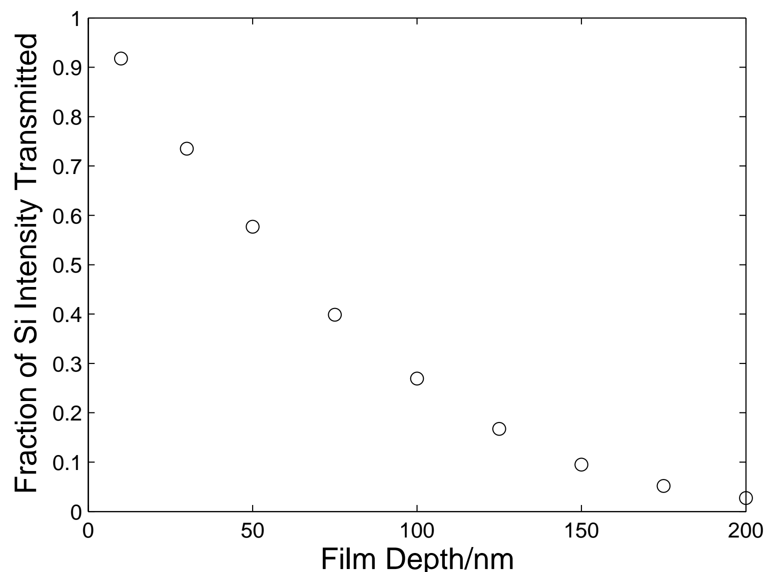

FIGURE 2.12: Transmitted X-ray intensity from a silicon substrate as a function of a Ge film layer depth.

It is clear that, for film depths between 70nm and 150nm, between 60% and 80% of the signal will be from the film with the remainder of the X-rays generated in the Si substrate.

Figure 2.13 shows the paths of 10 000 electrons in the Ge film and silicon substrate for electron acceleration voltages of 5keV and 20keV. The effect of electron energy on the penetration depth is shown and it is clear that lower energies are required for a measurable fraction of the x-rays to be generated in the film.

For the measurements reported in this thesis, the EDX analysis, unless otherwise stated, was performed in a JSM 5910 SEM and using an Oxford Instruments, 7247 detector. The measurement conditions are as follows:

- acceleration voltage of 7keV
- beam current of 0.426nA
- working distance of 20mm

This ensured, that more than 40% of the X-rays were routinely generated in the film allowing quantitive analysis of the film composition.

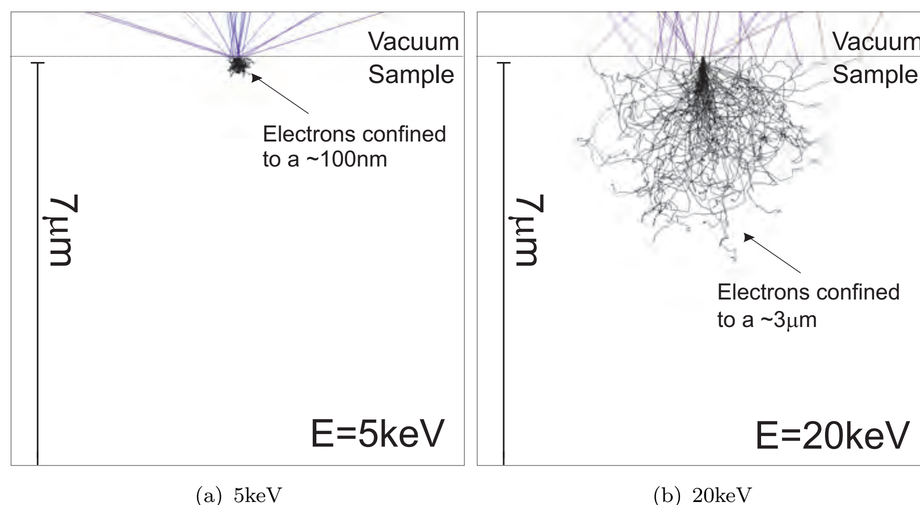

(a) 5keV

(b) 20keV

FIGURE 2.13: Monte Carlo simulation of electron trajectories in a film and substrate accelerated at (a)5keV and (b)20keV)

EDX analysis is fast; a useful spectra is achievable within 60 seconds, however the accuracy of the composition measurement is not better than 5%; this accuracy becomes even worse if elements with similar atomic transitions are analysed. By comparison the XRF-wavelength dispersive measurement is comparably slow with collection times for thin films around of 10 to 30 minutes depending on the composition of the film analysed. However, the compositional accuracy can be better than 1%. Another limitation of this technique is the size of the X-Ray spot on the sample; it is large, thus reducing the sample diameter also increases the detection time. For compositional spread films, where property trends are important, the accuracy can be compromised for time and then EDX is the most suitable analysis method. But for an accurate measurement of a specific composition, a wavelength dispersive method is the most suitable.

2.8.2 Optical Characterisation

Optical characterisations routinely carried out in this thesis works include transmission spectroscopy of the thin films samples using a Perkin-Elmer spectrophotometer and ellipsometry using a 532nm, NFT-2000, imaging ellipsometer.

Spectroscopy was primarily used to measure the electronic absorption edge and transmission properties of the chalcogenide films. This involved passing a broadband light source through a diffraction grating such that only a single wavelength could pass. This light was then passed through the film and a standard (usually a substrate without the film). Each beam then passes to a corresponding photodetector. The diffraction grating

is then rotated by a small angle such that another wavelength is selected and the measurement is repeated. The resultant measurements are used to build the transmission spectra of the sample.

Ellipsometry is a technique through which the refractive index or thickness of a thin film can be established. Electromagnetic waves undergo a change in phase upon reflection from a surface. This phase change is known as Δ. The reflected light intensity of the perpendicular, p, parallel, s, polarisation states is used to define the quantity Ψ. Where $\tan\Psi = \frac{|R^p|}{|R^s|}$, i.e. the angle whose tangent is the ratio of the magnitudes of the total reflected intensities. Each refractive index has an associated Δ and Ψ. Determination of the refractive index is carried out via a rather involved numerical procedure. The essence is that each refractive index is a point on a trajectory plot of Δ against Ψ. The trajectory is dependant on the thickness of the film. Hence Δ and Ψ are dependent on the film depth and the refractive index [84]. To find n, from a single measurement and a specific angle, it is necessary to know the film depth. Conversely it is also necessary to know the refractive index for a measurement of depth. A numerical algorithm, is used to find a trajectory for the specified depth of film which gives the measured values of Δ and Ψ. For measurements in this thesis an algorithm which uses the simplex routine, implemented by Dr B. Greef, University of Southampton, was used to find n and k from Δ against Ψ.

2.8.3 Electrical Characterisation

A four point probe was employed to measure the electrical resistivity dependence on the phase of the chalcogenide. The intrinsic electrical resistivity of the chalcogenide film is then simply the sheet resistance, R_s multiplied by the film depth, t; $\rho = R_s \times t$. A schematic diagram showing the experimental arrangement is given by figure 2.14.

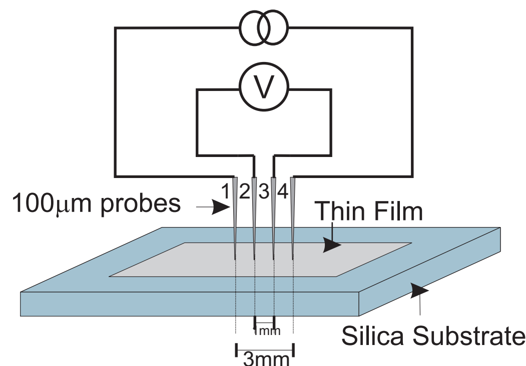

Figure 2.14: Schematic of the in-line Four Point Probe used to measure the sheet resistance of chalcogenide thin films

A constant current is driven across the outer two probes (1 and 4) and the voltage drop is measured across the inner probes (2 and 3). This way the arrangement eliminates the measurement problem of contact resistance. The driven current is set and is therefore independent of the contact resistance. The contact resistance on the voltage measurement probes can also be neglected since the voltmeter has a very high input impedance compared with the contact resistance. This means that very little current will flow through the probes and hence the difference in potential between the two probes will be far greater than the voltage drop caused by a very small current flowing through a resistive contact. This is a significant advantage over a two terminal measurement.

The spatial resolution of the four point probe is set by the probe spacing. All of the measurements undertaken in this thesis were made with a spacing of 1mm. Despite all four of the probe tips spanning 3mm, the measurement only involves the inner probes (2 and 3) therefore the actual resolution is just 1mm.

The sheet resistance is given by:

$$Rs = \frac{\pi}{\ln 2} \times \frac{V}{I} \times k \qquad (2.10)$$

where V is the measured voltage, I is the source current and k is a geometric correction factor [85], for a sample of infinite area, $k = 1$.

All of the four point probes used in this thesis had a probe spacing of 1mm and a tip diameter of $100\mu m$. An automated 4-Dimensions measurement system was employed to make multiple measurements at different positions on the same substrate. For measurements on single composition samples, a Keithley 238 and a Jandel RM3 electrometer were used.

2.8.4 Thermal Characterisation

The properties of phase change materials drastically change upon crystallisation. This transition is initiated at a definite temperature. Since the properties of the material change, they can be observed as electrical resistivity, optical transmission and reflectivity changes. Also the exothermic crystallisation reaction and the endothermic melting transition can be measured using Differential Thermal Analysis (DTA), but bulk or powdered samples are required for this.

In this thesis, all of the above techniques have been used to characterise the chalcogenide phase change materials. Optical reflectivity measurements, as a function of temperature, were made on thin film samples by placing the sample on a thin film heating plate and measuring the intensity of the reflected light from the sample with a CCD camera.

The heating ramp rate can be controlled up to $350°C$. The camera is mounted such that the whole of the sample is visible. A map of reflected intensity, as a function of sample position, is generated. The camera takes snap shots at a predefined temperature resolution. For samples in which the composition is spread over the entire sample, the optical response due to heating can be measured as a function of composition. Figure 2.15 shows a schematic of the set-up. A similar set-up was also used to make measurements at a specific wavelength or wavelength range. In this case a laser or broadband source was passed through the sample in a Linkham Scientific TK1500 microscope furnace. The transmitted light was then passed through a monochromator and collected by a photodiode. Again the temperature and heating rate could be controlled to within $\pm 1°C$.

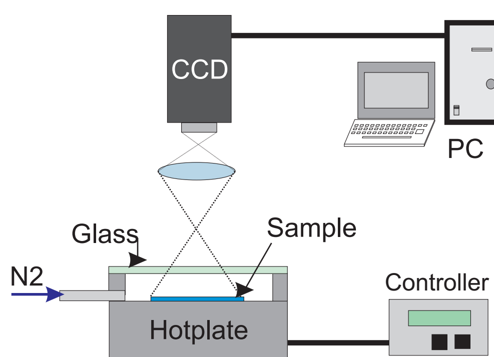

FIGURE 2.15: The hotplate and CCD camera arrangement used to map reflected intensity as a function of sample and position.

A purpose-built high temperature four point probe was also used to measure the electrical response as a function of phase change. A technical drawing of the four-point-probe is included in appendix B. For a heating plate arrangement there is a large thermal difference between the probe tips and the surface of a film. Hence the tungsten tips act to remove the thermal energy from the film. To make accurate measurements it is necessary to heat the whole arrangement in an oven or furnace. Electrical sheet resistance measurements (see section 2.8.3) are made as a function of temperature and at the transition temperature, a large reduction in the sheet resistance is observed with temperature.

Differential thermal analysis is based on the difference in temperature of a well thermally characterised inert reference (usually alumina powder) and an unknown sample. Both reference and sample are positioned on top of thermocouple at the centre of a small furnace where the temperature distribution is uniform. As the furnace temperature is increased, a difference in temperature between the reference and the sample is recorded. Upon crystallisation of the sample, energy is liberated in the form of heat (an exothermic reaction) this results in a large spike in the difference of temperature

between the reference-sample as a function of temperature. Similarly, sample melting results in a large dip in the DTA trace indicating an endothermic reaction. In this thesis two different Perkin-Elmer DTA systems were used; the DTA-7 and the more modern Diamond DTA/TGA. In both systems, the furnace was purged with flowing nitrogen to limit oxidation of the samples. Figure 2.16 shows a schematic of a thermogram, which is typical for some of the Ga:La:S materials studied in chapter 6 of this thesis. It is clear that the endothermic glass transition temperature, T_g, is observed as an endothermic dip in the thermogram.

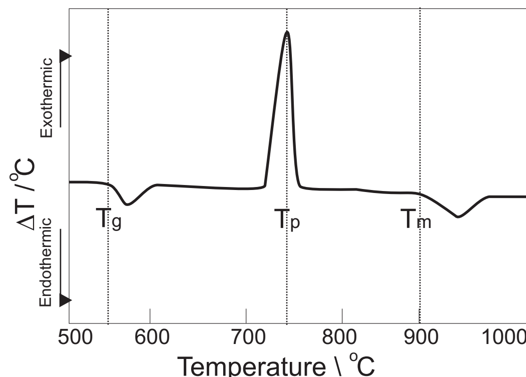

FIGURE 2.16: A schematic of a typical Differential Thermal Analysis thermogram

Since the DTA provides T_g, T_p and T_m, much information can be gained about single compositions. Some samples have more than two phases dissolved into one another. In such cases the peaks and dips for all of the associated phases can be observed. The width of the crystallisation peak also gives some information about how quickly the crystallisation is occurring. If a strong narrow peak is observed, the crystallisation is likely to be very quick. However, if the peak is broad and not so well defined, this is indicative of multiple crystallisation events occurring. Also, the separation between T_m and T_P gives some indication of the crystallisation viscosity; a small separation suggests a low viscosity [24]. For phase change memories, ideally crystallisation is single phased and has a low viscosity since the crystallisation growth rate increases with decreasing viscosity, η [15]. Therefore, for phase change materials, both the crystallisation peak and $T_m - T_p$ will be small.

2.8.5 Activation Energy Measurements

Activation energy is the threshold energy necessary for a the phase change to take place. The amorphous and crystalline states of a phase change material are effectively stable because they are minima separated by a barrier in potential energy. A schematic is given in figure 2.6 showing how the activation energies for crystallisation (ΔE_{ac}) and amorphisation (ΔE_{aa}) and enthalpy of formation (ΔH) are related.

Since the rate of crystallisation is dependent on temperature, crystallisation is an activated process and thus has an associated energy. For the crystallisation to happen at a high rate there must be a large proportion of atoms with energy above the activation energy. If all experimental conditions are fixed, with the exception of heating rate, measurements of crystallisation temperature result in a shift in temperature which is dependent on the heating rate. The higher the heating rate, the higher the crystallisation temperature. The faster the material is heated, the less time the atoms have at each temperature thus a lower proportion of the atoms have an energy greater than the activation energy. This means that the crystallisation temperature is shifted to a greater temperature where a larger proportion of the atoms are excited above the activation energy. This is the basis for Kissinger analysis, which allows the activation energy to be extracted from crystallisation measurements conducted at different heating rates.

DTA is a popular technique applied to the study of non-isothermal nucleation and growth during crystallisation of a material [86, 87, 88]. Phase transformations have been studied using both isothermal and non-isothermal techniques. The isothermal technique involves quickly ramping the glass' temperature above T_g to a constant temperature and then monitoring the heat involved in crystalisation as a function of time. The two main disadvantages of this technique are: (1) it is impossible increase to the test temperature instantly and (2) the sample's temperature takes some time to stabilise and hence no measurements are possible during this period. In contrast, non-isothermal techniques involve heating the sample at a constant rate. The heat involved in crystallisation is recorded as a function of both time and temperature. This method does not have the two drawbacks of the isothermal method previously described [87, 88].

The formal theory of phase transform kinetics was developed by Johnson and Mehl [89] and Avrami [90, 91, 92] and is known as the JMA model. In short, the theory is used to analyse the fraction of a material crystallised, x, as a function of time, t, the nucleation frequency per unit volume, I_v and the crystal growth rate, u.

Isothermal analysis of reaction kinetics was originally developed for the $solid \Rightarrow solid + gas$ reactions by Kissinger [86] and later applied to the kinetics of polymer crystallisation by Ozawa [93]. For a sample heated at a constant rate, the JMA-theory yields,

$$x = 1 - \exp(-g' I_v u^m t^n) \tag{2.11}$$

where m takes the values 1, 2 and 3 for one, two and three-dimensional interface controlled crystal growth respectively. For diffusion controlled growth, where the growth rate falls as $t^{1/2}$, m takes the values $1/2, 1, 3/2$ for respective dimensionalities of the growth. $n = m + 1$ for $I_v \neq 0$ and g' is a shape factor. It can be seen from equation 2.11 that the effective overall reaction rate is the product of g', I_v and u^m. This product is

assumed to take an exponential Arrhenian-type temperature dependence and is termed the reaction rate constant,

$$K = K_0 \exp(-E_c/RT) \tag{2.12}$$

where K_0 is a pre-exponential factor, E_c is the activation energy for crystallisation, R is the molar gas constant and T is the temperature of the sample. Thus the fraction of a sample crystallised can be expressed as,

$$x = 1 - \exp(-(Kt)^n) \tag{2.13}$$

The crystallisation process is thought to be well understood when the three kinetic parameters E_c, n and K_0 are determined [88].

Assuming a constant heating rate of α, the temperature of the sample is $T = T_0\alpha$t. Differentiating equation 2.13 with respect to time and taking consideration that the reaction rate constant is a function of time, through the temperature dependence on time, the rate of crystallisation is,

$$\dot{x} = nK^n t^{n-1}[1 + at](1 - x) \tag{2.14}$$

where $a = (\alpha E_c/RT^2)$.

Kissinger suggested that the term at could be neglected if $(E_c/RT^2) \ll 1$. So, rearranging equation 2.13 to make t the subject, substituting into 2.14 and neglecting $(E_c/RT^2) \ll 1$,

$$\dot{x} = AnK(1 - x) \tag{2.15}$$

where $A = [-ln(1 - x)]^{(n-1)/n}$

The peak of crystallisation occurs at a temperature T_p. At T_p the rate of crystallisation is a maximum and thus, on a DSC curve, the exothermic crystallisation event is also liberating the maximum amount of heat and, thus, is identified as the maximum of the peak. At maxima the rate of increase of the crystallisation rate is zero, $\ddot{x} = 0$. Assuming $A = [-ln(1 - x)]^{(n-1)/n}$ is constant with time and differentiating equation 2.15 with respect to time and equating to zero,

$$\ln(\alpha/{T_p}^2) = \ln(C) - E_c/RT_p \tag{2.16}$$

where $C = (ARnK_0/E_c)$, a constant.

From equation 2.16, it can be seen that a plot of $\ln(\alpha/{T_p}^2)$ against $1/T_p$ would reveal the crystallisation energy through the gradient of the plot.

2.8.6 X Ray Diffraction

X-rays interact with the electronic orbitals within an atom causing the incident X-ray photons to scatter. The penetrative power of the X-rays means that the photons can penetrate a large number of atomic layers, thus a large proportion of the scattered photons come from deep within the solid. Within a crystal, the regularly spaced atomic positions are repeated sequentially to form a superlattice. Each repetition forms a fundamental unit. Within the superlattice there are many possible planes of atoms. The frequency at which an atom occurs is dependent on the plane angle of intersection. Therefore reflection of X-rays occurs from a very large number of atomic layers. Superposition of the wavelets from each atomic layer leads to interference fringes. For constructive interference, the wavelets must be in phase, hence the difference in path length between that traversed by a wavelet from different planes must be an integer number of wavelengths. This only occurs at specific angles. Deviating from these angles results in destructive interference and a sharp drop in the reflected intensity. The condition for high reflectivity is called Bragg's Law and is given by equation 2.17 [94].

$$2d \sin\theta = n\lambda \tag{2.17}$$

where d is the separation of the reflecting planes and is known as the lattice constant, θ is the angle of the incident X-ray beam with respect the the crystal planes, n is an integer corresponding to the number of wavelengths traversed between the atomic planes and λ is the wavelength of the incident x-rays.

So, by measuring the reflected intensity as a function of angle, a number of peaks will occur at different intensities corresponding to reflections from different crystallographic planes. From this data it is possible to calculate the structure of a crystal and the lattice spacings.

For the diffraction measurements carried out in this thesis, a Bruker C2 instrument was used with a Cu target, generating $K - \alpha$ line $\lambda = 1.541\AA$ and spectra for $29^\circ < 2\theta < 62^\circ$. To increase the statistical distribution, each composition was typically measured for 600 seconds. The spatial resolution of this instrument is defined by its spotsize which is $\sim 100\mu m$.

2.9 Summary

The chapter has given background information and theory on chalcogenide glasses and phase change data storage materials. Deposition and characterisation methods which

have been applied in this research have also been described. Theoretical concepts for electrical conductivity and phase change have been described in some detail. These will be used in the analysis of measurements made on films in chapters 4, 5 and 6.

Chapter 3

High Throughput Static Tester

3.1 Introduction

The static tester apparatus designed and developed as part of this work is used to test the phase change kinetics of chalcogenide data storage materials. Unlike a dynamic disc tester, which is used to measure the performance of phase change materials in a spinning optical disc system, the samples here are static. This type of system is much more suited for measurement of intrinsic material properties (such as crystallisation time, reflectivity change, energy requirement) rather then engineering parameters (such as SNR, jitter, minimum marks lengths)of optical discs and lends itself well to the high throughput methodology.

In 1968, Stan Ovshinsky's $TeGeSbS$ research showed that an Ar-ion laser with pulses varying in length between $1\mu s$ to $16\mu s$ and powers between 10mW and 100mW (focussed through a $\times 10$ objective) could be used to reversibly change a material's phase. He then measured the thermal performance of the material by Differential Thermal Analysis (DTA); this allowed him to attribute the phase change as a purely thermal effect; the laser's role was simply to provide short pulses of heat [95]. The principle behind the optical measurement, to find the effect of heat energy on phase changed films, initiated a flurry of further papers from various research institutions [96]and companies [97] [98, 99, 100]. With the advent of the compact disc, in the early 1980s, and improvements in semiconductor technology, optically re-writable phase change material research peaked in the late 1980s and early 1990s. The term static tester was coined by Ross et al. in 1986 [101] to describe a system which was designed to test the phase change properties of static samples. In 1987 Rubin, of the IBM labs, published the first optical power, time, reflection matrix, called a Phase Transform Kinetics (PTK) plot [102]. This graphical representation of the effect on the material of different pulse conditions enabled the

selection of the ideal pulse parameters for crystallisation, amorphisation, and reading the written state. From these plots it was also possible to make a measurement of the quench rate for amorphisation and a figure of $\sim 4 \times 10^9 Cs^{-1}$ was suggested. The array of marks on the film could also be examined under a microscope and directly related to the pulse conditions.

In more recent times, Mansuripur published a number of papers discussing the design and use of static testers [103, 104, 105, 106]. His design is advanced; it is capable of measuring changes in polarisation and the ability of the material to hold a magnetic moment, by including a large electromagnet in the system next to the sample. The incorporation of a second, low power, cw laser to probe the heated spot allows reflectivity measurements to be made during the writing pulse. A high speed photodetector means that this measurement has a time resolution of 10ns. The whole system is based around a Scientific Instruments, Inc., MINIMAX microscope built with Olympus components including a 0.6NA objective lens. The two lasers are introduced to the microscope using a dichroic mirror. The diode lasers (680nm and 643nm) are limited to 50mW but can achieve pulses of 5ns. The combination of the two beams into the same optical path is achieved through a specifically designed optical stack which is placed at 45° to both beams. The stack reflects one of the lasers and transmits the other. Before entering the optical microscope the beams pass through a polarisation beam splitter, since both beams are polarized, they pass with minimal loss into the microscope. Upon reflection from the sample the beams are passed back to the polarisation beam splitter and are directed towards a detection optical circuit.

Mansuripur's static tester design has a number of very useful features. The dichroic mirrors and polarisation beam splitters for beam combination ensure that the system is power efficient; the pump/probe dual laser design in combination with fast detectors allows the measurement of the phase change dynamics. The ability to measure the Magneto Optic (MO) properties of materials is also useful for other data storage mechanisms. The design is however limited. The large electromagnet prevents measurement of the films' transmission, it is built around a commercially available microscope, thus this part of the hardware is fixed and also, finally, the diode lasers used are of relatively low power. All the measurements obtained are made in a multilayered film stack which might suggest that the optical power is too low for the amorphisation of single layer samples.

Another recent design by Wuttig's group automates the collection process by incorporating a knife edge auto-focus unit into a static tester set-up [107]. In this case a 830nm diode was focussed through a 0.9NA objective. This high NA lens enables measurement of samples, without a disc structure, at modest incident powers. However its small depth of focus means that a systematic, repeatable, focussing mechanism is required; hence

the autofocus. The autofocus is used to control a z-piezo stage, but the piezo's limited z-range reduces the sample's measurable area to $60\mu m$ by $60\mu m$. The substrates on which the chalcogenide films are deposited cannot be considered to be optically flat and any slope of the sample mounted on the stage could cause the system to require manual focussing outside the range of the piezo stage.

The aim of the static tester developed here is to aid the understanding of the materials' response to heat on a nanosecond time scale. The static tester described in this thesis will be used as a tool to analyze films with the hope of discovering improved phase change materials for predominantly electrical data storage devices. The choice of a static tester, over an electrical test chip for routine switching time measurements, was made due to the following drawbacks of a test chip:

- Many fabrication steps are required
- Time consuming direct e-beam writing or focussed ion beam etching is required to define sub-micron electrodes
- They are expensive
- Nanosecond time-scale, square pulses are required to travel within the chip, hence pulse deterioration, reflection, coupling and other RF design issues need to be considered
- The only active areas which can be tested are where the electrodes are present, therefore compositional resolution is limited
- It is not possible to achieve the three dimensional PTK array of data on compositional spread samples since the measurement is made on the same portion of material

The static tester's ability to measure a material's intrinsic switching properties on inexpensive simple substrates makes it an appealing tool which can be used as an intermediate measurement, between the primary screening and the final characterisation of the film's performance in the expensive electrical chips.

For this work, a static tester has been designed that is capable of measuring a composition spread sample. The design has been influenced by both Wuttig's and Manuripur's systems which were described earlier. However there are some important differences. It was decided that the incorporation of a commercial microscope was too limiting. Therefore, a simple, bespoke microscope has been built which is fully adaptable. An autofocus capability has been installed with the capability of focussing over a an entire substrate through control of both a long range stepper-motor stage and a high resolution

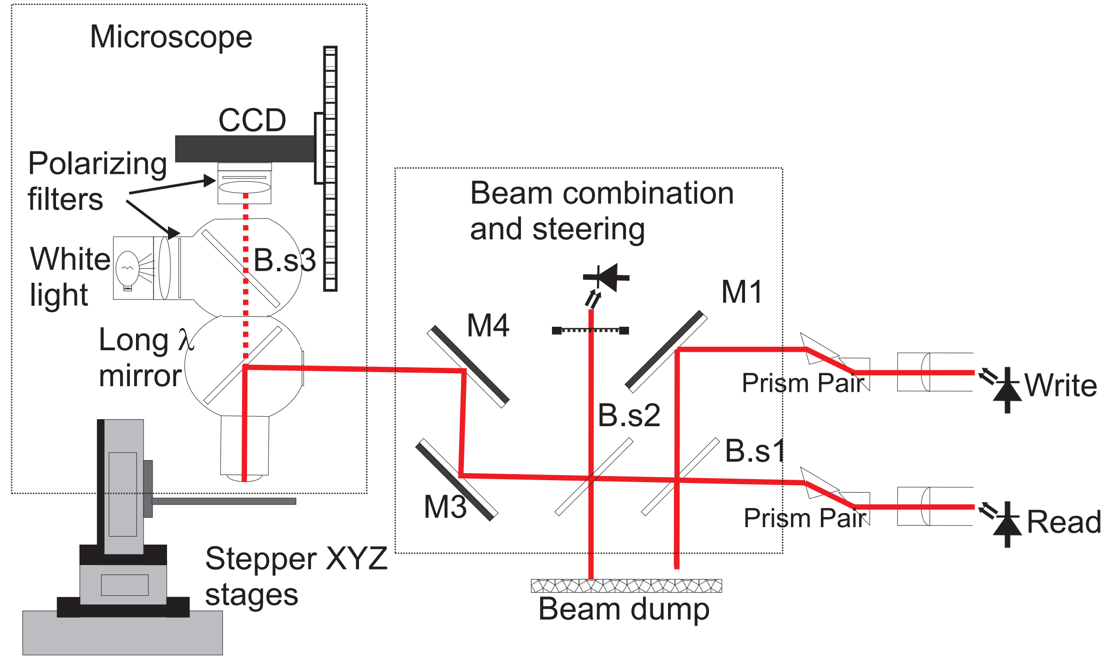

FIGURE 3.1: Schematic of the semi-automatic static tester

piezo stage; thus allowing automated focussing across all of the deposited compositions. Higher power, visible, diode lasers have been selected which allow phase change outside of a conventional disc structure. In this chapter the system and its various design considerations are discussed, before discussing the PTK measurements of composition spread films.

3.2 Set-up

Semi-automatic (figure 3.1) and fully automatic (figure 3.2) systems have been implemented; the set-up considerations are discussed. The main difference between the two systems is the ability to auto-focus. In the fully automated system an additional auto-focussing system with a $200\mu m$ piezo stage is incorporated into the system's design.

3.2.1 Laser Selection

The choice of laser is of critical importance when considering the design of a static tester, since any problem with the laser's performance will be passed on in turn to the phase change mark written on the film. The basic criteria for the choice of laser were:

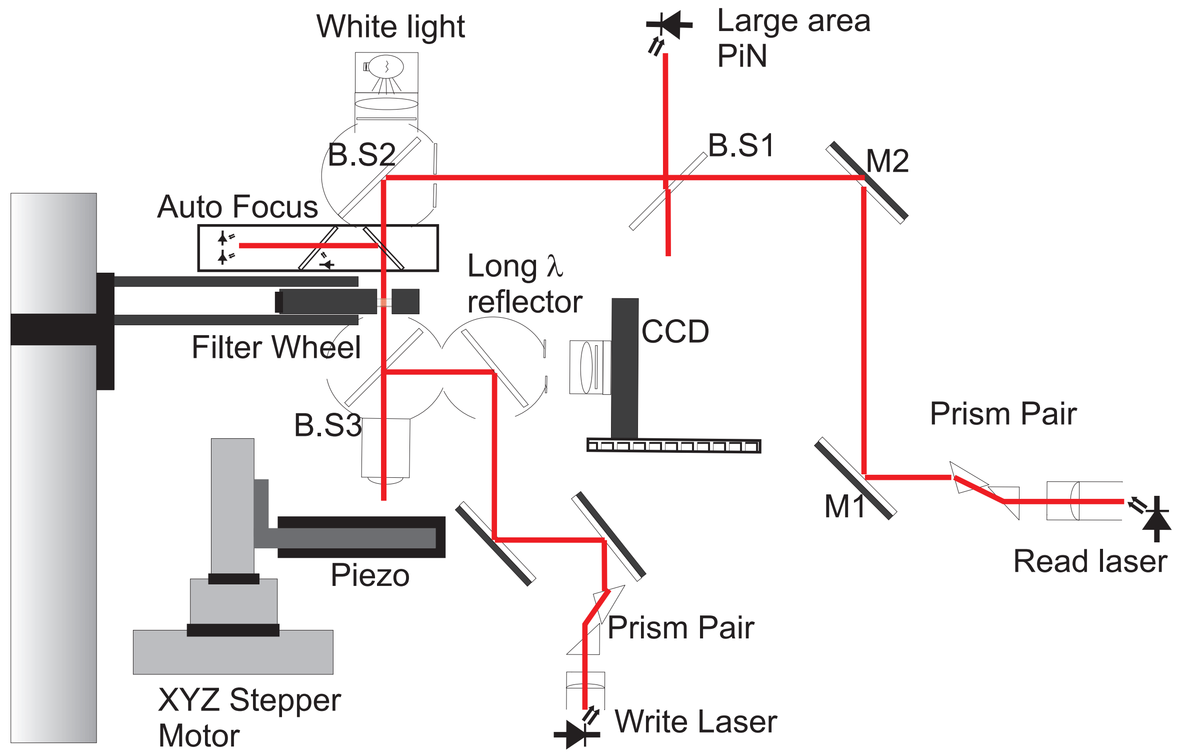

FIGURE 3.2: Schematic of the automatic static tester

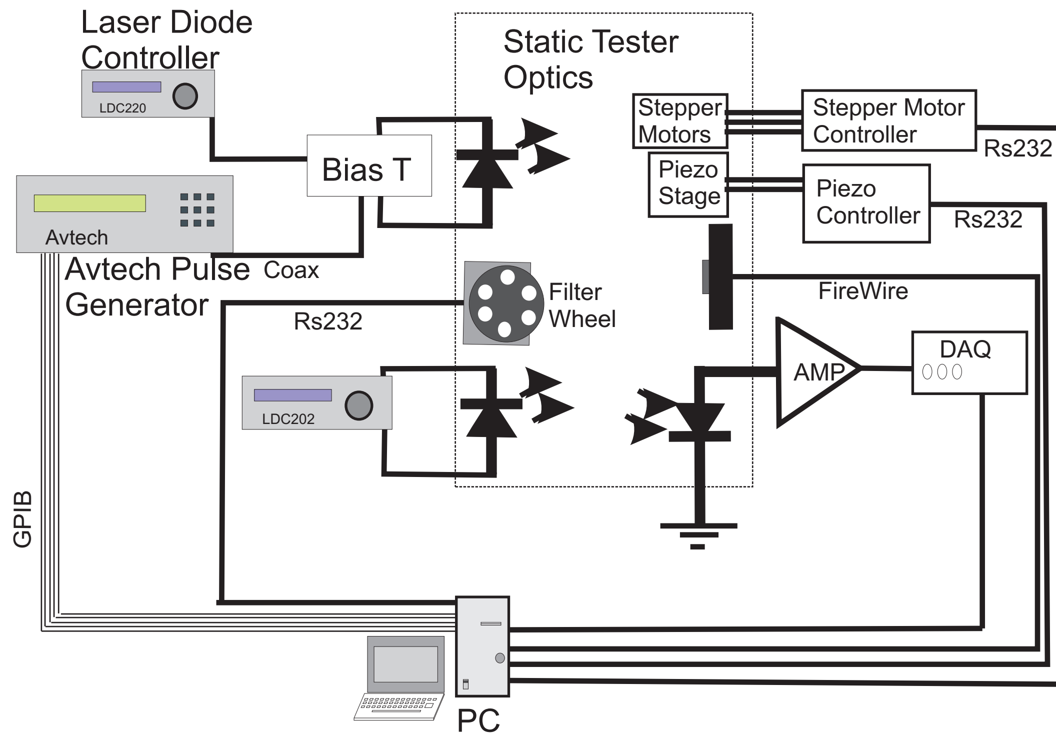

FIGURE 3.3: Schematic of the hardware connections for the automatic static tester

- Pulse duration
- Short Wavelength
- Power

Since the angular resolving power of a lens is limited at diffraction to $1.22\lambda/D$ [67], the read laser's wavelength is critical, if it is to be focussed within a written mark. Thus this puts a simple restriction that the reading wavelength should be less than the writing wavelength. The wavelength should be also absorbed by most chalcogenides, since most chalcogenides are transparent in the infrared and opaque in the visible, the lasers should have a visible wavelength. There is no standard wavelength for testing phase change materials, but there are three types of commercially available rewritable optical discs: CD, DVD and the more recent Blue-Ray disc. Each use a different wavelength diode; $780nm \pm 10nm$, $650nm \pm 10nm$ and 405nm respectively. Since data is available for these discs, a laser of a wavelength similar to one of the above would make comparisons easier. A diode laser was also preferred over a gas laser since since they are inexpensive, they can be easily pulsed on the nanosecond time scale using suitable drive electronics and they take up less space. 650nm red diodes, suitable for DVD drives, are inexpensive, visible (which makes alignment easier) and readily available. Hitachi offered a suitable 658nm (HL6535MG) which offered peak powers of 240mW when pulsed.

Simply supplying a diode with an RF signal is not recommended since any ringing on the signal would cause the diode to reverse bias and hence potentially cause damage. Thus the use of a bias-T is necessary. A bias-T allows the addition RF and DC signals. The bias-T had a bandwidth of 500MHz, therefore 2ns sinusoidal pulses are achievable, and consequently, square pulses of 10ns are also possible.

The read laser can be operated in CW; a 635nm diode was chosen. The 20nm difference between the read and write wavelengths gives a sufficient separation such that commercially available, off-the-shelf, filters can be employed to extinguish one of the two wavelengths. The shorter, read, wavelength also allows it to be focussed within the write laser's spot. This is discussed in section 3.2.3.

3.2.2 Filters

Two different dielectric filters are required for a manually focussed static tester, but five are required in the case of an auto-focussed system. For the manual system, a long pass filter is required on the detector and a 45° mirror at the write wavelength is required to direct the write laser into the objective whilst allowing white light to pass through it for the imaging system.

The auto-focussed system requires filters that allow:

- Only the AutoFocus Laser (AFL) to pass
- The read laser to pass and protect the autofucus system from the write laser
- Short wavelength light to pass but block the write and read lasers from the autofocus system. This short wavelength light can then be used for in-situ viewing of the writing process with the CCD camera.

3.2.3 Lens Selection

A correct choice of lens is of vital importance. The numerical aperture of the lens dictates the minimum spot size achievable, thus influencing the area of the written marks and, ultimately, in a data storage disc, the capacity of the disk. For this project, a somewhat more physical/thermal restriction is imposed by the spot size. As discussed earlier, the molten phase change layer needs to rapidly cool, or quench, into an amorphous structure. The cooling of the film is dependant on the heat energy stored in the film. Thus, a material with a large thermal capacity, or a large volume, will cool much slower than a smaller volume of the material at the same temperature. To demonstrate this a Finite Element Model (FEM) was used to simulate the cooling of a circular region within a $Ge_2Sb_2Te_5$ film, of depth 100nm on top of a Si substrate. The spot's diameter was varied and the time necessary for the spot to cool to $450°C$ was plotted. A five parameter exponential growth curve was fit to the data. This is given by figure 3.4. One can see that the cooling rate decreases with increasing spot size until it saturates at $20\mu m$. Although this model is very simple and does not accurately portray the heat trapped around the circular mark when the laser is switched off, it does demonstrate the basic principle that, for a smaller spot, the quench rate is greater and therefore the possibility of achieving an amorphous mark is greater.

The theoretical minimum waist size of a Gaussian beam TEM_{00} is is given by equation 3.1.

$$
\begin{aligned}
w(z) &= w_0[1 + (\frac{\lambda z}{\pi w_0})^2]^{\frac{1}{2}} \qquad (3.1) \\
w_o &= \sqrt{\frac{b\lambda}{2\pi}}
\end{aligned}
$$

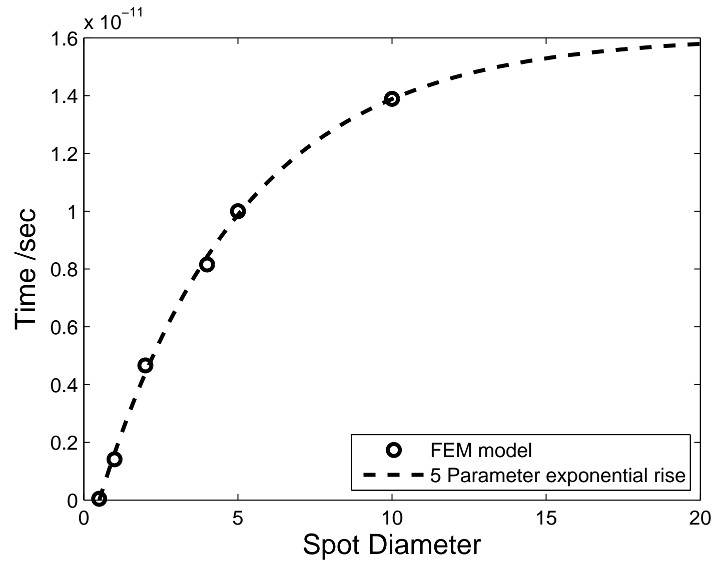

FIGURE 3.4: FEM model to demonstrate the quenching time as a function of spot size

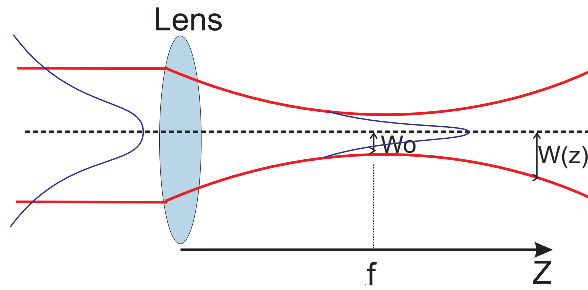

FIGURE 3.5: Schematic of the focussing of a Gaussian Beam

For a Gaussian beam focussed by a lens of focal length, f, this becomes (from Svelto, principles of lasers, [108])

$$\begin{aligned} w(z) &= w_0[1 + (\frac{\lambda f}{\pi w_0})^2]^{\frac{1}{2}} \\ w_2 &= \frac{\lambda f}{\pi w_1[1 + (\frac{f}{2R})^2]^{\frac{1}{2}}} \end{aligned} \tag{3.2}$$

But usually $Z_R >> f$ thus:

$$w_2 = \frac{\lambda f}{\pi w_1} \tag{3.3}$$

The numerical aperture of a lens is described by

$$NA = n\sin(\theta_{na}) = \sin(\tan(\frac{D}{2f})) \tag{3.4}$$

Making $\frac{D}{2}$ the subject and inserting into equation 3.3, the waist of the focussed beam becomes:

$$w_2 = \frac{\lambda}{\pi\tan(\sin^{-1}(NA))} \tag{3.5}$$

The chosen write diode has a wavelength of 658nm and the read has a wavelength of 635nm. Using equation 3.5, the theoretical minimum spot radii for a Gaussian beam would be 242nm and 236nm, thus the diffraction limited spot sizes are 484nm for the write beam and 472nm for the probe beam.

For such a system the depth of focus is defined by the point when the waist size expands to $\sqrt{w_0}$:

$$dof = \frac{2\pi w_0^2}{\lambda} \tag{3.6}$$

Therefore the focus depth of a 0.65NA lens at 635nm is 551nm. Other researchers have used a 0.9NA lens; for the wavelengths used in this project, the write and read spot radii then reduce to 101nm and 97nm. However further constraints are placed on the focussing accuracy. In fact the depth of focus becomes just 93nm; six times less than for the 0.65NA lens.

3.2.4 Auto-Focus System

To enable full automation of the static tester, an automated focussing system is required. The substrates under test are usually 32mm by 32mm. It has been shown, in section 3.2.3, that the depth of focus for the 0.65NA lens is just 551nm, thus practically ensuring that the lens is consistently within such a small displacement of the film is extremely difficult to maintain without an active focussing system.

A commercially available Prior Scientific microscope auto-focus system was chosen to enable automated focussing. The system encompasses a 690nm collimated, circular, beam which is cut by a knife-edge to create a semi-circular spot. This beam is passed through the microscope's focussing elements and reflected from the sample. The reflected image is analyzed using a Si split detector. When the sample is at the focus of the lens, the semicircular laser spot is reflected back onto the split detector. Moving in and out of focus causes the projected image to distort away from a perfect semi-circle and the signal on the detector is changed. By analysising the detector's signals, a quantative measurement of the focus is achieved. Autofocussing systems based on this principle,

and others, are quite common, many of which have been reviewed by Wolpert [109]. However this particular system was chosen as it is fully integrated and the disruption to the system and alignment procedure is minimal in comparison to other autofocussing mechanisms. It also has the advantage that it can be programmed to control a piezo controller such that focus is maintained or signals from the quadrant detector can be read by a computer for external control; this is useful for controlling the stepper motors.

Since the piezo stage is limited to a $200\mu m$ range of movement the stage has been fixed to a stepper motor. The stepper motor has a range of 50mm but its accuracy is limited to around 200nm. For fine adjustment to a diffraction limited focus the z-motion will be controlled by the piezo stage which is mounted on the stepper motor, see figure 3.2.

3.3 Development of the Static Tester

The development of the static tester has passed through a number of important design steps. The first system used a single laser to read and write. A 300nm thick, sputtered, $Ge_2Sb_2Te_5$ film was used to see whether crystallization via the static tester was possible. Since the film had not been capped to protect it from the atmosphere and it was quite thick, the laser pulse parameters for a phase change were unknowns. The focussing system was also primitive; the sample was mounted a top of a manual micrometer translation stage. The stage's resolution was just $50\mu m$. Since the focussing constraints placed on the system are demanding, the focussing procedure was highly inconsistent and extremely challenging. However, despite these difficulties, it was still possible to induce a phase change in the film and a voltage change on the detector from 2.1V to 2.3V was consistently observed when a 7V, 200ns pulse was applied to the laser above its threshold. Figure 3.6 shows a typical measurement where a DC current was set at 40mA and a voltage pulse of 8V was applied to the laser whilst the duration was incremented in 20ns steps. In this experiment, both lasers were implemented, the 658nm laser crystallised a small area of the film whilst the 635nm laser read the mark.

The detector sampled the reflected light for 1 second at 1kHz before and after the pulse. A knowledge of the laser's parameters for phase change allowed a judgement of how well aligned and focussed the system was. Over many iterative improvements to the basic system and its alignment, it was found that, in practice, it is possible to measure a 20% to 25% change in the as-deposited $Ge_2Sb_2Te_5$ film's reflectivity for a crystallising pulse of 200ns. Therefore, the system was judged to be setup well if such a change could be realised.

If one compares this experiment with a single laser measurement where the write laser is also used to measure the change in reflection of the film, an order of magnitude signal

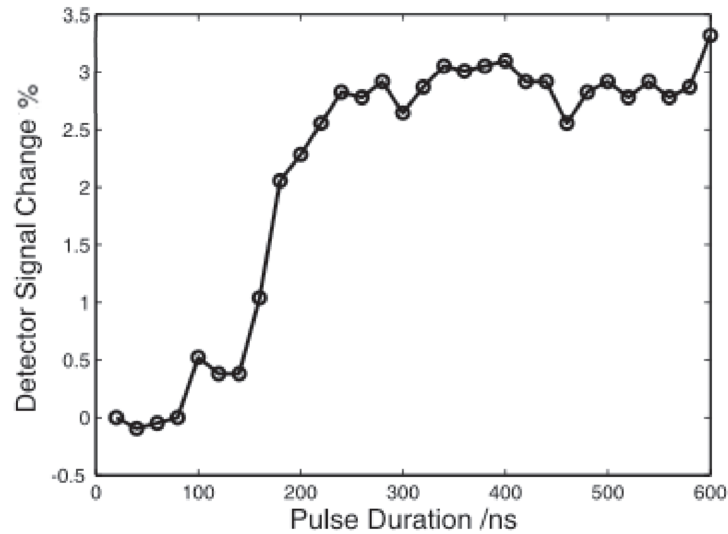

FIGURE 3.6: An early measurement of the reflection change as a function of pulse duration for a $Ge_2Sb_2Te_5$ film.

improvement is apparent, see figure 3.7. The poor signal, measured initially, is due to a misalignment of the read and write beams or is because the reading spot is not focussed to within the written mark. From this very early system some necessary improvements

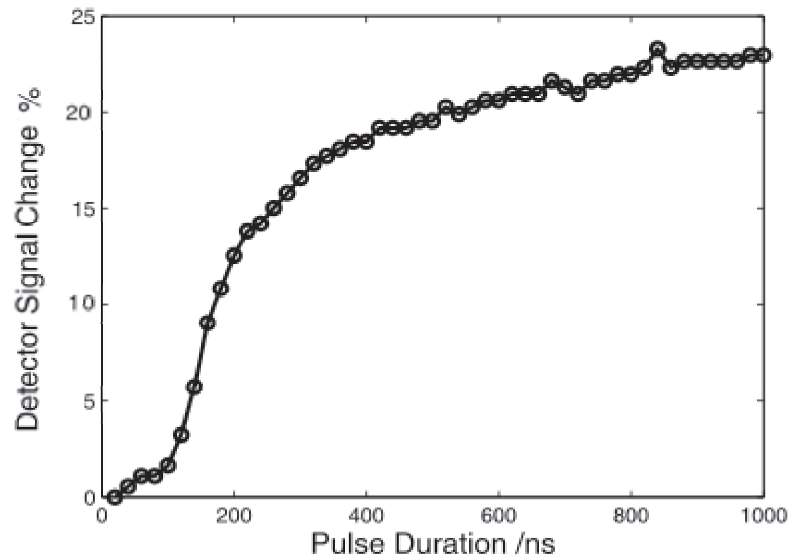

FIGURE 3.7: An early single laser measurement of the reflection change as a function of pulse duration for a $Ge_2Sb_2Te_5$ film.

were obvious:

1. Include a motorized z-stage with sub-micron resolution to aid focussing
2. Develop methodology to quantify the system's focus and alignment

3. Isolate the system from external vibrations
4. Improve the detector circuit such that a stronger signal is possible

3.4 Initialisation Steps

3.4.1 Alignment

Once both lasers have been collimated, their beams are set-up as per figures 3.1 and 3.2. It is essential that the two lasers are incident normal to the sample's surface, this implies that the beams should also pass through the optical axis of the objective. An error in beam positioning induces a swing in the reflected beam as the stage is moved in and out of focus. Since the PiN diode has a relatively small surface area, such a swing means that the modulation, as a function of z-measurement, is only possible over a short z-range; further, some materials change in depth upon crystallisation [110]; this change might be enough to swing the reflected beam off the detector, thus leading to an inaccurate measurement of the change in reflectivity. In addition there are other complications in that the reflectivity change is reduced as the angle of incidence is moved away from normal; this is discussed in section 3.4.3.

To overcome such problems a LabView script was used to oscillate the z-stage through ± 3000 motor steps. The swing can be observed, at first, on a screen next to the PiN, and later, on the CCD camera. The periscope set-up is then used to alter the position and the angle of the beams whilst simultaneously monitoring swing. The mirrors are altered to reduce the amplitude of the swing on the screen and hence, eventually, the CCD image. Once the spot's centre on the CCD image remains static, whilst the stage moves in and out of focus, the PiN is positioned such that its centre is in the centre of the reflected beam.

3.4.2 Manual Focussing

In order to make repeatable measurements of switching times, an assessment of the degree to which the sample is in focus is required. If the spot-size doubles in size, the laser's intensity is quartered; thus, ensuring that the sample is in focus is of great importance for reproducible data. Focussing by eye is a rather qualitative and time consuming method of focussing, for this work a quantitative method was sought; this is discussed later in this section.

When the system is focussed, the light reflected from the sample will be collimated if the light incident on the sample is collimated. For a well aligned system, this should mean

that the reflected power incident on the detector decreases as the spot is defocussed and beam collimation is lost. This allows some measure of how focussed the system is. Figure 3.8 shows how the voltage on the detector varies as the position of the sample on the z-stage is moved through the focus. The test was conducted using a single laser (power set to $< 1mW$) after minimisation of any focus wobble and repositioning the detector in the centre of the reflected beam. Measurements were made for z-increments of 100 motor steps.

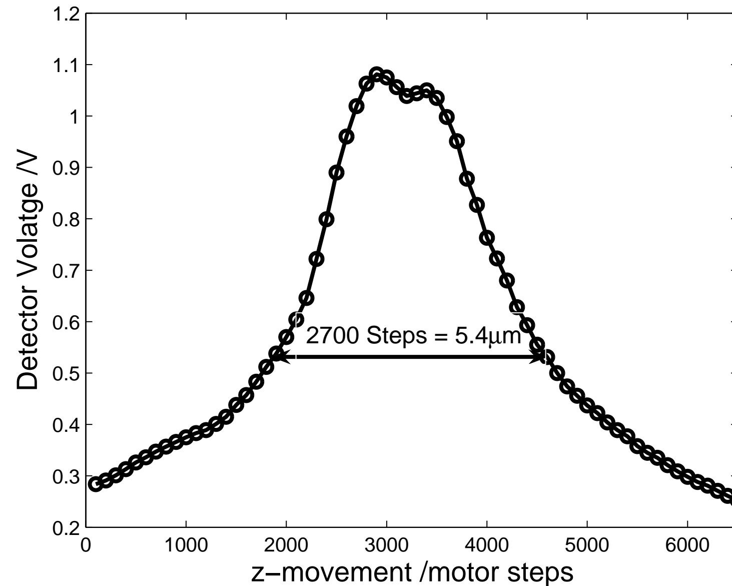

FIGURE 3.8: Detector voltage as a function of z)

It is shown that the curve has a FWHM of around $5.4\mu m$; this profile is too wide to allow the system to be focussed repeatedly to the diffraction limit. However this signal is still of use to position the stage initially in an approximate range of a more sophisticated, short-range, focussing system.

The chosen, manual, focussing method involved positioning a virgin sample of $Ge_2Sb_2Te_5$ under the lens and measuring the reflection of the laser before and after pulsing with a 200ns, 7V pulse (parameters described in section 3.3) then incrementing the z-stage by 20 nanometers and repeating the measurement; the result is a graph of modulation as a function of z height. The peak in the graph determines the z-height at which the sample is focussed. A control program was written to collect this data. This process can be used in an automated system but it is 'material expensive' and each substrate tested would require a standard phase change material to be deposited alongside the material under test. This is not desirable; thus a high magnification lens was introduced between

the camera and the objective. This increased the sensitivity of the imaging system to changes in z-position.

Now the same modulation, as a function of z-measurement, is only required as a calibration step. Once the system is determined as 'in focus', by looking at the modulation, the camera and imaging lens position is altered such that the image is focussed. For consequent focussing, the image is focussed and since it is in focus when the film is at the height for maximum modulation, the film is also considered as in focus. This action made focussing far more repeatable and much faster. Although the system is actually focussed by eye the calibration of the imaging system is quantative and the powerful imaging lens reduces the operator's error.

There are, however, some other issues regarding this measurement of modulation as a function of z-position. These are discussed in the later section 3.4.4.

3.4.3 Misalignment Effects

The focus wobble application, described earlier, has been used to ensure normal incidence of the laser's beams on the film. The affect of off-axis light incident on an objective lens will cause the angle of incidence on the film to move away from normal (see figure 3.4.3). This could lead to large variations in the reflectivity change, especially if the light is polarized. Since the NA of the objective is large (0.65), even a small deviation from the optical axis causes a large change in angle.

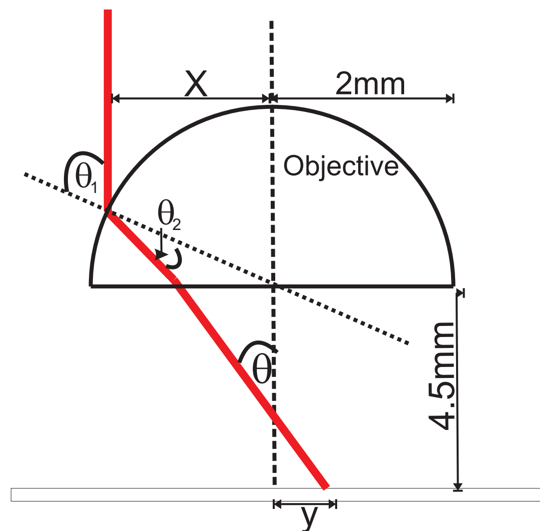

FIGURE 3.9: A schematic of how an off axis beam could lead to large changes of incident angle

By consideration of basic geometric optics, a model has been created to measure this effect. The objective was assumed to have a refractive index of 0.65 and be hemispherical with a radius of 2mm. A plot of the angle of incidence on the sample as a function of displacement from the lens' optical axis is given in figure 3.10. It can be seen that the system is sensitive to radial alignment; a misalignment of just 0.5mm leads to a 20° angle of incidence on the film.

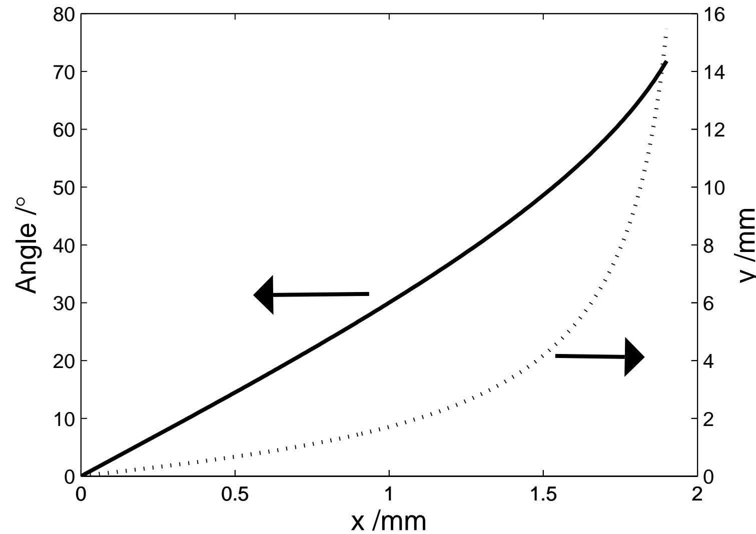

FIGURE 3.10: A model which shows the effect of incident angle and spot displacement as a function of the radial displacement from the objective's optical axis

The reflectance as a function of angle of incidence has been modeled using a commercial package called 'Concise Macleaod'. This package essentially calculates the reflectance and transmission by solving the Fresnel equations at each interface in a structure of thin-films. For this work it has been used to model the reflection of the single and multiple layer structures that the static tester is likely to encounter. Each measurement was made for both the crystalline and amorphous states from this reflectivity increase has been calculated and also plotted. Figure 3.11 shows (a) the reflection as a function of angle for a simple 300nm thick $Ge_2Sb_2Te_5$ film on top of a Si substrate and (b) the structure's corresponding reflectivity increase.

It is seen that, in this case, the unpolarised light shows very little sensitivity to angle and it is not until the angle of incidence is greater than 45° that the crystallised film's reflection begins to decrease, thus reducing the difference. However, should the read diode laser show some polarisation dependence, it is clear that a problem starts to occur. The difference in S-state polarisation decreases dramatically once the angle exceeds 10°. In contrast, the difference in reflection of the P state shows a radical increase; this is something that could possibly be exploited in both an improved static tester design or an optical disk reader.

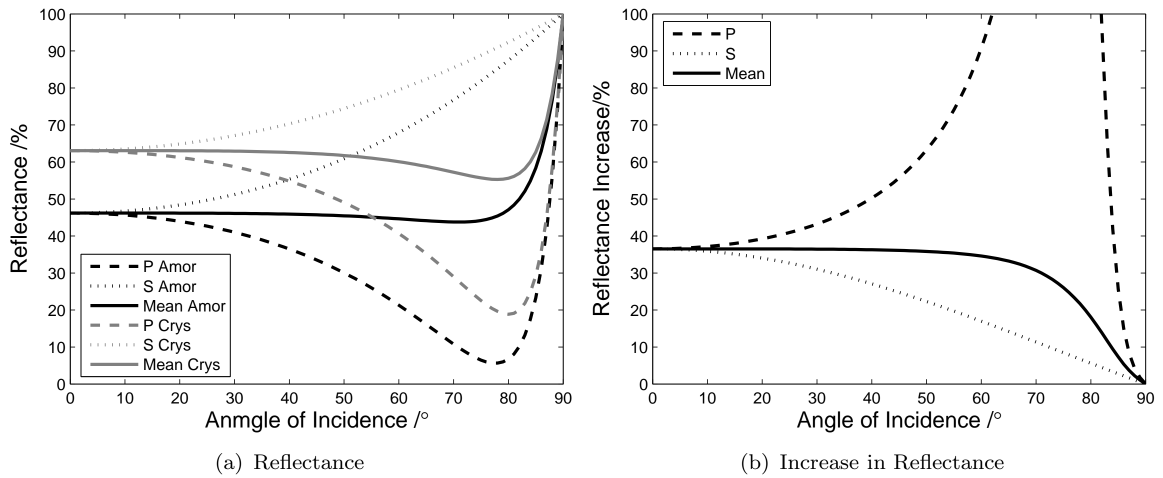

(a) Reflectance (b) Increase in Reflectance

FIGURE 3.11: (a)The reflectance of a 300nm GST film as a function of incidence angle (b) The percentage increase in reflectivity between the crystalline and amorphous marks as a function of incidence angle.

These problems become even worse when one considers a more complex and realistic disk structure. Figure 3.12 shows the results of a structure comprising an upper surface of $(ZnS)_{80} - (SiO_2)_{20}$ (115nm), a phase change layer of $Ge_2Sb_2Te_5$ (15nm), a lower $(ZnS)_{80} - (SiO_2)_{20}$ (20nm), a reflective layer of Ag (100nm) and a polycarbonate substrate. The mean reflectivity is strongly affected by the angle of incidence. It can be can seen that deviating by 40°, which equates to a radial lens insertion misalignment of 1mm leads to a drop in the reflectivity of 25%.

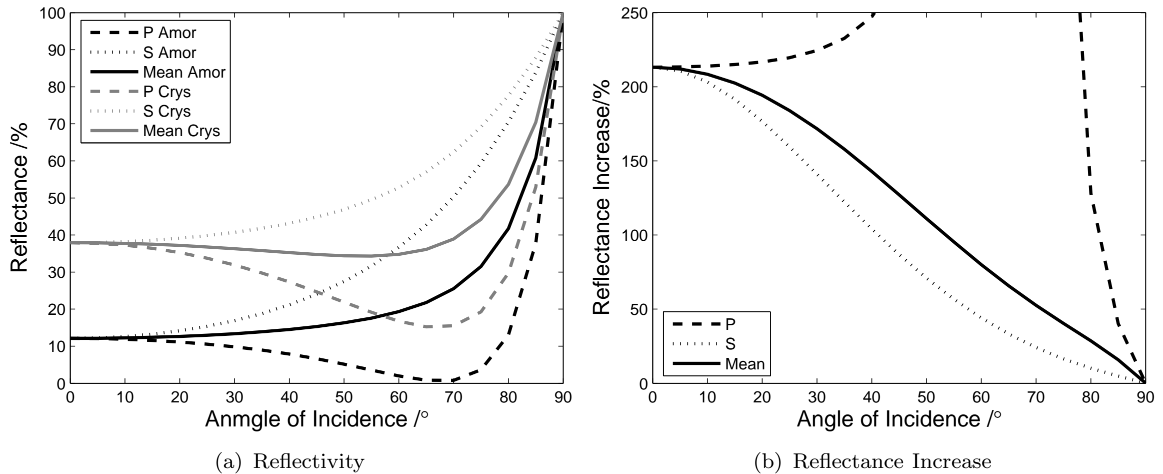

(a) Reflectivity (b) Reflectance Increase

FIGURE 3.12: (a) The amorphous and crystalline P, S and mean reflectivities of the plasmon stack (b) the amorphous and crystalline P, S and mean increase in reflectivity between the amorphous and crystalline states

Since diode lasers tend to have some intrinsic polarisation [111] good alignment of the beams onto the film is imperative for accurate measurements of reflectance change.

Probably the most challenging part of the alignment process is ensuring that normal incidence of the beams on the film is maintained whilst aligning the read laser, such that its centre is coincident with the write laser, thus projecting onto the written mark. The effect of misalignment is a disproportionate ratio of reflectivity signal from the unchanged film to that of the phase changed film. Clearly, this reduces the measured change in reflectivity. In practice, good alignment could only be guaranteed by checking the reflectivity change of a standard $Ge_2Sb_2Te_5$ film and comparing it with past measurements. The minimum standard at which the system was considered well aligned and with satisfactory beam coincidence was $\Delta R = 20\%$.

Clearly, the collimation of the lasers and the necessity of ensuring that both lasers are free from clipping apertures and edges are also important concerns for successful writing and reading of marks.

3.4.4 Effects of Over Power

On a number of occasions, when performing the measurement of reflection change as a function of z-height, a dip in the reflectivity peak occurred at the exact z-position where a peak was expected. This is apparent in figure 3.13. It is known that ablation of the film is possible for short, high power, pulses of laser light [15]. Images of the film were collected as the film is moved through the focus, see figure 3.14. At first normal crystalline marks are created in the film (picture A). Then the percentage change in reflectivity increases (approximately 1000 steps). At around 1500 steps the chnage stops increasing and tails off, this corresponds to the beginning of the film being ablated (picture B). As the ablated mark becomes larger (picture C) the modulation is quickly reduced. Picture D shows the film at a point very close to the focus; the mark is largest and this corresponds to the bottom of the valley (approx 2500 steps) in the reflectivity change curve. As the film is moved through focus and the spot expands, the intensity drops; thus ablating a smaller volume of material (picture E). Pictures F and G show the ablation mark reducing in size to zero corresponding to an increases in the modulation. Picture H shows no ablation and corresponds to around 4000 motor steps in figure 3.13

The dip in the modulation curve can be reduced to zero by careful selection of pulse energies. There is a minimum threshold power necessary for crystallisation and a maximum above which ablation occurs. This is further demonstrated by figure 3.15 which shows how the modulation dip decreases as the 100ns pulses vary in power. The measurement points 40 to 50 show a dip as the added voltage on the laser increases from 7 to 9V.

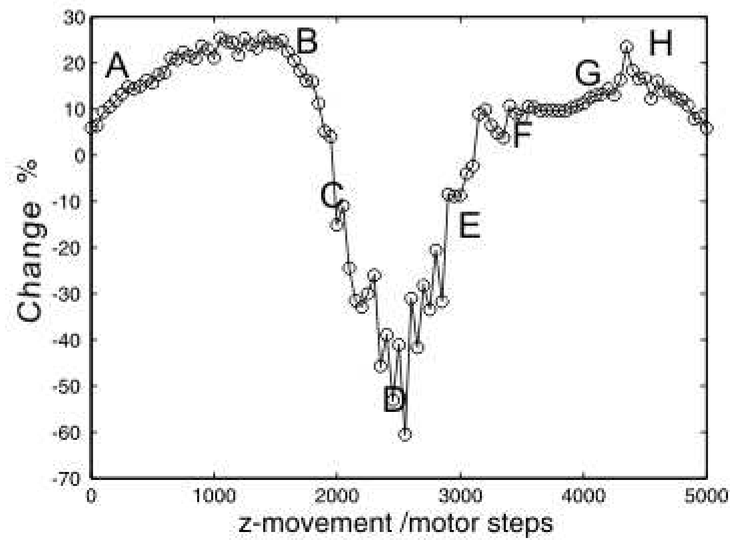

FIGURE 3.13: Modulation as a function of z position.

FIGURE 3.14: Marks showing ablation as the sample is moved through the laser spot's focus.

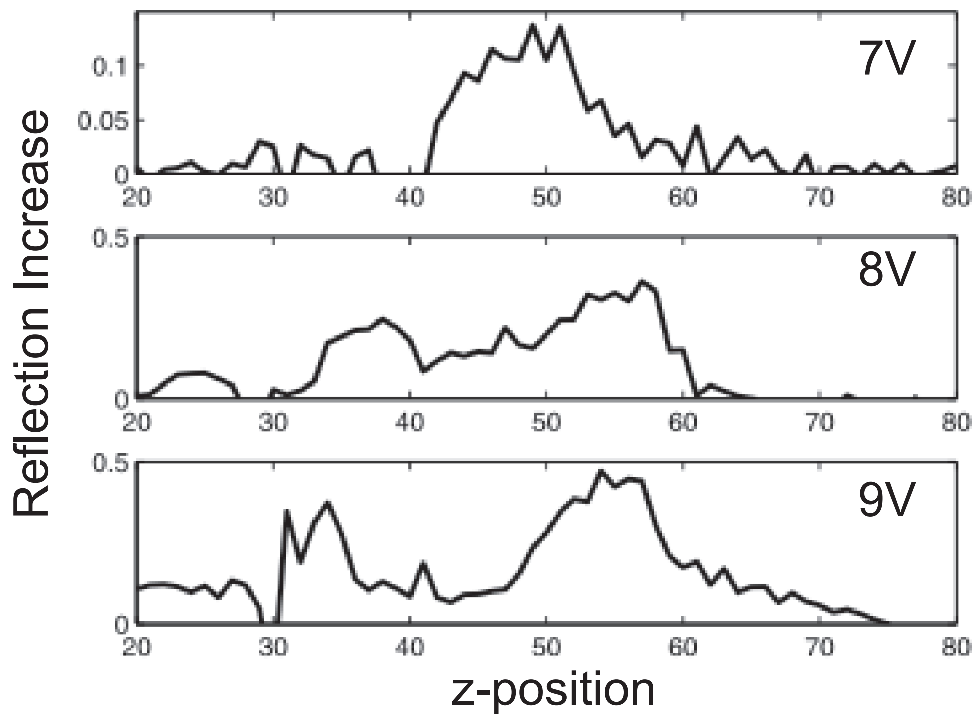

FIGURE 3.15: The affect of power on the modulation as a function of z-position

3.5 Application of Static Tester to a Graded Composition Film

This static tester has been designed for high throughput analysis of composition spread phase change films. To do this the system is programmed (described in section 3.5.1) to run a power, time, reflectivity measurement on each composition. A matrix of data is collected as a function of position on an array of samples deposited by PVD, as described in section 2.6. The result is a three dimensional power, time, reflectivity matrix within a two dimensional position matrix. For each position the corresponding power, time reflectivity data set is mapped against the compositional EDX data. This is by far the most complex data set described in this thesis.

Analysing this data set leads to a number of possible options. For instance one could:

- Analyse power or times for a specicific ΔR
- Analyse power or time for a maximum crystallisation rate by differentiating the reflectivity change - time data
- Plot the time or power for a specific trait in in the data such as a power/time inflection point

The main hardware parameters to consider when designing a system to operate over a breadth of compositions include:

1. Laser power required for unoptimised films
2. Focussing over a large area
3. Ability of high accuracy z movement across the whole substrate

The first item on this list is the power required to change the phase of these films. The system has been designed such that pulses of 100mW are possible on the film. This is five times the power required to amorphise $Ge_2Sb_2Te_5$. However problems may occur if new compositions are transparent to the 658nm laser, in which case a shorter wavelength should be considered or alternatively an electrical switching methodology adopted.

Since the depth of focus of the lens is just $0.5\mu m$, focussing at one corner of the 30mm by 30mm substrate almost certainly means that the system will not be in focus at the other corners of the substrate. However, each measurement of the PTK array is just separated by $5\mu m$ thus for a 20 by 20 PTK data set, the area needed to collect the measurements

is just 100um by 100um. It has been found that the system usually retains a good focus over such a small area and that refocussing is not necessary. The system is therefore designed such that, if the system is focussed on a new composition, the whole PTK plot is generated without refocussing, and then the sample is moved to a new composition upon which refocussing is performed before the PTK data is collected.

The system has been designed to cope with very uneven substrates which do not necessarily have to be perfectly flat. The high accuracy, piezo, z stage has a range of $200\mu m$ and is mounted on a stepper z stage with a range of 50mm. Consequently the system has a focussing range of 50mm with a resolution of 0.4nm. This makes the system extremely versatile and able to cope with thick as well as thin substrates. Since the substrate is unlikely to be perfectly perpendicular to the lens across its whole area, the system is able to refocus at each new composition with sub nanometer resolution.

The final point to be aware of is the compositional change over the analysis area. Usually, to collect a PTK matrix with reasonable resolution a $100\mu m$ by $100\mu m$ area is required. Over this area the composition of a film is assumed to be constant. However since the composition is deliberately varied, as a function of position, this assumption has some error. The worst possible scenario would be a chip which varied to cover the whole ternary system. This would mean that, for a ternary system of elements A, B and C deposited to cover all ternary space on a chip 32mm by 32mm, there is thus a variation of $0.3\%/100\mu m$ for each element. If the variation in A and B are opposite one another and element C is perpendicular to this line, the compositional variation over the $100\mu m$ area is $\sqrt{A^2 + B^2} = 0.42\%$. This worst case scenario is well within the accuracy of the EDX composition analysis and is therefore not considered to be problematic.

3.5.1 Control Software

The two main areas of software developed for the static tester are (1) Calibration Tools and (2) Data Collection[1]. Figure 3.2 shows how the hardware is connected and interfaced with the control PC. Table 3.1 lists the automated hardware, its connection and any comments.

The calibration software makes it possible to perform a test of modulation as a function of z and hence check the focus wobble (section 3.4.1). The control software for collection of compositional PTK matrices is more involved. The basis of the control flow is outlined in figure 3.16. Within this core procedure there are also two subroutines for collecting the PTK data for an individual composition (figure 3.18) and for focussing at each individual composition (figure 3.17).

[1]Acknowledgement: The initial PTK subroutine and alignment tools were developed my myself. The focussing subroutine and integration of the subroutines were developed by Ilika Technologies.

Hardware	**Interface**	**Comment**
Pulse Generator	GPIB	n/a
Stepper Motors	RS232	n/a
Piezo Stage and AF	Rs232	via USB adapter
Filter Wheel	RS232	via USB adapter
CCD Camera	FireWire	n/a
ADC	PCI	n/a

TABLE 3.1: Computer controlled static tester hardware

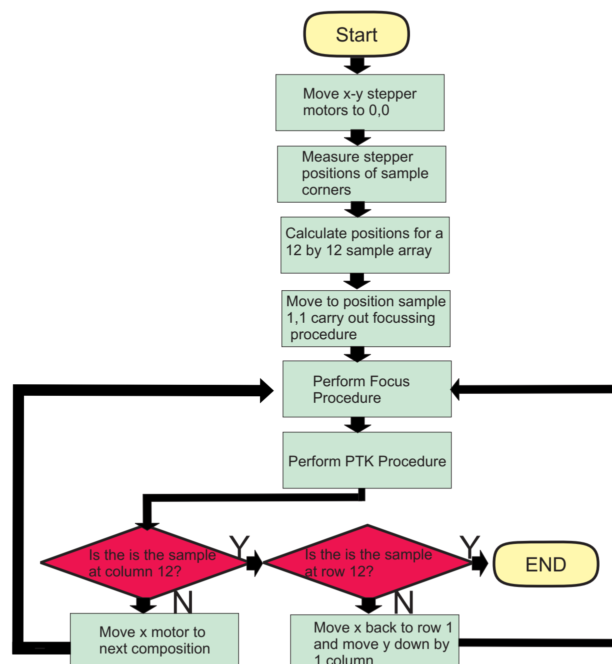

FIGURE 3.16: The main control flow for compositional mapping of PTK data

The software initially makes a measurement of the size of the deposition area and measures the corners of the deposited film relative to the stages' zero position. Once this measurement has been made it calculates the necessary Δx and Δy which each PTK array should be separated by for a predefined composition matrix. The x and y stages use these measurements to find the position of the first analysis area. At this point, the focussing subroutine is activated whereby the current generated by the detector photodiode is measured. The z-stepper motor is moved to increase this generated current. Once the peak in the generated electrical current is found, the stage is within the range of the high resolution piezo stage and the z-control is passed to the autofocus system; a command is sent to it, asking it to autofocus. Once focussed, the AFS is switched off and a command is sent to the piezo stage to maintain the voltage necessary for a focussed position. The filter wheel is moved to a 635nm notch filter. This allows only

the read laser to pass and protects the AFS from the 658nm write laser. The focussing subroutine is finished and control is passed to the PTK subroutine.

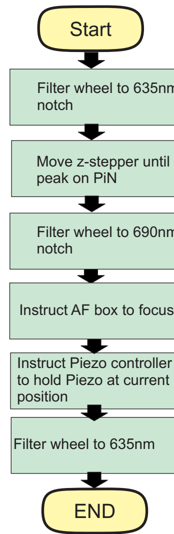

FIGURE 3.17: The control flow for focussing.

The PTK subroutine initially measures the signal on the detector via a transimpedance amplifier and the ADC within the Data Acquisition (DAQ) card. The filter wheel is then switched to a position which contains a beam block. The pulse generator then sends a voltage pulse to the bias T where it is coupled onto the laser diode. It is necessary to block the write beam from entering the AFS to protect the quad detector from damage. The filter wheel is then switched back to the 635nm filter and the signal of the detector is read again. If the number of time increments made for this power is equal to a predefined number of time increments, the flow continues to a check point to verify if the number of voltage increments is equal to a predefined number of voltage increments. If it is, the program ends and the data is saved to a text file. However, if it is not true, the program enters a concatenated loop whereby the time increments are increased until the first time query is met and then a second loop until the voltage query is met.

The final part of the program checks which position has been analyzed relative to the overall array of compositions. If the system is at the end of a row, it is moved back to column 1 and the y column is incremented. This is performed until the whole chip has been analsysed. The result for a 12 by 12 array is 144 text data files each containing PTK data for a specific position and consequently, a specific composition. Each file's composition is then linked ready for analysis in composition space.

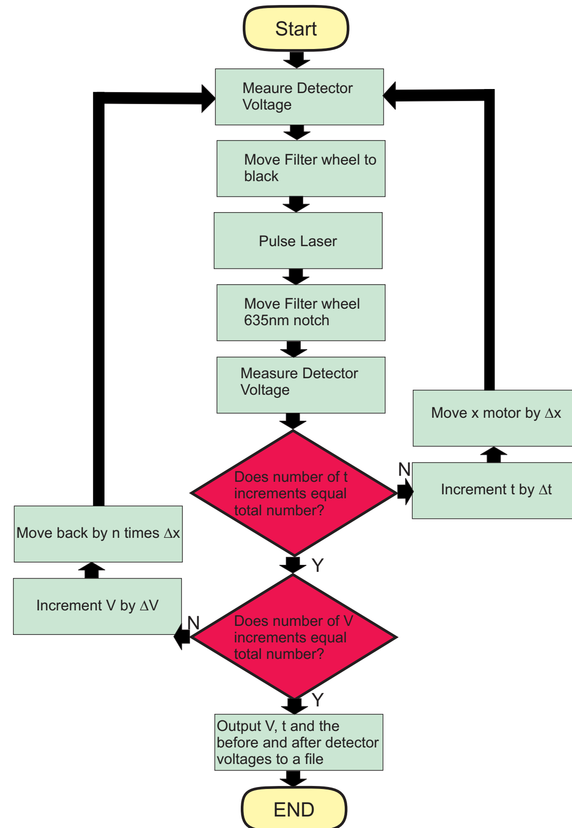

FIGURE 3.18: The control flow for collecting PTK data.

3.5.2 Phase Transform Kinetics Plots

A typical Phase Transform Kinetics (PTK) plot for a 300nm $Ge_2Sb_2Te_5$ film, prepared by RF sputtering, is given by figure 3.19 (a). The voltage on the write laser has been calibrated against optical power on the film. The plots therefore show the reflectivity increase as a function of optical power on the film and pulse duration. Data of this sort is commonly presented on logarithmic scales; the reasons for this will be discussed in chapter 4.

It is interesting to analyse this data by selecting a particular power and plotting ΔR as a function of time or vice-versa; picking a pulse duration and plotting the ΔR as a function of power; this data has been processed in this way and plotted in figures 3.20.

The graphs can then be differentiated to find the power or time necessary for the maximum crystallisation rate. For a compositional spread sample this figure can be then plotted on a compositional map to show promising fast crystallising phase change compositions. This is just one example of a wealth of information which can be extracted.

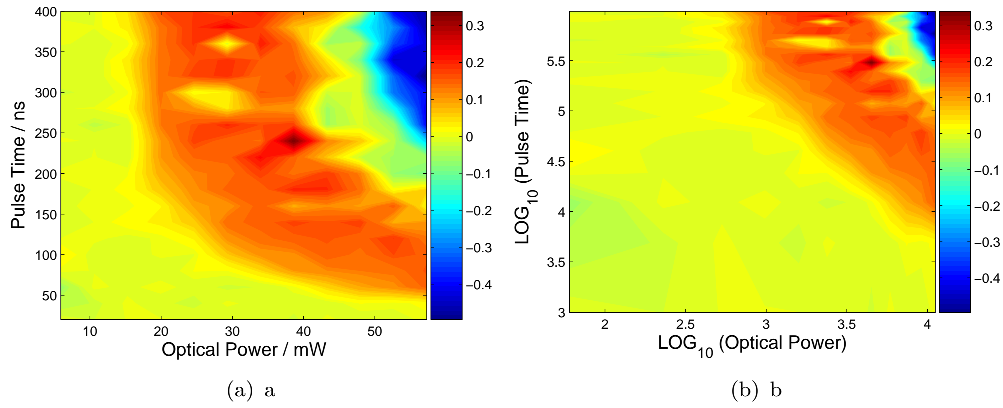

(a) a (b) b

FIGURE 3.19: PTK plot for crystallisation of as-deposited $Ge_2Sb_2Te_5$

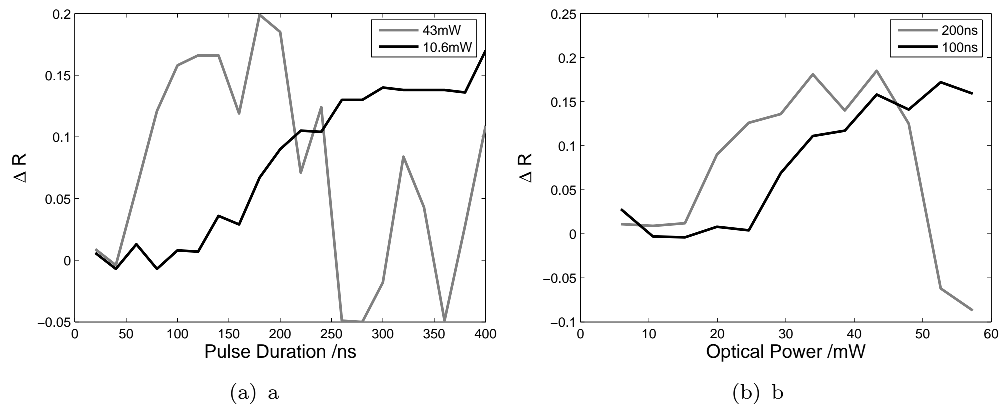

(a) a (b) b

FIGURE 3.20: Reflectivity increase plotted as a function of time(a) and optical power(b) for an as-deposited $Ge_2Sb_2Te_5$ film

To demonstrate the static tester's capability to measure composition spread samples, a Ge:Sb:Te was prepared by PVD. The sample's composition was deliberately spread around the $Ge_2Sb_2Te_5$ composition to ensure that known switching compositions were analysed. The resultant data was processed using the 'Paradise' Matlab toolbox [2]. The resultant PTK plots have been arranged in figure 3.21 as a function of position on the substrate. Even with this data in a relatively raw format, it is possible to see, positional, trends of crystallisation across the diagonal stretching from the top left hand corner to the bottom right hand corner of the PTK array.

To process this data, the time reflectivity plots have been averaged across all powers. The plots have also been plotted as a function of position on the substrate; shown in figure 3.22. Taking the mean reflection across all powers is a further tool to reduce the data to a more manageable average that can be used for relative composition comparisons.

[2] The Paradise toolbox was developed by John Tetteh of Ilika Technologies LTD to aid the data processing of high throughput measurements

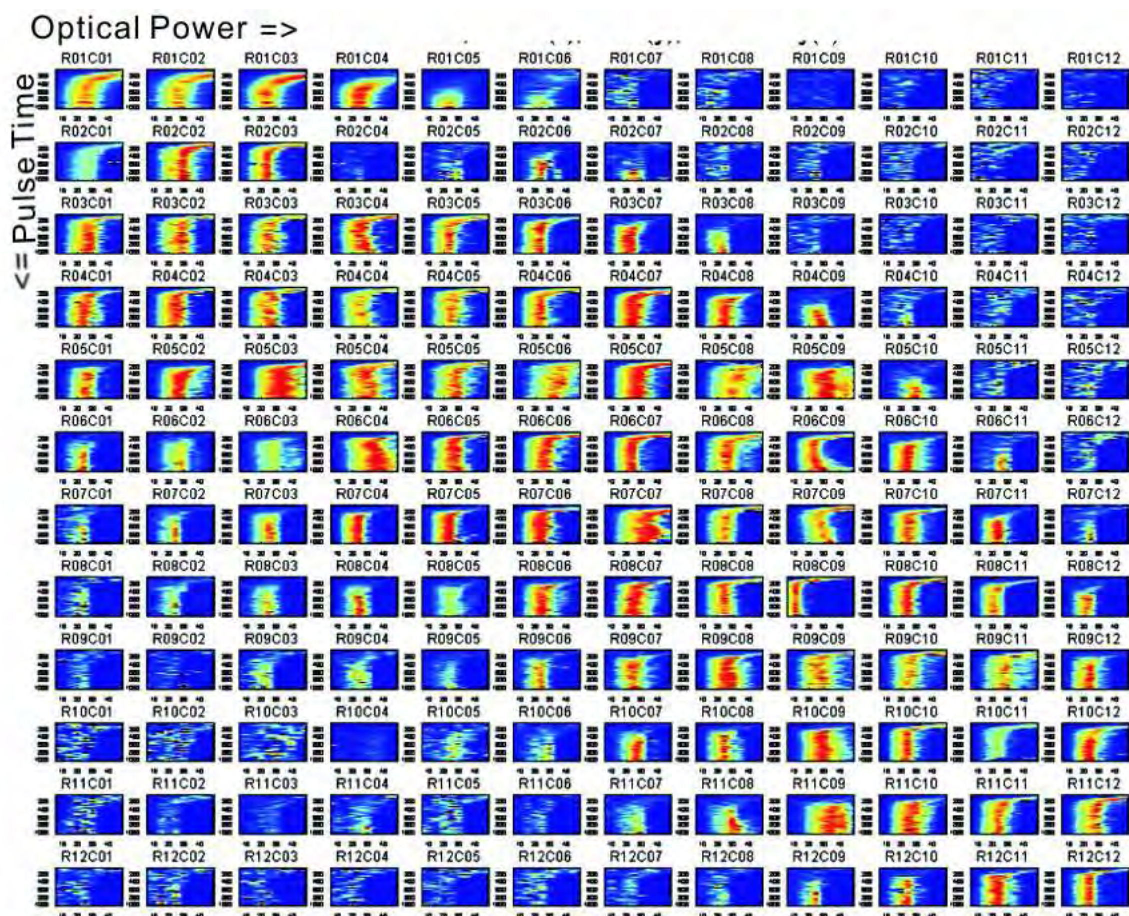

FIGURE 3.21: PTK plots as a function of relative substrate position

This also has the effect of smoothing the curves, which allows the differentiated plots' characteristics to be distinguished from noise more easily.

The data has been processed further by plotting in composition space, the crystallisation time for a 15% reflectivity increase at a power of 20mW. The colour of the marks are graded to show how the crystallisation time, for a 15% change in reflectivity, is dependent on composition. It can be seen that the fastest crystallising compositions are centred around the $Ge_2Sb_2Te_5$ composition. A full analysis of this system, including the crystallisation times, is presented in chapter 4 of this thesis.

3.6 Potential Development of the Static Tester

The static tester has potential to yield accurate data and other information related to the phase change of 658nm radiation absorbing materials. Improvements and future developments to the system are now discussed.

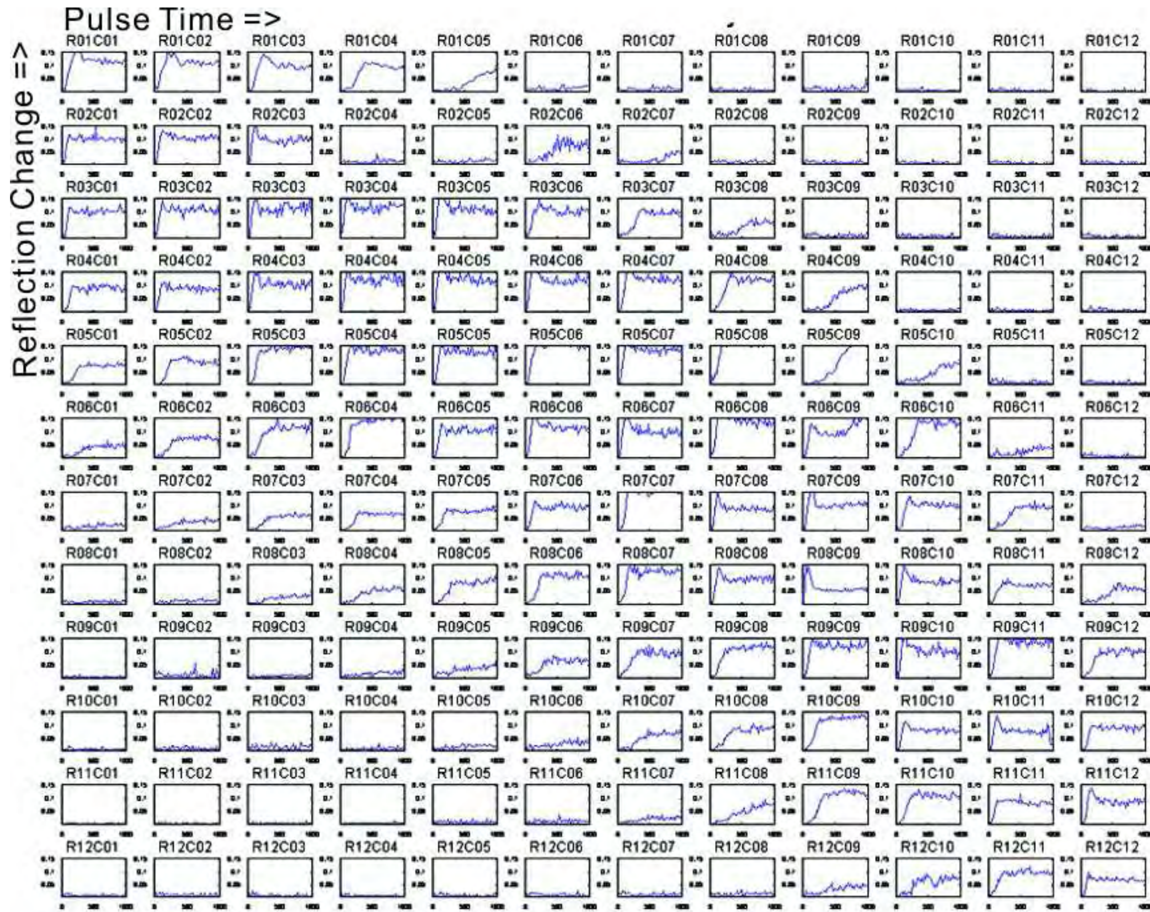

FIGURE 3.22: Mean reflection as a function of time plots as a function of relative substrate position

The most imminent development to the system is enabling it to not only generate PTK's of crystallisation but also vitrification, thus making possible re-writable PTK measurements. Some initial switching trials of $(ZnS)_8(SiO_2)_2$ clad GST have been successful but PTK measurements of compositional spread GST capped with just SiO_2 or Si_3N_4 have not been tried. To make such a measurement, the following subroutine is suggested. Initially a long crystallising pulse is delivered to the film, of pulse length, τ_0, and power P_0. The stages are not moved, so the focus is at the same location on the film as where the crystallised mark was previously created. A measurement of reflectivity is made. A short, τ_m, high power, P_n, pulse is then delivered to the film and the reflection after the pulse is measured again. At this point a crystallising pulse train could be sent to the mark with power, P_0, but pulse length, τ_p. A measurement of reflectivity increases is made between each pulse. The length of τ_p is increased until the reflectivity increase is equal to zero. The reflectivity change as a function of τ_p can be plotted to give some information on the time necessary to crystallise an amorphous mark in a crystallised matrix. Once these measurements have been made, the sample is translated by $5\mu m$,

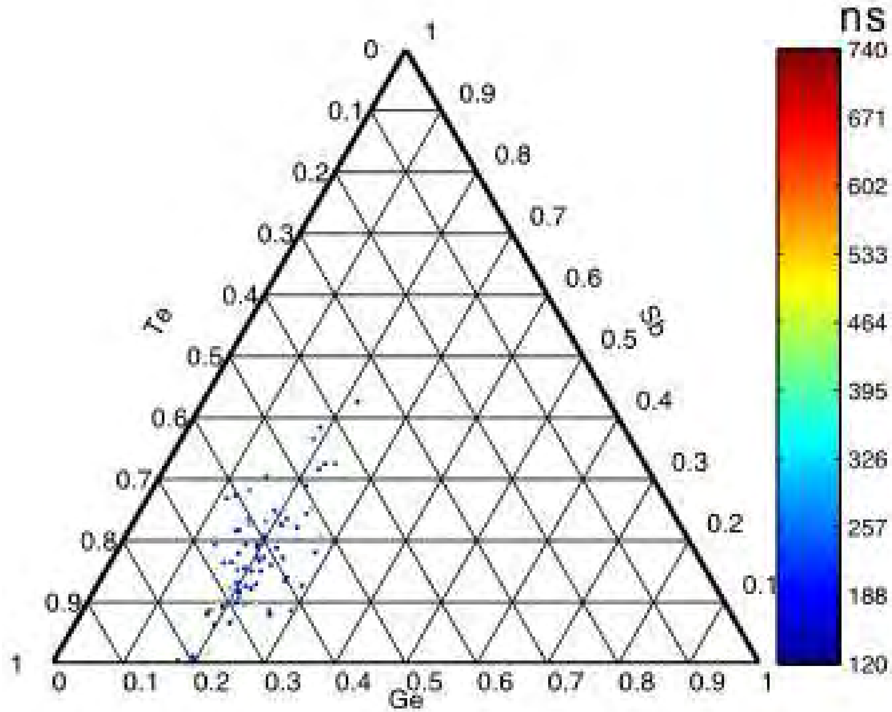

FIGURE 3.23: Crystallisation times for a 15% change in reflection, the colorbar shows the pulse time in nanoseconds

the same crystallising pulse is sent (length, τ_0 and power P_0) and the measurement repeated for a longer pulse τ_{m+1}, to amorphise the material. When all of the predefined pulse increments to amorphise the sample have been made, the power is increased to P_{n+1} thus building a PTK matrix for sample amorphisation and a data set of pulse energies required for recrystallisation.

An alternative to crystallising an area, before each amorphising PTK pulse, is to crystallise the whole film by heating it on a heating plate prior to the PTK measurement. The differences in the properties of the $Ge_2Sb_2Te_5$ film crytallised by laser heating and on a heating plate are known [112]. Te-Te bonds, which formed during deposition, disappear completely by heating on a hot-plate but are still present even after 5 passes of the crystallising laser. However, the Te-Te bonds contribute little to any physical colour change in the disc and thus heating by a hot plate could be considered.

The physical problems of creating amorphous marks are well known; the material must be quickly quenched, thus putting strict design constraints on the capping layers and thickness of the phase change layer. The material used to sandwich phase change material must act as a thermal insulator, when the laser is heating the phase change film, yet be able to dissipate heat through to the substrate when the laser is off. The thermal mass of the phase change layer might be significant and thus prevent the material from quenching into an amorphous mark. These problems need to be modelled, in order to

design an efficient structure which shows very little sensitivity to the intrinsic depth, thermal conduction and specific heat variation which occurs in compositionally spread films.

Once these aforementioned problems are overcome, repeatable reversible switching should be possible. The system is then in the position that it could be upgraded to make measurements of cycleability as a function of composition. This information is clearly of great importance for any engineer who is designing re-writable storage media or devices. Further extending the functionality to make archival lifetime measurements is possible too [29]. A heater should be installed onto the z stage such that the evolution of crystallisation into an amorphous mark can be monitored via measurement of the optical reflection as a function of time and temperature. Other researchers have adapted such static testing systems to make sub-nanosecond thermal reflectance measurements [106] [103], thus allowing the possibility of time resolved thermal conductivity and specific heat measurements as a function of composition.

At present the system has only been designed to measure the reflection change of the film. The ability to measure transmission through the sample is also desirable, since information on the volume of material changed can be found. For instance, by applying a number of pulses to the film of different energies, a larger volume of the material should crystallise as the energy is increased; the crystal is effectively growing into the depth of the film. This effect will saturate once the crystal has grown from the laser's incident surface through to the opposite surface of the film. This effect is not detectable when measuring the reflection since reflection is a surface dependent measurement. Another advantage of measuring in transmission mode is the nulling of the influence from the films' surfaces. That is, if one measures an uncapped film, oxidation of the surface is possible. By measuring transmission, the volume of film will yield the largest signal. Further, by comparing the reflected phase change modulation with the transmitted modulation, a potential measurement of the degree to which the film is oxidised, or at least some surface dependency is possible (like surface stress). The system was deliberately designed with this in mind, the piezo-z stage has a hollowed out centre to enable measurements of transmission.

One of the main problems an operator faces is the ability to achieve fast yet consistent, system alignment and the greatest alignment challenge is ensuring both pump and probe lasers are coincident on the film. To achieve greater stability, faster alignment and a generally more simple system, parts of the system could be replaced by optical fibre based technologies. By coupling both pump and probe lasers into the same fibre, coincidence of the beams is ensured. Single mode fibres also have the added advantage that only the Gaussian beam can propagate therefore ensuring good beam quality. Figure 3.24 shows a schematic of how such a system could be implemented.

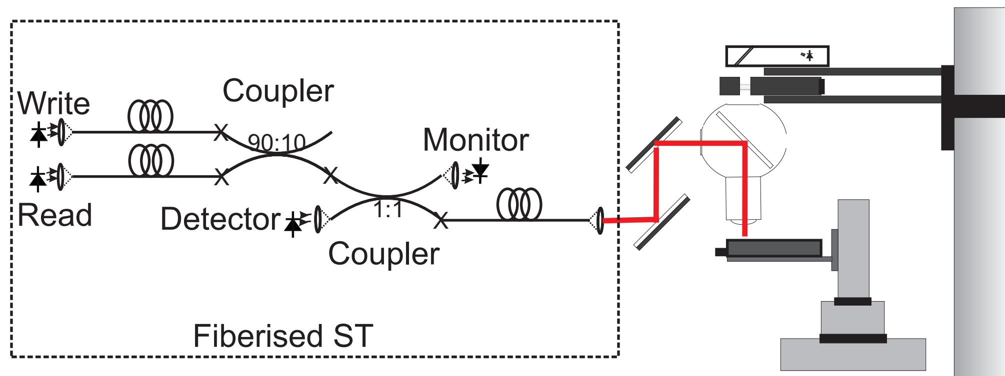

FIGURE 3.24: A schematic to show how the optical fibre components could be implemented in the static tester

At present, the system shows that both beams are combined through evanescent couplers. This is because such devices are commercially available, but the ORC has many years of expertise in the design of Fibre Bragg Gratings (FBGs) for optical communication research. In practice a more power efficient system would include add/drop gratings to incorporate and pick-off wavelengths to and from the system.

Some of the other improvements which should be considered for any future system work include:

- Inclusion of another PiN to measure the read and write laser's performance over time and deduct any changes in their performance as background from the measured signal.
- Use of blue 405nm diodes for investigation of sulphide based phase change films, which tend to transmit at wavelengths >500nm
- Calibration of the detector's voltage against known reflectance standards, such that the absolute reflectance of samples can be measured as well as ΔR.
- Systematic checking of focus during the PTK measurements of large data sets with high resolution
- Inclusion of a faster detector such that measurements of the phase change dynamics are possible and a time resolved measurement of the reflectivity, as a function of cooling, which would give information of the material's ability to quench or crystallise.
- An alert system which is activated if the automatic operation of the system experiences a problem. The system might automatically send an email, or text message, to its operator.

- The application of smart software. Over sampled measurements of a compositional spread sample are not efficient. Therefore the software runs fewer samples where there is little change in the measurements.

3.7 Summary

A static tester has been designed and built for high throughput analysis of composition spread films. It has successfully demonstrated its value at assessing the crystallisation time dependence on composition for films based on the elements Ge, Sb and Te. The measurement time is relatively long; if the system is fully automated and continuously running it can measure a 20 by 20 PTK within a 12 by 12 composition array in less than 14 hours. This time can be reduced by reducing the noise on the detector, which would allow a reduction in the time that the system averages the detector signal before and after each voltage pulse.

The static tester is limited to films which absorb the 658nm write laser radiation. If the films are transparent at this wavelength, efficient heating is difficult and large optical powers are necessary. Thus the system's results should always be presented against the imaginary part of the refractive index, k (the absorption). Some films which have weak absorption at 658nm will therefore have poor optical phase change characteristics. However these films should not be ruled out for electrical phase change materials. Short wavelength blue laser diodes are now commercially available and their cost is falling, therefore the feasibility of implementing a blue read and write system into the static tester should also be considered; thus extending the write functionality to cover films which are transparent in the green and red (such as GaLaS).

A number of possible improvements to the system have been outlined. Some of the most important of these are adding a detector to measure transmission through the sample and replacing bulk optical components with optical fibre based devices, thus making the system more robust, stable and ensuring single mode Gaussian beams. The alignment complications of the static tester will also be reduced.Table 3.2 summarises the static tester specification.

Property	Value
Write λ	658nm
Read λ	635nm
Read power on film	100 μW
Max Write Power on Film	100mW
Min Pulse Duration	6ns
Lens NA	0.65
Write SpotSize	1-2 μm
X-Y resolution	200nm
Z resolution	$<$1nm

Table 3.2: Specification of Static Tester

Chapter 4

Ge:Sb:Te High Throughput Deposition and Screening

4.1 Introduction

The first studies of phase change data storage materials were conducted in the early seventies [95]. At the time the element tellurium (Te) was known to have good glass forming capabilities and it was most frequently reported compounded with various other elements. The most interesting and frequently studied compositions were based around the binary system Ge-Te. The fastest switching composition occurred at equal atomic proportions of Ge and Te [113]. At this specific composition the material can melt without phase separation; this is evident in its phase diagram[114], see figure 4.2. When the molten state has been quenched into an amorphous film, it is possible to crystallise areas of this film in less than 100ns. This is possible since there is no migration of atoms and it is only the bond angles between atoms which need to change. A small deviation in composition leads to a sharp increase in crystallisation time; this is also seen in figure 4.1. Referring back to the Ge-Te phase diagram, one notices that the Ge-Te phase has very little compositional tolerance. Synthesising compositions off Ge_1Te_1 generates a phase separated compound. Crystallising such a compound requires atomic migration from the quenched molten state into phase separated crystallites. This is a time consuming process and a deviation of just 10 at.% increases the crystallisation time by 2 orders of magnitude.

Sensitivity to composition leads to difficulties in preparation of samples with the same characteristics; thus compositions with looser tolerances were sought. Doping Ge-Te with Sb, reduces atomic mixing and encourages the formation of two mixed phases [115]. Much of the phase change data storage material research involves the Ge:Sb:Te

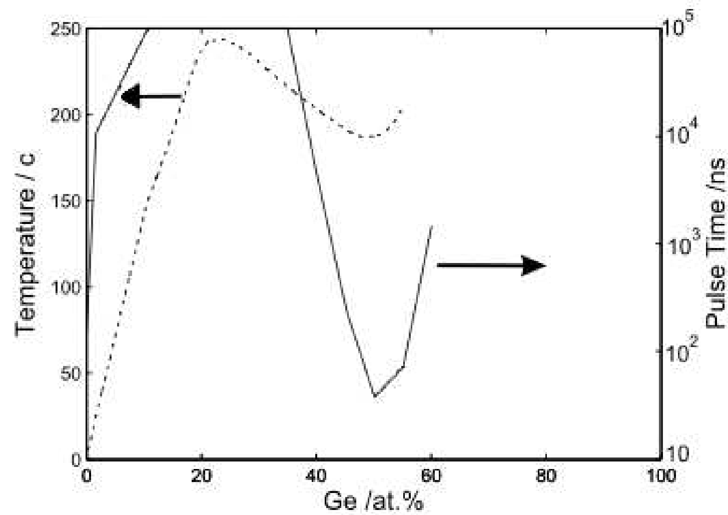

FIGURE 4.1: Ge-Te Crystallisation time as a function of composition [113]

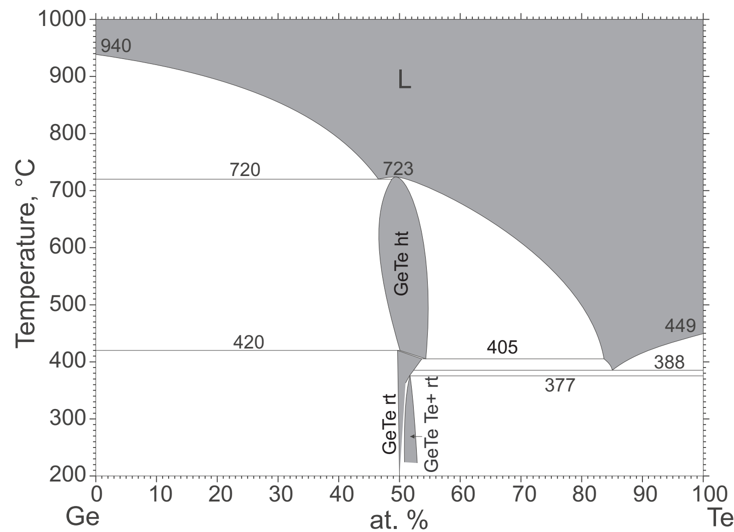

FIGURE 4.2: Phase Diagram for Ge-Te [114]

ternary system. Before analyzing this system, it is interesting to analyse the Sb:Te and Ge:Te binary phase diagrams, see figures 4.2 and 4.3. In the case of the Ge-Te system one should note that the material transforms from a crystal to a liquid with both phases retaining the same composition at Ge_1Te_1; this is known as congruent melting. At 85 at.% Te there is also a valley whereby the liquidus state solidifies simultaneously into two different phases at the same temperature, this is known as a eutectic. The Sb-Te system is characterised by two congruent melting points, the first at Sb_2Te_3 and the second with a wide composition range centred at 29 at.% Te. In the Te rich zone there is a eutectic at 89 at.% Te. Materials which melt without a change in composition are of interest since they are likely to switch without the time consuming atomic migration

into phase separated components. Thus the fastest switching Ge:Sb:Te compositions lie along a tie-line between the two invariant, congruent melting compositions $GeTe$ and Sb_2Te_3.

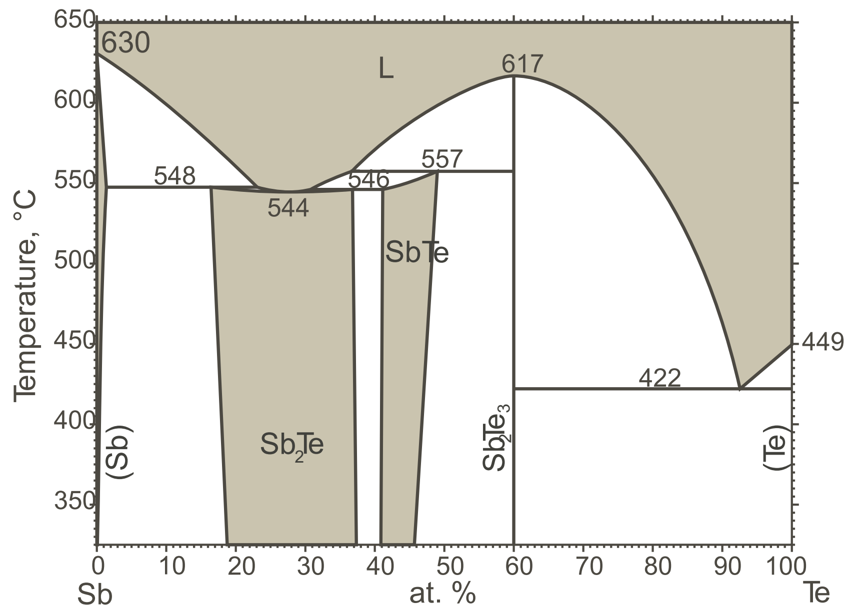

Figure 4.3: Phase Diagram for Sb-Te [116]

This pseudo-binary phase system has three intermediate compounds with similar structures: $Ge_2Sb_2Te_5$, $GeSb_2Te_4$ and $GeSb_4Te_7$, each crystallises into a NaCl lattice. Deviation from one of these stoichiometric compositions, results in a polycrystalline film which is a mix of the other stoichiometric crystals and individual elements[117]. Clearly, materials which solidify into a single compound are of interest because phase separation upon repeated heating and cooling cycles is minimised. It is this pseudo-binary system which is often exploited for re-writable optical storage media since it leads to compositions with favorable characteristics[15] such as short crystallisation times. Another material which has been commercially exploited is AgInSbTe; it is a multi-phase system, hence it has a comparably long crystallisation time of 200ns. This material is best suited to low data rate recording such as rewritable CD's (CD-RW).

The crystallisation rate of phase change data storage materials is determined by the composition of the recording layer, its thickness and the type of interface; all of which should be optimised to achieve a short crystallisation time while maintaining stability [63].

As discussed in chapter 2, there are two crystal growth mechanisms for phase change data storage materials. The crystallisation of $Ge_2Sb_2Te_5$ is a nucleation driven process as the optical power has been found to be constant for Complete Erase Time (CET) of

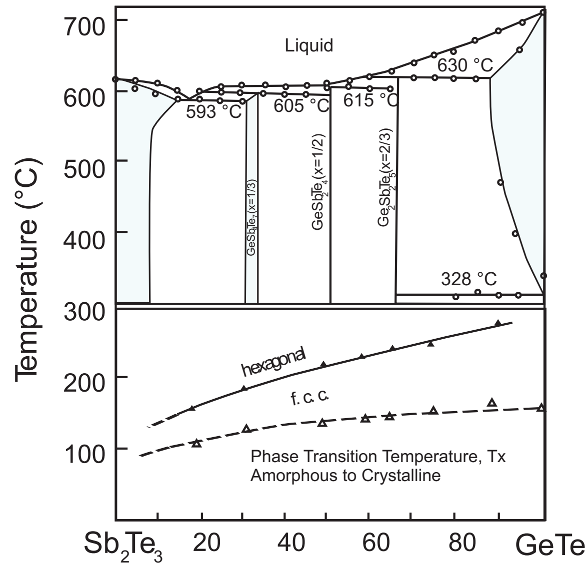

FIGURE 4.4: Phase Diagram for pseudo-binary system $Sb_2Te_3 - GeTe$ [118]

different diameter amorphous marks. This behaviour is indicative of a nucleation dominant process. As further proof, inspection of the written amorphous marks with a TEM also revealed that as the preceding, crystallising, erasure, pulse power was increased, the number of crystallites present increased and, at the threshold power for complete erasure, the mark was found to be filled with nanocrystalline grains with sizes ranging from 10nm to 30nm, indicating that the nucleation occurs before growth from the surrounding crystalline background[63]. The CET of $Ge_2Sb_2Te_5$ decreases with increasing film thickness, this is understood to be a result of competing interface and bulk effects. Below a threshold thickness the film crystallisation characteristics are dominated by interface effects. As the film is made thicker, the CET becomes less sensitive to these effects and bulk nucleation is predominantly the influencing factor. Consequently, below a critical thickness the interface material, surface energy and roughness all influence the nucleation rate of $Ge_2Sb_2Te_5$[63].

The crystallisation mechanism of Sb has been described as explosive[119]. That is, upon crystallisation an exothermic heat release causes a self sustained crystal fast growth, estimated to be $200ms^{-1}$, into its amorphous surroundings[120]. The main problem with pure Sb films is the amorphous phase stability; it is crystalline at room temperature. Alloying Sb with Ga or Ge has successfully increased the alloy's stability whilst retaining some of the fast growth crystallisation properties. The crystallisation temperature of Sb_2Te is around $103°C$ and in the Ge-Sb system, increasing the Sb concentration to $Ge_{15}Sb_{85}$ raises the crystallisation temperature to $250°C$. As mentioned in chapter 2, the phase stability and energy required for phase change are competing requirements and increasing the crystallisation temperature clearly means that more heat energy needs to

be put into the system. The crystallisation temperature is increased by adding elements that increase the average co-ordination number of the system thus giving an explanation for the stability of $Ge_{15}Sb_{85}$ [16][29]. The effect of Bi dopants on the Sb-Te binary system has been studied and will be discussed in chapter 5.

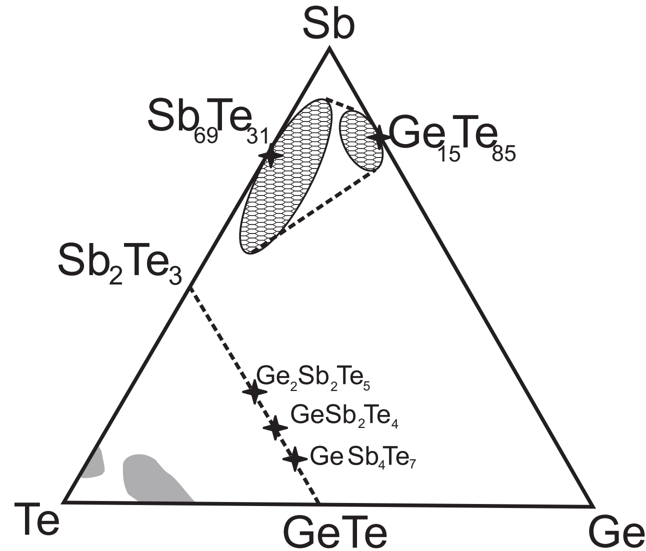

FIGURE 4.5: Ternary of Ge:Sb:Te. The pseudo binary line, the amorphous bulk and the fast growth compositional areas are indicated

4.1.1 Modification of $Ge_2Sb_2Te_5$

Over the past five years a number of groups have tried doping $Ge_2Sb_2Te_5$ with different types of dopants. Since nitrogen and oxygen are easily injected into sputtering chambers, research of their affect is among the most frequent reported. Table 4.1 summarises the effect of some common dopants on $Ge_2Sb_2Te_5$. One of the most important problems with $Ge_2Sb_2Te_5$ for electrical memory is its low intrinsic crystalline resistivity; hence many of the reports focus on increasing it.

4.1.2 Structure of Ge:Sb:Te

The crystalline structure of congruent compounds of Ge:Sb:Te along the $GeTe - Sb_2Te_3$ pseudo binary was reviewed by Yamada [117]. Each of the three compounds consists of planar layers which form long periodical hexagonal lattices; this is depicted in figure 4.1.2. When the composition deviates from these congruent compounds, the material forms a mixture of the three stoichiometric crystals and any excess elements.

Dopant	Effect	Reference
Chromium	Suppression of molten material flow	[121]
Fluorine	Reduction in crystallisation temperature	[122]
Nitrogen	Reduction in CET, increase in write endurance, decrease amorphous n & k, increase crystalline n & k for short wavelengths, increase in density	[63][123][5]
Oxygen	Reduction in CET, increase electrical ρ	[124][125]
Silicon	Increase in crystallisation temperature of both crystal phases, increase in electrical resistivity, decrease in melting temperature	[126]
Silver	Increases in crystallisation temperature and stability, increase in sheet resistance above $360°C$, slight increase in the threshold switching voltage, improvement in the optical reflectivity	[127][128]
Silicon + Nitrogen	Increase in electrical resistivity	[129]
Tin	Increased crystallisation speed	[130]

TABLE 4.1: Influence of common dopants on Ge:Sb:Te

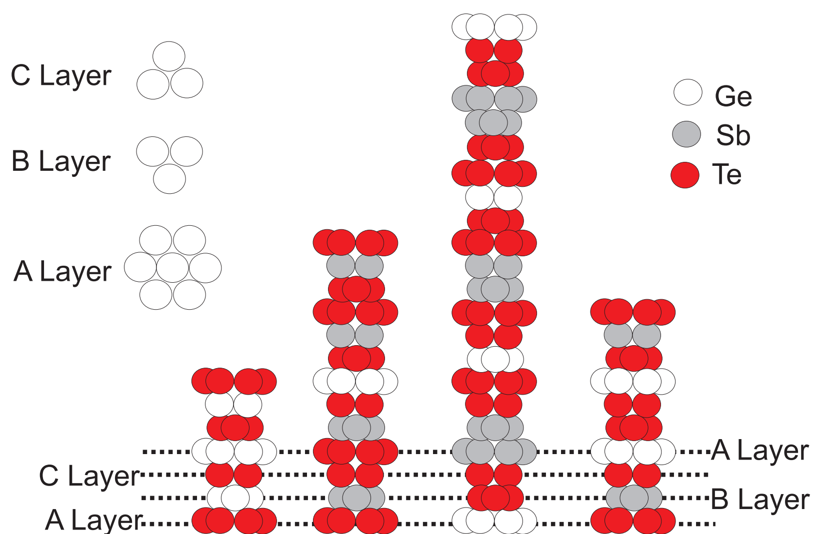

FIGURE 4.6: Stacking models for the three congruent compounds along the $GeTe - Sb_2Te_3$ pseudobinary system

Upon transformation from the amorphous state the material relaxes into the crystalline FCC structure at approximately $140°C$ (depending on the composition). On a DTA scan this is evident as a large exothermal peak. Heating to higher temperatures induces a second crystalline transformation to a hexagonal structure which is evident by a smaller peak on the DTA. Further heating to above $600°C$ will cause the material to melt, evident as an endothermic peak.

The true nature of the switching process for materials along the $GeTe - Sb_2Te_3$ pseudo-binary line is still providing intriguing questions regarding the atomic movement during the switching process. Koblov et al.[12] recently compared EXAFS, XANES and XRD structural data to suggest a model for the switching process from crystalline to amorphous. The study found that the amorphisation process does not disrupt the local environment around the Sb atom and that the Te sublattice is partially preserved. A conclusion was drawn that the breaking of strong covalent bonds does not occur, instead a flip in the position of the Ge atom is the only structural change. This model has some profound implications, probably the most important of which is that the material does not necessarily have to melt for amorphisation. This means that the local structure is well defined, thus enhancing the reversibility of the switch and the endurance to cycling. In 2006 this model was further validated by Zhao et al. [131], where a GeTe/Sb_2Te_3 superlattice structure was grown in a mole ratio 2:1, thus creating an effective composition of $Ge_2Sb_2Te_5$. The almost remarkable result was that, even after 10^7 switching cycles, the superlattice structure was retained which seems to imply that the material never melted. If the material had been molten, diffusion of the layers would have occurred and the structure would have been lost.

4.1.3 Electrical Properties

The electrical properties of multi-phase Ge:Sb:Te compositions are dependent on the material structure. In the polycrystalline state the resistivity is low and in the amorphous state the conductivities are low. For a practical phase change memory device it is crucial that the composition of Ge:Sb:Te used, exhibits threshold switching. That is, when the electric field across an amorphous volume of material exceeds a threshold, conducting filaments are formed. Within these filaments Joule heating induces the thermally activated phase transition. A major problem with the $Ge_2Sb_2Te_5$ composition is its inherent high threshold field [6] thus problems occur regarding the generation of voltages on a nanoscale device. Another major problem with a potential phase change device made from this composition is its low resistivity in the crystalline state; large currents are therefore necessary in order to generate enough resistive heating. To overcome this problem; lateral or line-type geometries have been suggested thus allowing some increase in the device resistance by reducing the cross-sectional area of the material

[6][132]. However the intrinsic high crystalline conductivity of $Ge_2Sb_2Te_5$ still remains. Some dopants have been shown to increase the resistivity namely oxygen[125], through oxidisation of Ge, and nitrogen by the creation of many small crystalline grains through the suppression of grain growth which therefore reduces the mean free path of electrons in the crystal. In an effort to overcome such problems, Lankhorst et al. chose to investigate the properties of Ge:Sb:Te films away from the Sb_2Te_3-$GeTe$ pseudo-binary system. They found that doped $SbTe$ also exhibited threshold field switching at 1V (for their line-memory) and that the resistivity was constant until the crystallisation temperature was reached[6]. With this finding in mind, the electrical properties of compositions far from the $GeTe - Sb_2Te_3$ pseudobinary line have been investigated using high throughput methodologies.

4.1.4 Optimisation of Ge:Sb:Te

Optimisation of phase change materials is predominantly an empirical process. However, in the last decade, some degree of understanding has been gained. The Sb content is known to determine the materials crystallisation rate. Ge and Te reduce the crystallisation rate but increase the amorphous phase stability; with Ge having the greater influence on phase stability because of its high bond strength and relatively high coordination number [29].

In order to find the stable amorphous phases of Ge:Sb:Te, a thermal study was conducted in the early 1990s[115]. The study involved fabrication and DTA measurements of 100 bulk samples as well as films deposited by flash deposition. Some basic trends were observed in this study; for tellurium rich samples ($\approx 80\%$), replacing Sb with up to 5% Ge resulted in a decrease in the glass transition temperature while the crystallisation temperature increased. At 6% Te the material crystallisation activation energy was exceeded by its environment. However the increase in separation between T_g and T_x signifies that, if the material is stored at a temperature below T_g (the lower limit for crystallisation [29]), the material's archival lifetime will increase with Sb content.

In order to speed up the process of material discovery, high throughput compositional spread methods are desirable. The large phase space and the necessary thin film characterisations make phase change thin film material research an ideal candidate for such methodology. As a result, Laurenzis et al. investigated such techniques and reported the outcome of deposition and characterisations of the Ge:Sb:Te system. The technique was based on simultaneous sputter deposition from three different target materials. However the achievable compositional variation for each element was at maximum, just 10 atomic percent[133]. High quality data of the crystallisation times for these materials was achieved but many samples were required just to cover the $GeTe-Sb_2Te_3$ pseudo-binary

tie line. Other important optical and electrical data were neglected from the report. The compositional spread approach and the measurements made on the $Ge_2Sb_2Te_5$ will be discussed in this chapter. In chapter 5 the high throughput methodology will be applied to a new ternary system.

4.2 Sputtered $Ge_2Sb_2Te_5$ Films -fabrication and characterisation

Films of $Ge_2Sb_2Te_5$ were prepared for by RF sputter deposition for subsequent investigation. All of the films discussed were deposited at 100W RF power with a argon background gas at 0.5Pa. The temperature of the substrate was $20°C$.

4.2.1 Composition Spread Trials

A single magnetron sputtering system is usually used for the deposition of films whose composition is the same, or similar, to that of the target. However, the composition of the film can be adjusted by either reactive sputtering in the presence of a reactive atmosphere or by creating a composite target by attaching other materials to another target. The latter of the two techniques tends to be used for doping a film with low concentrations of another material. By using more than one magnetron, simultaneous co-sputtering is possible; in this case each magnetron is controlled separately. By adjusting the magnetron's power it is possible to create films which consist of a combination of each target. Helicon Wave Plasma (HWP) assisted sputtering systems are similar to conventional RF-sputtering systems except for the addition of a RF-coil just above the target [134] which allows some control of the plasma. The principle advantages of HWP sputtering is that it allows a higher density, low ion energy plasma. This in turn enables a reduction in the deposition RF-magnetron power. Further, the HWP can be excited far from the sample outside the deposition chamber which allows increased control of the deposited film's composition and quality through a reduction in the higher energy ions. In this work some preliminary trials on the effect of target substrate separation and coil RF power on the deposition rate were investigated. A HWP sputtering system, capable of simultaneous deposition from three different targets, was used. The deposition pressure was controlled at 0.5Pa, whilst the RF coil power was varied between 0 and 40W. The target separation from the substrate was also varied by up to 32mm. Both of these alterations failed to have any significant effect on the deposited wedge, from a single target. The maximum variation in deposition rate at the substrate was just $0.002 Å s^{-1} mm^{-1}$. However, despite these limitations, using a Sb (50W RF) and Ge_2Sb_2Te5 (RF power=50W) targets simultaneously, the resultant Ge:Sb:Te films Sb

content could be altered between 60at.% and 80at.% over an 80mm substrate length. Figure 4.7 shows the ternary plot with the compositions measured using X-ray fluorescence spectroscopy.

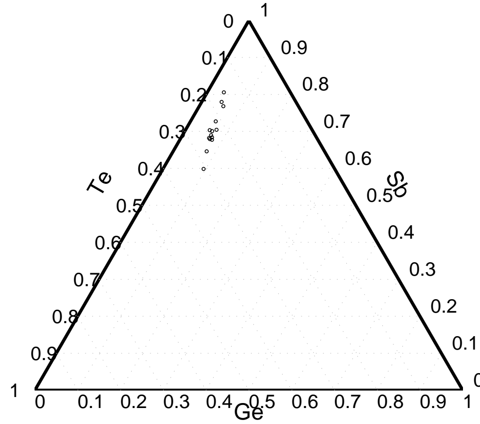

FIGURE 4.7: Compositions deposited by helicon sputtering of a $Ge_2Sb_2Te_5$ target and a an Sb Target. The compositions were measured by XRF spectroscopy.

Although composition spread deposition is possible using the HWP sputtering system the range is limited by the geometry of the targets relative to the substrate. Even when the target power is altered, the wedge of that target deposited has a constant gradient which limits the compositional coverage achievable on a single substrate. This methodology is probably best suited to examine compositions where the approximate composition range of interest is known.

4.2.2 Crystallisation Temperature

The crystallisation temperature has been measured on a film deposited in an atmosphere of 0.5Pa argon.

The reflectivity of the films across all visible wavelengths was measured by use of the hotplate and and CCD camera setup described in section 2.8.4. During heating, at $2°Cmin^{-1}$, the sample chamber was flushed with a flowing nitrogen atmosphere. The measurement of reflected intensity as a function of temperature is given in figure 4.8. The peak crystallisation temperature was found to be $145 \pm 2°C$.

4.2.3 Electrical Properties

The electrical sheet resistance, R_s, of the $Ge_2Sb_2Te_5$ film deposited at an argon pressure of 2.55Pa was measured as a function of temperature with a, self-built, four point probe (described in section 2.8.3 and appendix B). The probe was placed in contact with the

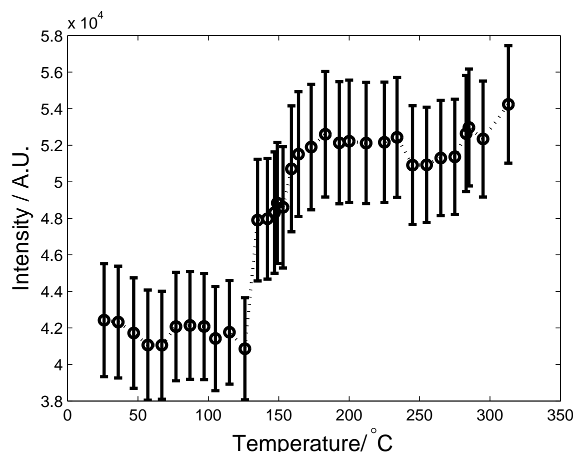

FIGURE 4.8: Reflected intensity of a broadband visible source from a sputtered $Ge_2Sb_2Te_5$ film as a function of temperature.

sample and the whole arrangement was fixed inside a chamber furnace. A thermocouple was placed close to the sample and the sheet resistance was recorded as a function of temperature. The temperature of the furnace was set to ramp at $5°C\ min^{-1}$ however, due to the relatively low temperatures and the lack of feedback between the sample thermocouple and the furnace controller, the acutal heating rate varied with temperature from 0 to $10°Cmin^{-1}$. The resultant plot of sheet resistivity as a function of sample temperature is given in figure 4.9.

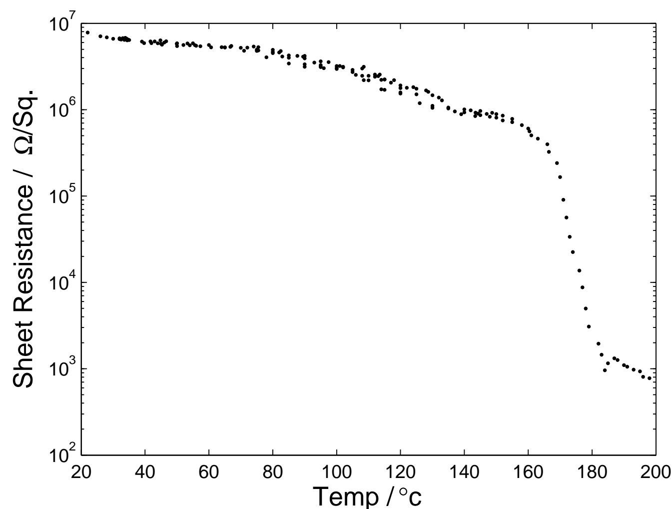

FIGURE 4.9: Sheet Resistance of a 200nm ±20nm $Ge_2Sb_2Te_5$ film as a function of temperature

Since the crystalline films have a significantly higher electrical conductivity than the as-deposited amorphous phase, one can see that there is a clear transition at $170°C$ from a resistive, as-deposited, amorphous phase to a conductive crystalline state. From

this plot the phase transition temperature is clear since the electrical resistivity drops by more than three orders of magnitude.

4.2.4 X-Ray Diffraction

XRD was performed on an as-sputtered film, a film heated to $200°C$ and a sample of the sputtering target material. The sputtered films were deposited in an Ar atmosphere at 4Pa. The diffractograms are presented in figure 4.10. On this scale, no peaks are present for the as-deposited sample. The annealed sample does, however, show a strong reflection at $2\theta = 43°$. The diffraction pattern of the bulk, sputtering target is also given.

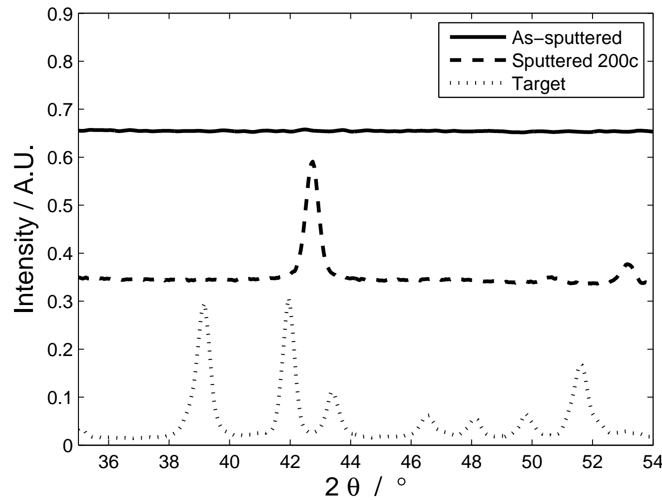

FIGURE 4.10: XRD spectra of $Ge_2Sb_2Te_5$ thin films and target

4.2.5 Crystallisation Time

The static tester, extensively described in chapter 3 of this thesis, was used to measure the crystallisation time of the as-deposited $Ge_2Sb_2Te_5$ films. The results are presented in a PTK plot format in figure 4.11. The PTK is made of a 20 by 20 array of data points. The optical power incident on the film was varied between 5 and 60mW whilst the time was incremented in 20ns pulses up to 400ns.

Figure 4.12 shows a cross-section of the PTK map of the reflectivity as a function of time and reflectivity.

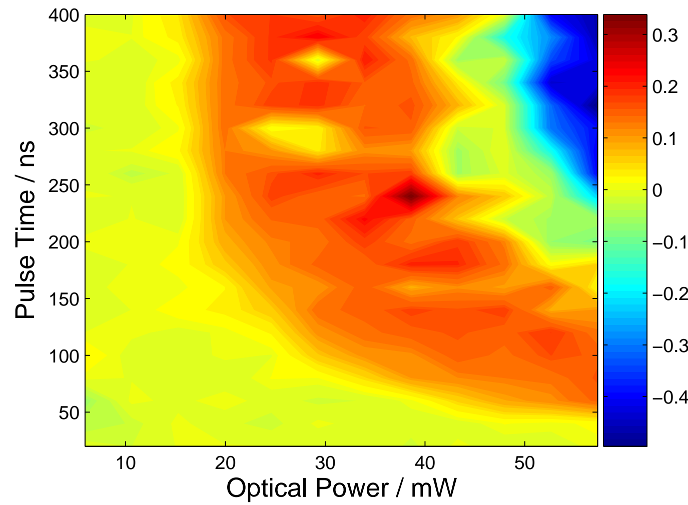

(a)

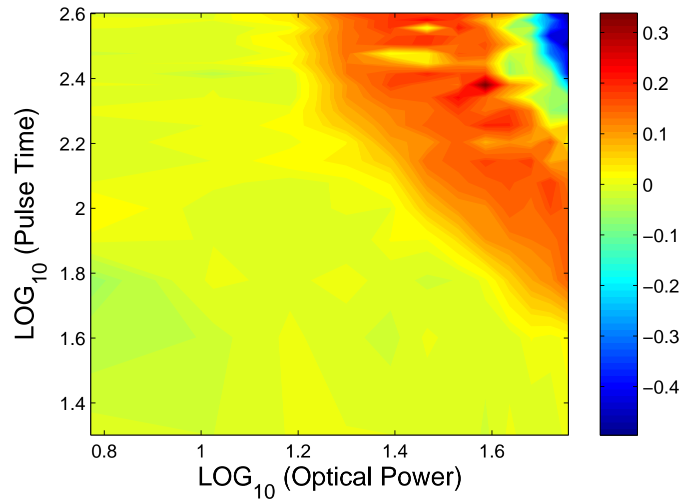

(b)

FIGURE 4.11: Phase Change Kinetics Plots; (a) linear scale (b) Logarithmic scale

4.2.6 Amorphisation Phase Change Kinetics

As well as crystallisation, the static tester can be used to amorphise phase change materials in their crystalline state. To do this it is critical the the sample is in the focus of the write laser. To switch from the crystalline state, it must be heated rapidly to its melting temperature. To reduce the possibility of oxidisation of the molten volume, the film was capped with a 220nm layer $ZnS - SiO_2$. A 500μm by 500μm area was crystallised by rastering the static tester's write laser at $1 mmsec^{-1}$ and optical power of approximately 20mW.

Once the crystalline area had been prepared by the static tester, the PTK algorithm described earlier was set to increment the optical power in steps of 5mW and the pulse

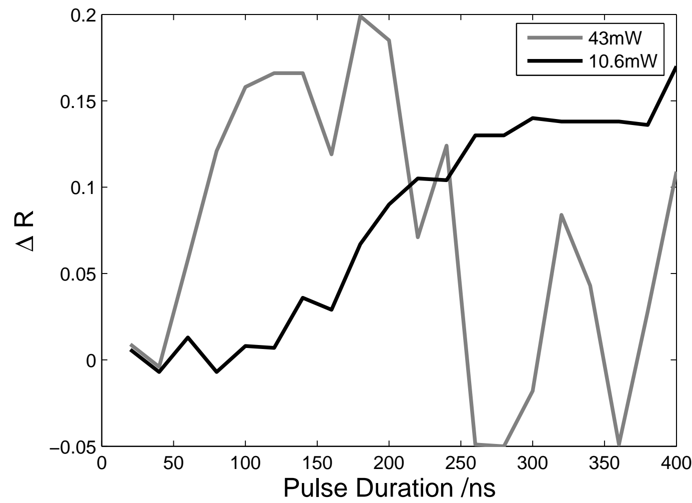

(a)

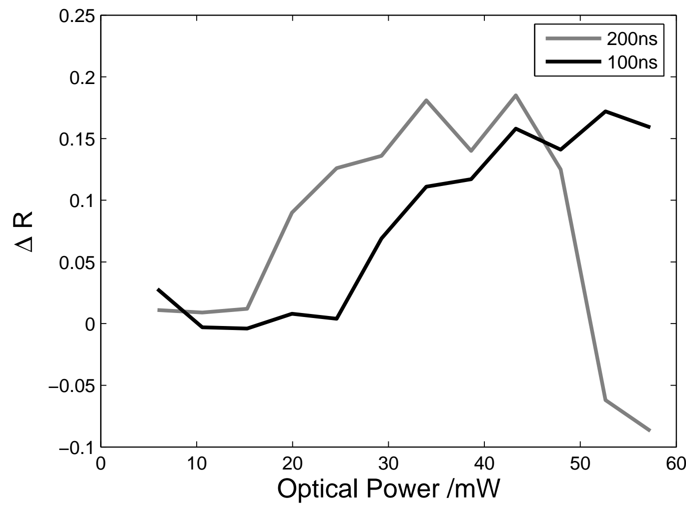

(b)

Figure 4.12: (a) Reflectivity as a function of time (b) Reflectivity as a function of power

duration at 5ns up to a maximum of 65mW and 100ns. The resultant PTK is shown in 4.13.

To demonstrate the switching nature of $Ge_2Sb_2Te_5$ the same $ZnS-SiO_2$ capped sample was subjected to a series of amorphisation-crystallisation cycles of 50mW for 50ns and 20mw for 250ns. In figure 4.14 the detector signal of the read laser has been plotted as a function of cycle iteration.

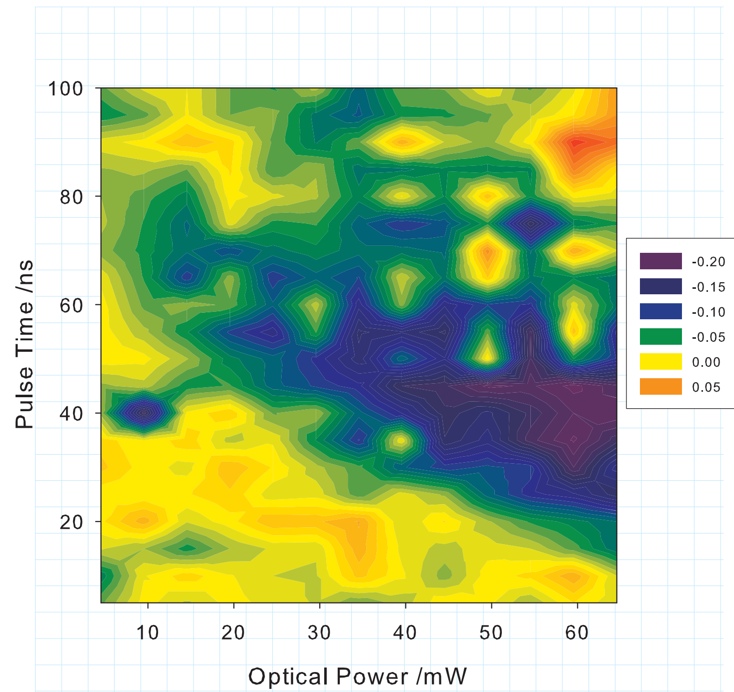

FIGURE 4.13: Phase Change Kinetics plot for the amorphisation of $Ge_2Sb_2Te_5$ thin film

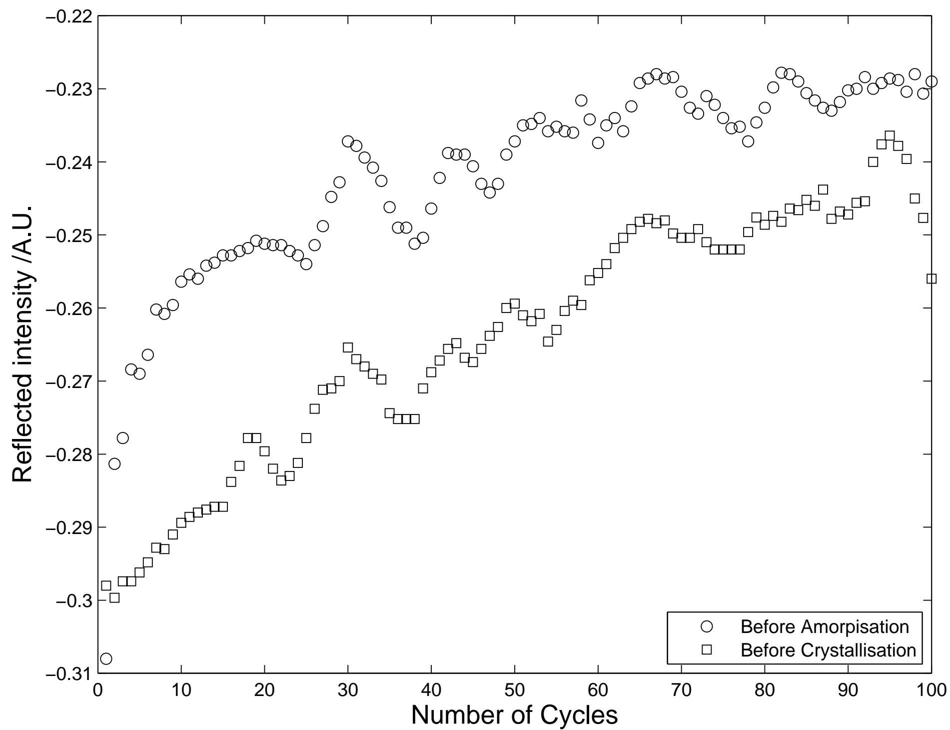

FIGURE 4.14: Phase Change Kinetics plot for the amorphisation of $Ge_2Sb_2Te_5$ thin film

4.3 Compositional Spread Films

4.3.1 Composition Ge:Sb:Te Ternary

The Physical Vapour Deposition (PVD) technique, described in 2.6.1, was used to generate compositional spread samples. The majority of the measurements presented in this chapter were made on the compositions given by figure 4.15. This area covers the $GeTe$-Sb_2Te_3 tie line compositions, such that comparisons with published data are possible. Samples reported in figure 4.15 were deposited such that Ge, Sb, Te compoisitions for wedges were 0-65%, 4-99% and 0-73% respectively. This was achieved by evaporating the Sb and Te in k-cells at 430°C and 545°C whilst the Ge was melted using an electron-gun (e-gun).

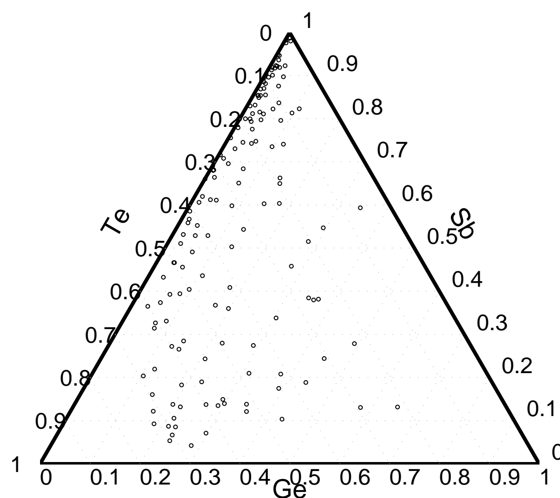

FIGURE 4.15: GeSbTe Compositions synthesised

4.3.2 Crystallisation Temperature as a Function of Composition

The crystallisation temperature as a function of composition was measured by use of the heating stage described in section 2.8.4. It is clear from figure 4.16 that, even at 273°C, areas of the film still remain in the as-deposited state. For this reason only the compositions which showed a phase transition have been plotted; this is given by figure 4.17.

The transition temperatures of compositions close to the $GeTe$-Sb_2Te_3 pseudo-binary have been analysed. The reflected intensity, as a function of temperature, for several compositions along this tie-line are presented in figure 4.18 whilst the crystallisation temperatures have been plotted as a function of composition in figure 4.19. In order

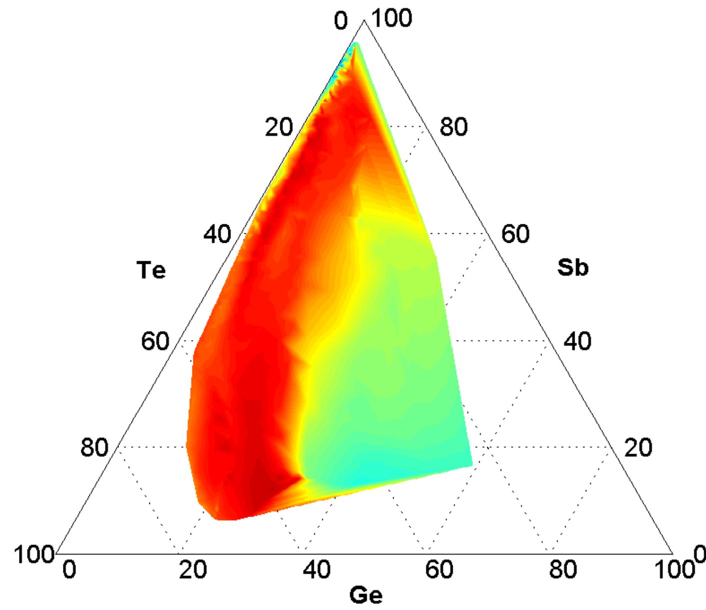

FIGURE 4.16: Ge:Sb:Te map of crystalline areas at 273°C. The red area denotes compositions which have phase changed.

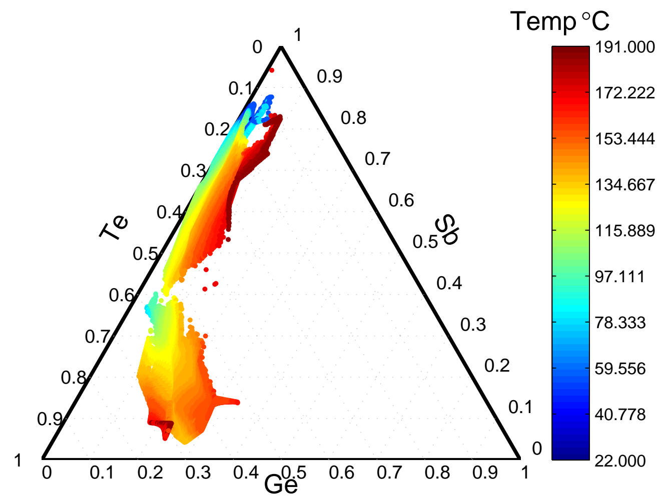

FIGURE 4.17: Ge:Sb:Te transition temperature map (sample 1310)

to aid the reader make comparisons with published data, measurements presented by Yamada et al. [117] have also been included in figure 4.19.

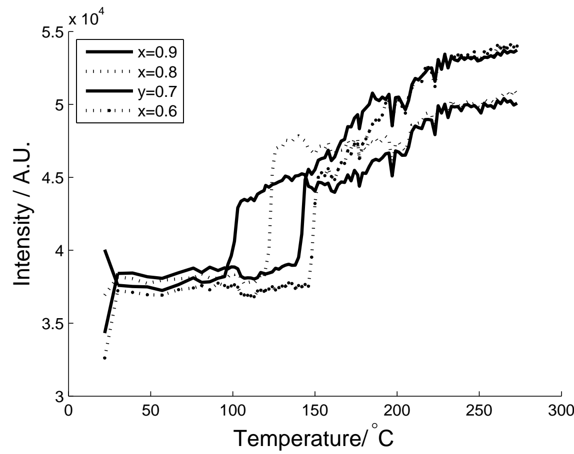

FIGURE 4.18: Ge:Sb:Te reflected intensity along the pseudobinary tie line. Where x represents the fraction of $GeTe$ to Sb_2Te_3 $((GeTe)_x(Sb_2Te_3)_{x-1})$

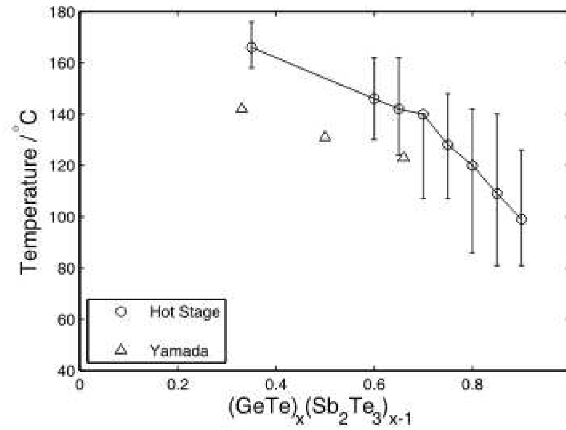

FIGURE 4.19: Ge:Sb:Te crystallisation transition temperature along the pseudo-binary tie line. Where x is defined by $((GeTe)_x(Sb_2Te_3)_{x-1})$

4.3.3 Electrical resistivity as a function of composition

A Four Dimensions 280, automated 4 point probe was used to make room temperature sheet resistivity measurements on a 12 by 12 array of compositions in both the as-deposited and annealed ($270°C$) states. The sheet resistance as a function of composition is presented in figure 4.20 whilst the crystallised and as-deposited sheet resistance as a function of composition along the $GeTe$-Sb_2Te_3 is given in figure 4.21.

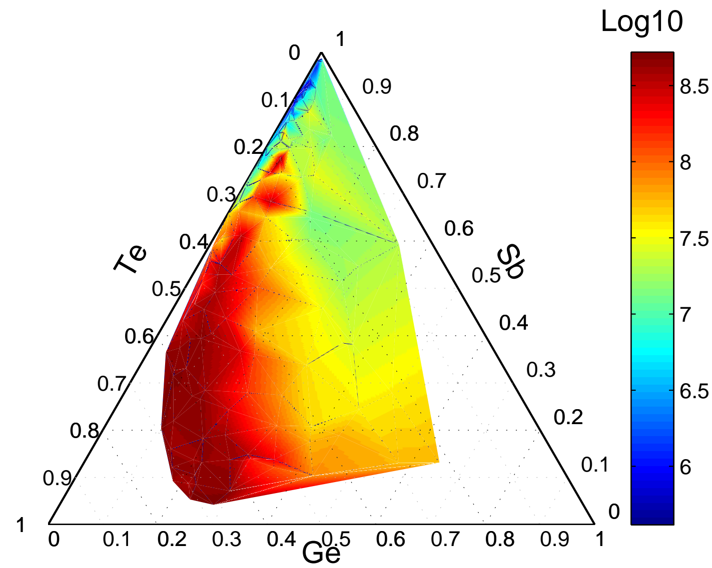

(a) As-deposited

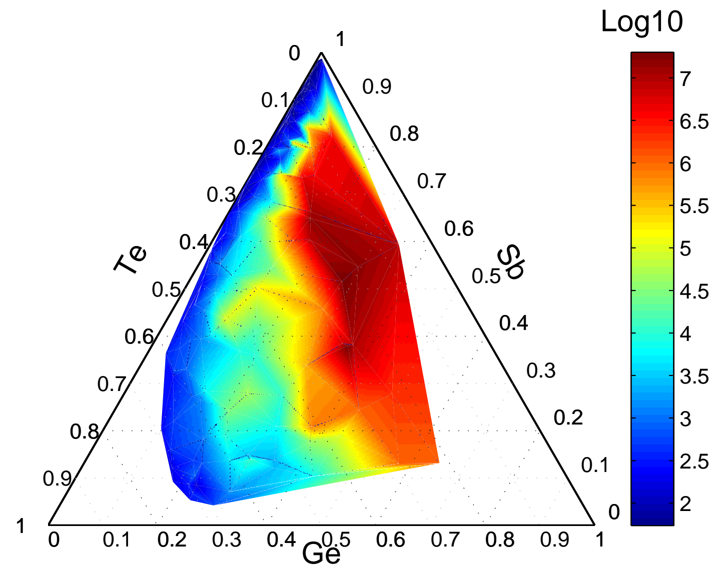

(b) Annealed at 272C

FIGURE 4.20: Sample 1309 sheet resistance; (a) as-deposited (b) annealed at 272°C

4.3.4 Refractive index as a function of composition

An imaging ellipsometer was used to measure the ellipsometric parameters, Ψ and Δ[1], as a function of composition. The refractive index, n, and the extinction coefficient, k, were obtained using in-house software that uses a Simplex routine to fit Ψ and Δ

[1] Ψ is the angle whose tangent is the ratio of the magnitudes of the total reflection coefficients and Δ is the difference in phase difference of the parallel and perpendicular component of an electromagnetic wave after a reflection . Each refractive index has a specific plotting Ψ versus Δ plot, thus by measuring Ψ and Δ over a range of angles the refractive index can be identified[84]

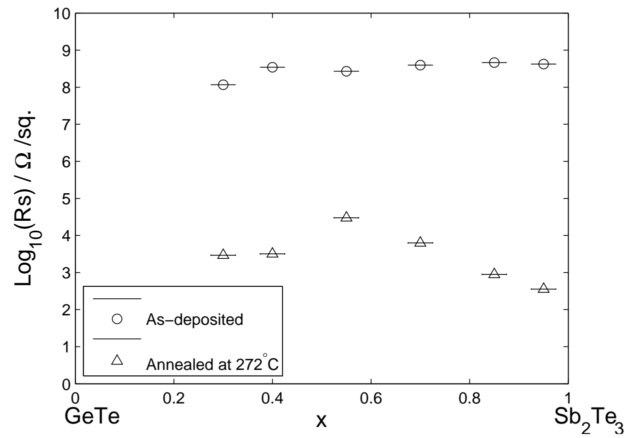

FIGURE 4.21: Sheet Resistance of sample 1309 after annealing at 273°C; where x is defined by $GeTe$ to Sb_2Te_3 $((GeTe)_x(Sb_2Te_3)_{x-1})$

trajectories to different values of n and k. This was performed for a 23 by 23 array of compositions in both the as-deposited and annealed (272°C) states; the data for each state is presented in figures 4.22 and 4.23 respectively.

The n and k values along the pseudo-binary have been extracted and plotted in figure 4.24 for both annealed and as-deposited states.

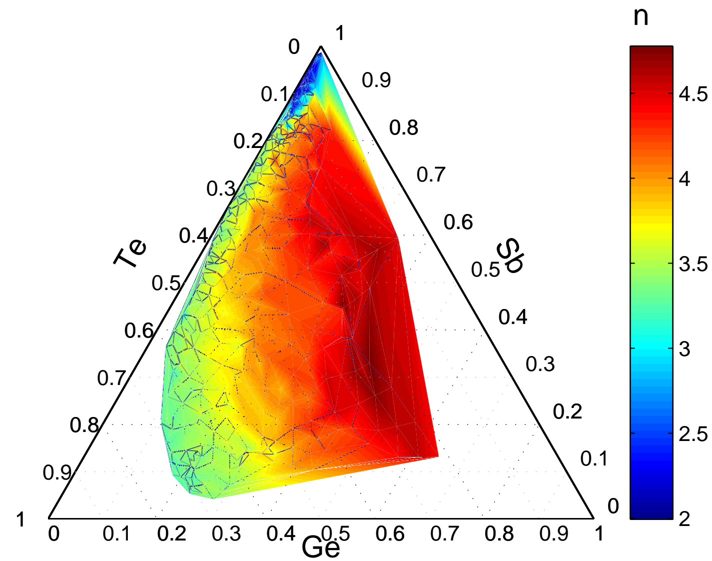

(a) n

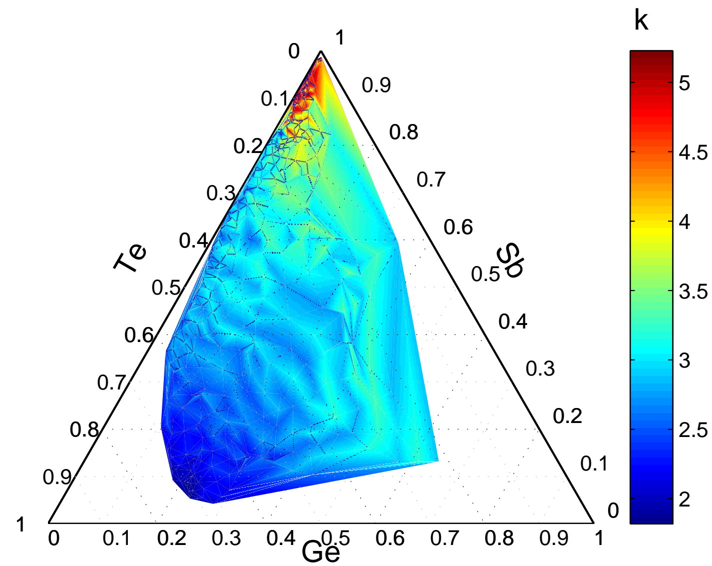

(b) k

FIGURE 4.22: Sample 1310 as-deposited refractive index and extinction coefficient (assuming infinitely thick film)

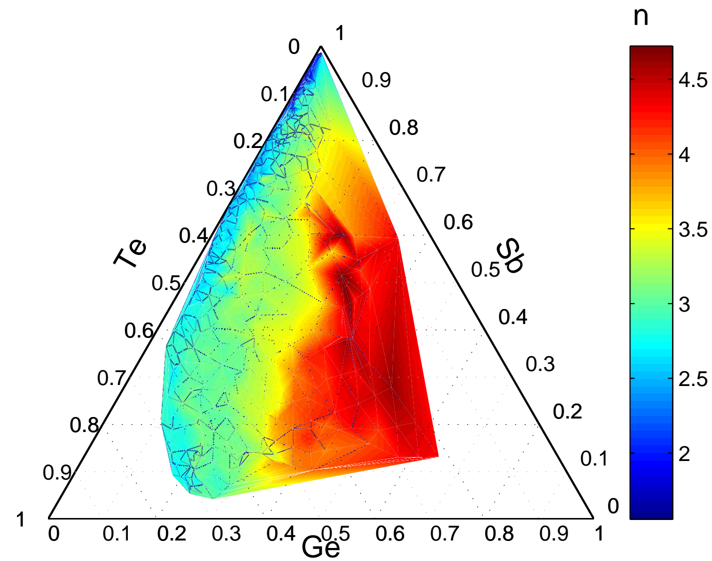

(a) n

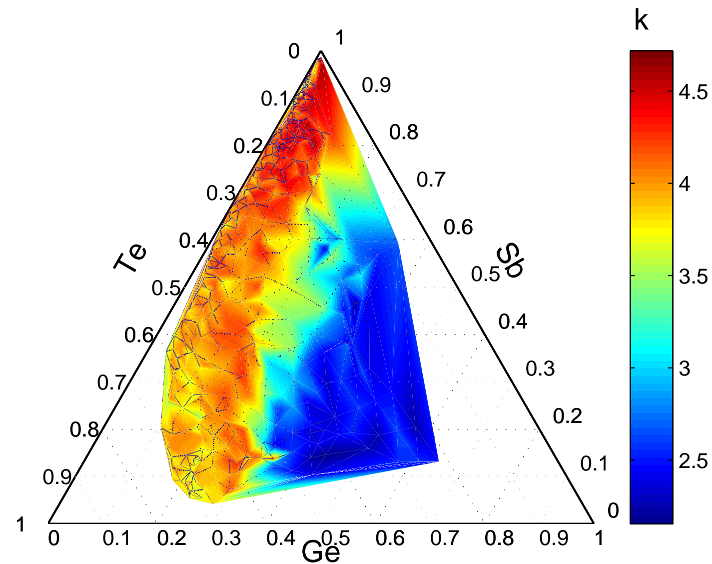

(b) k

FIGURE 4.23: Sample 1310 refractive index and extinction coefficient after annealing at 272°C (assuming infinitely thick film)

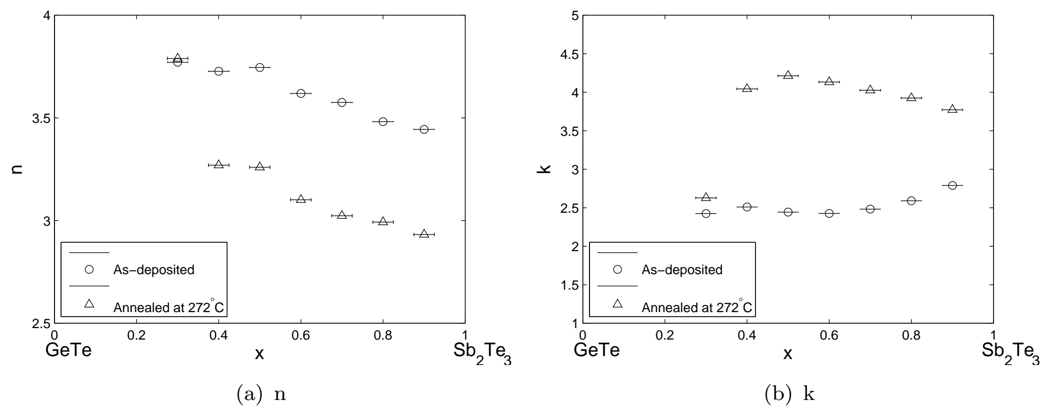

(a) n

(b) k

FIGURE 4.24: Sample 1310 assuming infinitely thick; where x is defined by $GeTe$ to Sb_2Te_3 ($(GeTe)_x(Sb_2Te_3)_{x-1}$)

4.3.5 XRD as a function of composition

The compositional XRD spectra were processed by principal component analysis[2]. For the as deposited sample, nine different diffraction patterns were observed. The sample was annealed at $273°C$ and the measurement repeated. Two of the original spectra were also observed in the annealed film but the extent of compositional coverage had increased. The remaining seven, original, as-deposited spectra have been included in appendix A.

Figure 4.25 shows a material which seems amorphous; there are no strong peaks, just a broad between $20 < \theta < 35$. This spectrum is typically found for Sb rich compositions ($> 40\%$ Sb).

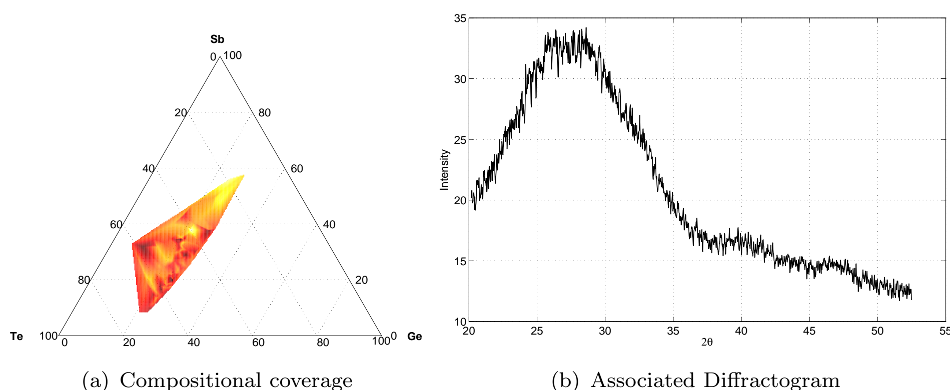

(a) Compositional coverage (b) Associated Diffractogram

FIGURE 4.25: Ternary plot indication compositional coverage of the amorphous spectra shown in (b)

For compositions with less than 40% Sb, spectra occur with more pronounced peaks resulting in a number of strong diffraction patterns. Figure 4.26 shows the peak with the greatest intensity. For this as-deposited sample the compositions which show this spectra are confined to a small composition range ($25\% > Sb > 30\%$ $20\% > Ge > 25\%$ and Te 40% to 50%).

However if one compares this with figure 4.27, which has been annealed at $273°C$, the compositional range which exhibits this spectrum is extended to compositions with Sb in the range 10% to 30%, Ge 20% to 25% and Te 40% to 70%. Thus heating the sample allowed compositions rich in Te and light in Sb to also form the same structure.

Another structure for which the compositional coverage was extended after heating is given in figure 4.28. As-deposited samples show this spectrum for Ge concentrations between 20 and 23% and Te greater than 40%. However after heating to $273°C$ the spectra is extended lower Ge concentrations, see figure 4.29.

[2]The principle component analysis was performed using the Paradise toolbox developed by John Tetteh of Ilika Technologies LTD

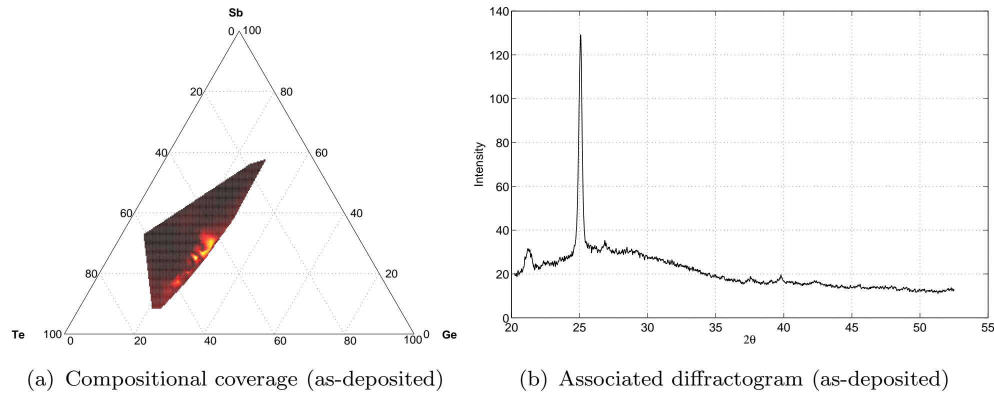

(a) Compositional coverage (as-deposited) (b) Associated diffractogram (as-deposited)

FIGURE 4.26: Ternary plot (a) showing the areas which have the as-deposited crystalline phase shown by the diffractogram of (b)

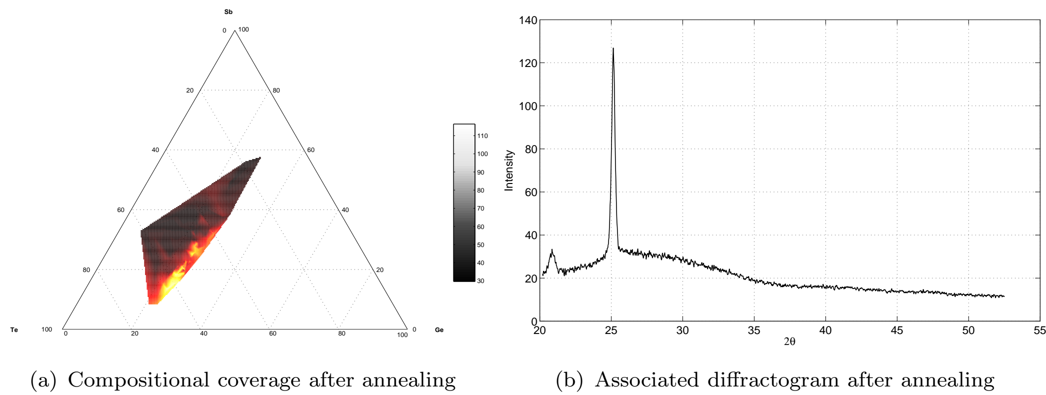

(a) Compositional coverage after annealing (b) Associated diffractogram after annealing

FIGURE 4.27: Ternary plot (a) showing the location of spectra (b) for sample annealed at 270°C

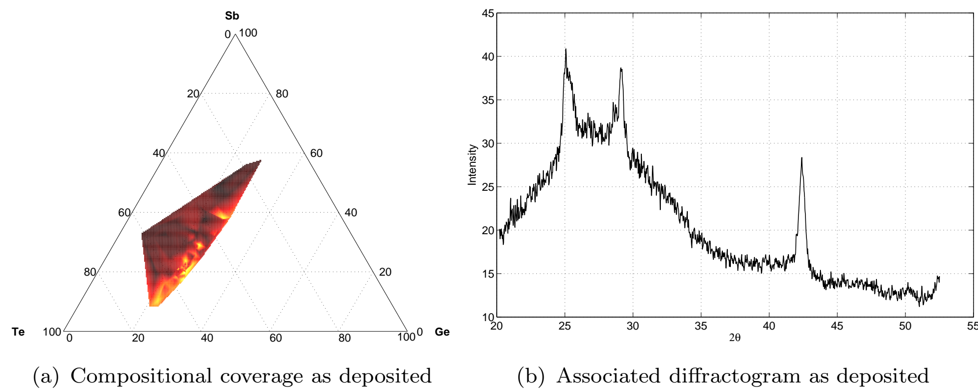

(a) Compositional coverage as deposited (b) Associated diffractogram as deposited

FIGURE 4.28: Compositional coverage and associated diffraction pattern of a third crystal phase as deposited

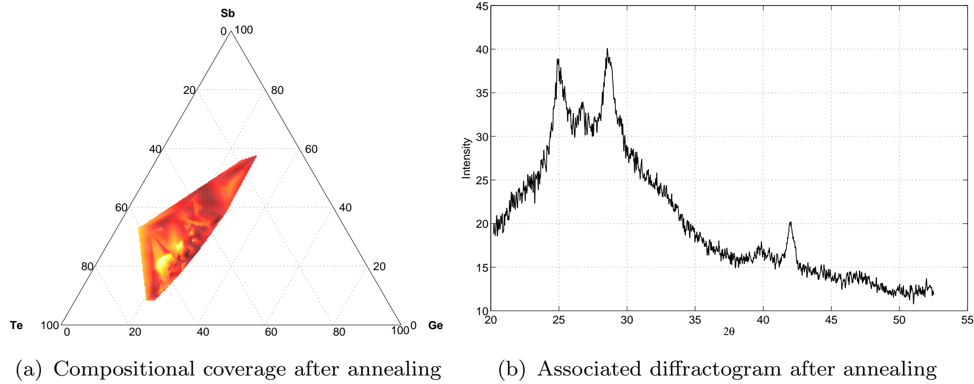

(a) Compositional coverage after annealing

(b) Associated diffractogram after annealing

FIGURE 4.29: Compositional coverage and associated diffraction pattern of a fourth crystal phase after annealing at $270°C$

4.3.6 Crystallisation time as a function of composition

The static tester, which was described in chapter 3, was used to create PTK plots of each composition on a compositionally varying chip. For this measurement the films were deposited such that the majority of the compositions surrounded the $GeTe - Sb_2Te_3$ tie line. These compositions are known to vary considerably in crystallisation time, between 30 and 200ns [117]. The whole substrate was capped with a layer of $ZnS - SiO_2$ by RF sputtering at 5×10^{-3}mBar and 200W. The depth of the film was deposited to be 220nm. This wavelength was chosen since it is the depth necessary for anti-reflection between the air and chip interface. To show this, a simulation[3] was performed to calculate the change in reflectance as a function of $ZnS - SiO_2$ layer depth, for 650nm illumination. The result is shown in figure 4.30.

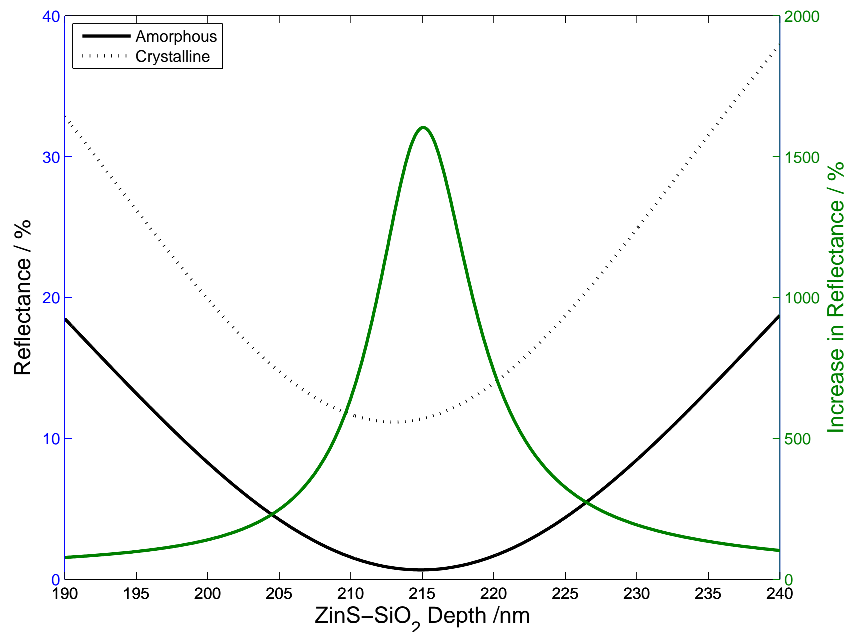

FIGURE 4.30: Reflectance as a function of $ZnS - SiO_2$ film depth for a SiO_2/GST/$ZnS - SiO_2$ structure. The green line shows the percentage change in reflectance as a function of $ZnS - SiO_2$ layer depth.

The crystallisation time as a function of composition has been analysed by taking the the mean of each reflectivity versus pulse time plots for the incident powers of 41mW, 46mW and 52mW. This allowed a somewhat smoothed curve to be differentiated. The time taken for the reflectivity increase to be saturated has been plotted in figure 4.31(a). By simultaneously analyzing the mean plot and the differentiated plot, it was possible to distinguish the point at which the reflectivity increased at the highest rate, this is plotted

[3] A commercial software called the Consise Macleod was used to calculate the Fresnel Equations at each interface of a structure consisting of SiO_2, $Ge_2Sb_2Te_5$ (100nm), $ZnS - SiO_2$ (190nm-240nm), air. The refractive indices used were 1.47, 4.06, 3.87, 2.15 and 1.0 for the glass substrate, amorphous $Ge_2Sb_2Te_5$, crystalline $Ge_2Sb_2Te_5$, $ZnS - SiO_2$ and air respectively

in figure 4.31(b). The nucleation time for the material can be easily distinguished by the time at which the crystal begins to grow, and this is plotted in figure 4.31(c).

A laser power of $1.25 \times P_{T_{melt}}$ is generally used to write amorphous marks where $P_{T_{melt}}$ is the minimum power required to melt that phase change material. This means that the written marks in different materials should be approximately the same, allowing direct comparison [63].

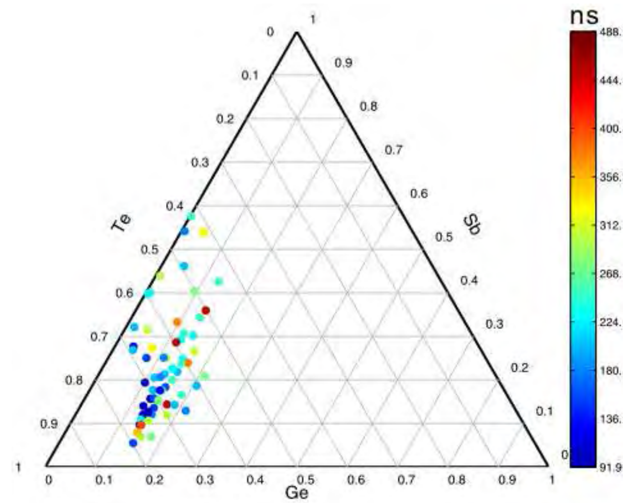

(a) Complete Erase Time (CET)

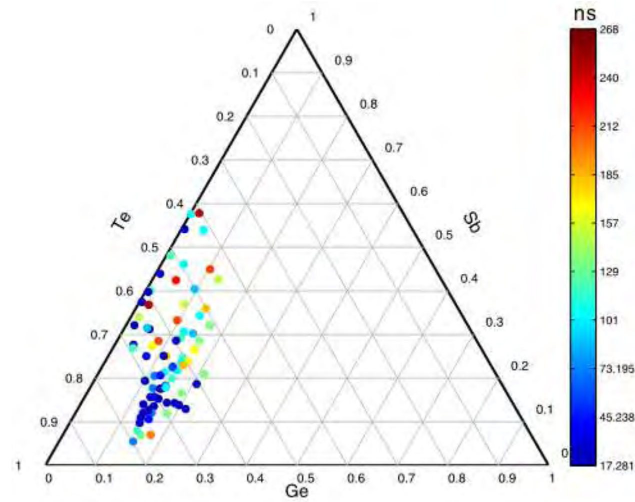

(b) Peak Crystal Growth Time

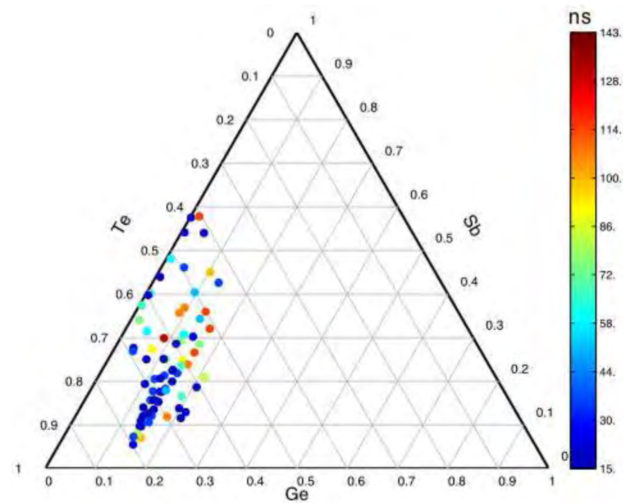

(c) Nucleation time

FIGURE 4.31: Crystallisation time as a function of Ge, Sb and Te. The color bar indicates time in nanoseconds.

4.4 Discussion

Single composition $Ge_2Sb_2Te_5$ films have been prepared by RF-magnetron sputter deposition whilst Ge:Sb:Te compositions, covering the ternary space, have been prepared by thermal evaporation such that large areas of compositional space can be deposited on a single substrate. The sputtered film showed a crystallisation phase transition at $145°C$. This is displayed by figure 4.8. The phase transition temperature is defined as the temperature at which the crystallisation rate is maximum (when there is a peak in dR/dT). The transition is clear and is observed as an abrupt 20% increase in the material's reflectivity and a four orders of magnitude reduction in the sheet resistance of the sample. This observed drop in sheet resistance is due to a change in the film's electronic structure. To confirm that these drops are a result of structural reorganisation, X-ray diffraction analysis was performed on the as-deposited film, an annealed film ($273°C$) and the sputtering target. This data was presented in figure 4.10. The results show that annealed film has a sharp diffraction peak at $2\theta = 42°$ and a further feature at $2\theta = 52°$. A search an match analysis of the ICSD database[135] identified these peaks as corresponding to a Face Centered Cubic (FCC) structure, whilst the sputtering target also showed peaks attributed to a Hexagonal Close Packed (HCP) structure. This data is consistent with that published by others [136]. It has been suggested that the lower temperature, highly symmetric, cubic phase plays some role in the short transition time[137] which was observed in the static tester experimentation (see figure 4.11).

In order to prove the validity of compositional spread thin films with those of single composition sputtered films, figures 4.19, 4.21 and 4.24 have been used to compare the crystallisation transition temperature, electrical resistivity and refractive index measurements along the compositional spread Ge:Sb:Te films with that of published data along the $GeTe - Sb_2Te_3$ pseudobinary tie-line. In figure 4.19 it is clear that there is a discrepancy in the crystallisation temperature between the measurements, made by high throughput techniques, and the published data on sputtered materials. Further, figure 4.8 shows that the crystallisation temperature measured on a sputtered film $Ge_2Sb_2Te_5$ is in good agreement with that of other published data. Thus, the film itself is different in someway to sputtered films. The properties of sputtered films are known to vary depending on the background gas (usually Ar) pressure and RF-power. These cause, mainly, defects and Ar inclusion into the film respectively [75]. The compositional spread films were deposited as single atoms at 10^{-5} Pa. These films can have a different structural arrangement of the constituent atoms [138] which could alter the strength of the bonds and increase the crystallisation temperature. Reliable values of electrical resistivity along the tie line are not widely available in the literature but the resistance of $Ge_2Sb_2Te_5$ is consistent with published material[6]. The refractive index measurements are also difficult to compare since most measurements have been made at

633nm, a HeNe wavelength, compared to the 532nm, frequency doubled Nd:YAG, wavelength used for these measurements. However reported spectroscopic data is consistent with measurements on $Ge_2Sb_2Te_5$ made at 532nm [139] [140].

The increased electrical conductivity, observed in figure 4.9, has been explained by Pirovano et al. [40]. Amorphous chalcogenide materials act as semiconductors with an energy gap. The covalent interatomic bonds give rise to bonding (valance) and anti-bonding (conduction) bands. The existence of lone pair chalcogen atoms result in a localised density of states close to the valance band edge. The lone-pair interaction with the amorphous surroundings sets up a spectrum of states with varying bond strengths and charge configurations. The localisation of these states has the effect of giving a very low carrier mobility.

The crystalline state, in contrast, shows a metallic like conducting behaviour, in that, as the temperature of the film is increased, it becomes more electrically resistive due to scattering of electrons. The high density of localized states is sufficient to provide a concentration of free electrons thus making metallic-like conduction possible [48]

Pirovano looked at the absorption spectra of $Ge_2Sb_2Te_5$ in both the crystalline and amorphous states. Absorption of electromagnetic radiation occurs when the photon energy/frequency is sufficient to excite an electron from the valence band into the conduction band, creating an electron-hole pair. Thus the absorption spectra gives a measure of the energy gap, E_g, in semiconductors [141]. The $Ge_2Sb_2Te_5$ absorption spectra show an optical gap of 0.5eV and 0.7eV for the crystalline and amorphous states respectively. This also explains the increase in extinction coefficient observed in figures 4.23 and 4.22. The crystalline spectra revealed that it is predominantly an indirect semiconducting material. The lack of long range order in the amorphous state and lone pair bonding result in a poorly defined absorption edge, this is commonly termed the Urbach tail. In the case of amorphous $Ge_2Sb_2Te_5$ this tail is 200meV in extent.

Both states have structural vacancies which lead to acceptor-like traps. Small polaron theory[142] is a possible explanation for these traps. That is, when an electron is added to the site of a positive ion, the charge distribution is changed and the neighbouring atoms are displaced causing a ‘self induced potential well’ for the electron. This well could be sufficiently deep to prevent the electron’s movement through the material. Amorphous materials have a higher probability of forming these electron traps since the disorder, ‘slows down’ the electrons. This means the electrons spend a longer time at an atomic site thus increasing the probability of neighbouring atom displacement and the creation of the potential well. These acceptor like traps allow the electrons to sit in a higher energy level above the valence band.

Upon crystallisation from an amorphous state the material band-gap, state density, trap density and their respective energy values are all changed. The acceptor-like trap energy is shifted to above the Fermi-level thus the probability of electrons existing there is low.

Electrical conduction is possible in the amorphous state via polaron hopping to energetically identical atomic sites. The electron is released from these traps when the surrounding structure of the material is altered. This is the case at an interface with a conducting electrode. The Fermi energy for an amorphous material is above the acceptor-like trap energy, hence the probability of finding an electron in them is high. However the probability of electron traps having the same energy is low since the amorphous atomic arrangement causes a spread in the strain energies associated with the atomic displacement caused by the electron existing in a trap. Thus electron mobility is limited and the material's resistivity is high.

Examining figure 4.20, in the crystalline phase, the sheet resistance should decrease as the Te concentration is increased. To demonstrate this, the sheet resistance as a function of Te for two different ratios of Sb to Ge, 80:20 and 70:30 are plotted in figure 4.32 for both the crystalline and amorphous phases.

It is interesting that the Te concentration effect on electrical resistance is opposite for the two different states. That is, in the as-deposited, amorphous state, $Log_{10}(R_s)$ is proportional to at.% Te whereas in the crystalline state $Log_{10}(R_s)$ is inversely proportional to at.% Te. In the annealed crystalline state, increasing the Te concentration increases the concentration of free electrons and hence the material conductivity. It is known that, during crystallisation the electronic configuration of the Te and Sb atoms is changed thus enhancing their electron energies to a level close to the Fermi level [13] and resulting in metallic like conduction.

Ovshinsky [48] proposed that in amorphous chalcogenide materials there is the possibility of two different types of interactions dependent on the electron configurations; (1) the arrangement of bonding electrons (which have a lower energy than non-bonded lone pairs) and (2) the distribution of lone-pair electrons spread over a range of energies, which are not primarily responsible for cohesive energy in the material. However reducing the ratio of cross-linking group 4 and 5 atoms, the chalcogen lone-pair electrons interact with structural bonds thus stabilising distortions around the localised holes. These structural rearrangements are possible due to the reduced number of strong covalent cross-linking bonds [48]. Hence these materials are much less structurally stable. Figure 4.32(b) is direct support for this model. As previously mentioned, in the amorphous state, chalcogen lone pair bonding increases the concentration of trapping localised states. Therefore, the electrical resistivity increases with Te content in the amorphous state. Since, at low temperatures, conductivity occurs in amorphous chalcogenides due

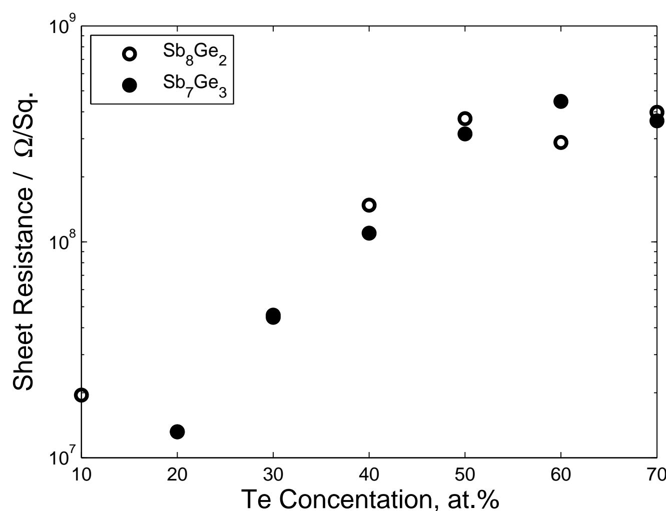

(a) As-deposited

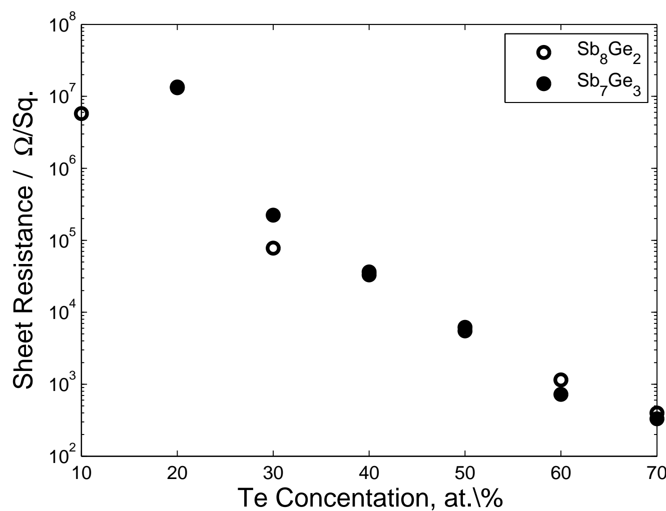

(b) Annealed at 270°C

FIGURE 4.32: The influence of tellurium on the Sheet Resistance of Ge:Sb:Te

to polaron hopping in the network of structural vacancies [46], one would expect conductivity due to polaron hopping to increase with Te content, however this has not been measured. The decrease in conductivity is simply due to the increased availability of trapping states. Another factor which is dependent on trapping states is the threshold voltage for switching. Switching occurs when all of the traps are filled with charge carriers [3, 40], so an increased number of traps should also increase the threshold voltage; the investigation of the threshold voltage dependence of Te content experiment is planned for the near future.

From figure 4.9 one should notice that the electrical resistivity of amorphous $Ge_2Sb_2Te_5$ as a function of temperature gradually decreases. This is in contrast to metallic conductors that show an increase in resistivity with temperature since the conduction electrons

collide with thermally excited lattice vibrations, resulting in electron-phonon scattering. The decrease in R_s, in the case of amorphous $Ge_2Sb_2Te_5$, is a characteristic of semiconducting materials. In this case the temperature allows the electrons in the valence band to gain sufficient energy to overcome the energy gap and reach the conducting band.

In an electrical data storage material the resistance change is of paramount importance. In figure 4.33 the resistance change, on a logarithmic scale, has been plotted as a function of composition.

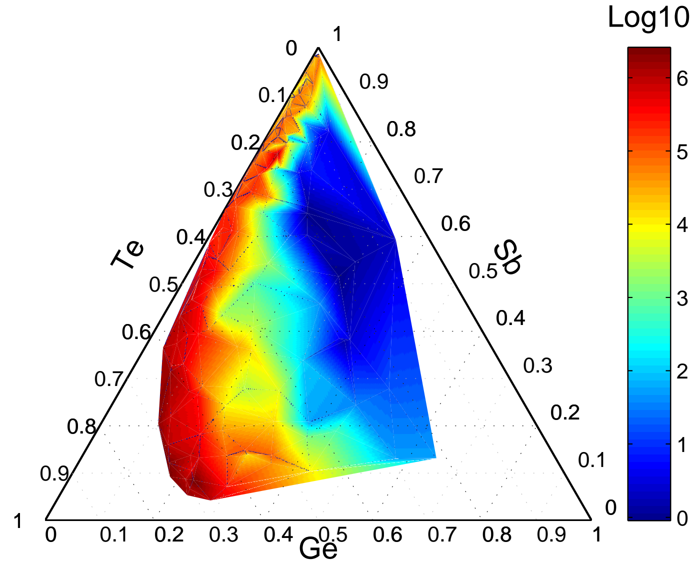

FIGURE 4.33: Change in sheet Resistance, R_s, as a function of composition.

The greatest change in resistance occurs for high concentrations of Te due to the lone pair Te atoms increasing the resistivity of the amorphous phase, whilst in the crystalline state, oppositely, Te increases enhance the electron energy level making conduction possible. High values of resistivity in the crystalline phase are desirable to increase the power efficiency, $(P = I^2R)$, of the heating process. One can see from figure 4.32, that the most efficient heating would occur at low proportions of Te. However, even at Te concentrations between 30 and 40 at.% the difference in resistivity is three orders of magnitude which means that the resistivity difference within the switchable range of compsoitons is not of great importance in this material system.

The effect of Te on the refractive index is also quite interesting; see figure 4.34, 4.22 and 4.23. As the Te content is increased the refractive index decreases in both states. The classical description of refractive index is explained as the motion of an electric dipole in an alternating electric field. The refractive index can be described as 4.1

$$n^2 = \frac{2\alpha + \rho}{\rho - \alpha} \tag{4.1}$$

Where α is the polarizability of valence electrons and ρ is the particle density in the medium. Hence, for a change in refractive index to occur there must be either change in the electronic polarizability or charge density. From the study of electrical resistivity, it was assumed that in the crystalline state there is a greater density of free electric charge at higher Te concentrations. However, the refractive index decreases with Te therefore the material must become less polarized with increasing Te. Polarizability can have several physical origins; (1) distortion of electric charge distribution relative to an ion core, (2) in covalent materials, bond polarizability resulting from the distortion of electronic charge density in covalent bonds and (3) in ionic solids displacement of oppositely charge ions. It is the second point which is of interest here. The effect of adding Te must decrease the polarizability of the material, perhaps by reducing the average bond polarization by saturating the material with Te-Te lone pairs.

In contrast the extinction coefficient, k, slightly increases for the annealed but decreases for the amorphous phase. This indicates two different effects. In the crystalline state the energy gap is slightly reduced by increasing Te which also supports figure 4.32 that the electrical conductivity should increase with Te content since the energy gap is reduced. Thus further supporting the model that in the crystalline film more electrons are in the conduction band for increasing concentrations of Te. In the amorphous state, the energy gap becomes small thus the amount of photons absorbed is reduced for increasing proportions of Te.

The Fresnel equations have been used to calculate the change in reflectance of the sample as a function of composition. The change in reflectivity can be expressed by equation 4.2 where R_c and R_a are the reflectance of the crystalline and amorphous states respectively while n_c and n_a are the refractive indices at 532nm of the crystalline and amorphous states. The refractive index data is plotted in figure 4.22 and 4.23 and was used, with equation 4.2, to generate figure 4.35.

$$\Delta R_c = \frac{R_a - R_c}{R_c} = \frac{(n_a - 1)^2 (n_c + 1)^2}{(n_A + 1)^2 (n_c - 1)^2} - 1 \tag{4.2}$$

One can see that the material's reflectance change varies between 0.2 and 0.6, with the highest changes occurring close to the Sb-Te binary system. The reflectance change along the $GeTe - Sb_2Te_3$ binary system is around 0.25.

The crystallisation PTK plots, figure 4.11, show that there are essentially three areas to the data where; (1) the energy is too low to cause a phase transition, (2) the power and time are above a threshold for crystallisation and below that necessary for ablation and (3) where the pulse ablates material from the film. The threshold power for crystallisation follows an exponential curve. At high powers the films crystallises in a

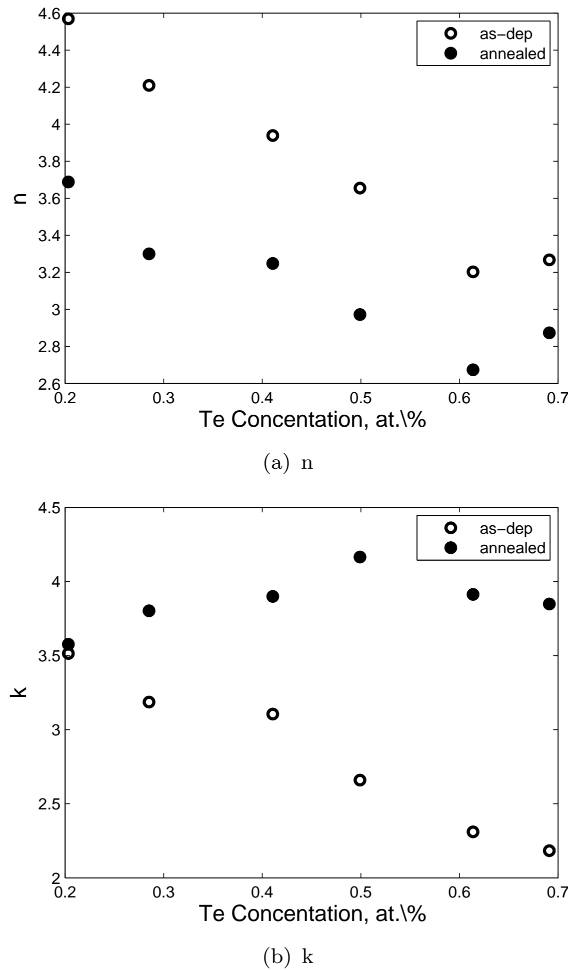

(a) n

(b) k

FIGURE 4.34: The influence of tellurium on (a) refractive index, n, and (b) extinction coefficient, k, of Ge:Sb:Te

short duration but as the power is decreased the time required for crystallisation does not decrease linearly; a much longer pulse is required. This can be explained by thinking about the effect of the substrate. At low powers the film will need more time to reach the crystallisation temperature. However, this also means that the heat energy at the surface of the GST film will have more time to dissipate into the film's depth and eventually reach the substrate. If the substrate has a high thermal conductivity and heat capacity, the energy will be conducted away at a high rate; hence, even more heat energy will be needed to reach the crystallisation temperature of the film. Evidence for this behaviour is given by figure 4.11(b) and the fact there the $\log_{10} P$ is proportional to $\log_{10} t$. Figure 4.36 shows the optical power versus pulse time for nucleation to be completed and the time at which crystal growth occurs. This was found by analysing the $Ge_2Sb_2Te_5$ PTK plot and plotting the boundary power and time at which crystal growth begins. The graph shows that at lower powers the time nucleation time is longer than at higher powers; this is further support if the heat dissipation argument; for short

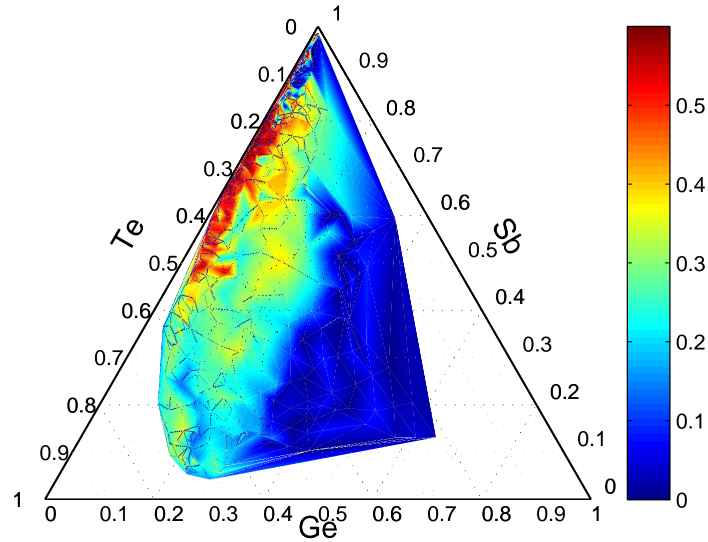

FIGURE 4.35: Reflectance change at, 532nm normal incidence, as a function of composition

pulses the heat energy is concentrated in the film but for longer pulses of lower power, the heat energy has sufficient time to dissipate through the phase change film and into the substrate which, due to its relative size, acts as a heat sink.

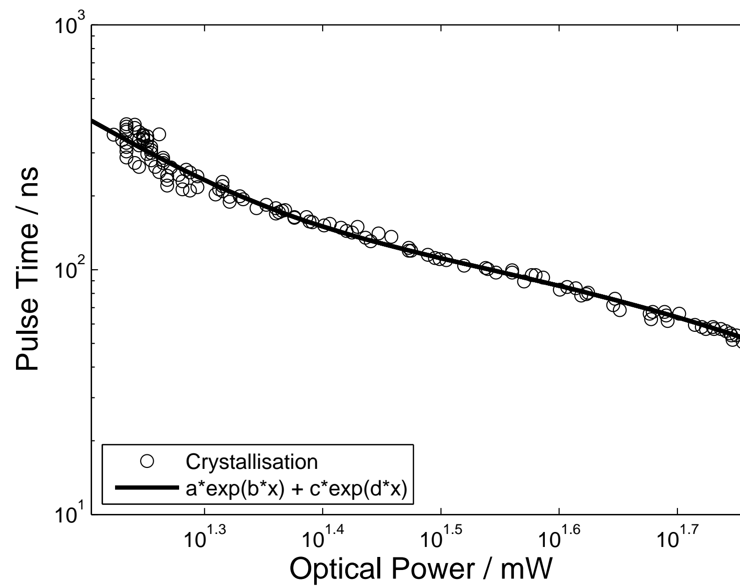

FIGURE 4.36: The power-pulse duration threshold for crystal growth

The as-sputtered $Ge_2Sb_2Te_5$ film crystallised in 80ns this is evident in figures 4.11 and 4.12. This is consistent with other published data for this composition [117].

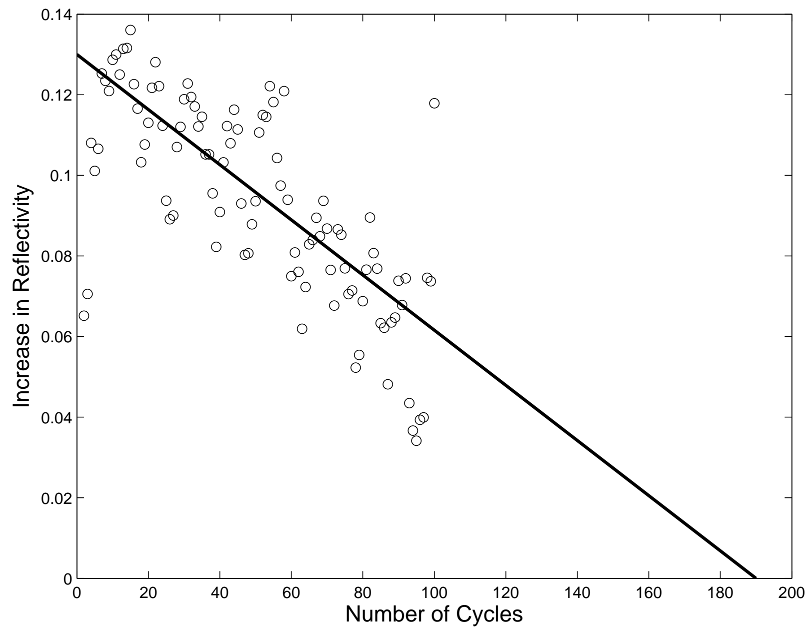

FIGURE 4.37: The deterioration of increase in reflection as a function of cycle

The static tester has also been used to write amorphous marks in a laser crystallised film. A PTK showing the data has been included in figure 4.13. It is clear that the minimum crystallisation time for this PCM is approximately 30ns. This is consistent with reports in the literature [15]. The short pulse of relatively high power heats the film to a temperature sufficient for melting. Since the pulse is short, the molten volume cools quickly into the amorphous phase. The top right-hand corner of the PTK plot demonstrates the problem of a relatively long pulse; its energy is dissipated into the surroundings thus, the molten volume cools at a rate below that required for amorphisation and the materials forms a melt crystallised state.

The affect of cycling on the reflectance is shown in figure 4.14. The difference between the detector voltage of the crystallised and amorphised states is reduced with cycle number. With this data it is possible to make an estimate of the cycle endurance. Figure 4.37 shows the increase in reflectivity after crystallisation as a function of cycle endurance. A linear fit has been applied to data, extrapolating this fit such that the change in intensity is zero, the cycle endurance is found to be approximately 190 write/erase cycles. This limitation is likely to be imposed by the non-ideal write/erase energies applied to the film. The film heats to a higher than necessary temperature which induces high stresses due to thermal expansion. However, the application of read/write cycles to compositional spread films would be interesting and should be considered as a future advancement of the static tester to achieve a relative measurement of maximum read write cycles as a function of composition.

Comparing figures 4.27 and 4.29, it should be noted that the crystalline zone extends when heated. The crystalline zone which formed after annealing is centred around the $GeTe - Sb_2Te_3$ pseudo-binary tie line. This means that, upon heating, this system crystallises into a predominantly FCC structure. Since all of these compositions form the same crystal, the affect of dopants on this region is of interest and has the potential for new phase change alloys away from pseudo-binary system. It would also be interesting to know whether this region has similar crystallisation characteristics. It is suspected, that this fast forming FCC structure could be predominantly nucleation dominated, but this should be confirmed.

The crystallisation time as function of ternary composition was given in figure 4.31. The figure displays the ternary plots for the CET, which was assumed to be equivalent to the time taken for the material's reflectivity to be completely changed. The time at which the reflectivity changed at the greatest rate was also plotted, this can be assumed to be the time for greatest crystal growth. Finally, the nucleation time was plotted by determining the time at which the reflectivity started to increase. All of these results indicate that a composition of 13% Ge, 75% Te and 12% Sb give rise to the shortest CET, the shortest nucleation time and has the shortest time required to reach the fastest crystal growth rate.

It is interesting to compare these results with other crystallisation time studies over similar composition ranges. Laurenzis et al.[133] performed such a study of GeSbTe films within a multilayer stack along the $Sb_2Te_3 - GeTe$ pseudobinary. For samples close to the $GeTe$ composition, the study found the shortest crystallisation time to be approximately 50ns. A clear correlation was observed of decreasing crystallisation time from approximately 300ns for Sb_2Te_3 with increasing $GeTe$ content. The majority of the composition along the tie-line crystallised in around 100ns. However compositions with less than 20% Sb_2Te_3 crystallised in less than 100ns. In contrast, for results presented in this chapter, a strong correlation is observed in an orthogonal direction. The fastest crystallising compositions occurred for the composition $Ge_{13}Sb_{12}Te_{75}$. Maintaining constant Ge content and reducing the ratio Te:Sb, one finds that the crystallisation increases to approximately 300ns. Similar trends are also found in both the crystallisation nucleation time, and the peak crystallisation pulse duration. The $Ge_2Sb_2Te_5$ composition has been measured to switch in 180ns, this is considerably longer than the 100ns reported by Laurenzis. However, at this composition one should note that the crystallisation time has some composition sensitivity. Indeed, examining Laurenzis paper, it is found that deviating from this composition by just five atomic percent causes a factor of three increase in crystallisation time. A five percent composition deviation is within the error of the EDX composition analysis. One of the principal problems with compositional analysis is the inability to distinguish the effect of composition from other effects that might affect the measurement. The trend noticed in this measurement is an increase

in crystallisation time with a reduction in Te:Sb ratio. There is a possibility that this might be an artefact of the sample rather than the composition. The $ZnS - SiO_2$ coating has been assumed to be homogeneous across the sample. However, a small deviation in depth could have a profound effect on the optical power incident on the film. One can see from figure 4.30, that just a 20nm error in the capping coating could result in a factor of 15 reflectance change. To confirm any inhomogeneity in the layer depth, a $ZnS - SiO_2$ layer, sputtered under the same conditions was measured with a P16 profiler. The actual mean layer depth, from 32 measurements, was found to be 257nm with a standard deviation of 41nm. Such a large variation in depth will undoubtedly affect the amount of power delivered to the phase change layer and consequently create a large variation in measured crystallisation time. Despite these difficulties, some important conclusions can still be drawn from these measurements; the compositions centred on $Ge_{13}Sb_{12}Te_{75}$ showed fast crystallisation (around 90ns) and very short nucleation times (15ns) thus they can be classed as growth dominated materials and will prove particularly useful for future nanoscale optical data storage. Such a composition is not suitable for electrical storage since it has a very low crystalline resistivity (see figure 4.20). The crystallisation times of less than 500ns occurred over a very broad composition range (Te 40 to 70%, Sb 5 to 55%, and Ge 0 to 20%). Since the electrical resistivity is dependent on the concentration of Te, an energy efficient, nanoscale electrical device with high proportions of Te could be considered. It seems, from these results that the direct over write, crystallisation time, might be quite slow for such devices but further studies should be performed with a uniform capping layer of $ZnS - SiO_2$.

4.5 Summary

High throughput combinatorial deposition techniques have successfully been applied to the Ge:Sb:Te ternary phase change system. The films were deposited by thermal evaporation in a UHV chamber resulting in marked differences in the film's characteristics from those prepared by the conventional sputter deposition method. These differences have been attributed to the sputter deposition's far greater deposition pressure. The most considerable difference appeared in the crystallisation temperature of the films, which seemed to crystallise at some $20°C$ higher temperature than equivalent compositions prepared by RF magnetron sputtering. Other measurements of electrical resistivity and refractive index were found to be comparable at the $Ge_2Sb_2Te_5$ composition.

Since, in a manufacturing environment, the materials are more likely to be prepared by sputter deposition some trials of composition spread Ge:Sb:Te sputtering were carried out using a HWP sputtering system. The effect of coil power and sample height had a negligible influence on the depth gradient of each target, limiting the sample to

compositions within 20 at.% of the target. Such films could be of interest for finer characterisation of a system where the approximate composition range of interest is known.

Analysis of the electrical resistivity in these materials found that Te-Te lone pair interactions were responsible for a large difference in resistivity of the crystalline and amorphous states. Increasing the Te concentration also increases the number of Te-Te bonds and thus increases the resistivity of the amorphous state, whilst decreasing it in the crystalline state. Therefore the greatest change in resistivity was achieved at compositions with a high Te content. Further analysis of the optical properties resulted in the conclusion that Te also decreases the polarizability of the material and thus causes a correlated reduction its refractive index.

The crystallisation time has been studied and the composition $Ge_{13}Sb_{12}Te_{75}$ was found to crystallise in 90ns. However, difficulties with capping layer uniformity has made composition characterisation difficult. None-the-less, materials over a wide composition range were found to crystallise in less than 500ns.

In chapter 5 the effect of Bi on the Sb:Te system is investigated. The effect of Te in such a system will also be discussed.

Chapter 5

BiSbTe System

5.1 Introduction

The properties of Bi doped $GeTe - Sb_2Te_3$ have been identified to have short crystallisation times and their properties have been investigated by a number of researches[71, 143, 144]. However these promising results were reported for a limited number of compositions. Appreciation of the crystallisation mechanism of bismuth in Sb:Te compounds could aid the understanding in the somewhat more complex Bi doped $GeSbTe$ ternary systems. With this in mind, the affect of Bi has been studied over a wide range of Sb:Te compositions.

When bismuth is doped into GST, ultra-fast crystallisation has been reported with crystallisation in just 10ns [71]. In the same paper, results are presented for the crystallisation of the as-deposited film. The paper emphasises the 10ns recrystallisation time but neglects to suggest a possible reason for this considerable difference between as-deposited and laser amorphised; this will be discussed later. However the Bi mechanism is suggested to reduce the activation energy for crystallisation and lower the crystallisation temperature without affecting the crystal structure or its lattice parameters[71]. The effect of bismuth of GeSbTe alloys was reported by Lee et al. [145]. It was found that substitution of Bi for Sb in $Ge_4Sb_1Te_5$ can lower the crystallization temperature, measured using Kissinger analysis, from $227°C$ to $202°C$ and activation energy for crystallization from 4.03eV to 2.70eV [145].

Sb:Te binary compositions are also well known phase change materials[146, 117, 6]. The crystallisation time of these materials have found to be dependant on the ratio of Sb to Te; the shortest crystallisation times occur for high concentrations of Sb[147]. High Sb concentrations also show growth dominated crystallisation as oppose to nucleation dominated. Since the introduction of high NA objectives and blue writing wavelengths,

growth dominated crystallisation materials have become increasingly important because they possess the attractive characteristic that the data write rate scales inversely with the spot size of the laser[29]. This also makes these materials very attractive for future nanoscale devices wherever decreasing volumes of phase change material are utilised. This scaling has been presented by the Philips group [147]. Figure 5.1 shows how the Complete Erase Time (CET) varies with mark size. This is the time necessary to crystallise amorphous marks of different radii. It can be seen that the for both ratios of Sb:Te the marks take longer to crystallise as the size is increased. The other important point is the radical 2-fold reduction in CET when the Sb:Te ratio is increased from 3.5 to 7.2. This important result shows that high Sb proportion phase change materials are not only fast crystallising but also growth dominated. The materials therefore demonstrate potential for electrical data storage devices[6]. They, in particular, exhibit electrical properties which are useful for phase change electrical switching; they have a low threshold field and constant resistance as a function of temperature. This is desirable otherwise complicated electronics are required to compensate for the change in the materials electrical resistivity, ρ, as it heats.

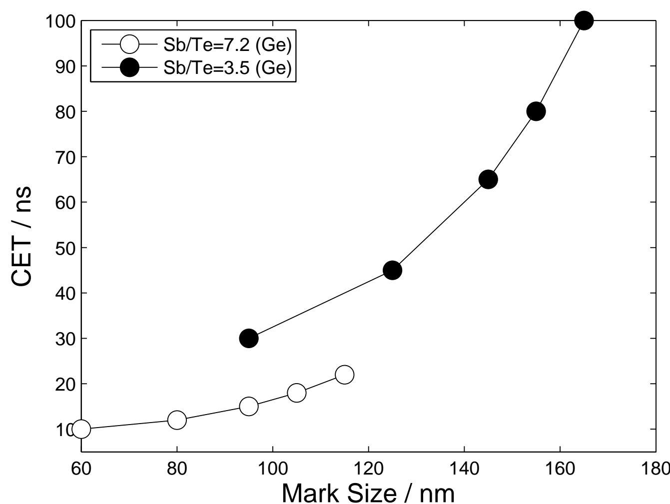

FIGURE 5.1: Complete Erasure Time (CET) as a function of mark size for Ge doped Sb-Te phase change materials with various Sb/Te ratios [147]

The $Sb{-}Te$ phase diagram was given in figure 4.3, one of the key points about this system is its lenience to compositional variation; this is typified by the wide compositional range of the, congruent, Sb_2Te phase. The phase diagram reveals a further congruent melting event for the Sb_3Te_3 composition and in Te rich zone there is a eutectic at 89 at.% Te. The phase diagram for the $Bi - Te$ binary system is given in figure 5.2. In this system, there are two congruent melting events, one at around 92% Te and the other at at the Bi_2Te_3 crystal. The system also has a further eutectic melting event at 2 at.% Te.

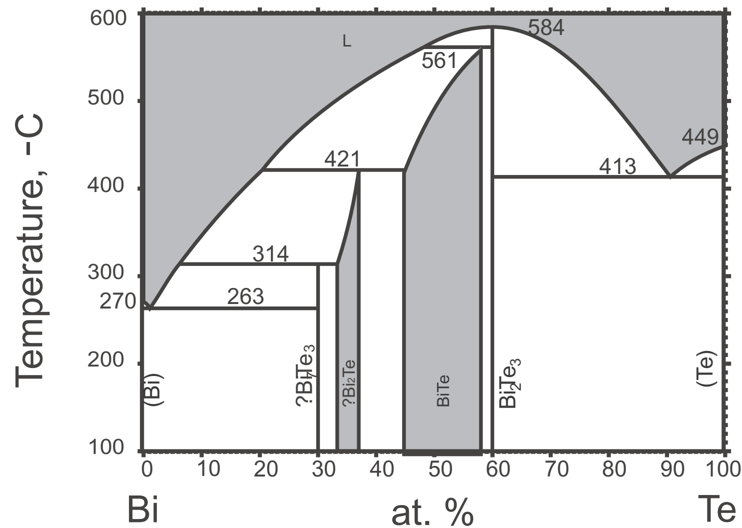

FIGURE 5.2: $Bi - Te$ Phase Diagram

BiSbTe thin films are probably better known for their thermoelectric properties rather than phase change. However evidence does exist that these material might exist in both glassy and amorphous phases[148]. However, there is no reported work on the application of such films to phase change data storage. Usually one would expect the amorphous range of Sb:Te ratio to increase as another element such as bismuth is introduced. However, it is hypothesised that this might not be the case for these films. From a thermodynamic standpoint, adding a third element should increase the entropy of mixing and allow increased stability of the amorphous phase. However in the case of bismuth it, interestingly, enters the amorphous network with a coordination number of 6 and it does not obey Motts '8-N bonding rule' which would normally suggest 8-N=3 [149]. Thus the bonding of the bismuth atom is likely to have a metallic character and reduce the amorphous range of compositions. In the amorphous state the structure and characteristics will be dependent on the Sb-Te bonds whilst annealing above the crystallisation temperature will change the character such that they are dominated by the bismuth atom's metallic bonding[150]. For this reason it is speculated that the resultant change in optical and electrical properties will be greater than Ge doped Sb:Te films.

The aim of this work is to gain an understanding of how Bi can decrease the crystallisation time in GST and use this information to suggest novel fast crystallising compositions. To do this, the problem has been simplified to a Bi doped Sb-Te system. At first samples were prepared by sputter deposition from $BiSbTe$ composite targets and then from this initial study, compositional ranges were identified. The combinatorial, PVD, approach was then used to identify optimum compositions and to gain a more global understanding of the system.

5.2 Sputtered BiSbTe Films

Inspection of figure 4.3 reveals a wide composition congruent melting composition centred on Sb_2Te. This, in particular, shows a tolerance in Sb content ranging from 63 to 81 at.%. Since this crystal can form over a wide Sb range it is anticipated that it will show some acceptance of the Bi atom. To investigate this a Shibaura 4ES sputtering system was used to deposit the films by RF sputtering from Sb_8Te_2, $SbTe$ and Sb_2Te_3 targets. The Bi content was varied between 0 and 15 atomic percent by attaching pure Bi pieces to create composite targets. Sputtering was performed in an argon atmosphere controlled at 0.5 Pa and with a RF power of 100W. Films, of depth 100nm, were deposited onto Si and SiO_2 substrates. The film composition was measured by x-ray fluorescence spectroscopy using a Rigaku RIX 2100 system. Figure 5.3 shows the ternary diagram of compositions fabricated.

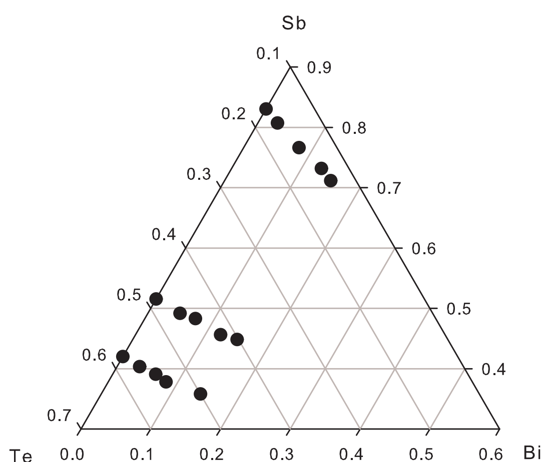

FIGURE 5.3: Sputtered BiSbTe compositions measured by X-Ray Fluorescence (XRF) spectroscopy

5.2.1 Crystallisation Properties

The crystallisation temperature and its activation energy were measured by monitoring the reflection across all visible wavelengths as a function of temperature using a Linkam microscope furnace. The optical reflectivity at 633nm as a function of temperasture for Bi doping into $SbTe$, Sb_2Te_3 and Sb_8Te_2 has been plotted in figure 5.4 (a), (b) and (c) respectively. The samples were subjected to a constant heating rate of $20°Cmin^{-1}$.

From the measurements presented in figure 5.4 it is clear that the Bi doped Sb_8Te_2 composition has a crystallisation event which occurs over a narrow temperature range; this is indicative of a single phase crystallisation. Such events are desirable in phase

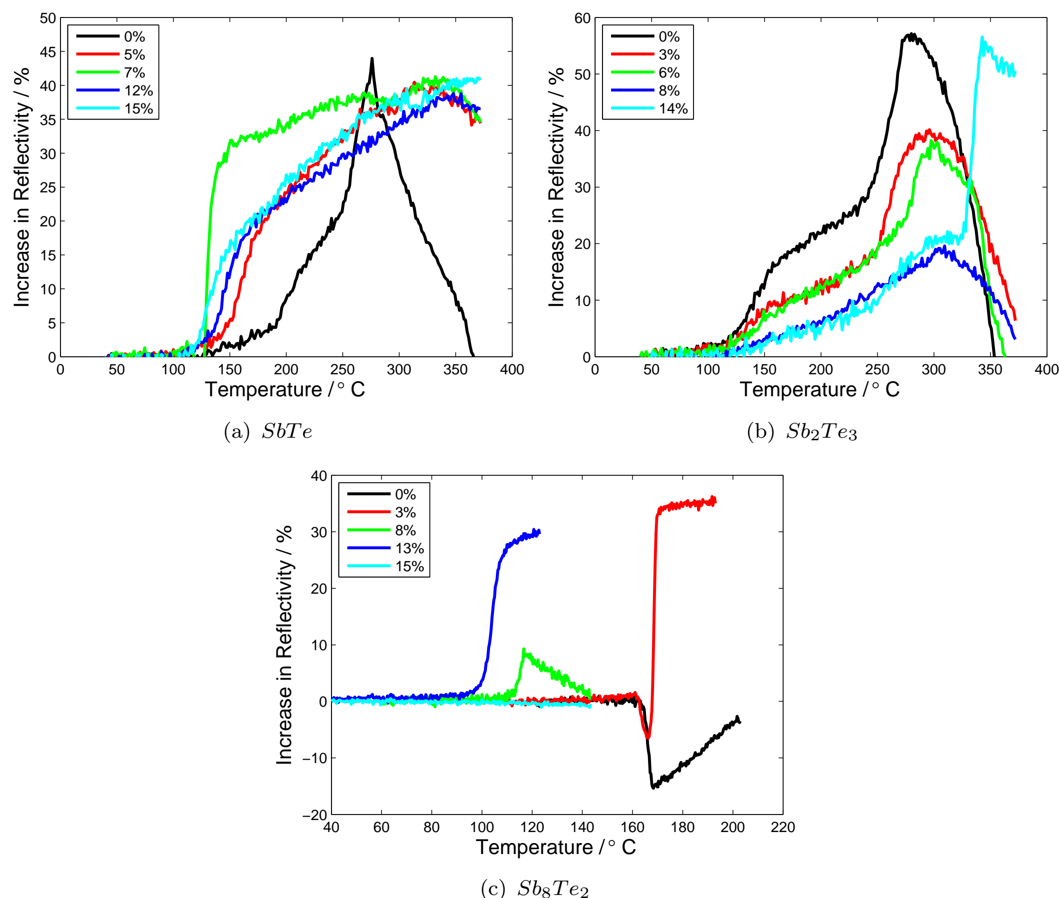

(a) $SbTe$

(b) Sb_2Te_3

(c) Sb_8Te_2

FIGURE 5.4: Increase in reflectivity at 633nm for $(SbTe)Bi$, $(Sb_2Te_3)Bi$ and $(Sb_8Te_2)Bi$ films as a function heating rate

change materials since phase segregation can be avoided. Therefore the Bi doped Sb_8Te_2 compositions will be characterised in more detail in the following section of this thesis.

The non-isothermal Kissinger analysis (described in section 2.8.5) was performed on the Bi doped Sb_8Te_2 films by repeating the above heating-reflectivity experiment at heating rates of 5,10,15,20 and $25°Cmin^{-1}$. Again, the films were heated under a flowing Ar atmosphere. Figure 5.5 shows typical plots which were achieved for the $(Sb_8Te_2)_{92}Bi_8$ sample. The peak crystallisation temperature was taken to be the point at which the rate of crystallisation was maximum. Thus by differenting the curves in figure 5.5(a) and finding the peak, the peak crystallisation temperature was obtained (see figure 5.5(b)) and used to generate the Arrhenius plots, presented in figure [86]. For the readers convenience, the resultant activation energies are displayed against each curve.

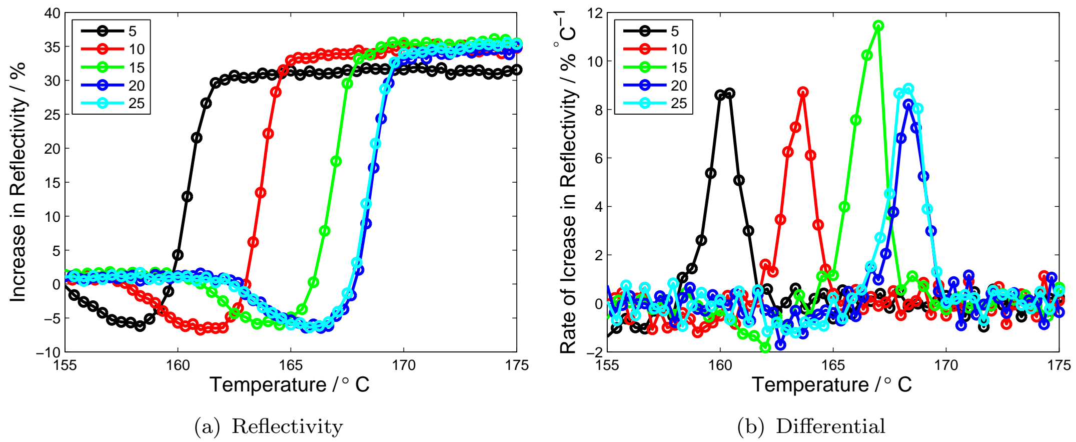

(a) Reflectivity

(b) Differential

FIGURE 5.5: (a)Reflectivity as a function of temperature for $(Sb_8Te_2)_{97}Bi_3$ films heated at 5, 10 ,15, 20 and 25$°Cmin^{-1}$, (b) Differential of reflectivity as a function of temperature for $(Sb_8Te_2)_{97}Bi_3$ films heated at 5, 10, 15, 20 and 25$°Cmin^{-1}$

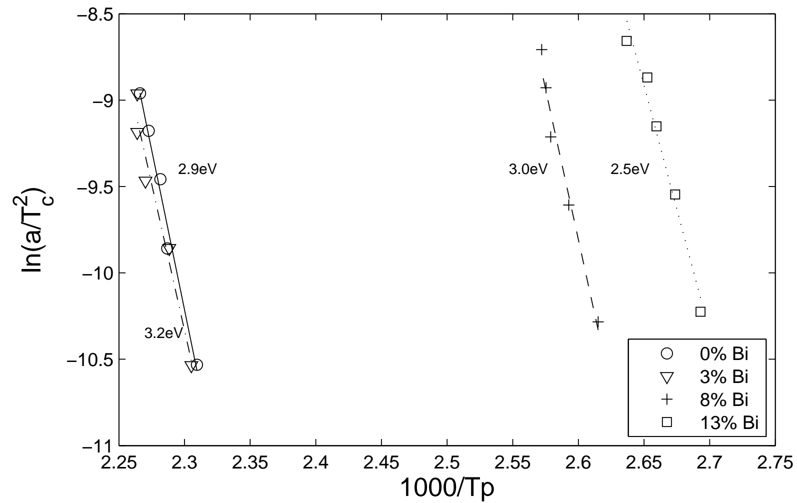

FIGURE 5.6: The Arrhenius plots used in the non-isothermal Kissinger analysis of $(Sb_8Te_2)Bi$ films

5.2.2 Optical Properties

A NFT, I-Elli2000, imaging ellipsometer has been used to measure the films elipsometric parameters at 532nm as a function of Bi content. A simplex fitting routine was then used to determine the real(n) and imaginary (k) components of the refractive index dependence on Bi; the results are plotted in figure 5.7.

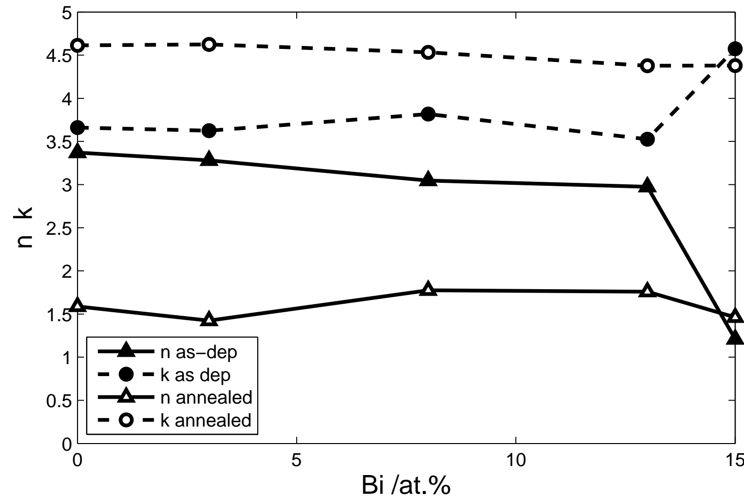

FIGURE 5.7: Refractive index, n, and extinction coefficient, k, before and after annealing at 532nm. (Lines linking the data points have been included to aid the reader.

5.2.3 Electrical Properties

The electrical sheet resistance was measured with a Jandel four point probe ($300\mu m$ tip) and an RM3 electrometer before and after annealing at $180°C$ in a nitrogen atmosphere. A curve showing the affect of Bi is given in figure 5.8.

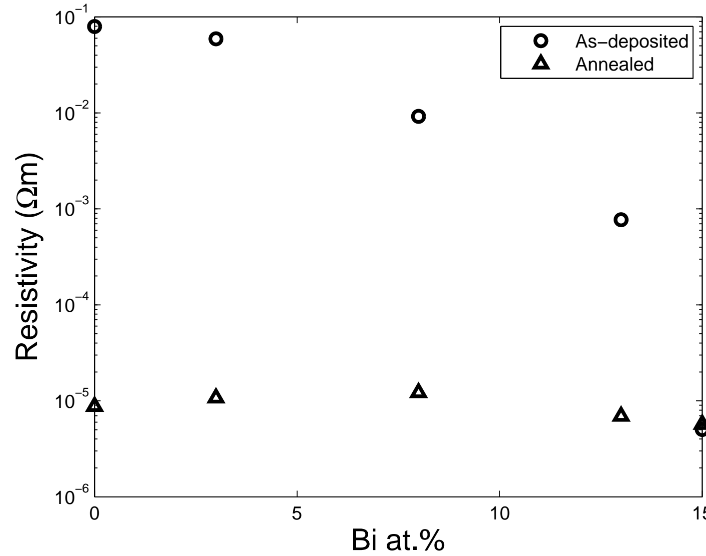

FIGURE 5.8: $(Sb_8Te_2)_{x-1}Bi_x$ electrical resistivity as a function of Bi content

5.2.4 Crystallisation Time

The crystallisation time for each composition was measured using the dual laser static tester [96, 97] described in chapter 3. A 658nm diode laser was focussed to a diffraction limited spot through a 0.65NA objective and used to locally heat the sample. Its incident power was incremented from 5mW to 58mW and for each power setting the pulse duration was varied from 10ns to 500ns in steps of 10ns. The reflectivity of a second, 635nm, diode laser with an optical power of $100\mu W$ co-incident on the sample was used to monitor the change in reflectivity from the film's surface. Measurements were conducted on uncapped films deposited on top of SiO_2 substrates. For each composition, a matrix of optical power, pulse duration and change in reflectivity was generated and plotted. The resultant PTK[97] plots for increasing levels of Bi doping have been included in figure5.9.

The PTK plots have been further processed by selecting three different powers; 30mW, 39mW and 48mW, and plotting the change in reflectivity as a function of pulse time.

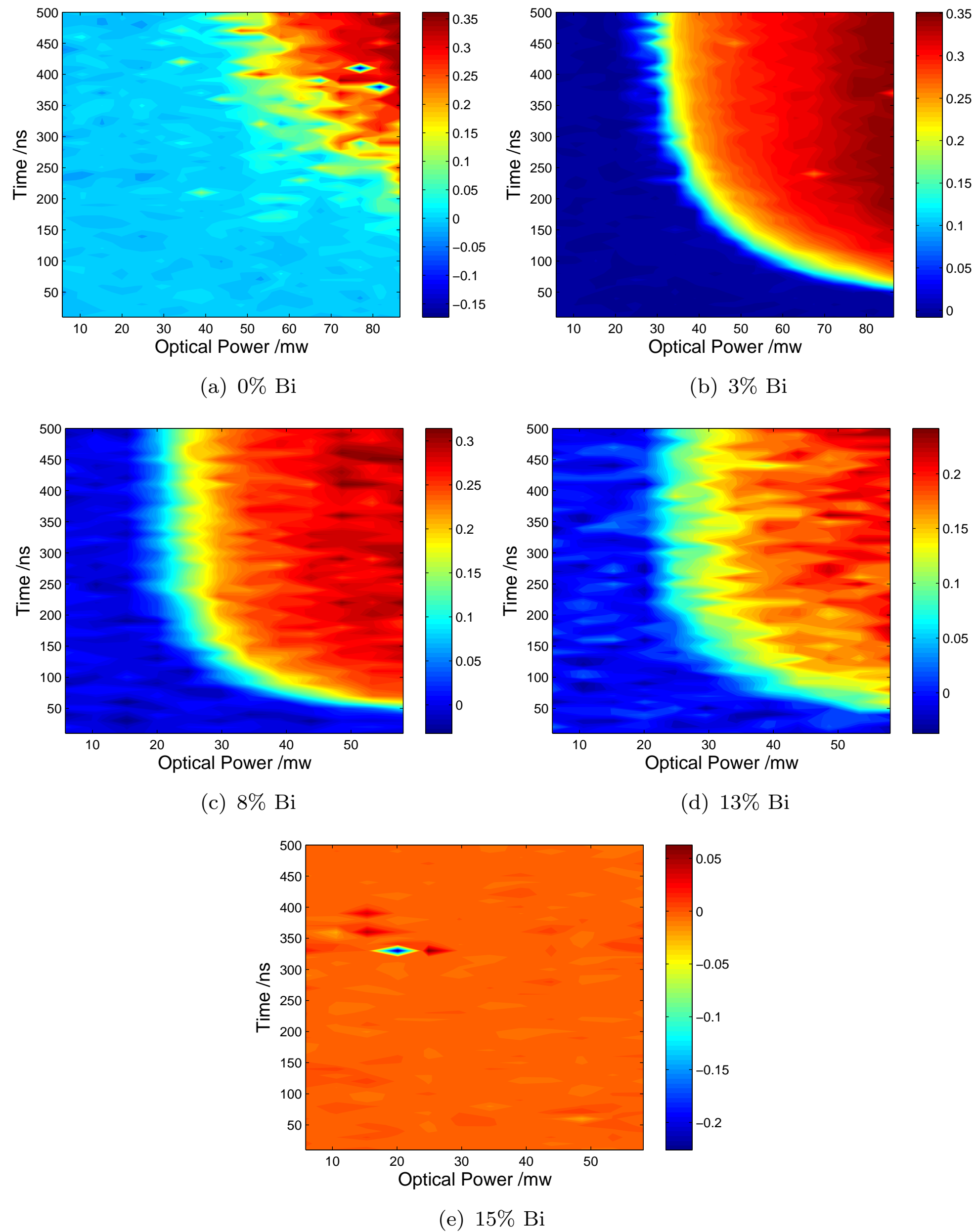

(a) 0% Bi

(b) 3% Bi

(c) 8% Bi

(d) 13% Bi

(e) 15% Bi

FIGURE 5.9: Phase Transform Kinetics (PTK) plots of a Sb_8Te2 as-deposited films doped increasing proportions of bismuth

The highest crystallisation rate at these three different incident powers was then found. These times are plotted as a function of Bi content and this is given in figure 5.10.

For comparison the crystallisation time analysis has been repeated for the Bi doped $SbTe$ films. The resultant time necessary for crystallisation as a function of pulse time for these four incident optical powers in figure 5.11.

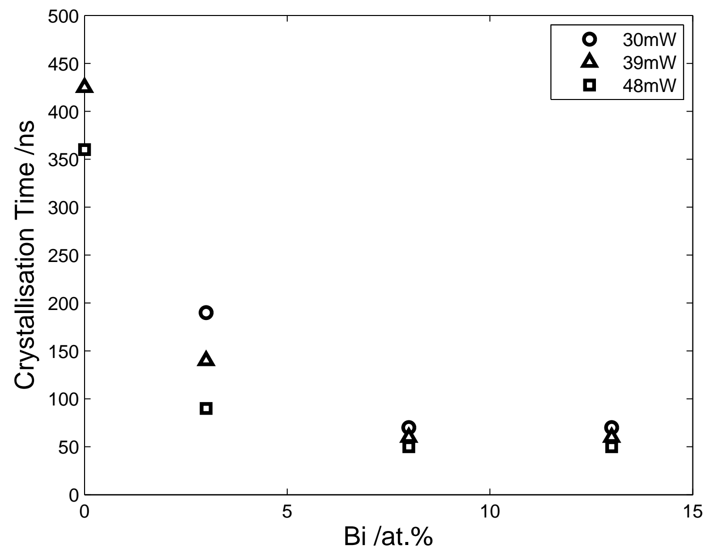

FIGURE 5.10: $(Sb_8Te_2)_{x-1}Bi_x$ crystallisation time

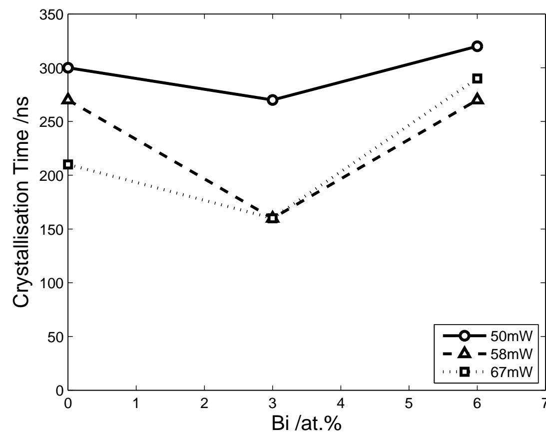

(a) Sb_2Te_3

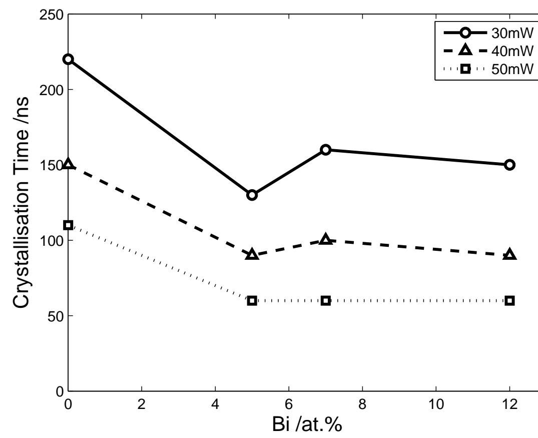

(b) $SbTe$

FIGURE 5.11: Crystallisation time as a function of Bi concentration $SbTe$ and Sb_8Te_2 based phase change films

5.2.5 XRD

Room temperature, X-ray diffraction was performed on the as-deposited samples and after annealing at 180°C. Figure 5.12(a) shows the diffractograms for the as-deposited samples whilst figure 5.12 shows the same films after annealing at 180°C. One can see that there is a clear dopant threshold between 13 and 15 atomic percent Bi at which point the material is crystalline at room temperature.

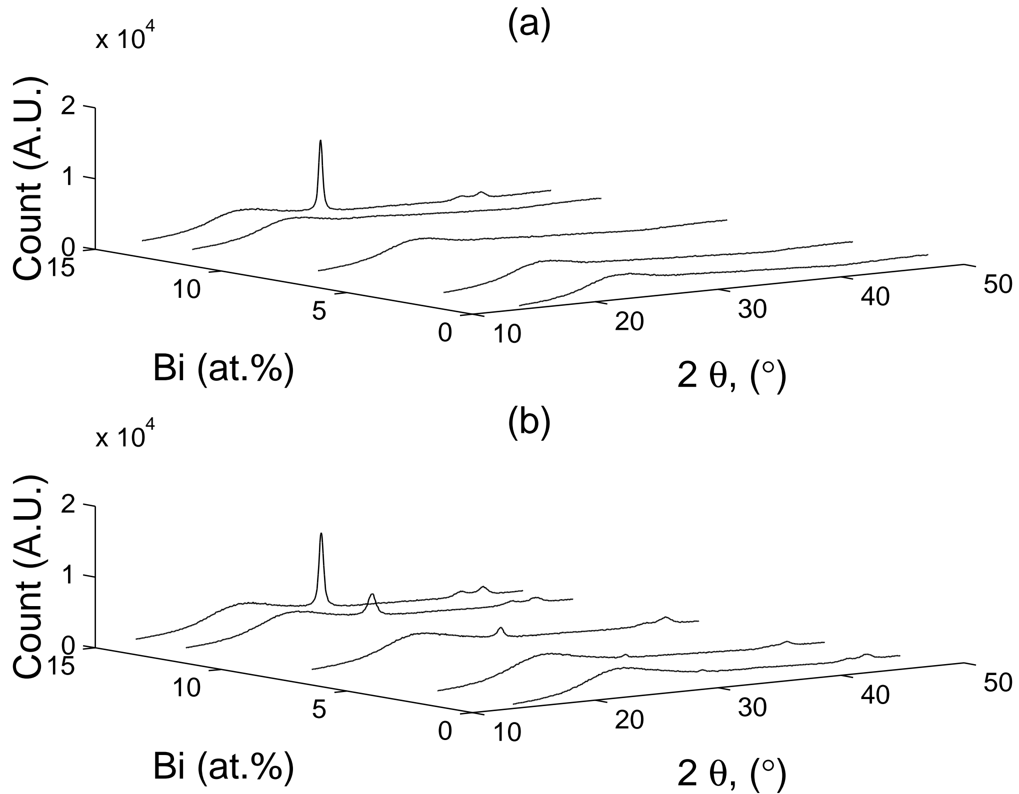

FIGURE 5.12: X-ray diffraction spectra as a function of Bi content. (a) as-deposited (b) annealed

TABLE 5.1: Summary of crystallisation temperature, refractive index and electrical resistivity measurements.

Bi %			as dep			annealed		
	T_x	E_a	n	k	$\rho(k\Omega m)$	n	k	$\rho(k\Omega m)$
0	165	3.2	3.37	3.66	794	1.59	4.61	0.88
3	168	2.9	3.28	3.62	591	1.42	1.76	1.07
8	115	3.0	3.05	3.82	92.1	1.78	4.53	1.22
13	103	2.47	2.98	3.53	7.71	1.76	4.38	0.69
15	-	-	1.21	4.57	0.51	1.46	4.38	0.57

5.3 Compositional Spread Results

The composition spread analysis, which was used to analyse the Ge:Sb:Te ternary system, has now been applied to optimise the Bi:Sb:Te system. The measurements made on the sputtered film indicate that high concentrations of Sb are required for fast amorphous to crystalline phase transitions. Therefore Sb rich samples were prepared and analysed. All elemental sources were deposited by knudsen-cell evaporation under vacuum of typically around $10^{-5} Pa$. Figure 5.13 shows the compositions synthesised from two depositions. A total of 288, unique, composition points have been selected for analysis.

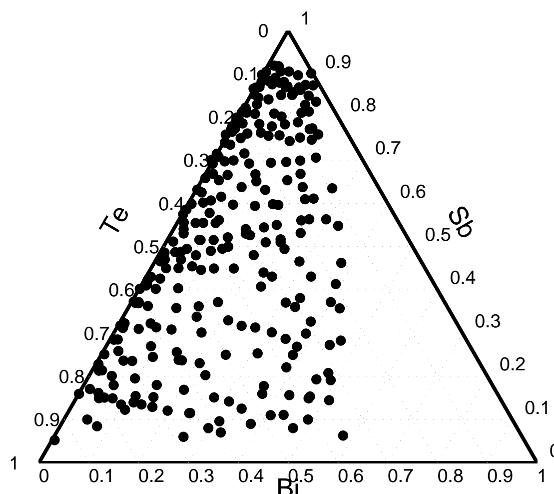

FIGURE 5.13: BiSbTe compositions synthesised and measured by EDX

5.3.1 Electrical Resistivity as a Function of Composition

The electrical sheet resistance, R_s of the 288 compositions has been measured with the Four Dimensions 280 four point probe system. The sheet resistance of the as-deposited film is given in figure 5.14(a) whilst figure 5.14(b) shows the sheet resistance after annealing in a nitrogen atmosphere at $200°C$. The factor by which sheet resistance has decreased after annealing is given in figure 5.14(c).

By filtering out some of the data points in figure 5.14. It has been possible to plot the electrical sheet resistance of the amorphous and crystalline films for constant proportions of Bi. Figure 5.15 shows the result plot for constant Bi proportions of approximately 0%, 10% and 35%. For each measurement the compositional error is around 4%.

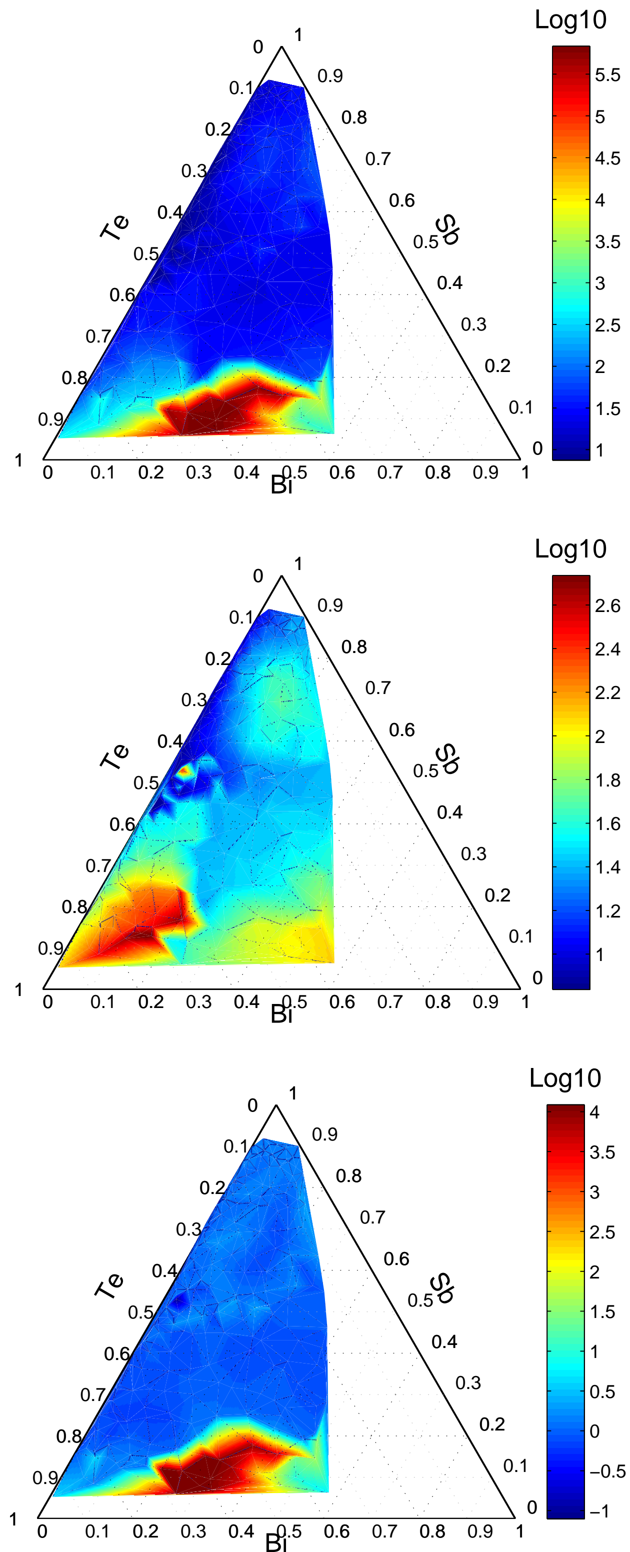

FIGURE 5.14: Electrical sheet resistance, R_s as a function of composition (a) as-deposited state, (b) annealed state and (c) factor decrease

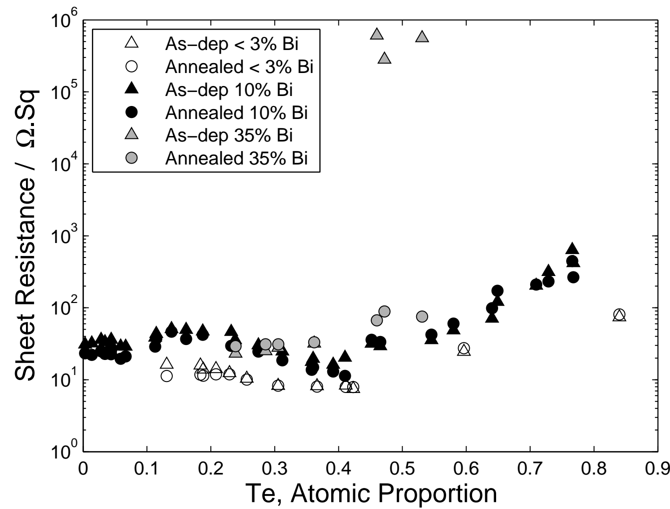

FIGURE 5.15: Electrical sheet Resistance, $R_{,s}$ of BiSbTe films

5.3.2 Refractive Index as a Function of Composition

The refractive index and extinction coefficients of the BiSbTe compositions have been calculated from ellipsometric measurements made by use of a NFT, I-Elli2000, imaging ellipsometer. The measurements were made on the same films before and after heating at $2°Cmin^{-1}$ to $200°C$ in a flowing nitrogen atmosphere. The resultant measurements of refractive index, n and extinction coefficient, k, have been mapped onto ternary plots. These are presented for the as-deposited film and after annealing in figures 5.16 and 5.17 respectively.

The ellipsometric data revealed that the real part of the refractive index for samples with approximately 60% Sb showed a value of less than unity. Although this seems strange, it is important to realise that the imaginary part of the refractive index had a very large value, approximately 5. For films which are highly absorbing, refractive indices less than one are possible. However, it is also important to consider the reliability of ellipsometry as a means of measuring absolute values of refractive index. For the work reported in this thesis, the ellipsometry technique has mainly been used as a way for analysing relative changes in refractive index as a function of composition and thus the absolute value is of lesser importance.

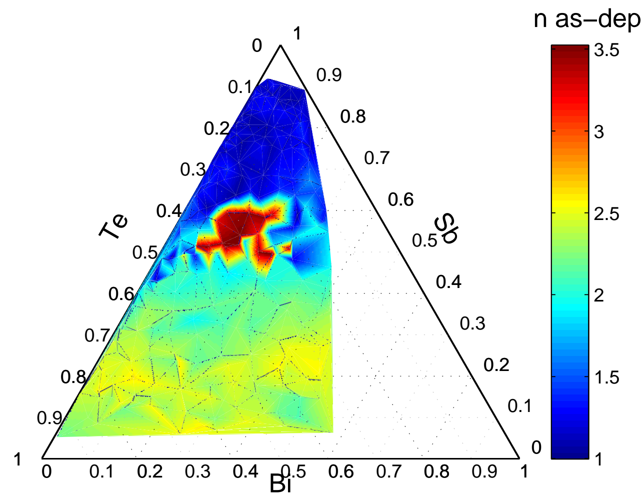

(a) n annealed

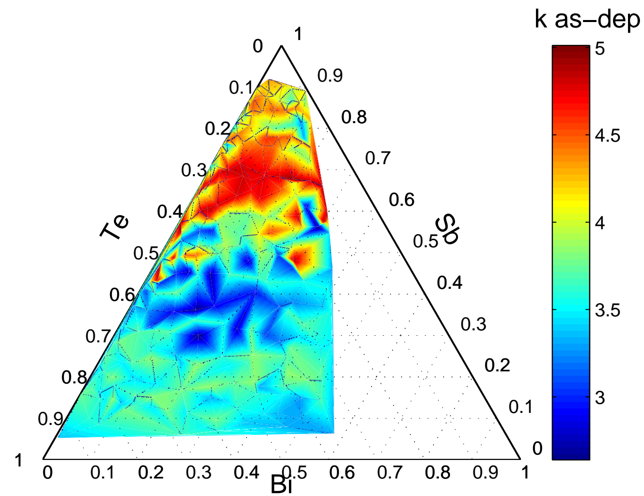

(b) k annealed

FIGURE 5.16: Refractive index, n, and extinction coefficient, k, for as-deposited Bi doped Sb-Te compositions at 532nm

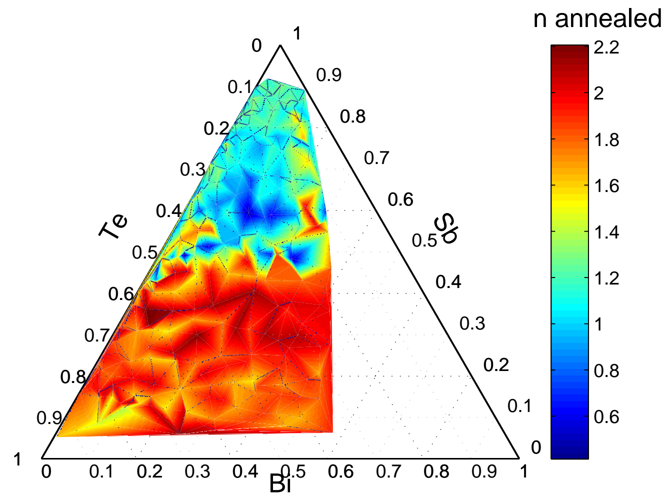

(a) n annealed

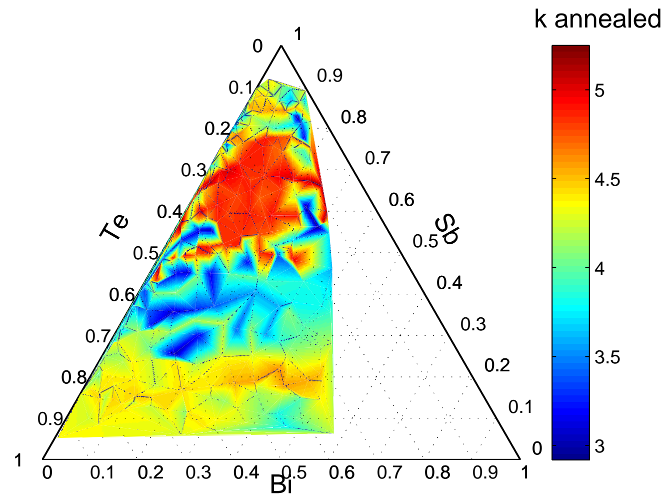

(b) k annealed

FIGURE 5.17: Refractive index, n, and extinction coefficient, k, for Bi doped Sb-Te compositions annealed at 200°C at 532nm

5.3.3 XRD as a function of composition

The X-ray diffraction patterns of 144 different compositions close to the $(Sb_8Te_2)_{(1-x)} : Bi_x$ composition line have been studied for both, before, and after heating at $2°C min^{-1}$ to $200°C$. A principal component analysis tool[1] was used to find the position on the substrate of X-ray spectra with common components. In total six different spectra were found and are given in figure 5.18(c). Their corresponding composition has been mapped against the EDX data and plotted in ternary form. Figure 5.18(a) shows the common spectra before annealing, and after figure 5.18(b) after.

[1]A Matlab tool designed by John Tetteh of Ilika Technologies, to plot on a cartesian grid, the locations of XRD spectra with common components.

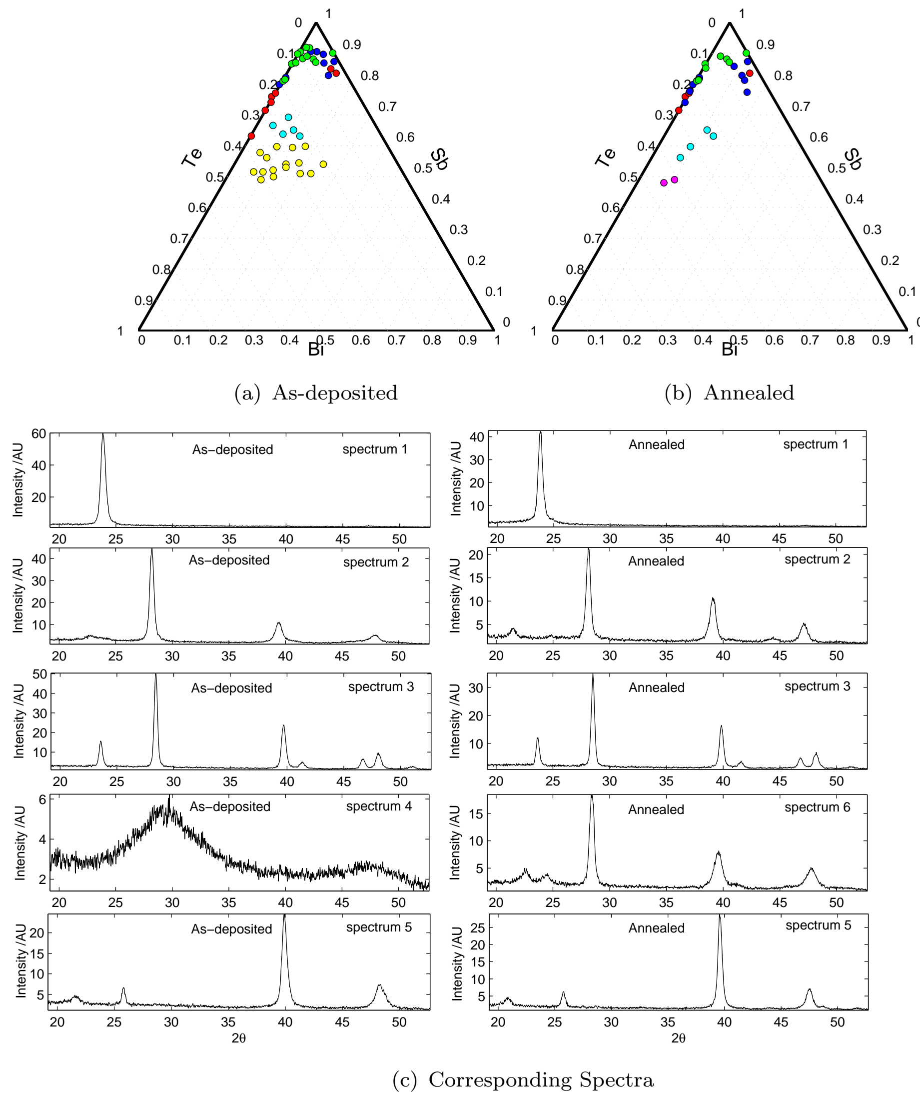

(a) As-deposited (b) Annealed

(c) Corresponding Spectra

FIGURE 5.18: (a) Compositions of observed spectra in the as-deposited state (b)Compositions of observed spectra in the as-deposited state (c) Corresponding observed spectra. KEY: Spectra 1: red, Spectra 2: blue, Spectra 3: green, Spectra 4: yellow, Spectra 5: cyan, Spectra 6: magenta.

5.3.4 Crystallisation Time as a function of composition

The crystallisation time of the BiSbTe compositions in the vicinity of the $Sb_{80}Te_{20}$ composition has been investigated with the static tester described in chapter 3. The samples were prepared such that the BiSbTe layer was sandwiched between a $ZnS_{0.8}SiO_{20.2}$ capping film and the SiO_2 substrate. The intended upper layer thickness was 220nm whilst the depth of SiO_2 substrate was 1mm. Of the 244 compositions studied, the actual switching composition range was limited to the Bi rich region of compositions. The measured increase in reflection was also very small; usually between 3 and 5%. To generate the crystallisation time ternaries, the reflection time plots for the top three laser powers were averaged. From the resultant plot, the pulse time necessary for reflection saturation, nucleation and pulse energy for crystallisation were established and then plotted as a function of composition. Figure 5.19(a) shows the time (ns) necessary to crystallise ,(b) the nucleation time and (c) pulse energy required for crystallisation.

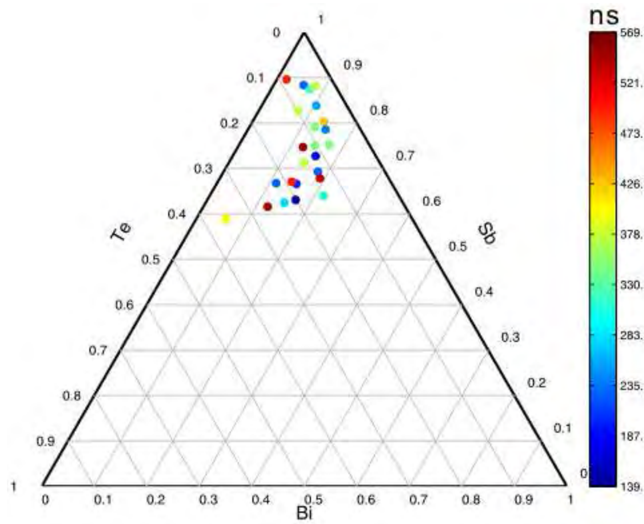

(a) Crystallisation Time

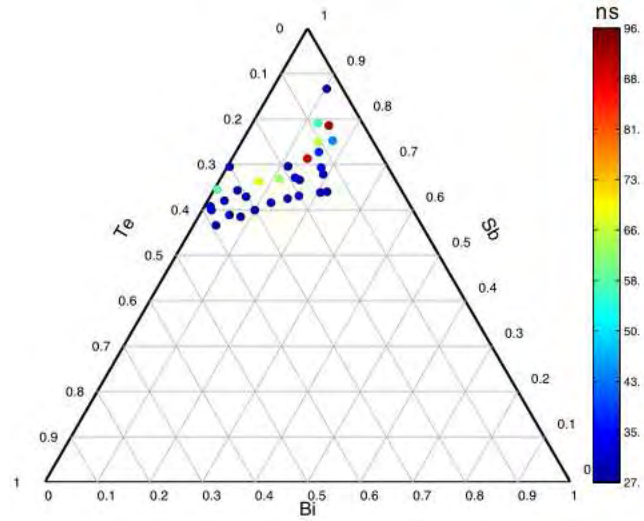

(b) Nucleation Time

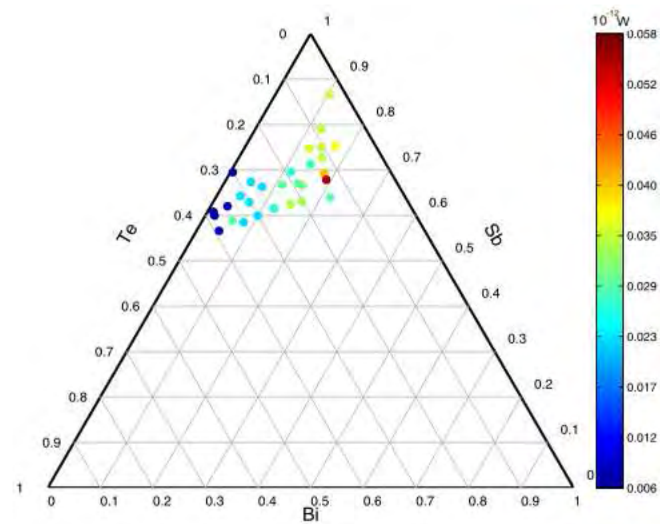

(c) Pulse Energy

FIGURE 5.19: The static tester (a) crystallisation time (ns), (b) the nucleation time (ns) and (c) pulse energy for crystallisation

5.4 Discussion

5.4.1 Sputtered BiSbTe Films

The affect of doping Sb_8Te_2 sputter deposited films with just 3 at.% Bi is to reduce the crystallisation time. Analysis of figures 5.9 and 5.10 reveals that such doping can reduce the time for crystallisation by a factor of two. An order of magnitude reduction is observed for concentrations of 8 at.% Bi, at which point the effect saturates. Doping with concentrations greater than 13 at.% Bi seemed to caused the films to be in a crystalline state at room temperature. The phase of the films has been confirmed by XRD, see figure 5.12. All of the Sb_8Te_2 films have been found to crystallise, upon annealing (see figure 5.4) into the same structure. In fact the as-deposited, crystalline, $(Sb_8Te_2)_{85}Bi_{15}$ film's structure was also found be the same as the annealed films. A search and match analysis of the X-ray diffraction patterns revealed that the films show consistency with that previously reported patterns for the well known optical data storage material, silver and indium doped antimony telluride ($Ag_{3.4}In_{3.7}Sb_{76.4}Te_{16.5}$)[151]. These films take an A7-type structure with Sb and Te randomly occurring on all sites. By assuming an $R\bar{3}m$ space group, the lattice parameters are found to be a=b=4.29$\mathring{A}$ and c≈11.22$\mathring{A}$ [2]. The 15 at.% Bi sample, which also holds this A7-type structure was found to have lattice parameters, a=b=4.45$\mathring{A}$ and c≈11.36$\mathring{A}$ (also space group $R\bar{3}m$)[3] with Bi, Sb and Te occurring on all sites with the probability defined by the alloy's composition. For the readers reference, the A7-type structure has been included in figure 5.20[151].

Sb_8Te_2 phase change materials have been identified as having growth dominated crystallisation[29]. That is, nucleation occurs very quickly, whilst the growth of the crystal occurs slowly. Figure 5.10 shows that the crystallisation time for this material is reduced by an order of magnitude through the addition of Bi. The rate of crystal growth is dependent on activation energy for crystallisation[152]. However, from the Sb_8Te_2 measurements shown in figure 5.6, the activation energy is marginally reduced by the addition of Bi. Therefore the effect of activation energy on the crystal growth can be neglected. This is contrary to that reported in the nucleation dominated $Ge_2Sb_2Te_5$ material, where doping with Bi reduces the activation energy for crystallisation [71] and therefore increases the probability of an atom joining a nucleus resulting in a greater crystallisation rate. In $Ge_2Sb_2Te_5$, the reduction in activation energy effectively increases the probability of crystal nucleation and thus decreases the crystallisation time.

[2] The lattice parameter calculation and the identification of $R\bar{3}m$ space group was performed by P. Fons, CAN-FOR, AIST, Tsukuba, Ibaraki, Japan

[3] $R\bar{3}m$ is one of 230 space group crystal structures which can be used to explain variations to the 17 Bravais structures. The space groups consider combinations of translational symmetry of the unit cell together with reflection, rotation, skewing and gliding symmetry operations.

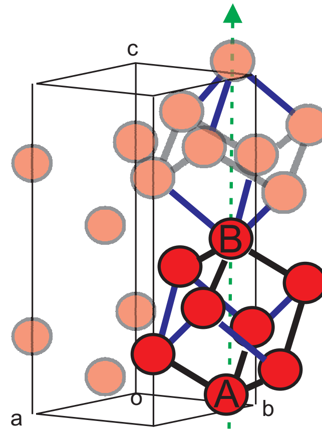

FIGURE 5.20: The A7-type which has been assigned to the crystallised Sb_8Te_2:Bi compositions. The atomic positions are marked by the red circles. The black and blue lines represent, respectively, the long and short atomic bonds of the R$\bar{3}$m space group.

It can be seen in figures 5.10 and 5.11 that the reduction in crystallisation time for a 50mW pulse is 7%, 36% and 91% for Sb_2Te_3, $SbTe$ and Sb_8Te_2 respectively. As the ratio of Sb:Te shifts to greater proportions of Te, the increased crystallisation rate effect of Bi is reduced. It is known that materials which lie along the Sb_2Te_3-Ge-Te tie-line are nucleation dominated, whilst at the other extreme of pure Sb, the crystal growth mechanism can be descried as explosive [119]. This might suggest that as the Te content is increased, the crystallisation mechanism is transferred from growth dominated to nucleation dominated. Once again, considering the work of Sir Nevill Mott, a possible model is suggested to explain this behaviour. Increasing the proportion of chalcogen atoms in the amorphous matrix will increase the number of dangling bond defects[41]. These defects might act as nucleation centres for crystallisation. For pure Sb and Sb-rich compositions there are few nucleation centres and the crystallisation growth occurs from the edge of the focussed spot. This is due to the large thermal gradients that are present which can induce stresses and defects. As the tellurium concentration is increased, the proportion of dangling bond defects increase and nucleation occurs predominantly from their locations.

To explain the apparent reduction in crystallisation time with negligible reduction in crystallisation activation energy of the $(Sb_8Te_2)Bi$ material, a viscosity reduction is considered. A reduction in the materials viscosity would increase the growth rate of the crystal. Therefore its affect would be most prominent when, for complete crystallisation, the growth must occur over a large area. Such a condition is met when there are few nucleation centres forcing growth from the edges. If the aforemention theory is correct, the lowest density of dangling bond defects (and thus fewest nucleation centres) would be most clear for large proportions of Sb. Thus for $(Sb_8Te_2) : Bi$, it is supposed that

the order of magnitude reduction in crystallisation time seen in figure 5.10 is due to a considerable decrease of the materials viscosity.

In the introduction to the chapter the crystallisation time measurements of Wang et al.[71] were discussed. Analysing this paper in detail, a significant, 100ns, difference between the crystallisation time of the, laser, melt quenched samples and as-deposited amorphous samples is clear. This significant difference also fits the model suggested above. The melt quenched marks are different from the as-deposited amorphous films in two ways; (1) they are within a crystalline matrix and (2) quenching from a melt is known to leave nucleation sites within the amorphous matrix [153]. The paper presents a crystallisation activation energy reduction with bismuth content. However the crystallisation time of the as-deposited sample is comparable to the undoped $Ge_2Sb_2Te_5$ samples presented in chapter 4 of this thesis. Therefore the Bi only affects the films with nucleation centres already present and does not increase the probability of crystal nucleation. Thus, in $Ge_2Sb_2Te_5$ the Bi must increase the rate of crystal growth. The crystal simply grows; only from the increased number of nucleation centres and not the edge of the film which was observed for measurements presented in figure 5.10.

It is important to realise that in the case of measurements made on the Sb_2Te_3 and $SbTe$ samples, although there are point defects present at dangling bonds, which could act as nucleation centres, they maybe much smaller than the critical radius for a stable crystal nucleation site, see equation 2.5. The influence of Bi will be negligible until a stable crystal nucleus has formed. Since these, high Te, compositions are expected to be nucleation dominant [29], if the Bi atom significantly reduced the activation energy for crystallisation, the as-deposited film would also show ultra-fast crystallisation; this is not the case. Therefore for nucleation dominant compositions, only melt quenched samples are expected to show sensitivity to bismuth and allow ultrafast crystallisation.

From a thermodynamic perspective heteronuclear bonding is favourable for increasing the entropy of mixing, leading to a more homogeneous mixture of atoms. Whereas homonuclear bonds lead to a reduction in the glass transition temperature and an increase in the Gibbs free energy, resulting in a less stable amorphous film[149]. This may explain the effect of Bi introduction on the crystallisation temperature seen in figure 5.4. The Bi atoms may strongly compete with Sb and tend to inhibit Sb-Te bonding (Dissociation Energy[154], D°_{298} = 277.4 ±3.8 kJmol^{-1}) in favour of Bi-Te bonds(D°_{298} = 232.2 ±11.3 kJmol^{-1}). This could, in turn, increase the proportion of Sb-Sb bonds (D°_{298} = 299.2 ±6.3 kJmol^{-1}) and reduce the stability of the structure. The combination of a lower mean dissociation energy and the instability in the amorphous structure incurred due to an increased proportion of Sb-Sb, homonuclear bonds, allows a significant reduction in the crystallisation temperature from $165°C$ for an undoped film to $115°C$ for a film doped with 8 atomic percent Bi. This compositional range also corresponds to

an order of magnitude reduction in crystallisation time. Since the material crystallises at lower temperatures, for increasing amounts of bismuth, the viscosity is expected to show a corresponding reduction. This is also in agreement with the crystallisation time reduction previously discussed; the Bi dopant decreases the viscosity and thus, by the Becker and Döring equation[152], provides an increase in the crystal growth rate.

An ellipsometric measurement was used to find the film's refractive index and extinction coefficient. The resultant refractive index and extinction coefficient was found by a trace through the plot of Δ and ψ. Since the film absorbs well at 532nm, the film was assumed to be infinitely thick for the fitting routine. The resultant refractive index and extinction coefficient was presented as a function of Bi content in figure 5.7. It can be seen that as the bismuth concentration is increased up to 13 at.%, a gradual reduction in the refractive index of the as-deposited state is achieved. At 13 at.% Bi, the refractive index is approximately 3, a reduction of 0.4 in comparison to the undoped film. The impact of bismuth on the extinction coefficient in the as-deposited state is minimal. After annealing the material at $180°C$, the refractive index is reduced by, on average, approximately 55%. Increasing the concentration of Bi in the crystalline state has a corresponding influence in the refractive index, increasing it from approximately 1.5 for the undoped film to 1.8 at 13 at.% Bi. Again the absorption of the film seems to show little sensitivity to Bi doping at this wavelength.

The fact that the amorphous refractive index is reduced with increasing Bi concentration is unexpected since doping with a larger atom should produce a more polarisable material. Also the increase in valence electrons associated with the Bi atom should also help increase the refractive index. This effect has been seen in other chalcogenides [155]. However, a possible explanation for this apparent reduction is that by incorporating the larger atom, structural changes occur. A similar effect has been noted for increasing the propotion of the heavy La atom in GaLaS. Bi is known to enter an amorphous chalcogenide structure with a coordination number of 6. Perhaps this addition effectively reduces stresses in the amorphous network since more bonds are available.

In comparisons to the resistivity of the GeSbTe compositions reported in chapter 4, the resistivity of $(Sb_8Te_2)Bi$ is orders of magnitude lower. This likely to be due to the low tellurium content permitting a low concentration of dangling bond, point defects[46] . However despite this low concentration, Sb_8Te_2 may still have a small proportion of charge traps that can be filled by introducing Bi atoms into the amorphous system. Adding Bi, which prefers to form metallic bonds[149], to Sb_8Te_2 reduces these charge traps permitting a strong, correlated reduction in the amorphous electrical resistivity; this is seen in figure 5.8.

Electrical phase change RAM (PCRAM) is reliant on the ability to amorphise materials at low electrical currents. Low Bi concentrations ($<$ 8 at.%) increases the electrical resistivity of the crystallised state of Sb_8Te_2. This would allow a reduction in the writing current for a possible electrical PCRAM device. A more realistic application suited to this materials is near-field optical recording. The material shows good optical contrast and since the crystallisation of Sb_8Te_2 is a growth dominated, the crystallisation time, scales with the laser spot size.

5.4.2 Composition Spread BiSbTe Films

To analyse the effect of Bi over a larger range of compositions, BiSbTe composition spread samples were successfully deposited by PVD using the combinatorial method described in section 2.7. The majority compositions seem to have been deposited in a crystalline state. This was clear from the XRD spectra in figure 5.18. It can be seen that there is a narrow amorphous zone with an approximate compositional coverage of 5%>Bi>25%, 48%>Sb>60% and 20%>Te>42%. The amorphous, sputter deposited, BiSbTe samples, described earlier, were possible at greater Sb concentrations. A plausible reason for this is that sputter deposition is a relatively cold process in comparison to the PVD, thermal evaporation technique. The PVD deposition vacuum is approximately 10^{-7}mB. At such low pressures, the substrate is not cooled by its atmosphere. Since the k-cells were at temperatures up to $700°C$, the affect of radiative heating cannot be ignored. It is known from table 5.1 that the peak crystallisation temperature of the $(Sb_8Te_2)_{100-x} : Bi_x$ composition is between $100°C$ and $163°C$ depending on the Bi concentration. It is thought that the samples would have crystallised during the deposition process. The fact that the GeSbTe sample didn't crystallise can be explained by the deposition process. The Ge sample is usually deposited by e-beam evaporation. In this process only a small volume of the target material is molten. A small molten well of the material is formed within the materials solid phase [73]. Therefore, the majority of the target is cold due to water cooling of the target holder; usually referred to as a 'hearth'. Further, Bi is known to have metallic-like bonding properties [149]. Thus to form amorphous films, metallic alloys usually require the substrate temperature to be orders of magnitude cooler than the melting temperature of the alloy. This is due to the non-directionality of the metallic bonds which enables the constituent atoms to settle into a crystalline arrangement with relative ease[73]. The other consideration with GeSbTe is the composition, usually the films were deposited with around 50 at.%Te such that compositions close to $Ge_2Sb_2Te_5$ could be studied. Te forms covalent bonds with Ge and Sb. Covalent materials have directional bonds which crystallise with less ease[73] than those with metallic bonding character, like Bi. Support of this statement can also be seen in figure 5.18(a). As the Te content is increased to approximately 20

at. %, an amorphous XRD spectrum (spectrum 4) is observed. After annealing these materials at $200°C$, a crystalline diffractogram was observed (spectrum 6).

Compositions close to the Sb_8Te_2 composition show the crystalline diffraction pattern given in spectrum 3 in figure 5.18. This spectrum was the only one which could be identified using the Inorganic Crystal Structure Database (ICSD)[135]. It showed peaks in the same position as the $Ag_{3.4}In_{3.7}Sb_{76.4}Te_{16.5}$ data storage material whose structure was reported by Matsunaga[151]. This diffraction pattern and composition is consitant with that reported for the sputtered films. Thus it was assumed that it also exhibits an A7-type structure.

The sheet resistivity as a function of composition was given in figure 5.15 for both the as-deposited and annealed states. Figure 5.15 shows the decrease in resistivity after annealing. There is very little change in resistivity apart from the compositional range 20%>Bi>45%, Sb>20% and 40%>Te>70%. The XRD spectra did not cover this compositional range but the 4 orders of magnitude reduction in sheet resistance after annealing at $200°C$ is believed to be as a result of a phase transition.

Compositional refractive index analysis of the as-deposited film is given in figure 5.16. It shows 30% refractive index increase, in comparison to the compositions outsie the range 20%>Te>40%, 50%>Sb>60% and 5%>Bi>25%. This difference corresponds well with the amorphous region (spectrum 4) found by XRD given in figure 5.18. After annealing at $200°C$ the refractive index for this region showed a vast change from approximately 3.2 to 1.2, the extinction coefficient also increased from 3.8 to 4.7. Compositions surrounding this zone showed a negligible change in the both refractive index and extinction coefficient. For optical data storage, the optical contrast in reflection is important. Therefore the increase in reflectivity has been calculated using the Fresnel coefficient for reflection at an interface, given by equation 5.1, before and after annealing.

$$R = \frac{[(n-1)^2 + k^2]}{[(n+1)^2 + k^2]} \tag{5.1}$$

These reflectivity coefficients were then used to calculate the increase in reflection after the phase change. This is plotted as a function of composition in figure 5.21. The crystallised region shows a clear 60% increase in reflected light after crystallisation. This large change in reflectivity would give sufficient contrast for possible implementation for optical recording media.

The static tester data, can also give an indication of the crystallisation time for this region of phase change. As discussed in section 4.4, the interference problems associated with the capping layer has made measurement of the minimum crystallisation time difficult. However, in figure 5.19, the nucleation time for this region has been found

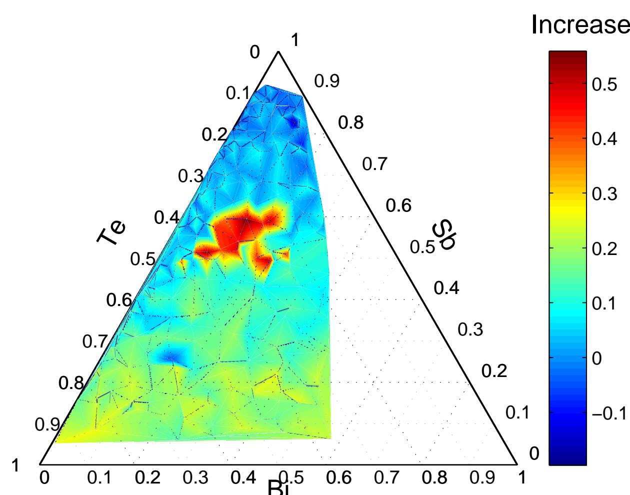

FIGURE 5.21: Increase in reflectivity factor as a function of composition for 532nm light at normal incidence

to be between 20ns and 30ns, whereas the time necessary for crystallisation is between 300ns and 550ns. Thus it is likely that these materials also show growth dominated crystallisation characteristics.

The affect of composition on the electrical resistivity and refractive index of amorphous BiSbTe has been difficult to establish due to the majority of film being deposited in the crystalline phase. Considering figures 5.14 and 5.15, it can be seen that, in the crystalline phase, the electrical resistivity shows a gradual, two orders of magnitude increase with increasing tellurium for low bismuth concentrations. For low tellurium concentrations and levels of bismuth greater than 10 at.%, as the concentration of Bi is increased, the crystalline resistivity also increases. In the crystalline state, there are very few charge carrier traps associated with point defects. The material shows electron, metallic like, conduction. As such, the electrons are sensitive to scattering and consequently the electrical resistivity may increase with impurities, small crystal grains and other scattering centres. The XRD spectra has revealed many crystalline phases throughout this region and therefore a possible explanation for the increased electrical resistivity is many different crystalline grains acting to scatter the electrons resulting in increased resistivity.

The refractive index as a function of composition was given in figures 5.16 and 5.17. To show the affect of tellurium and bismuth on the film's refractive index, the refractive index has been plotted in figure 5.22 as a function of tellurium for two different levels of bismuth, $<1\%$ and 10%. With the exception of between 30 and 45% tellurium, it is shown that the refractive index has little sensitivity to Bi doping in the crystalline state. This also supports the measurements made on the sputtered films. The tellurium however, does affect the refractive index, increasing it from approximately 1.2 to 2.2

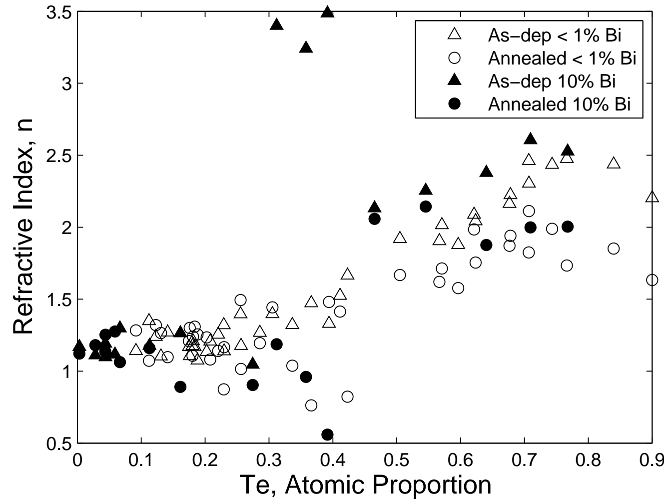

FIGURE 5.22: The refractive index as a function of tellurium for < 1% Bi and approximately 10% bismuth

between 30% and 60% tellurium. This is opposite to the case of the GeSbTe system discussed in chapter 4. This affect is not fully understood and is therefore a subject of future work.

From this compositional analysis of BiSbTe, it is difficult to judge the phase change properties for compositions close to the Sb:Te binary since these materials were deposited crystalline. However for the compositional range 5%>Bi>25%, 48%>Sb>60% and 20%>Te>42%, an amorphous region was deposited and stable. Its application to phase change data storage is now considered. The four orders of magnitude change in electrical resistivity is of sufficient contrast for a practical electrical device. The measurement of crystallisation time was inconclusive due to the problems associated with capping layer interference. However, it was possible to deduce that the system has a nucleation time shorter than 30ns whilst the crystallisation time was shorter than 300ns. However, the major drawback with this system is its low electrical resistivity in the crystalline phase, approximately $15\Omega Sq.$ which corresponds to $1.5^{-6}\Omega m$. This is two orders of magnitude lower than the electrical resistivity of the FCC phase for $Ge_2Sb_Te_5$[6]. Thus a large electrical current would be required to change its phase. This could clearly be reduced by moving to smaller phase change dimensions. However, the transistor dimensions, which are used to address the cells, will also be reduced and it is this transistor current which, ultimately imposes the maximum current which can be used to set a phase change cell.

5.5 Summary

It has been experimentally shown that the optical crystallisation of $(Sb_8Te_2) : Bi$ can occur in just 50ns. This material shows growth dominated crystallisation and therefore it has potential for shorter crystallisation times in a PCRAM device where the volume of the active material can be much smaller. The material showed two orders of magnitude reduction in electrical resistivity and this has been attributed to a reduction of the trapping states thus allowing metallic conduction. In the amorphous phase a slight increase in refractive index with increasing bismuth incorporation has been attributed to extended atomic bond lengths within the amorphous network.

Previous work has shown that a $Sb_{45}Te_{65}$ alloy will crystallise in the shortest time in relation to other proportions of the alloy. In this chapter it was demonstrated that the addition of Bi to much larger concentrations of Sb has far superior properties and decreases the crystallisation time by an order of magnitude. The general trends of Bi dopant in $Ge_2Sb_2Te_5$ seem to be consistent with this work in Sb_8Te_2; that is: for low concentrations of Bi the crystal structure is not affected and that the introduction of Bi reduces the crystallisation time and temperature. However in this case the reduced crystallisation time it is suspected to be due to a reduction in viscosity with increasing Bi whereas in $Ge_2Sb_2Te_5$, which has a nucleation dominated crystallisation mechanism, bismuth tends to decrease the crystallisation activation energy. Upon crystallisation the material crystallised into an A7-type structure. This structure is consistent with that reported for the well known optical data storage material ($Ag_{3.4}In_{3.7}Sb_{76.4}Te_{16.5}$)[151].

Combinatorial analysis of the BiSbTe system for low bismuth concentrations has been performed. A stable amorphous region, of composition in the range 20%>Bi>45%, Sb>20% and 40%>Te>70%, was found by XRD. This region showed relatively fast nucleation times, the time necessary for crystallisation was found to be less than 300ns. A four order of magnitude reduction in electrical resistivity was also found after annealing at $200°C$. The low crystalline resistivity of this material deems it unsuitable for electrical phase change ram devices. Other regions which were amorphous when sputter deposited, were crystalline when deposited by PVD. This is most likely due to the heat generated during the deposition process.

Chapter 6

Ga:La:S phase Change Materials

6.1 Introduction

Sulphide-based phase change materials using a number of physical methods have shown potential as the active medium for data storage. These mechanisms include storage of charges within deep levels in the semiconductor band-gap [156], sulphurization of metallic elements in the film [157] and structural phase transitions [158]. GLS materials are known to be stable in both their crystalline and amorphous phases [159]. The covalent bond strength of chalcogen atoms is greatest for sulphur and is reduced through selenium and is lowest for tellurium [16]; this allows a corresponding reduction in the materials' glass transition temperature. Generally for phase change data storage, tellurium based materials are chosen [63] since they are good glass formers and have a lower glass transition temperature than sulphides and selenides [16]. However, as one moves down the periodic table from sulphur to tellurium, the atomic bonds become more metallic and isotropic, the energy gap decreases and electronegativity decreases, resulting in a material with higher electrical conductivity. Phase change materials, with a high electrical resistivity in the crystalline phase, are desirable since the electrical current required to Joule heat them can be low. This becomes increasingly important as the device dimensions are reduced, for instance, since the size of the transistor used to address the phase change RAM (PCRAM) cell is also reduced, the maximum current that can be supplied to the cell is limited by the transistors current passing capacity. The high glass transition, T_g, peak crystallisation, T_p, and melting, T_m, temperatures of sulphide and selenide chalcogenides clearly means that more heat energy is needed for phase change. However cell dimensions of sub-100nm in diameter are now possible and these high temperatures are achievable. Using novel line-type cell design, interface reactions can be limited and an increased quench rate [6] is possible. With this in mind, Ga:La:S material is proposed as a novel phase change material.

Gallium Lanthanum Sulphide (GLS) is a chalcogenide material which was first reported by Lozach et al. in 1976 [160]. In a glassy phase it is a semiconductor with a band-gap of 2.6eV, corresponding to a wavelength of 475nm [24], consequently GLS glass takes a deep orange colour. GLS has many useful properties. Initially the low phonon energy of these glasses attracted significant interest as a host for near- and mid-infrared emitters with applications in telecommunications and sensing. In addition, their large nonlinear refractive index has also led to investigation of active waveguides, switches and routers [24]. Other important properties of this material include: (a) its ability to exist in both glassy and crystalline forms[161, 159], (b) that ultraviolet radiation can be used to induce photo-compaction and photochemical changes (hence the demonstration of directly written surface structures such as waveguides[24]) and (c) it is an excellent rare earth host. Indeed lanthanum itself is a rare earth element and lends GLS to the possibility of achieving infrared lasers and optical amplifiers.

As with all the chalcogenides reported in this thesis, the phase of the bulk is determined by two key factors: (1) the material composition and (2) the rate at which the molten material is cooled. These variables can be controlled to manipulate the final phase of the material. Until now there have been no reports of the speed at which this material crystallises.

The structure of the glass consists of Ga-S bonds, with a length of $2.26\AA$, and La-S bonds of length $2.93\AA$. It has been reported that the Ga-S distances in the glassy state are identical to those in the crystalline state [28]. Therefore it is only necessary to change the bond angles and, thus, it is hypothesised that GLS has the potential to be a fast switching phase change material.

In the Ga_2S_3 crystal (see figure 6.1) it should be noticed that two out of three sulphur atoms (S_1 and S_2) are each bound to three gallium atoms. These sulphur atoms have two normal covalent bonds to two of the gallium atoms. The third Ga-S bond is dative or coordinate covalent (one of the atoms provides both electrons). The third sulphur atom, S_3, is bound to just two gallium atoms and is thought to be a bridging atom. The average sulphur coordination number is greater than two; sulphide glasses usually have coordination numbers less than two. Experimentally, Ga_2S_3 has not been observed in a glassy state. There exists a GaS_4 unit within the Ga-S crystal; it has been noted as the glass former. The La-S bond is ionic and likely to be a network modifier. By adding an ionic sulfide to the crystal, like La_2S_3, it is possible to modify the crystalline Ga_2S_3 into a vitreous structure. Of all the rare-earth sulphides, lanthanum gives the largest extent of vitreous compositions [28].

The effect of adding an ionic sulphide modifier (like La_2S_3) molecule to the crystal is to break one of the Ga-S dative bonds and replace it with a S^{2-} anion. This anion links

the gallium atom such that its tetrahedral environment is not altered, but what was a tri-coordinated S atom now becomes a di-coordinated bridging atom. This is illustrated by figure 6.2. This process creates a negative void which can then be filled by a La^{3+} cation. Electrically, the effect of adding La_2S_3 is to give the glass an essentially ionic character [28]. Ionic conduction in GLS is covered in section 6.2.3 of this report.

Oxides are generally resistant to crystallisation and slow cooling rates are necessary to create crystalline structures. Materials that are ionic in nature tend to produce crystals, whereas those with covalent bonding structures produce glasses[28]. In the past is has been necessary to increase the glassy qualities of GLS whilst retaining its IR optical transmission performance[24], thus oxides (La_2O_3) were added to the material in order to stabilise the glassy network and hence decrease the possibility of crystallisation [24].

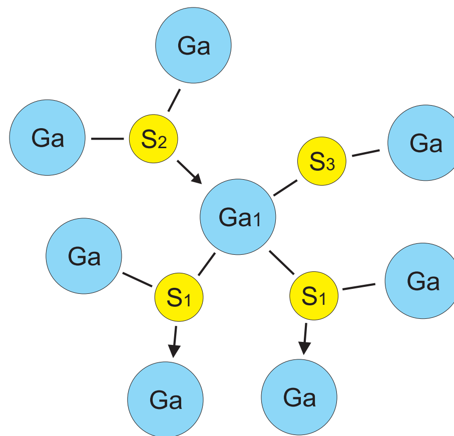

FIGURE 6.1: The covalent Ga_2S_3 crystalline network [28]

From investigations of stable Ga:La:S compositions[24] for fibre fabrication, bulk glass forming compositions are achieved for $GaS_{1.4}$ molar proportions ranging from approximately 60% to 77.5% and La_2S_3 ranging from 16.5% to 37% with the remainder 3 to 6% being La_2O_3. It was experimentally confirmed that increasing the La_2O_3 content also increases the range of $GaS_{1.4}$ proportions which form glassy bulks. However, for fibre fabrication it was not deemed advantageous [24]. For phase change applications, the amorphous film needs to be crystallised with as little input energy as possible; whilst the crystalline phase should be easily changed back into an amorphous structure. Clearly, optimising the balance of network stabilisers (La_2O_3), crystalline network modifiers (La_2S_3), and glass formers (GaS_4) is of great importance to make a fast crystallising, efficient and stable phase change memory device.

La_2O_3 and other oxides could prove to be useful components of future phase change Ga:La:S compositions. R. Li et al. reported the formation of two crystal phases (phases A & B) in crystallised GLS glasses [161]. The dominating crystal phase was highly

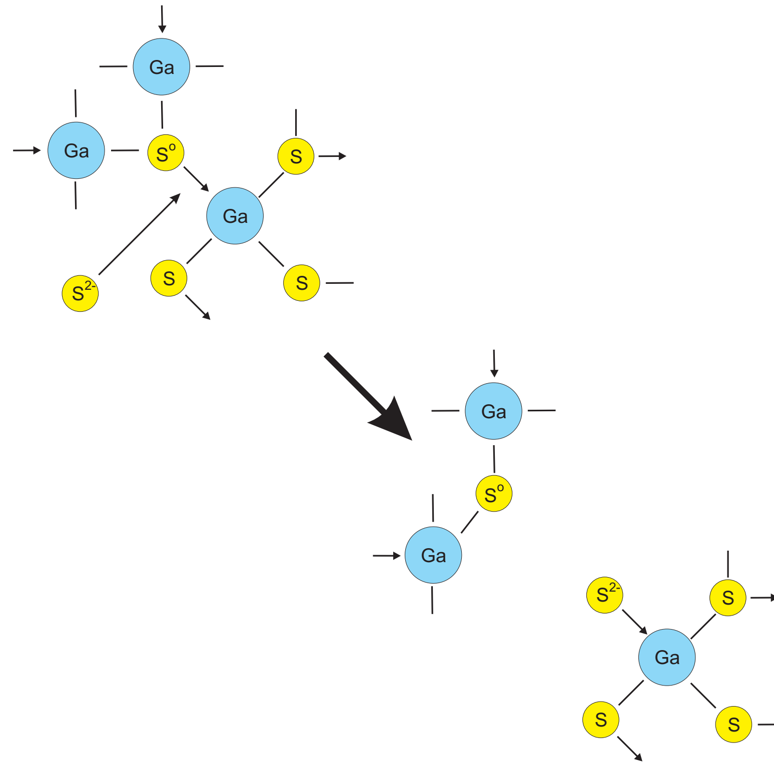

FIGURE 6.2: Effect of La_2S_3 on Ga_2S_3[28]

dependent on the amount of oxygen. In fact, for Ga:La:S materials with a gallium-lanthanum molar ratio of 7:3 and containing less than 0.49 wt% oxygen, it is only possible to form crystal phase A. For oxygen contents between 0.49 and 1.30 wt% both A and B phases are possible. And for GLS with significant proportions of oxygen, ($\geq$ 2.12 wt%) only crystal phase B is formed. It was also noted that for oxygen content ranging between 0.49 and 1.30 wt%, two of the glasses analysed showed crystal growth of both phases occurring simultaneously, and not one followed by the other; as one might expect for two independent phases. This suggests a possible eutectic crystal growth of phases A and B[161] and highlights the importance of oxides in the formation of GLS glasses, which can exist with different crystal phases.

Early research into the compositions of GLS and GLSO [162] found the eutectic point for GLS and GLSO to be approximately 0.79(Ga_2S_3)0.21(La_2S_3) and 0.9(Ga_2S_3)0.1(La_2O_2S) respectively; this is shown in figure 6.3. It is possible to dope Ga:La:S with other metals, this should allow for some tailoring of its data storage properties.

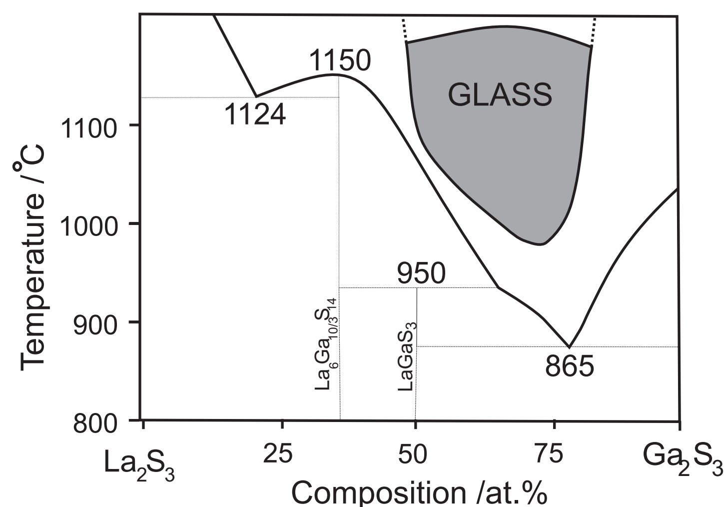

(a) Ga_2S_3-La_2S_3

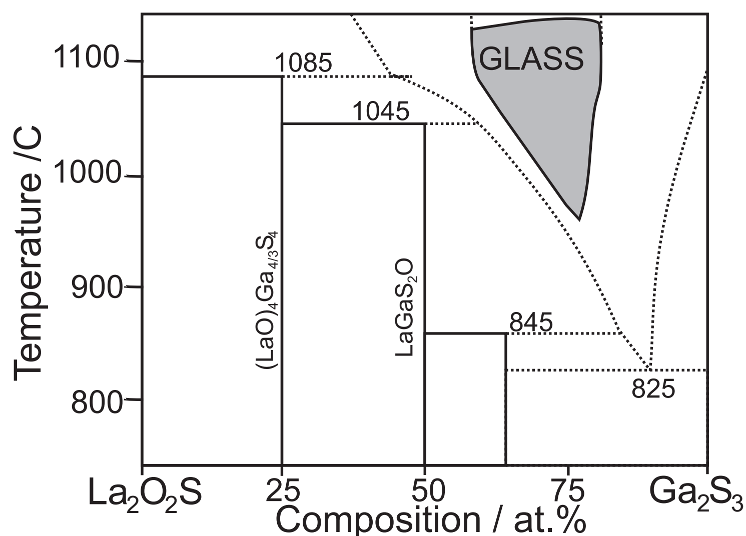

(b) Ga_2S_3-La_2O_2S

Figure 6.3: Phase Diagram for (a) Ga_2S_3-La_2S_3 and (b) Ga_2S_3-La_2O_2S systems. The shaded area shows bulk glass forming compositions. (Redrawn from Flahaut et al.[162]).

6.2 Bulk Ga:La:S Glasses

6.2.1 Synthesis

The fabrication of gallium lanthanum sulphide is achieved through melting a mixture of gallium sulphide and lanthanum sulphide precursors. Often, in the production of GaLaS glasses, lanthanum oxide is also added as a network stabiliser [163, 24].

The precursor materials are loaded into vitreous carbon crucibles whilst in a controlled nitrogen environment. They are then transferred (using a nitrogen atmosphere 'transfer pod') into a dry argon purged furnace. At this point the furnace is heated from room temperature to 1150°, normally at a temperature increase of $15°C$ per minute. The samples are held at $1150°C$ for 24 hours. They are then pushed into a water cooled jacket; this quenches the 'melt' into a glass. Unlike the $Ge_2Sb_2Te_5$ phase change data storage material, amorphous structures of these materials can form with relatively modest quench rates. Once the glass has cooled to room temperature it is then annealed. The Ga:La:S bulk is removed from the crucibles and placed in vitreous carbon boat. Once again this is placed into the furnace and heated to 550°C at a rate of 0.5°C per minute and then held at 550°C for 6 hours before being cooled down to room temperature at 0.5°C per minute.

The optical and electrical properties of Ga:La:S materials are highly dependent on the purity of the precursors. There are commercial suppliers of gallium sulphide, lanthanum sulphide, lanthanum oxide and lanthanum fluoride. However, these materials are unsuitable for fabrication of optical glasses due to their levels of impurities (purity $<$ 99.999%)[24]. To reach the levels of purity required for optical glasses, in-house production of $GaS_{1.4}$ and La_2S_3 is performed through sulphurization. Whilst the purity of La_2O_3 and LaF_3 is increased by heat treatment in a flowing dry argon atmosphere at $1250°C$. A key advantage of a flowing reactive atmosphere is its ability to sweep reaction by-products out of the reaction hot-zone and thus prevent them from reacting[164]. The composition of the resultant material is assumed to be equal to the atomic proportions of the precursor materials; this assumption is only really valid for a closed melt environment. However, as mentioned, a flowing system is usually used to synthesise the glasses since such methodology has purity benefits. Thus when the composition of the material was considered to be very different from the constituent molar proportions, EDX was performed. A good measure of whether the material can be considered to have the same composition as its constituents is the weight loss after melting.

6.2.2 Thermal Properties of Ga:La:S Bulk Samples

Over many years, the thermal properties of many Ga:La:S samples with varying compositions and dopants have been studied. The characteristic temperature measurements made on these samples have been examined and collated. Measurements on these samples were always presented as a function of the constituent precursors rather than the actual atomic composition. For this work, it was deemed useful to know the role or effect of individual elements rather than the precursors, thus figure 6.4 presents the glass transition temperature (a) and peak crystallisation temperature (b) of 21 different Ga:La:S glassy samples on a ternary diagram. It can be seen that there is a general trend of

increasing glass transition temperature and decreasing crystallisation temperature, as the gallium content is increased. Over this small compositional range the sulphur has little effect, thus the glass transition temperature, peak crystallisation temperature and melting temperature of all 21 samples is plotted as a function of Ga/La in figure 6.5.

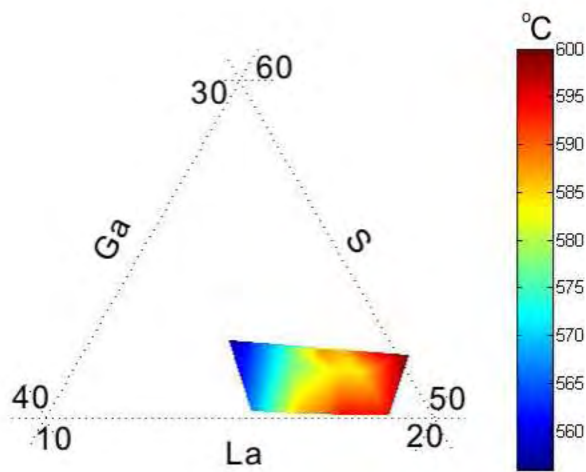

(a) Tg

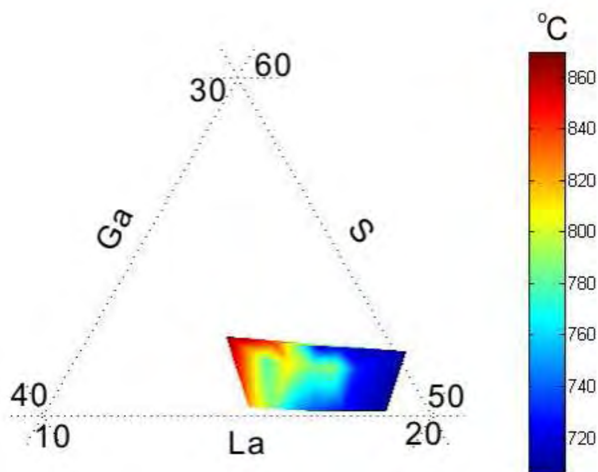

(b) Tp

FIGURE 6.4: Glass transition (T_g), crystallisation (T_p) and Melting (T_m) temperature ($°C$) as a function of composition.

There have been limited studies of crystallisation activation in amorphous GLS bulks. R. Li and A. B. Seddon have reported high crystallisation rates when GLS glass is heated to temperatures between 620 and 660° but no quantative studies of crystallisation activation energies were performed. The crystallisation activation energy has been studied

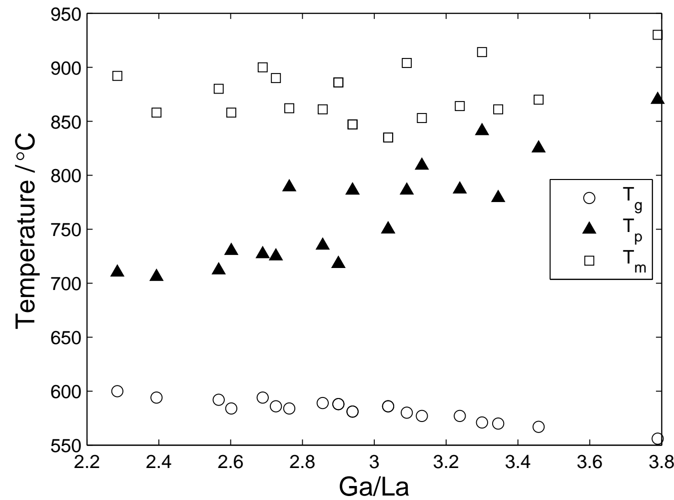

FIGURE 6.5: Glass transition (T_g), crystallisation (T_p) and Melting (T_m) temperature as a function of Ga:La ratio.

using the Kissinger analysis, described in section 2.8.5. The measurement is presented in figure 6.6. The activation energy was measured to be 3.4eV.

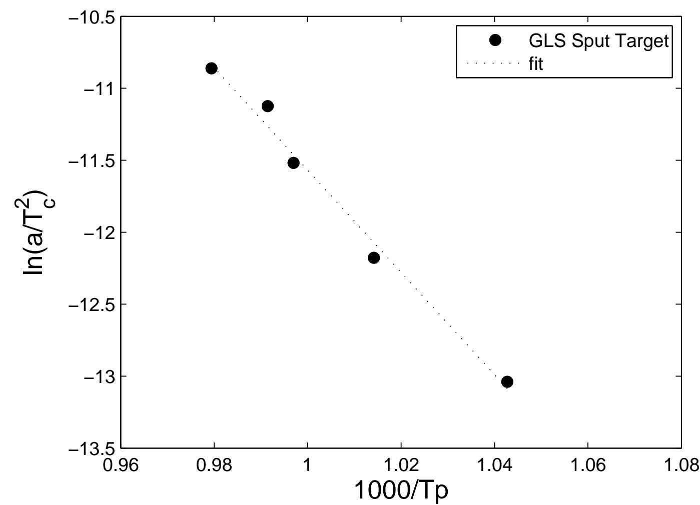

FIGURE 6.6: Arrhenius plot used in Kissinger analysis to calculate the crystallisation activation energy of GaLaS glass

For fast crystal growth materials with a low viscosity are sought. The viscosity of GaLaS and GaLaSO glasses have been measured using a Perkin Elmer TGA-7 by D.Brady [164]. For this work, the viscosity of different compositions has been compared at $640°C$. This temperature was chosen since it is between the glass transition and peak crystallisation temperatures of all the samples in figure 6.5. It is clear in figure 6.7 that the viscosity decreases with gallium concentration. This is also is suggested in figure 6.5 by the fact that the separation between T_g and T_x decreases[24] with increasing gallium .

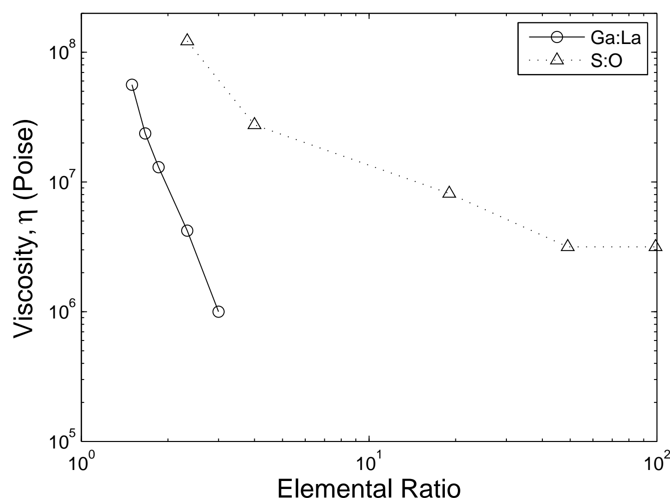

FIGURE 6.7: Viscosity as a function of Ga/S and S/O at 640°C

6.2.3 Electrical Properties of Bulk Ga:La:S Glasses

Ga:La:S discs, 1mm thick, were fabricated by the methodology described in section 6.2. The batch atomic composition of the discs was $(GaS_{1.4})_{70}$: $(La_2S_3)_{24}$: La_2O_{36-x} : $(Ag_2S)_x$ where samples were fabricated for $x = 0.05$, 0.1 and 0.3. The electrical resistivity of the GLS discs was measured using a Glassman High Voltage (FC series) DC source capable of generating 30kV and a 2400LV Keithley amp-meter. The set-up is shown in figure 6.8. The voltage was increased by 500V increments, every 30s, up to a maximum of 7kV. The current was measured by the Keithley meter and data was sent to a computer. Figure 6.9 shows the current response over the 30s intervals for samples 1, 2 and 3 at room temperature. The average resistivity over the 30s interval has been plotted and is shown in figure 6.10. Measurements were repeated in the same sample with a guard electrode surrounding the high voltage anode, this ensured that the effect of surface current could be eliminated. These measurements are also plotted on the same axes.

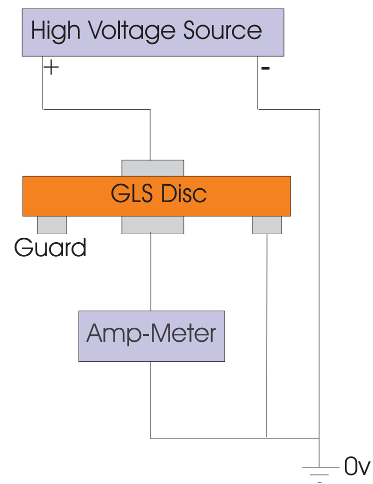

FIGURE 6.8: The experimental setup used to measure the current as a function of voltage

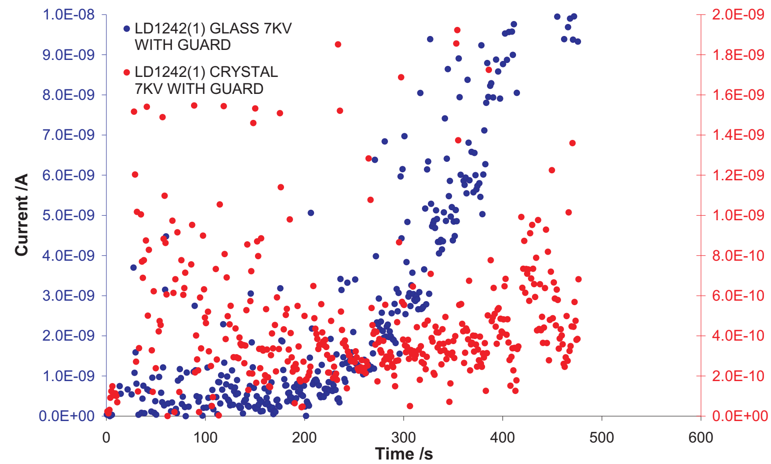

(a) Sample 1 (0.05% Ag_2S)

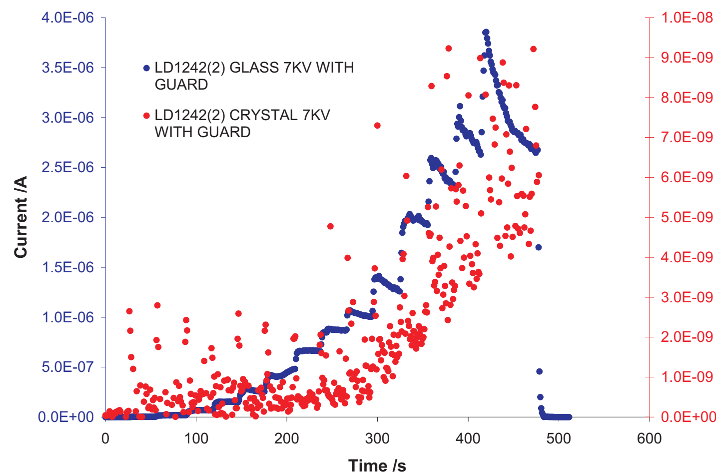

(b) Sample 2 (0.1% Ag_2S)

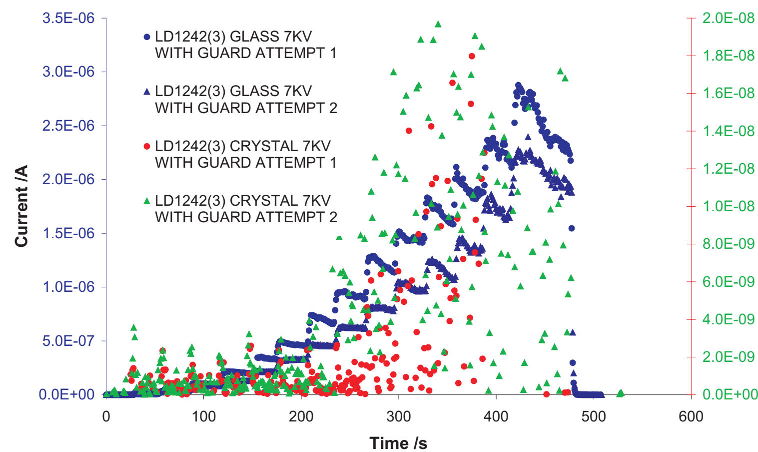

(c) Sample 3 (0.3% Ag_2S)

FIGURE 6.9: Samples 1, 2 and 3 glass and crystalline current for 500V increments at 30s intervals. Blue shapes- glassy discs, red and green shapes- crystalline discs. For multiple measurements; circles- 1st measurement, triangles- 2nd measurement

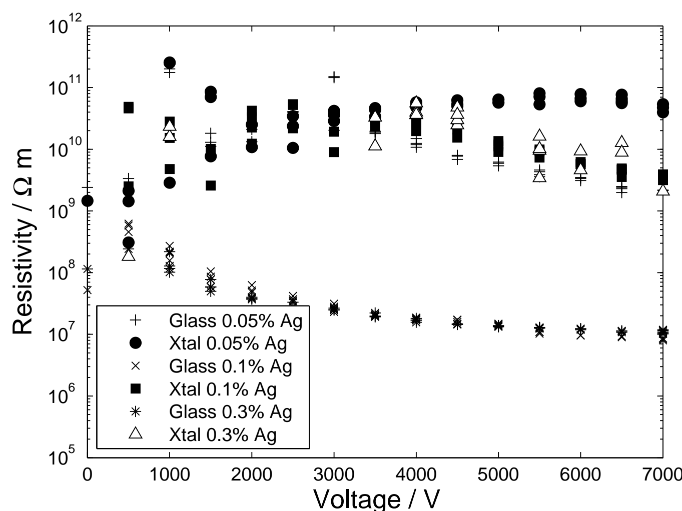

Figure 6.10: Average resistance of GaLaS glasses and crystalline samples for 3 different Ag concentrations. The resistivity was measured over a 30s period for each 500V increase.

The crystalline resistivity of these materials is higher than the amorphous phase resistivity. Indicating that the crystalline phase may not be behaving with metallic conduction like the other Te materials studied. To give possible insight into the conduction mechanism, ultraviolet, visible and near infrared absorption spectra of the bulk samples were measured with the dual beam Cary 500 spectrophotometer. The absorption spectra are given in figure 6.11.

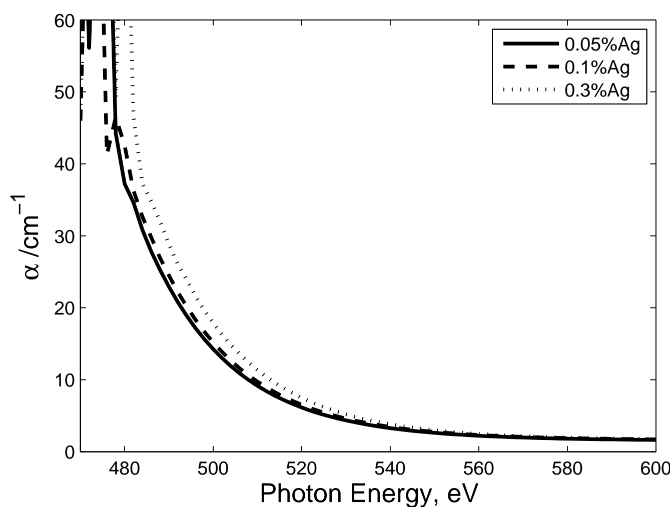

Figure 6.11: Absorption spectra of Ag doped GaLaS at the electron band edge.

.

From this absorption spectra, the optical band-gap of the material has been calculated using Tauc analysis. Generally, the absorption coefficient, α, of semiconductors follows equation 6.1.

$$\alpha hv = C(hv - E_g^{opt})^r \tag{6.1}$$

where h is Planck's constant, v is the photon frequency, C is a constant and E_g^{opt} is the optical band-gap. The exponent r is dependant on whether the semiconductor is direct or indirect. An indirect transition occurs when the maximum of the valence band and the minimum of the conduction band occur at different values of k. When an electron absorbs a photon both energy and momentum must be conserved. If the momentum of the photon is much smaller than the momenta of the conduction band electrons, the electron can only be promoted to the conduction band by higher energy photons with sufficient energy to free the valence electrons. However, in indirect transitions, the large momentum and low energy phonons within the crystal supply additional momentum to the electron simultaneously to the electron absorbing a photon, thus satisfying the energy and momentum for absorbtion [141]

Tauc and co-workers showed that for indirect transitions, $r = \frac{1}{2}$ but for direct transitions, $r = 2$ [165]. In amorphous semiconductors, the lack of crystal structure, removes the possibility of phonon momentum; thus the transition must be direct and $r = 2$. The optical energy gap, E_g, can be found from equation 6.1, such that $(\alpha hv)^{\frac{1}{2}} = Chv - CE_g^{opt}$ and plotting $(\alpha hv)^{\frac{1}{2}}$ against $hv - E_g^{opt}$ and then extrapolating the curve to zero, gives the energy of photons.

Thus for this analysis of a glassy GLS a value of $r = 2$ was chosen and for the crystalline state $r = 1/2$ in equation 6.1. This is consistent for those of other phase change alloys[166]. To show the linear fits for r=2 and $r = 1/2$, figure 6.13 has been included.

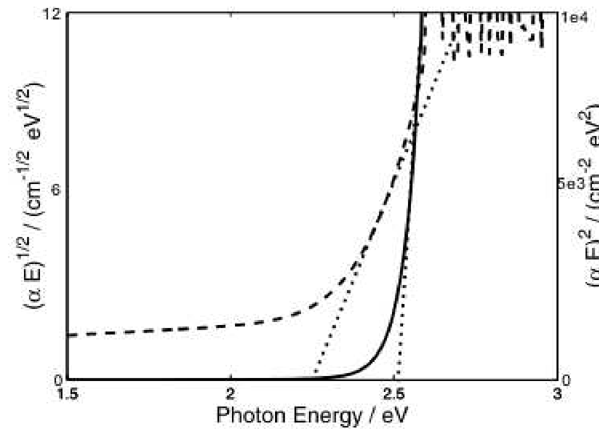

(a) Assuming (r=2)

FIGURE 6.12: Tauc analysis to calculate the electronic band-gap of Ga:La:S glass. For dashed line use left y-axis for solid line use right y-axis.

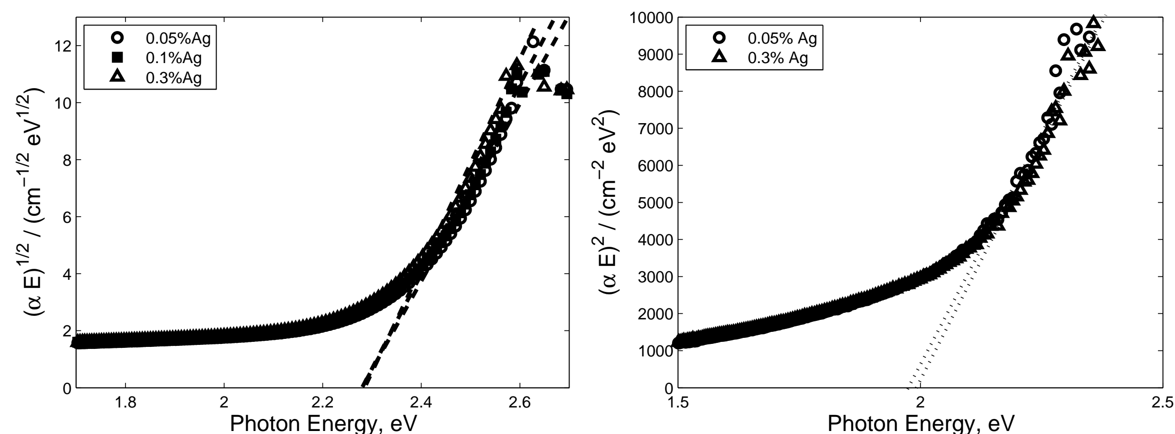

FIGURE 6.13: Tauc analysis of (a) glassy and (b) crystalline Ga:La:S bulk materials

From figure 6.13 a linear fitting procedure was used to calculate the band-gap of the GaLaS glassy and crystalline materials. In the glassy state the material's electronic band-gap, E_g, was found to be 2.29, 2.30 and 2.28eV for the samples doped with 0.05%, 0.1% and 0.3% Ag. For the crystalline state the band-gap was reduced to 1.99eV and 2.06eV for the samples doped with 0.05 and 0.3 % Ag.

6.3 Ga:La:S Thin Film Deposition

6.3.1 Ga:La:S Pulsed Laser Deposition

Pulsed Laser Deposition (PLD) was used to deposit GLS films more than a decade ago [5-7]. Rapid quench rates are inherent to the PLD technique, through condensation of the vapour phase onto room temperature substrates. The small thermal mass of the vapour allows much greater quench rates to be realised compared with that of the water cooled jacket which was used to quench bulk glasses. This allows the possibility of extending the amorphous compositional phase outside the conventional bulk glass compositional range.

In this section experiments have been performed using PLD in an effort to synthesise and explore new compositions of Ga:La:S amorphous materials which would normally be unfeasible through water cooling of a molten bulk. Compositional analysis of the Ga:La:S system for both nanosecond and femtosecond PLD regimes is presented in this section. The elemental ratios of Ga, La and S have been controlled by the careful selection of the deposition parameters. By varying the Ga:La:S ratio, the effect on the optical and crystallisation properties of bulk GaLaS is explored.

Both nanosecond and femtosecond PLD experiments were conducted in the same vacuum chamber, with an argon ambient gas pressure ranging between 2×10^{-4} mbar and 2×10^{-1} mbar. The target was rotated spirographically in order to increase the usable target area during a deposition run. For the femtosecond PLD experiments, a Ti:sapphire laser was used to ablate the target material with 130 fs pulses at a wavelength of 800nm operating at a repetition rate of 1kHz. The fluence was varied by adjusting the position of a focussing lens to alter the incident spot-size on the target's surface. The spot-size itself was measured using the knife-edge technique. All depositions were conducted for a duration of 5 minutes and all films were deposited at room temperature. The nanosecond PLD experiments were conducted in the same vacuum chamber using a frequency-quadrupled Nd:YAG laser (at 266 nm)with repetition rate of 10 Hz. GaLaSO was deposited on silicon, CaF2 and quartz substrates under both regimes. To investigate the effect of off-axis deposition on the stoichiometry of the film, a larger Si substrate (8 cm x 1 cm) was used.

The target material was synthesised from high purity $GaS_{1.4}$, La_2S_3 and La_2O_3 precursor materials, according to the method described in section 6.2. The precursor material 72.5 $GaS_{1.4}$ - 21.5 La_2S_3 - 6 La_2O_3 (molar %) was batched into a vitreous carbon crucible under a nitrogen atmosphere. Each glassy target was formed by melting the load inside the crucibles at $1150°C$ in a flowing argon atmosphere for 24 hours and then quenching in a water-cooled jacket. In order to remove stresses from the targets, the resultant glass was then annealed for 6 hours at $550°C$ before cutting and polishing to an optically flat surface.

The composition of the resultant samples was determined by the EDX technique, described in chapter 2. Compositional measurements for each sample were taken at the centre of the film (where the film depth was greatest). For analysis of off-axis deposition, measurements were taken over a range of distances, along the surface of the film, up to 20mm from the centre. An X-ray diffractometer (Siemens D5000) was used to investigate the crystallinity of the films. Film thicknesses were determined using a P16 surface step profiler.

The film's composition dependence on deposition conditions for ns and fs films are given figures 6.15 and 6.14. The figures show all the compositions synthesised and how they relate to their target composition and the bulk glass formation region.

Composition coverage of a single deposition was also analysed by depositing onto a large silicon substrate for 5 minutes at 5×10^{-4} mBar with a fluence of $2.0Jcm^{-1}$ and a target substrate separation of 25mm. The samples were measured with EDX spectroscopy and the ternary is given in figure 6.16.

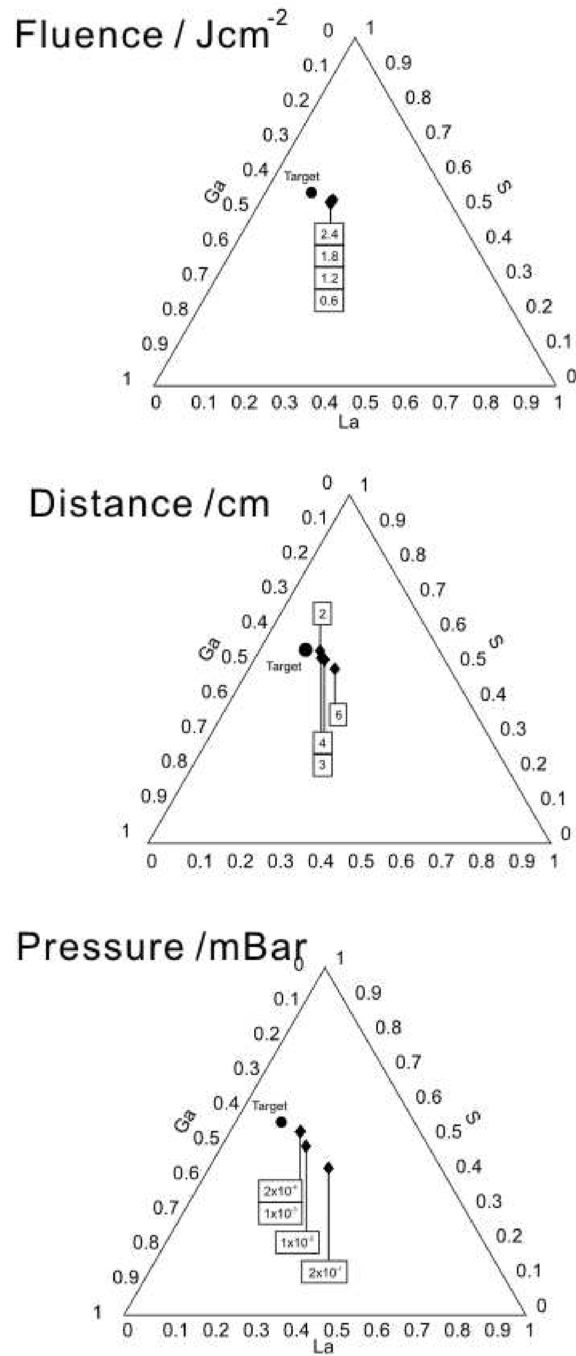

FIGURE 6.14: Ternary diagrams showing the effect of fluence, material path length and deposition pressure on the resultant films' composition for films deposited by nano-second pulsed laser deposition.

The ultraviolet, visible and near infrared transmission spectra of the films was collected using the Perkin Carey 500 photospectrometer. The films depths were measured with the P16 profiler. The depth data was used in conjunction with the transmission spectra

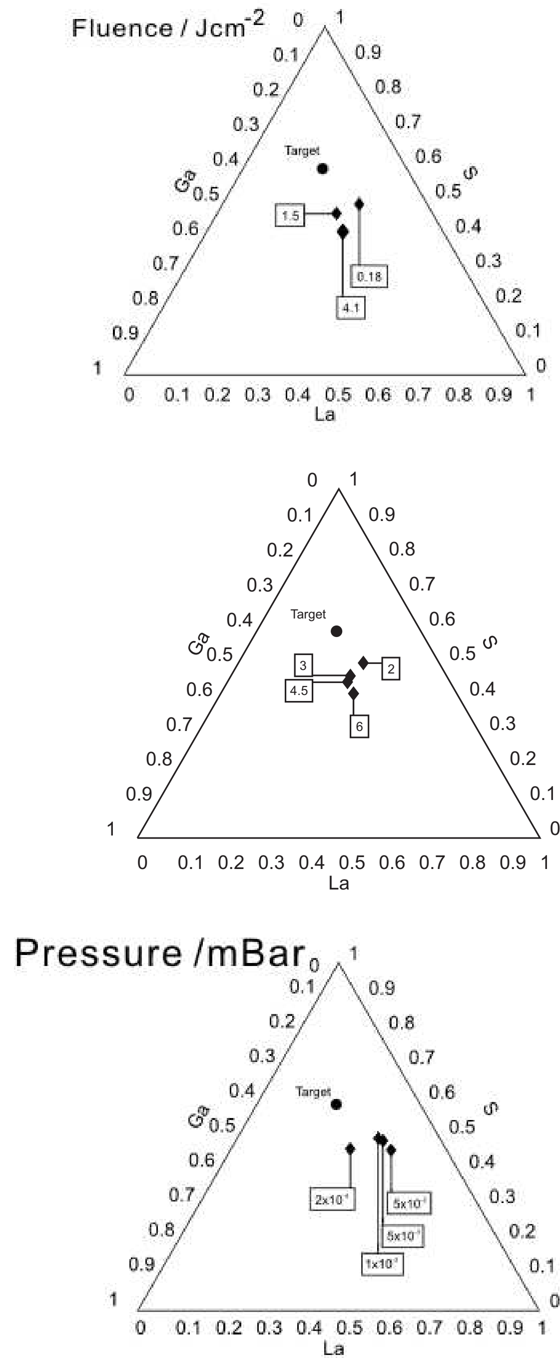

FIGURE 6.15: Ternary diagrams showing the effect of fluence, material path length and deposition pressure on the resultant films composition for films' deposited by femtosecond pulsed laser deposition.

to calculate the energy gap of the films by Tauc analysis. The Tauc plots are given in figure 6.17. The calculated energy gap, E_g, was mapped in ternary space using the composition data collected by EDX. This is given in figure 6.18.

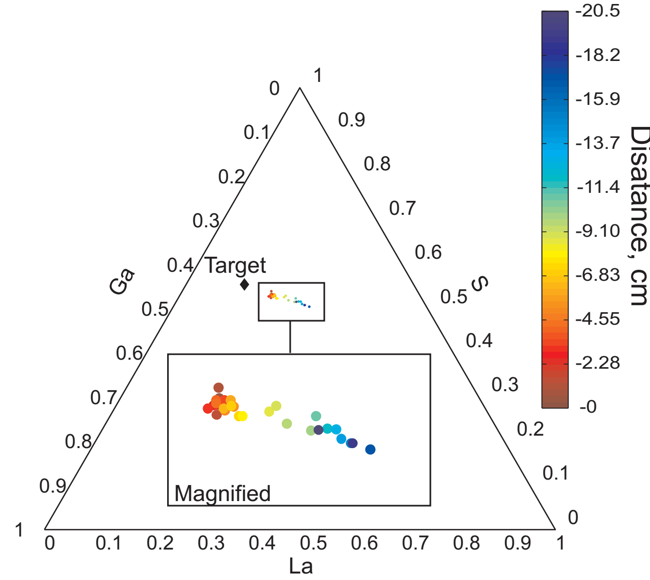

FIGURE 6.16: Composition spread across a single silicon substrate for an off axis deposition from a Ga:La:S target.

The refractive index of the films was calculated from the 'single transmission technique'[167]; that is, refractive index dispersion can be measured by interpolating along the upper and lower interference fringes which occur due multiple reflections at the interfaces of transparent media. The refractive index is calculated according to equation 6.2. This technique was chosen over ellipsometry due the film's low absorption at 532nm; the wavelength of the imaging ellipsometer. Although it is normal to measure transparent films, an accurate measurement of the film depth at the analysis point is required. Since the film's depth profile is not uniform, the single transmission measurement, which can be performed without the additional knowledge of depth, allows measurement of refractive index free from the introduction of additional error sources.

$$n = \sqrt{N + \sqrt{N^2 + s^2}} \tag{6.2}$$

Where $N = 2s\frac{T_M(\lambda)-T_m(\lambda)}{T_M(\lambda)T_m(\lambda)} + \frac{s^2(\lambda)+1}{2}$, $s(\lambda)$ is the refractive index of the substrate and can be calculated according to $s(\lambda) = \frac{1}{T_s(\lambda)} + \sqrt{\frac{1}{T_s^2(\lambda)} - 1}$, $T_s(\lambda)$ is the transmission of the substrate, $T_M(\lambda)$ is the maximum interpolated transmission value, $T_M(\lambda)$ is the minimum interpolated transmission value. The dispersion accuracy of this method is determined by the interpolation. If the frequency of peaks is high, the accuracy is also high and is said to be within ±1nm. The maximum absolute accuracy of T_M and T_m is ±0.001 [168].

The electrical resistance of GLS films synthesised by ns-PLD has been measured. However, the resistivity of these materials was too great for the four point probe set-up, hence a chip with a sandwich structure was fabricated. The GLS PLD film was deposited on top of a series of ten chromium electrode strips (1mm by 50mm by 200nm). Each electrode strip was separated by 5mm. After deposition of the GLS film, the top, Cr, electrode was evaporated using an Edwards coater. The structure was coated with photoresist and once again 1mm wide strips were defined. An Oxford instruments Reactive Ion Beam Etcher (RIBE) was used to dry etch the exposed Cr to leave a series of ten, top electrodes in the GLS film surface. A photograph of the resultant structure is given in figure 6.20.

The I-V characteristic of each cell sandwich was measured using a Keithley 238 electrometer. The electrometer was programmed to increase the voltage in 1V steps and measure the current flowing through the sample for 100ms. The electrical resistivity of the material was calculated from the measurements. The spread in resistivity as a function of position on the chip is plotted in figure 6.21. Black circles have been included to show that some of the cells tested switched to a lower resistivity phase.

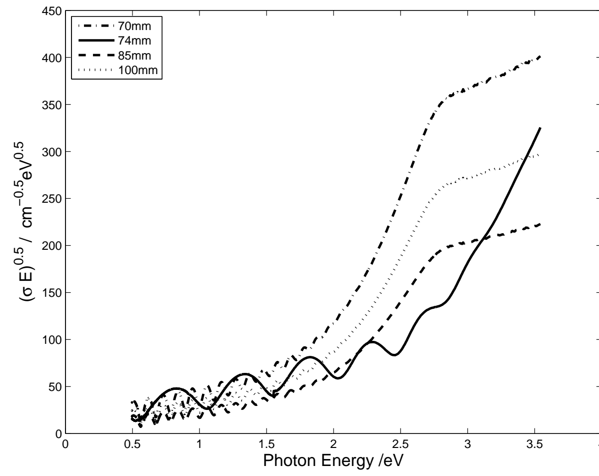

(a) Fluence

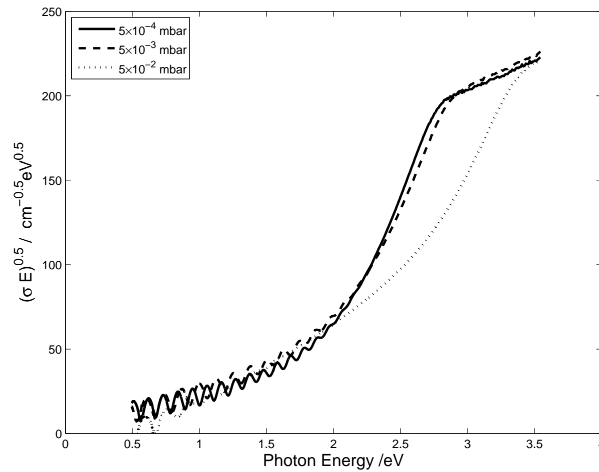

(b) Pressure

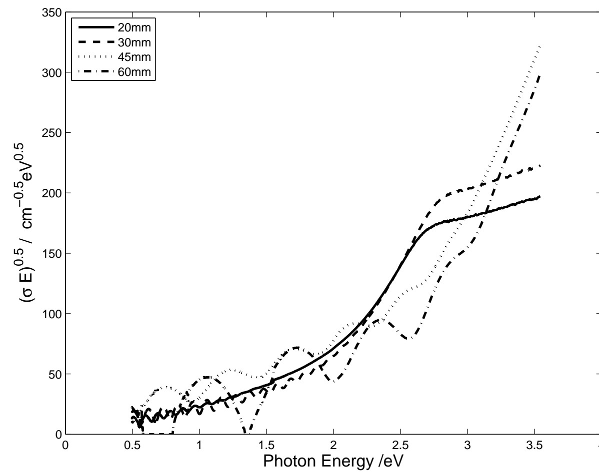

(c) Path distance

FIGURE 6.17: Tauc Analysis of GaLaS films prepared by femto-second pulsed laser deposition under different conditions

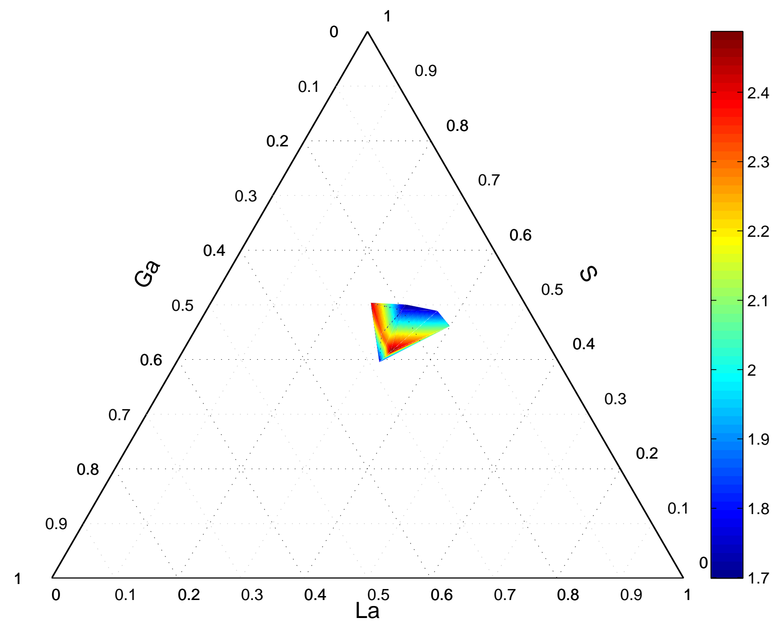

FIGURE 6.18: Optical band-gap, E_g, of Ga:La:S thin films deposited by femto-second and nano-second pulsed laser deposition

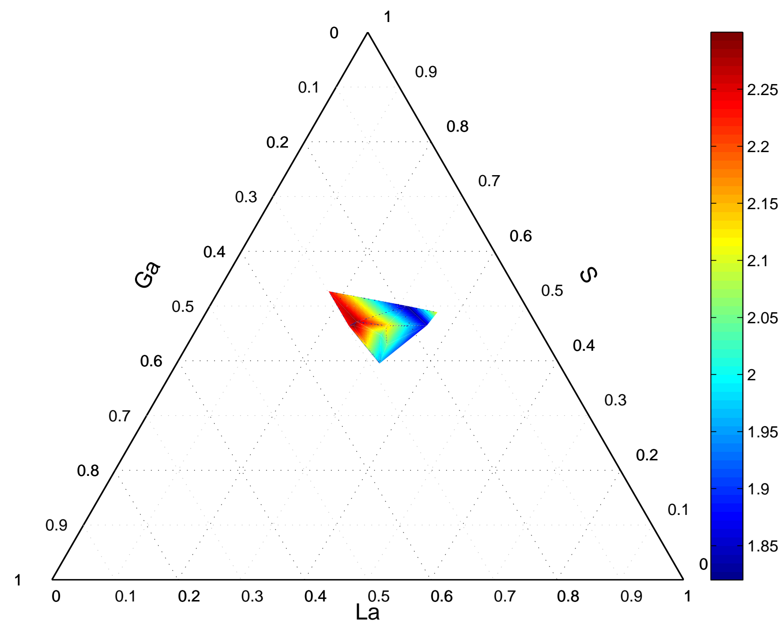

FIGURE 6.19: Refractive index at $1.5\mu m$ of Ga:La:S thin films deposited by femto-second and nano-second pulsed laser deposition

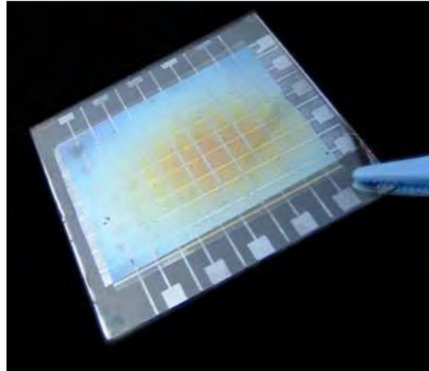

FIGURE 6.20: GLS PLD electrical test structure

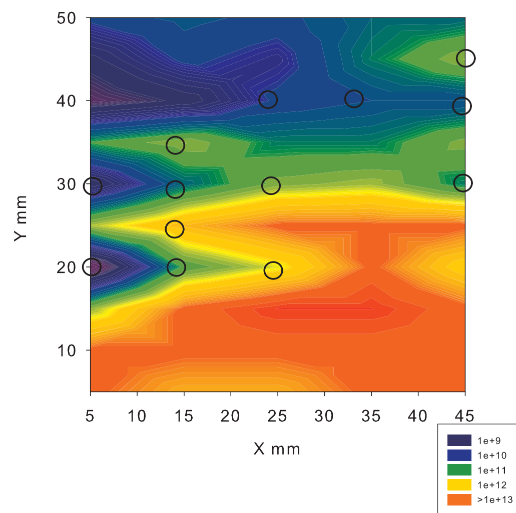

FIGURE 6.21: Electrical resistivity of GLS prepared by nanosecond PLD as a function of position on the substrate. Circles indicate compositions that switched. The graph legend shows the measured values of electrical resistivity (Ωm).

	Ga at.%	**La at.%**	**S at.%**	**Cu at.%**
Without DSS	16	10	8	66
With DSS	27	15	14	44

Table 6.1: Composition of Ga:La:S:Cu films deposited by RF sputtering with and without a Dark Space Shield (DSS)

6.3.2 Ga:La:S Sputtering

A 66mm diameter sputtering target was fabricated by remelting Ga:La:S glass of composition 72.5 $GaS_{1.4} - 21.5La_2S_3 - 6La_2O_3$ (molar %) in a vitreous carbon crucible. The target size was limited to 66mm by the internal dimensions of the furnace which was used to remelt the glass. The molten glass was quenched using a flow ($5Lmin^{-1}$) of argon gas at room temperature. The resultant glassy disc was annealed by heating it at a rate of $0.5°Cmin^-1$, then holding it at $550°C$ for 6 hours, and finally cooling it to room temperature at at a rate of $0.5°Cmin^{-1}$. The resultant disc was attached, with a uniform layer of silver loaded epoxy, to a Cu backing plate that was 100mm in diameter. The disc was glued in the centre of the copper backing plate.

An Oxford instruments sputtering system was employed to deposit the films in an argon:oxygen atmosphere with argon:oxygen ratios 10:0, 10:1, 20:1 and 100:1 at a pressure of 5x10^{-3} mbar, and an RF power of 100W. This allowed some degree of oxygen inclusion into the film. The system accepts targets that are 100mm in diameter. Hence during Ga:La:S sputtering, some impurity in the resultant film was expected from the Cu backing plate. In an effort to reduce the amount of Cu impurities included into the film, a Dark Space Shield (DSS) was fitted to the sputtering chamber. This acts to shield the copper backing plate from the Ar plasma and consequently reduce its sputtering rate. Films were prepared both with and without the DSS.

The films of depth $300nm \pm 15nm$ were prepared on top of borosilicate microscope slides. The slides were coated with 20nm of Au such that their composition could be determined by EDX spectroscopy. EDX is not sensitive to oxygen, hence only the ratios of Ga, La, S and Cu could be determined. The composition of the films are given in Table 6.1. It can be seen that the effect of the DSS is to reduce the Cu atomic percentage by around 33 at.%.

Despite the large copper concentration of these films it is interesting to note that the material shows no crystalline peaks in the XRD diffraction pattern. Figure 6.22 shows the diffraction pattern of a 300nm thick film deposited, without the DSS, in an Ar:O atmosphere of 100:1.

The effect of sputtering conditions on the resultant film's optical energy gap, electrical resistivity and phase change properties have been investigated. The optical band-gap of

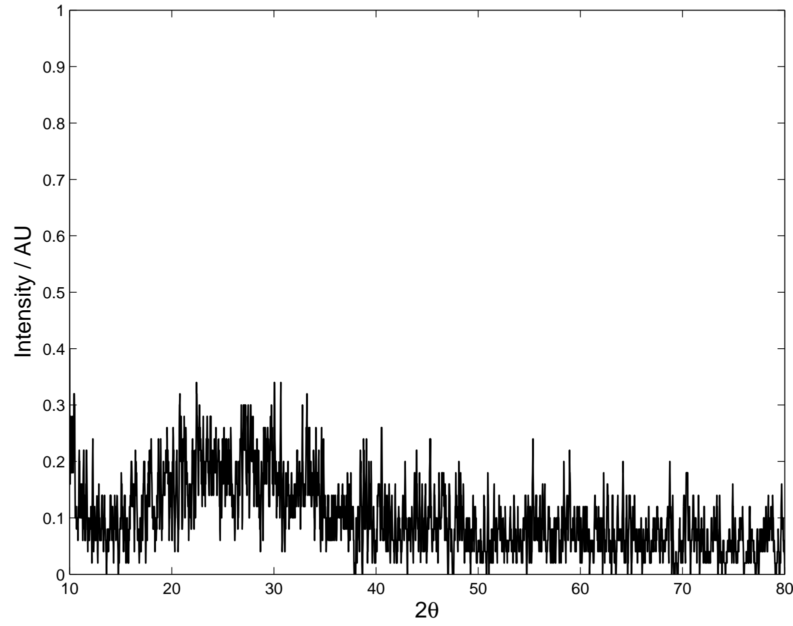

FIGURE 6.22: XRD spectrum of a Ga:La:S:Cu film in its as-deposited state

the films was measured using Tauc analysis. The spectra used for this analysis are given in figure 6.23, along with the energy gap as a function of oxygen content.

The electrical resistivity of these films is high and consequently it was not possible to measure the electrical resistivity of the films deposited by PLD with the four point probe set-up, since the system could not drive the minimum current required for a measurement. This indicates that the PLD films had a sheet resistance greater than $2 \times 10^9 \Omega Sq$. However, the Cu inclusion into the film reduced the as-deposited resistivity and allowed a resistivity measurement to be made on two of the films. Table 6.2 summarises the measurements of optical energy gap, E_g and electrical resistivity, ρ, of the films in their amorphous state as a function of oxygen:argon sputtering gas mixture.

O:Ar	E_g	$\rho\Omega m$
0	0.55	-
0.1:100	0.86	-
1:100	1.3	3.91
1:20	1.61	-
1:10	2.32	0.03

TABLE 6.2: Energy Gap, E_g, and, where measurable, electrical resistivity as a function of O:Ar ratio during sputter deposition

The crystallisation temperature of Ga:La:S films synthesised by nanosecond and femtosecond PLD, have been measured by analysing the transmission of a 633nm, 3mW laser diode through the film whilst it was heated at $10°Cmin^{-1}$ in a Linkam Scientific furnace.

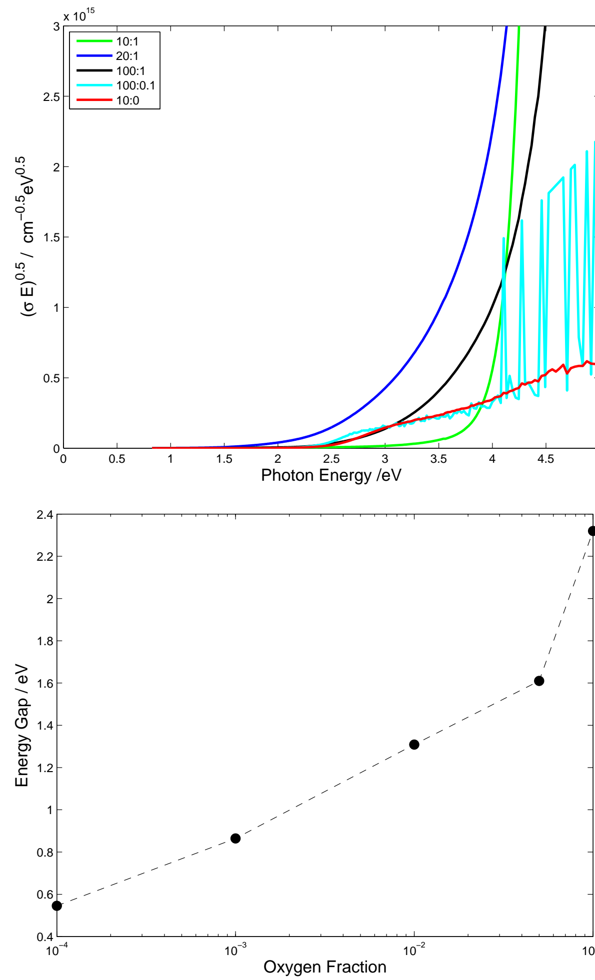

FIGURE 6.23: (a) Tauc analysis curves used to calculate the (b) energy gap, E_g of the Ga:La:S:Cu films as a function of oxygen fraction to argon background sputtering gas.

The transmitted intensity was measured as a function of temperature via a Tektronix oscilloscope. Strong crystallisation events were made clear by a large reduction in the transmission. Not all of the films showed such a change in transmission but the measurements where this was most clear are given in figure 6.24(a). To find the peak crystallisation rate, the transmission-temperature measurement was differentiated such that large changes in transmission with respect to temperature were clear. Figure 6.24(a) shows all the points which crystallised on a ternary diagram. The color bar indicates their respective peak crystallisation temperature, which was found by the peak of the differentiated temperature-intensity trace.

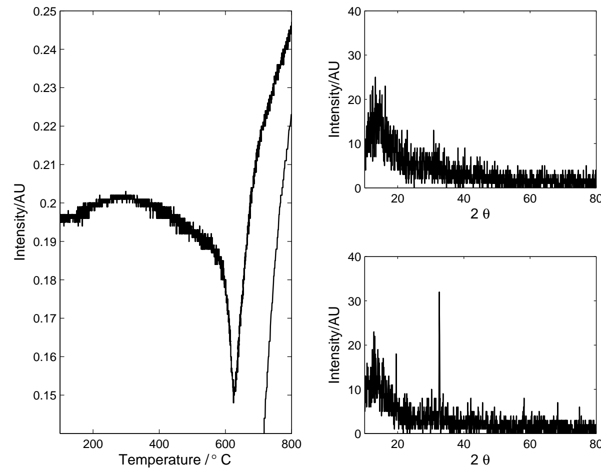

(a) Typical trace and XRD spectra of as-deposited and crystalline states

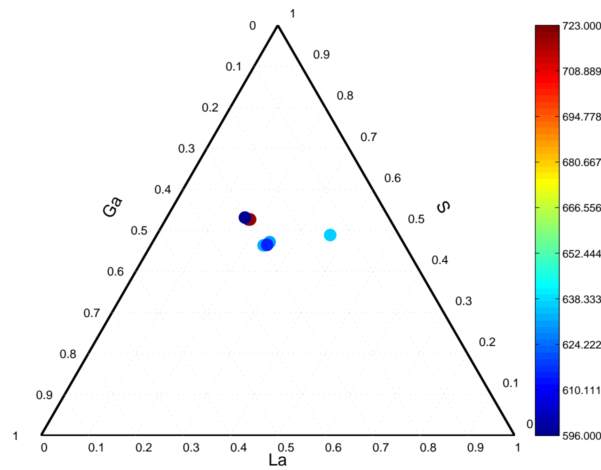

(b) Ternary of compositions

FIGURE 6.24: (a) A typical measurement of transmission of 633nm laser through GaLaS thins films fabricated by pulsed laser deposition and on the right hand side, XRD spectra for asdeposited (top) and annealed (bottom) states. Figure (b): Ternary showing the crystallisation temperature as a function of composition.

6.4 Phase Change of Ga:La:S Thin Films

In this section, the phase change properties of Ga:La:S:Cu materials are investigated and their applicability to electrical phase change memories is discussed.

In order to test the electrical properties of the material, a simple test chip was fabricated on crown glass substrates. The substrate was coated with a 200nm thick chromium film. A subsequent coating of photoresist, in combination with standard lithographic techniques, defined 1mm by 1mm square chromium electrodes. The GLS layer, 200nm thick, was sputtered on these electrodes before the final 200nm chromium layer was evaporated. Again, the top layer was outlined by photolithography while a reactive ion beam etch was used to define the top electrode contact area. This dry etch was necessary in order to prevent damage to the chalcogenide layer between the electrodes.

A Keithley 238 electrometer was used to measure the I-V characteristics of the as-deposited Ga:La:S:Cu film in this simple sandwich structure. The film was subjected to 10ms pulses of increasing voltage whilst the current was simultaneously monitored.

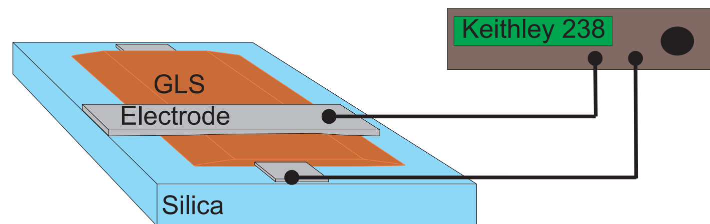

FIGURE 6.25: The set-up used to measure the Ga:La:S:Cu I-V characteristics

In order to measure the crystallisation time of the films, 200nm thick films were sputtered onto crown glass substrates in a argon:oxygen mixture of 100:1. The resultant samples were studied using the dual laser pump probe static tester arrangement, described in chapter 3. The optical power incident on the film was varied between 60 and 130mW, whilst the pulse length was controlled between 5ns and 400ns, the cw power was maintained at $100\mu W$ on the film's surface. Correlated measurements of pulse time, optical power and reflectivity were used to generate the PTK plots. The average of 3 PTK plots of samples created with and without a DSS are given in figure 6.27.

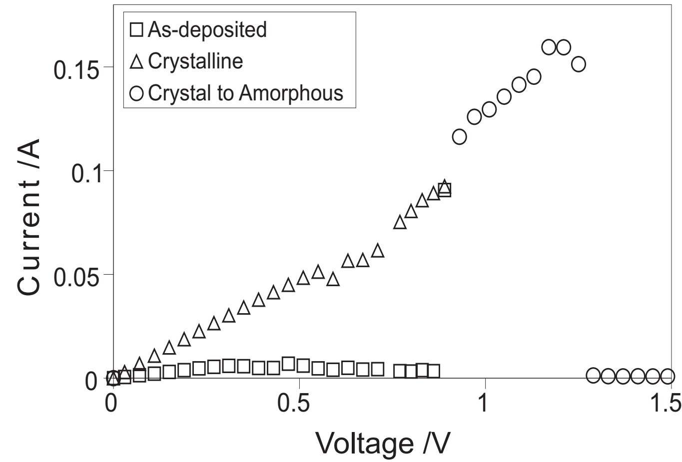

FIGURE 6.26: Current Voltage of a 200nm thick GaLaSCu sputtered film

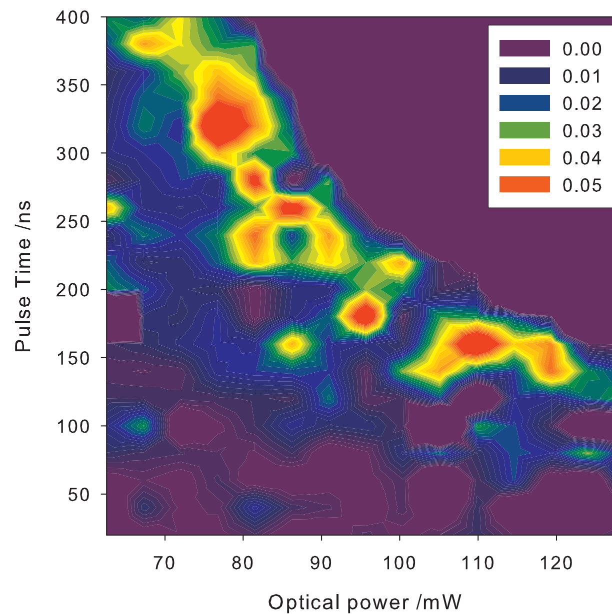

FIGURE 6.27: PTK plot of Ga:La:S:Cu sample.

6.5 Discussion

The electrical resistivity of Ga:La:S bulk materials has been studied. The electrical resistivity was shown in figure 6.10. For the case of 0.05% Ag, the sample showed a resistivity of around $1 \times 10^{10} \Omega m$ at 4kV in the glassy phase and around $5 \times 10^{10} \Omega m$ in the crystalline phase; indicating a $\times 5$ increase in electrical resistivity.

For glasses doped with greater proportions of Ag, the conductivity increases by $\times 1000$

indicating an ionic conduction mechanism. In the glassy phase, ions move through the bulk allowing some conduction. This is further confirmed by the relatively slow decrease in current as a function of time for a constant voltage, seen in figure 6.9. If the materials' electrical response spiked due to an increased in applied voltage, it could be assumed that the material is being poled and the conductivity increases due to the alignment of dipoles within the glass. However this gradual reduction in electrical current is characteristic of ion migration. The effect is clear for higher proportions of the Ag ion. The Ag ions move through the glass to the cathode where they are stored. As the Ag ions build up, they begin to repel one another, hence an even greater potential is required to maintain the same current. Another indication of poling is a negative current spike when the voltage applied to the material is switched off; this is also not evident in figure 6.9. In the crystallised sample the ionic conduction is diminished. The overall effect is a material which shows some conductivity in the glassy phase but does not conduct in the crystalline phase.

If the absorption spectra of these materials are analysed, a slight (0.3ev) decrease in the optical band-gap is observed between the amorphous and crystalline phases, see figure 6.13. However, even in the crystalline phase the band-gap was measured to be around $2eV$, thus semiconductor conduction is likely to have a secondary effect in comparison to ion transport. What is more, traps within the gap will reduce electronic conduction further in the glassy phase.

The crystallization temperature dependence on heating rate was measured and Kissinger analysis was performed to make an estimation of the crystallization activation energy. For a bulk material of $65GaS_{1.4}29La_2S_36La_2O_3$, the activation energy was found to be around 3.4eV, but it was found to have some compositional dependence. As expected, this is slightly higher than telluride based films and, as such, the materials show promising long archival lifetimes. Figure 6.5 shows the glass transition temperature, T_g, peak crystallisation temperature, T_p, and melting temperature, T_m, as a function of the Ga:La ratio. It should be noted that the melting temperature is largely insensitive to any composition change; unlike the glass transition and crystallisation temperatures. Increasing the proportion of gallium reduces $(T_m - T_p)$ and reduces T_g. A small separation of T_m and T_p is indicative of a material which crystallises with a low viscosity [15]. This is confirmed by figure 6.7, which shows the viscosity of the material as a function of Ga:La ratio at $640°C$ (this temperature is approximately halfway between the T_g and T_p for most of the compositions studied). It should noticed that viscosity is extremely sensitive to the Ga:La concentration and, increasing the ratio from 5:1 to 3:1 reduces the viscosity by roughly two orders of magnitude. The crystal growth rate is clearly of great importance in phase change data storage since it dictates the time taken to crystallise a previously written data bit in growth dominated materials. Hence it has the potential to limit the data transfer rate. The crystal growth rate is dependent on

the atomic mobility and has an indirect dependence on $1/\eta$, hence GLS compositions, which have a high concentration of gallium, are of interest for fast crystallising phase change materials. In contrast to a high crystallisation rate at elevated temperatures, the material's crystallisation rate at operating temperatures should ideally be zero. The glass transition temperature can be considered as the minimum temperature at which crystallisation can occur [29], and therefore materials with a high T_g are also sought. Figure 6.5 shows that the highest T_g compositions also have the highest lanthanum content. However, since the glass transition temperature of these materials is very high in comparison to other well-known data storage materials [29], the materials are expected to have superior archival properties.

Figures 6.14 and 6.15 show the compositional data points for nanosecond and femtosecond PLD grown films in comparison to elemental ratios for conventional melting [169]. Films were deposited over a broad range of deposition conditions. The results indicate that both femtosecond and nanosecond PLD films have compositions that range well outside the conventional glass-formation region. A notable point here is that the nanosecond PLD films all have a roughly constant gallium percentage, whereas the femtosecond PLD films occupy a broader region of the ternary diagram, that includes compositions that are richer in lanthanum. All the films studied had a lower Ga:La ratio than the target. It was found that the greatest effect on composition allowed a 44% change in the ratio of Ga:La for over, approximately, three orders of magnitude decrease in pressure. This resulted in a film that is higher in lanthanum content and lower in sulphur; the fraction of gallium is insensitive to pressure variation. The effect of target-substrate distance on the film's stoichiometry shows a similar correlation; affecting the composition along a line of roughly constant gallium. At closer target-substrate distances, the film composition more closely follows the target stoichiometry. Compositions did not appear to vary significantly for any of the fluences investigated ($0.6Jcm^{-2}$ to $2.4Jcm^{-2}$).

For films deposited by femtosecond PLD, a target with a composition of $Ga_2La_2S_6$ was used. The elemental ratios of the films deposited by femtosecond PLD for various fluences, target-substrate distances and pressures are shown in figure 6.15. The effect of ambient gas pressure was again the most influential parameter on the film's composition, reducing the Ga:La ratio by 50% for a pressure variation of 2×10^{-4} to $5 \times 10^{-2} mbar$. Contrary to the nanosecond deposited films, pressure change did not affect the film's composition along a line of constant gallium; rather the lanthanum content was affected to a greater extent, resulting in films higher in lanthanum for films deposited under higher background pressure. Similar to the nanosecond PLD experiments, closer target-substrate distances resulted in film compositions more closely comparable to the target material. The effect of off-axis deposition, on the composition of the film deposited by femtosecond PLD, is shown in figure 6.16. Measurements were taken along a range

of 7.5 cm from the centre of the film. These results reveal the nature of the non-stoichiometric transfer of target material at various distances on the substrate. Material deposited further from the centre of the plume is increasingly deficient in sulphur and gallium, and richer in lanthanum. The atomic weight of sulfur, gallium and lanthanum is $32gmol^{-1}$, $70gmol^{-1}$ and $140gmol^{-1}$ respectively; thus, if one considers the momentum transferred to each atom upon bombardment in the deposition plume, the S atoms mean free path length is likely to be a lot longer than La. Since the atomic weights are spread over $108gmol^{-1}$, the atomic spreading is clear in figure 6.16. This makes Ga:La:S an ideal candidate for compositional spread depositions which may be exploited for high throughput material discovery.

These results have demonstrated that careful control of the deposition parameters allows synthesis of novel compositions far from the target material's composition. Teaming this functionality with the intrinsic radial spreading of film composition allows a compositional area to be studied, rather than a single composition, for each deposition. Application of this suggested technique to Ga:La:S is still in its infancy and further development work is necessary to ensure repeatability.

Ga:La:S:Cu have been successfully sputter deposited as amorphous thin films with Cu concentrations of 66 at.%. An oxygen:argon atmosphere of greater than 1:100 was necessary during deposition in order to achieve amorphous films. Reducing this ratio resulted in polycrystalline films; as confirmed by X-ray diffraction, see figure 6.22. In the case of bulk Ga:La:S glasses, it is known that the addition of a small proportion of lanthanum oxide, or gallium oxide can act as a network stabiliser, and substantially reduce the material susceptibility to crystallisation by increasing the separation of the glass transition and crystallisation temperatures. Similarly in this case, the increased stability against crystallisation during deposition has been attributed to oxygen inclusion into resultant Ga:La:S:Cu film. Phase change data storage is reliant on the reversible crystalline-amorphous phase transition. It was assumed that the amorphous films, deposited in an atmosphere with the lowest concentration of oxygen, should be the least stable and therefore have a lower crystallisation activation energy, in comparison to films deposited in atmospheres with a greater oxygen content. Figure 6.27 shows the PTK plot averaged over 3 measurements. The x-axis shows optical power incident on the film, the y-axis is the pulse duration and the z-axis shows the reflectivity percentage increase after application of the laser pulse. There is a clear band of crystallisation, which extends from 400ns at 70mW to below 150ns, at optical powers greater than 110mW. Reducing the Cu content to 44 at.% increased the minimum crystallisation time to 350ns. In comparison to the well known optical phase change material $Ge_2Sb_2Te_5$ [117], the powers required are relatively high; this is due to the energy of our pump laser being below the electronic band-gap of the material, thus the intrinsic absorption is weak. The reflectivity change was measured to be around 8% which is also small in comparison to $Ge_2Sb_2Te_5$

but it is the electrical properties and, in particular, the Joule heating efficiency which are of interest. These films were found to have a very large electrical resistance in their amorphous state. Figure 6.26 shows a typical I-V curve for a film of the same composition (GaLaSCu) sandwiched between 2 chromium electrodes. The resistivity of the material in its crystalline state is $40\Omega m$, in contrast to the crystalline resistivity of $Ge_2Sb_2Te_5$: $7 \times 10^{-6}\Omega m$ [6]. The I-V curve in figure 6.26 shows three states of the material, as-deposited, crystallised and melt quenched. The as-deposited material showed a high resistivity until 0.87V. Increasing the pulsed voltage above this value resulted in a switch to a more conductive state. When the material's I-V measurement is repeated the material displays a low resistivity until 1.25V, at which point the material switched once again to its high resistivity, initial, state. The changes were stable and could only be altered by application of voltage to the film.

Since the crystalline resistivity of Ga:La:S:Cu films is 6 orders of magnitude greater than $Ge_2Sb_2Te_5$, a vast improvement in the heating efficiency of the material is possible. To show this, Comsol Multiphysics has been used to numerically solve the heat diffusion and current balance differential equations, thus allowing an estimate of the cell temperature as a function of time for a Ga:La:S:Cu active element. A schematic of the structure is given in figure 6.28(a). To aid the reader, the actual chalcogenide element size in this picture is a lot larger than used for the model. To simulate the heating of such a device, the following assumptions were made:

- The material has threshold switched
- The material conductivity is that of the crystalline state
- The electrical resistivity is constant with increasing temperature
- The affect of melting is ignored

These assumptions have allowed a simulation of the heat distribution in the chip and it is depicted in the thermogram of figure 6.28(b). The temperature as a function of time, at the centre of a chalcogenide element with a constant width of 20nm but variable cell length, is given in figure 6.29. The current density input into the cell was $0.06 \times 10^6 Am^{-2}$ for the GaLaSCu cell whilst $400 \times 10^6 Am^{-2}$ for the $Ge_2Sb_2Te_5$ cell. This equates to an input current of $0.37\mu A$ and $2.5mA$ for the $GaLaSCu$ and $Ge_2Sb_2Te_5$ films respectively. The melting temperature of $Ge_2Sb_2Te_5$ is approximately 900K and this can be achieved, with a 2.5mA pulse, in 2ns for the 100nm by 20nm. This is of similar value to the experimental result of 1.5mA required to melt other doped SbTe based compositions in a structure of similar shape and size [6]. The current of 2.5mA found from these simulations is an over estimate since it applies to a square 2ns pulse.

In reality, if the material takes 30ns to switch, a longer, lower power pulse, could be applied. This would account for this over estimate.

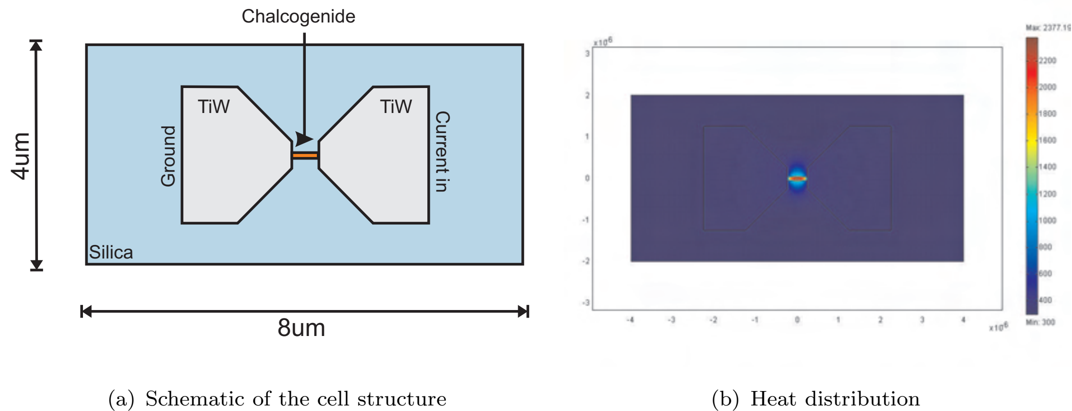

(a) Schematic of the cell structure (b) Heat distribution

FIGURE 6.28: (a) Schematic of the cell structure used for the Finite Element Modelling and (b) an example of a large cell heat distribution

GaLaS based materials have a number of key properties which need further development to realise an efficient phase change device. The optical contrast between phases of the limited compositional range studied is low in the far-visible spectrum and near infrared spectra. Optical absorption measurements, presented in figures 6.13, showed that the optical band-gap is increased from approximately 2eV to 2.3eV upon crystallisation. Therefore, for an optical phase change disk the operating wavelength should be shorter than 500nm for efficient heating and increased optical contrast. The high electrical resistivity of these materials allows for the possibility of a highly efficient electrical device. Studies of viscosity have shown that the material's viscosity decreases with gallium content and since crystal growth rate increases with decreasing viscosity, gallium rich compositions are of interest. The glass transition temperature has also shown some decrease with the Ga:La ratio; thus, lanthanum rich compositions are sought for archival purposes. However, since all of the compositions studied had a relatively high glass transition temperature, the stability at normal operating temperatures is expected to be sufficient and thus, the fast crystallising, gallium rich, samples are a greater priority.

Optical band-gap measurement for films deposited by sputter deposition and PLD have showed a dependence on the deposition parameters. By altering the fluence, path distance and background Ar pressure, the band-gap compositional dependence has been measured. Increasing the gallium content increases the material's band-gap. For the compositional range studied, the increase was from approximately 1.7eV to 2.4eV. Tauc analysis of the Ga:La:S:Cu films deposited in an oxygen atmosphere had an even greater effect on the optical absorption. A fit with $r = 1/2$ showed a better fitting than $r = 2$, which was used for the films deposited by PLD. This in itself shows that the semiconductor behaviour of the films is very different to that of the PLD films. An $r = 1/2$ is

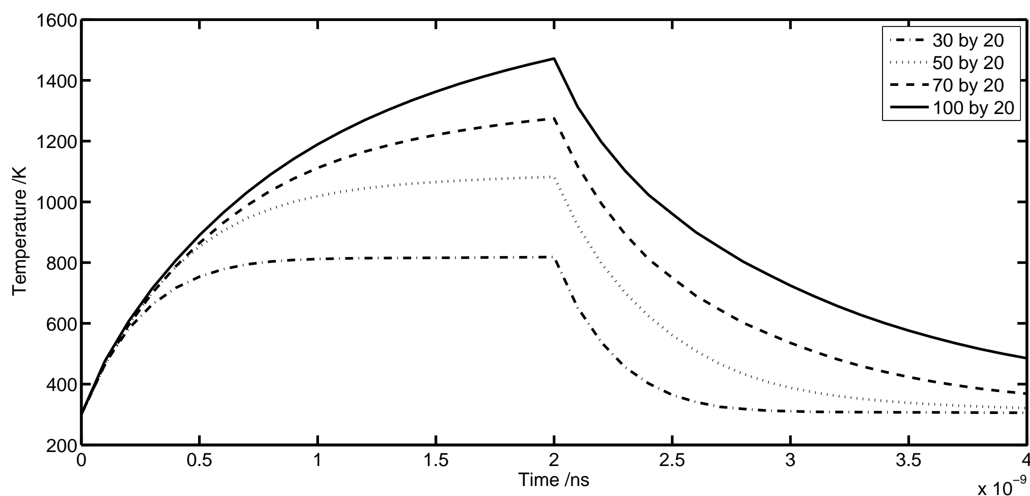

(a) Ga:La:S:Cu, I=0.37μA

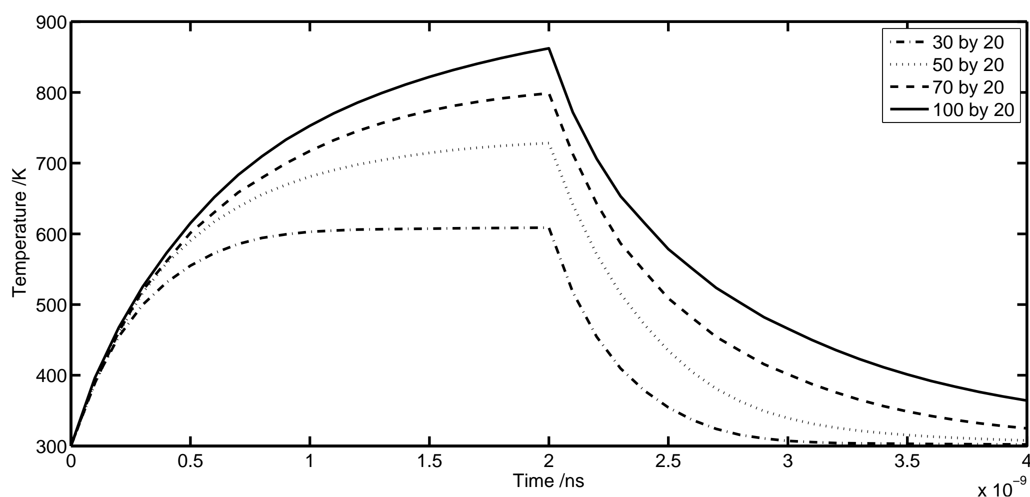

(b) $Ge_2Sb_2Te_5$, I=2.5mA

FIGURE 6.29: Temperature of crystalline cell as a function of pulse duration for (a) Ga:La:S:Cu and (b) $Ge_2Sb_2Te_5$

usually a signature of phonon assisted, indirect band-gap semiconductors. The band-gap was increased from 0.55eV up to 2.3eV for a 1:10 oxygen:argon atmosphere. Samples deposited in an atmospheres with less than a 1:100 ratio of O:Ar were visibly crystalline. The inclusion of Cu into the film therefore had the effect of decreasing the optical band-gap. This allowed increased optical heating efficiency at 658nm (1.88eV) and allowed a crystallisation PTK plot to be realised (see figure 6.27).

6.6 Summary

PLD has shown itself to be a particularly useful deposition method for the fabrication of GaLaS films with a wide range of compositions. The influence of the deposition parameters on the composition of deposited films is a useful means for engineering film compositions to a tailored application. Femtosecond PLD has shown itself to be a highly non-stoichiometric deposition method, with film compositions with over three times more lanthanum than the target material. An investigation into film composition for off-axis deposition shows how the film material can be fabricated with a diverse range of compositions on the same substrate. The compositions we have engineered are far from the conventional glass-formation region for GLSO, and were previously uncharacterised.

Ga:La:S:Cu thin-films have been successfully sputter deposited and amorphous films with up to 66 at.% Cu were achieved by reactive deposition in an oxygen atmosphere. The electrical phase change ability of these films and their application to data storage has been demonstrated. An optical measurement of the phase transition time has shown that these materials are capable of crystallisation within 150ns, but reducing the Cu content to 44 at.% increased the crystallisation time to 350ns. The large resistivity and fast crystallisation times of these films make them an ideal choice for low current, electrical, phase change devices. Finite Element Modelling (FEM) has revealed that if such a material was incorporated into a line-type phase change memory device structure, the current required to re-set the crystalline volume to amorphous would be around $0.4\mu A$; four orders of magnitude improvement on that of a $Ge_2Sb_2Te_5$ film. The drive for high data transfer rates means that the 150ns, intrinsic, crystallisation time of the Ga:La:S:Cu would be the shortest direct overwrite time in such a device. However, this is comparable to the $GeTe-Sb_2Te_3$ pseudo binary compositions which have crystallisation times between 30ns and 100ns [117] . Moreover, the addition of modifiers and dopants provide the potential for reducing the crystallisation time without compromising the low re-set currents. The use of such modifiers is the focus of ongoing research.

Further analysis of the thermal and optical properties of these films may reveal them to hold superior properties for a range of applications. Work is currently underway to this effect.

Chapter 7

Conclusions and Future Work

7.1 Conclusion

The principle objective of this thesis was to investigate new chalcogenide materials for electrical and optical phase change data storage applications. Three material systems have been investigated, *GeSbTe*, *GaLaS* and *BiSbTe* and a high throughput, fully automated, static tester has been designed to analyse the crystallisation and amorphisation times of the materials. Combinatorial screening of both the *BiSbTe* system and the *GeSbTe* system has allowed further understanding of electrical, optical and crystallisation dependence on composition. The original contributions of this work are listed below:

- New results on the GaLaS family of materials have demonstrated that this material can be used as an efficient phase change data storage material. This work has led to the a patent publication.
- The BiSbTe family of materials have been found to show fast crystal growth characteristics. These materials would find application in nanoscale optical and electrical data storage applications.
- Widest compositional study of the optical, electrical and crystallisation characteristics of the GeSbTe ternary system.
- Development of a fully automated thin-film test system (static tester) to study the crystallisation dynamics of compositional spread chalcogenide films.

These original contributions are now reviewed in more detail. They are also linked to the list of project aims given in section 1.2.

7.2 GaLaS Phase Change Materials

Assess the potential of GaLaS based films for optical and electrical data storage.

The GaLaS family of materials have, for the first time, been investigated for phase change properties. The results have shown that the material does indeed change phase and the inclusion of copper will enhance the rate at which the material crystallises. Crystallisation times of 150ns were found using the static tester. The fact that GaLaS is not efficient at absorbing the static tester's write laser wavelength could mean that even shorter crystallisation times are possible.

Optimisation of crystallisation time for such compositions is the focus of current research. The development of a PCRAM test cell of area 20nm by 100nm to assess the electrical phase change properties in the focus of future research. Figure 7.1 shows the test cell.

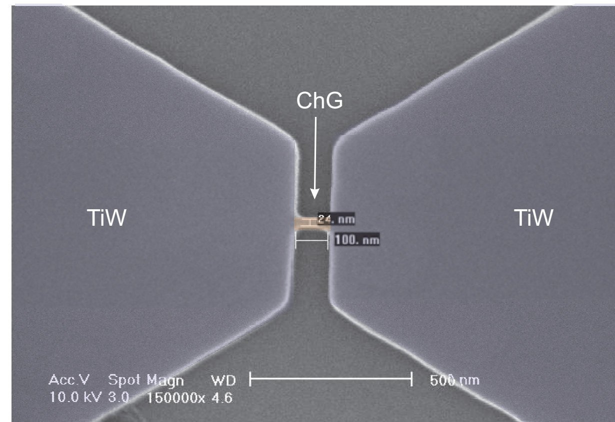

FIGURE 7.1: Scanning Electron Microscope image of a nanowire test structure for sulphide based phase change memory materials (developed in collaboration with the University of Taiwan)

In the past, chalcogenide phase change materials based on sulphur have been ruled out due to their high crystallisation, glass transition and melting temperatures. However, the GaLaS materials reported in this thesis have an extremely high electrical resistivity; greater than $4\Omega m$ in some cases. This high electrical resistivity allows electrically efficient heating. Analysis and comparison with $Ge_2Sb_2Te_5$ shows that the material has a four order of magnitude reduction in electrical current to achieve each materials, respective, melting temperature. Further, in a practical PCRAM device, the reduction in write current allows the use of much smaller addressing transistors and thus this material can be used in a highly scalable device. This is clearly of great importance. Although this material shows significant potential for electrical phase change RAM but the poor

absorbtion of visible laser radiation deems it unsuitable for conventional optical phase change media.

Assess pulsed laser deposition for combinatorial deposition of Ga:La:S materials.

In order to test varying compositions of Ga:La:S films, pulsed laser deposition has shown itself to be a particularly useful tool. Thin films of GaLaS are deposited from a composite target. However, due to the wide range of atomic mass of the constituent atoms a natural composition profile is achieved on the substrate's surface. Further, by varying the deposition conditions, the position of the central composition within ternary space can be manipulated. This allows a high degree of control in the synthesis of compositionally spread films. The amorphous compositions, deposited in this thesis, were far from the known bulk glass formation region. The optical and thermal properties of these novel compositions have been characterised. The refractive index was found to increase with decreasing lanthanum content whilst the optical energy gap increased.

This GaLaS research, in particular, has suffered from the loss of fabrication facilities. However, these initial results are promising and it is therefore recommended that additional resources are used to investigate this new phase change system further. The ideal solution would be a GaLaS combinatorial synthesis and high throughput screen of the properties.

7.3 BiSbTe Phase Change Materials

Analysis of the effect of Bi on SbTe films through single deposition and combinatorial techniques. Compare with Bi effect on $Ge_2Sb_2Te_5$ films.

Previous work has shown that a $Sb_{45}Te_{65}$ alloy will crystallise in the shortest time in relation to other proportions of the alloy [146]. However, in this thesis it has been demonstrated that the addition of Bi to much larger concentrations of Sb has far superior properties and, for the first time, the Bi doped Sb_8Te_2 compositions have been found to reduce the crystallisation time by an order of magnitude when 8 at.% Bi is incorporated in the film. This allows crystallisation in just 50ns. In the amorphous state, these materials showed a two orders of magnitude reduction in electrical resistivity with increasing Bi content. This has been attributed to a reduction of trapping states, thus allowing metallic conduction. It was possible to incorporate up to 13at.% into a stable amorphous phase. After annealing, above the crystallisation temperature, the material was found to crystallise into an A7-type structure with lattice paramters a=4.29$\mathring{A}$ and c≈11.22$\mathring{A}$.

Previous reports have shown that the crystallisation time of $Ge_2Sb_2Te_5$ is reduced by the addition of Bi[71]. However, in the case of $(Sb_8Te_2)Bi$ the reduced crystallisation time is due to a reduction in viscosity with increasing Bi. This reduction allows an increased crystal growth rate and hence a shorter crystallisation time. In contrast, $Ge_2Sb_2Te_5$, which has a nucleation dominated crystallisation mechanism, it is believed that bismuth tends to decrease the crystallisation activation energy and thus decrease the crystallisation nucleation time.

High throughput synthesis has also been used to deposit Bi doped Sb:Te compositions. The materials are mostly deposited in a crystalline phase. This made a full analysis of the amorphous system difficult. However the compositional range 5%>Bi>25%, 48%>Sb>60% and 20%>Te>42% was found to be amorphous and stable. Crystallisation time measurements of this system were difficult due to the interference effects of the capping layer. However, it was possible to deduce that the system had a nucleation time shorter than 30ns whilst the crystallisation time was shorter than 300ns. Similarly to the Bi doped Sb_8Te_2 compositions, these materials also shown growth dominated crystallisation. The electrical resistivity of these materials in the crystalline phase was orders of magnitude lower than that of $Ge_2Sb_2Te_5$. Practically, this could rule out the use of this material in electrical phase change applications. However, the good optical contrast means that this material would be suited to optical phase change disks. Since the materials show growth dominated crystallisation, clearly, a smaller phase change volume would be most appropriate for fast crystallising applications. Therefore it is suggested that this material is trialed in near-field phase change recording.

These results have helped understand the role of bismuth in phase change media and could allow faster switching Tellurium based compositions to be engineered.

7.4 Static Tester

Design, build and characterise a high throughput static tester to analyse the crystallisation dependence on compositions.

An automated static tester system has been developed to measure the crystallisation and amorphisation duration of phase change materials which absorb at 658nm. The system has the ability to automatically test composition spread samples. Static testers have been developed in the past by other laboratories. However, the unique aspect of this system is its ability to test multiple positions on a single substrate without the need for the assistance of an operator. The system has been successfully applied to both composition spread samples and single composition samples. It has been used

throughout this thesis research to gain novel results on the crystallisation time of phase change materials.

Some films have weak absorption at 658nm and therefore poor optical phase change characteristics. However these films should not be ruled out for electrical phase change materials. This is indeed the case for GaLaS chalcogenide films where the photon energy of the static tester is below the absorption edge of the films and thus efficient heating of the material with a red diode is not possible.

To prevent the samples from oxidising it is necessary to cap them with a projective layer. The sputtering system employed to do this is not set-up to produce films of thickness within the tolerances necessary for optical crystallisation measurements and therefore this has proven problematic for the static tester compositional spread analysis. Therefore, for a good crystallisation time result set, the capping layer deposition process should be reviewed.

This system is now an indispensable tool to the continued phase change research program initiated by the works reported here.

7.5 High Throughput Deposition and Analysis of the GeSbTe Phase Change System

Characterise the optical, electrical and crystallisation of GeSbTe phase change films, deposited by thermal, combinatorial techniques.

The research of the GeSbTe phase change system served to initially test the high throughput methodologies which were then applied to other phase change systems. The composition spread was achieved by off-axis deposition from multiple Knudsen cell and e-beam sources and controlled positioning of a shutter to grow wedges of each element on a substrate.

Differences in the properties of the sputter deposited films to thermally deposited films have been attributed to the deposition pressure and conditions. For the $Ge_2Sb_2Te_5$ films the greatest difference between the two deposition methods appeared in the crystallisation temperature. The films seemed to crystallise at some $20°C$ higher temperature than equivalent composition prepared by RF magnetron sputtering. Other measurements of electrical resistivity and refractive index were found to be comparable with the $Ge_2Sb_2Te_5$ composition.

Experimentation to achieve compositional spread sputter deposition was also carried out using a HWP sputter system. The effect of coil power and sample height had a negligible

influence on the depth gradient of each target, limiting the sample to compositions within 20 at.% of the target. However such a deposition tool could be of interest for finer characterisation of thin films where the approximate composition range of interest is known.

The analysis of the composition spread film allowed some new results to be obtained. Primarily, the materials properties have been tested over the entire ternary composition range. From these measurements new analysis of the electrical and optical properties has been performed and the electrical resistivity has been experimentally proven to obey the model of increased charge carrier traps proposed by Sir Nevil Mott for amorphous semiconductors in the 1970s. That is, the chalcogen atoms induce point defects in the amorphous network which act to trap charge carriers. This was evident in the electrical measurement conducted in this research. As the chalcogen (Tellurium) atom's concentration increased, the electrical resistivity in the amorphous state showed a correlated increase due to, what is suspected to be, an increase in charge carrier traps. Whilst in the crystalline state, the opposite characteristic was observed; the electrical resistivity decreased with Te content. Therefore the greatest change in resistivity was achieved at compositions with a high Te content. This allowed a suggestion of Te rich compounds for efficient electrical phase change materials. Further analysis of the optical properties resulted in the conclusion that Te also decreases the polarizability of the material and thus its refractive index.

7.6 Further Work

The power of high throughput deposition and characterisation is clear. In this thesis a number of screening techniques have been both designed and exploited for screening of materials. The high throughput static tester has proven a useful tool for characterising the dynamics of the phase change material; however, it is still a long measurement and accurate alignment is a very time consuming process. Hence, the static tester has still room for further development. The major alignment issues and long term stability can all be vastly improved by moving to a fiberised system. Coupling both pump and probe lasers into a single fibre and feeding the output into the objective lens will remove all of the mirrors which are usually used to make both beams coincident on the same spot of the film. A further advantage of using a single mode fibre is the mode field shape. The single mode fibre will only allow a Gaussian beam to propagate. There is also a need to improve the detector electronics. A simple trans-impedance amplifier is used to convert the current generated by the Si detector into a voltage, which can then be amplified. However, the amplifier will also amplify any other signals present on it, thus a future step will be to include a lock-in amplifier, and to modulate the probe laser.

This should allow a considerable increase in the detector's sensitivity and thus reduce the measurement time. Incorporation of a detector to monitor the probe laser will also allow compensation of the probe signal which is known to be unstable on occasions; probably due to self induced heating. A third detector would be helpful and, if the transmission through the sample is significant, it would also permit the analysis of bulk crystallisation, as opposed to surface crystallisation. For measurement of high energy band-gap chalcogenides such as GLS [19], the static tester should also be modified to operate at 405nm or shorter wavelengths. The transmitted intensity has been compared at this wavelength to the 658nm absorption, using measured values of PLD deposited films and the Beer-Lambart law, $I = I_0 exp(-\mu x)$ [170]. The transmitted intensity for $Ge_2Sb_2Te_5$ at 658nm is also included as a reference [1]. This is displayed in figure 7.2. It can be seen that 50% of the light intensity is absorbed within 140nm in GLS at 405nm. At 140nm, with the existing 658nm laser, only 10% of the incident intensity is absorbed. For comparison the intensity of of $Ge_2Sb_2Te_5$ has also been plotted for the 658nm wavelength. $Ge_2Sb_2Te_5$ has an optical absorption edge of approximately $1\mu m$ thus it strongly absorbs at 658nm, and hence 50% of the light is absorbed in just 12nm. An additional benefit of moving to shorter wavelengths is that the lens NA, necessary to focus to a $1\mu m$, spot is significantly reduced from the 0.65 NA lens currently used for the red lasers. This also has the effect of increasing the depth of focus; thus reducing the sample positioning accuracy requirments.

With the emergence of novel near-field disc structures, a suitable rig should be designed to measure the crystallisation and optical properties of these materials in the near-field. This might be designed around a conventional SNOM. Clearly the crystallisation times of growth dominated phase change materials are likely to show the most promise in such applications, however there will be a mark radius where the material is no longer dominated by the time taken for the crystal to grow but instead by the nucleation or incubation time. A near-field system would allow marks with diameters of 50nm to be achieved, thus allowing an assessment of the material's ability to nucleate faster than the growth time for such small radii.

In the coming years I believe the majority of PCM research will concentrate on the electrical application. For this reason it is important that a high throughput electrical test cell is developed. The cell should essentially allow the compositional spread films to be tested on a chip, such that the threshold switching, I-V, electrical phase contrast, power , cyclability, set and reset can all be characterised. The ability to quickly screen phase change materials for the threshold switching will not only allow suitable low threshold field materials to be identified but, also, aid the understanding of how the individual atoms influence this unique property. Development of such a test chip has

[1] Values for optical absorption at 658nm were taken from work by Bong-Sub Lee et al. [166]

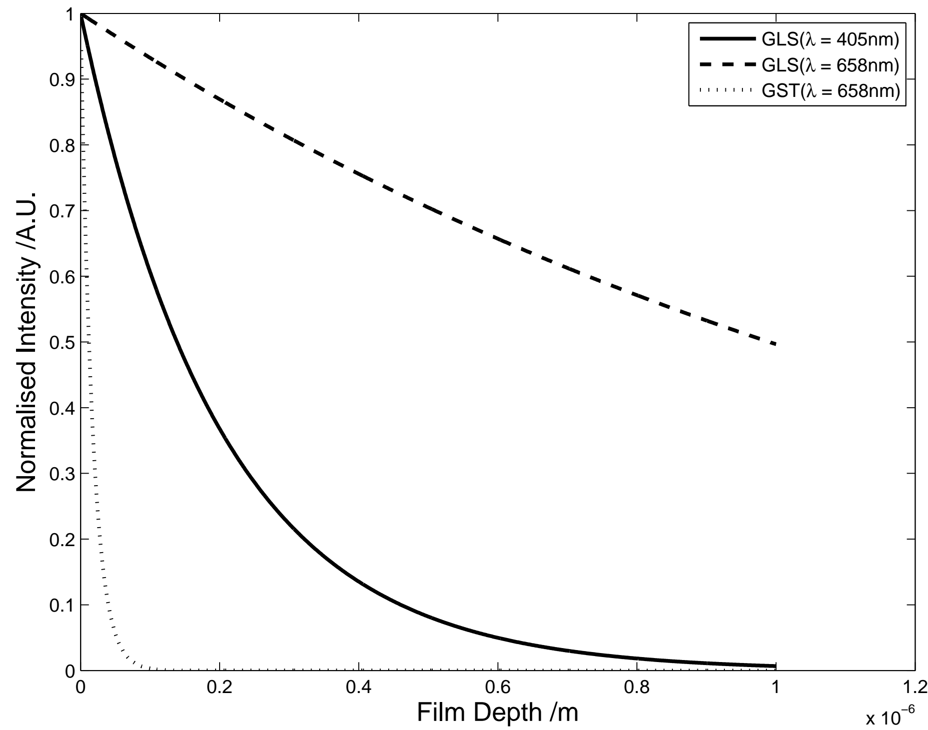

Figure 7.2: Absorption as a function of depth simulation for GLS at 405nm and 658nm and $Ge_2Sb_2Te_5$ at 658nm

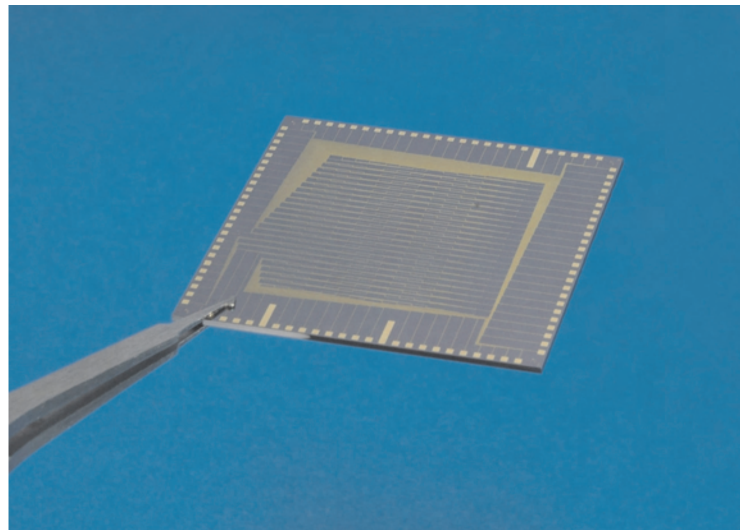

Figure 7.3: First generation high throughput electrical chip

already started and figure 7.3 shows a photograph of the first generation chip. Each cell is pulsed via a series of multiplexes which can be automatically connected to either an electrometer or a pulse generator. This allows either the I-V characteristic to be measured or a pulse to be sent and then the resistance measured.

In this work, a clear trend with the Te concentration has been shown to dictate the

electrical conductivity of the as-deposited state. This work can be easily extended by performing compositional spread Raman spectroscopy. The amplitude of the Te-Te peak would then be correlated against the electrical resistivity. This would prove the aforementioned dependence.

Large sections of this work are based on the foundation that thermally grown, compositionally spread films will essentially perform the same way as the conventional, sputter deposited films. However, some key differences are apparent; in this thesis a clear difference in crystallisation temperature was apparent for the GeSbTe compositions along the $GeTe - Sb_2Te_3$ pseudobinary tie line. Sputter deposition is a low vacuum process and thus the films' density is affected by the background gas [75]. This in turn influences the optical, electrical and crystallisation properties. It is therefore necessary to perform a fundamental study of the structural properties between equivalent films prepared by both methods. I expect the as-deposited properties to be very different but, as both films are annealed, their properties to become increasingly similar.

The compositional analysis of BiSbTe has shown that the composition range 5%> Bi >25%, 48%> Sb >60% and 20%> Te >42% is deposited as an amorphous film. This area should be studied in much closer detail. Once the problems associated with capping the films have been overcome, the crystallisation time should be investigated with the static tester. For the sputter deposited $Bi(Sb_8Te_2)$ it was found that the materials refractive index decrasesd with increasing Bi in the amorphous state. This should be investigated over the range 5%> Bi >25%, 48%> Sb >60% and 20%> Te >42% and related to a structural study. This would allow some justification to the theory that the Bi atoms have the effect of altering the amorphous network to reduce the refractive index.

There are key differences between the crystallisation mechanism of $Ge_2Sb_2Te_5$ films and Bi doped Sb_8Te_2. It has been suggested that the crystallisation activation energy is reduced by the addition of Bi to $Ge_2Sb_2Te_5$ [71] however, in this thesis, the role of Bi in Sb_8Te_2 is to increase the growth rate and thus this has been attributed to a reduction in the material's viscosity. The effect of Bi on the viscosity of Sb_8Te_2 should be measured on bulk samples using a Thermal Mechanical Analyser (TMA).

The activation energy of crystallisation is an essential measurement which can be used to gain stability of written amorphous marks and thus allow estimates of archival lifetimes. However achieving such measurements in a high throughput, efficient, manner is difficult because at least five data points, taken at different heating rates, are necessary for a confident fit to the Arrhenius plot required for Kissinger analysis [86]. To achieve measurements on compositional spread films, this imposes the requirement that at least five identical samples are prepared which is impractical and inefficient. To overcome

such difficulties, a novel, non-isothermal heating stage has been designed. This allows the sample to be placed on the stage and its surface heating rate to be varied along one axis. So, at one extreme end of the surface, the heating rate might be $10°Cmin^{-1}$ and at the other end $1°Cmin^{-1}$. The optical reflectivity, as a function of position on the sample, would be measured with a CCD camera. This essentially allows the optical reflectivity to be measured as a function of position. A similar concept was described in section 2.8.4. This means that if the sample has a single composition along the axis of a varying heating rate, the time taken for different areas of the sample to crystallise will change depending on the position and the corresponding heating rate. In a single run this would allow the activation energy to be measured. This is already a significant increase in measurement throughput in comparison to measurement of individual samples.

Since the heating rate is only varying in one dimension of the sample surface, the composition can vary in the orthogonal axis. Thus a full compositional spread measurement is achieved in one run. This would allow very quickly an assessment of the compositions effect on crystallisation activation energy.

The key to achieving a position dependent heating rate, is the delivery of different amounts of heat energy to different positions on the sample. For this novel idea, a single heat source is used which heats a copper block at one end. Protruding from the Cu block are heating elements, each separated by a thermally insulating ceramic. Each heating element is of a different thickness. This thickness of the heating element affects the amount of heat delivered to the heating blocks' surface. To check the principle of this design, a finite element heating model[2] has been implemented. Figure 7.4 shows how the heat through the block changes as a function of position. It can be seen that the surface, where a large amount of heat is supplied, is hot whilst the other edge of the surface is cool. The heating rate of the copper block can be varied to achieve a constant heating rate. However, from this initial modelling, where radiative and convective losses have been ignored, a constant heat source has been shown to give a constant heating rate at the surface of the film, see figure 7.5 which shows the heating rate as a function of position along the axis of varying heating rate.

A prototype stage has been built and, at present, this is undergoing calibration ready for testing single composition films. For this, the system will need to be enclosed in an inert atmosphere if the film is uncapped. It can easily be envisaged that this system could also be used to test other mechanisms that could affect the activation energy. For

[2]For this model a constant heat supply was assumed, the system was assumed to be thermally insulated from its surroundings. Although a temperature scale is given, the important characteristic for this model was the ability to have a linear heating rate for each position on the surface. The actual temperature achieved would clearly be dependent on the balance between input energy and heat losses, but with careful control of the input energy, it has been assumed that the system could be calibrated to allow a linear heating rate. For the purposes of this model the heating elements are copper, and the insulator is silica.

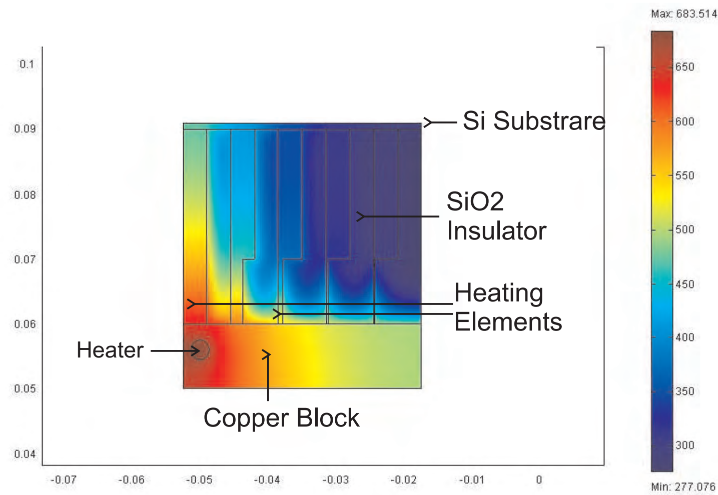

FIGURE 7.4: Thermogram modelled using Finite Element simulation of the non-isothermal heating stage

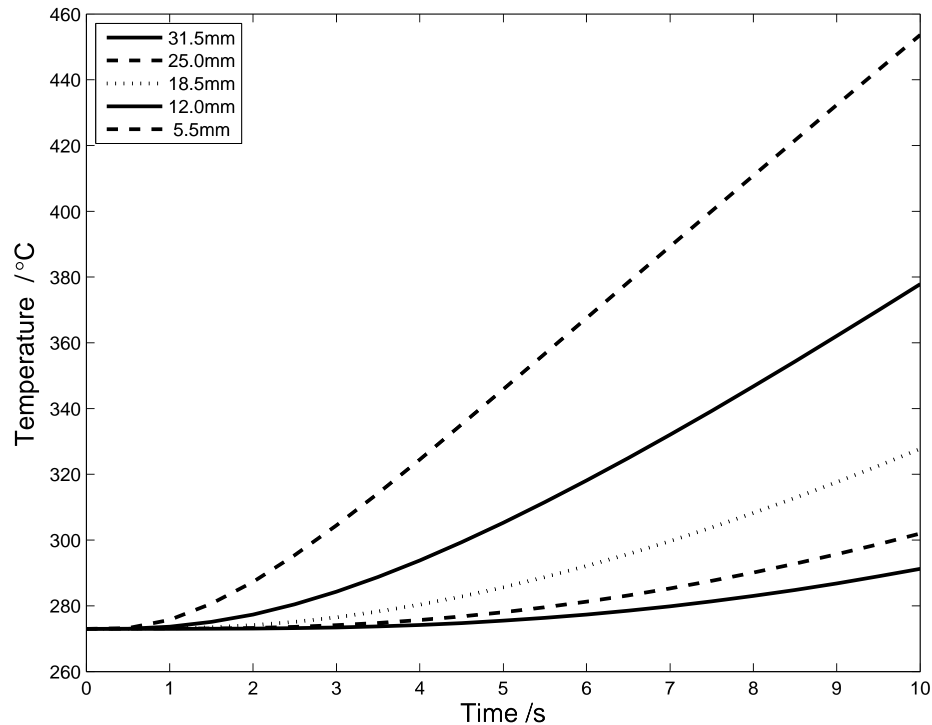

FIGURE 7.5: Heating rates on the surface of a silicon substrate atop of the non-isothermal heating stage

instance, growth of a single composition film with a capping layer of $ZnS - SiO_2$ which varies in depth from 0nm to 100nm across the surface. The activation energy as function of layer depth could then be plotted.

The introduction to this thesis described a famous talk by Richard Feynman titled

'There's plenty of room at the bottom'. Nearly fifty years ago, he had the idea of storing data in a small volume of material. Now, fifty years on, the ability to store large quantities of data within a small volume of a film is becoming possible. The hardware and technology for holographic storage is available but a suitable material for the media is still being optimised [171]. I believe that the high throughput methodologies applied to phase change materials should now be exploited for novel holographic materials. Some chalcogenide materials are known to have photorefractive properties; indeed the Ga:La:S materials studied in this thesis are themselves photorefractive[38]. A simple interferometer set-up could be automated to assess the most suitable compositions of chalcogenide materials for holographic purposes. This could even be performed, in conjunction, on the chalcogenide materials currently assessed for phase change data storage. Of the holographic materials currently under investigation, polymer materials show the greatest potential; therefore a future combinatorial approach to polymer holographic data storage material should be considered.

Appendix A

Ge:Sb:Te Ternary Maps

This section gives supplementary electrical resistivity, refractive index and X-ray diffraction data plotted in Ge, Sb and Te ternary space.

A.1 Electrical Resistivity

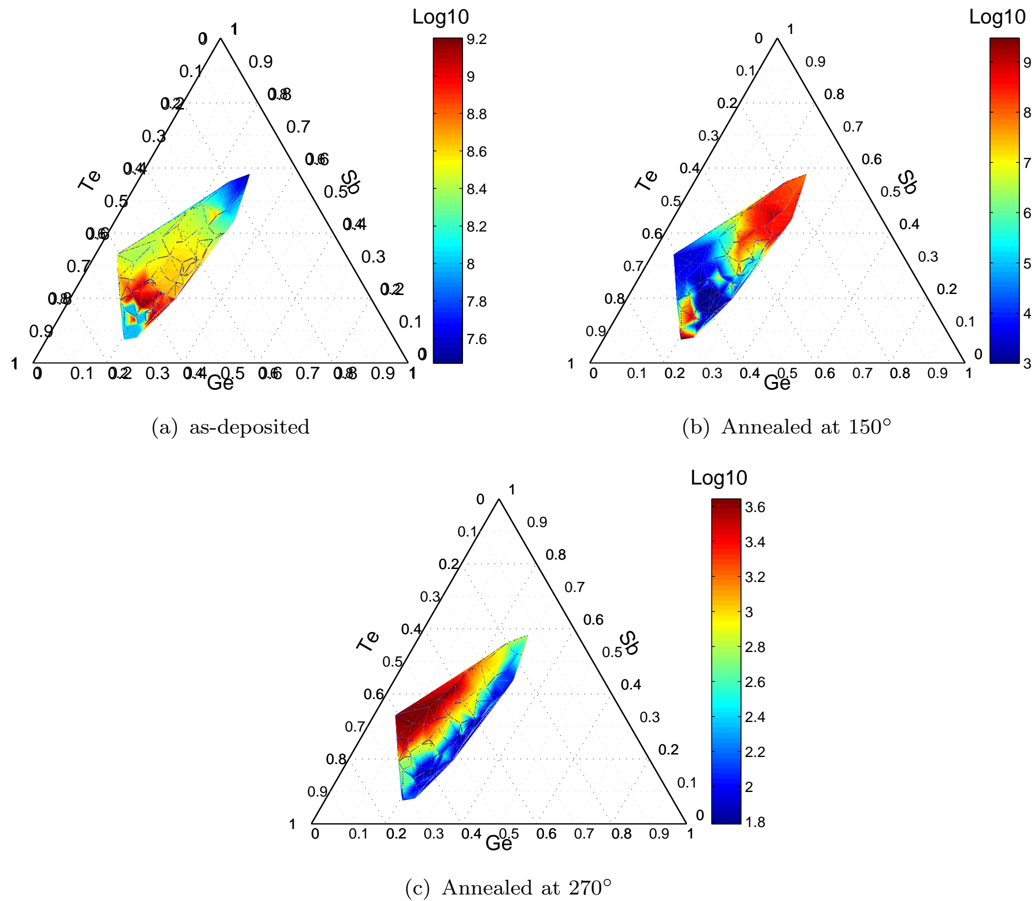

(a) as-deposited

(b) Annealed at 150°

(c) Annealed at 270°

Figure A.1: Sample 781 Sheet Resistance

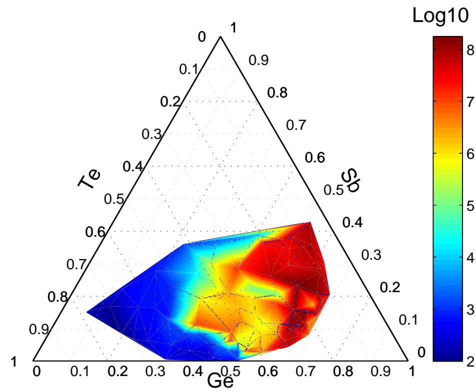

Figure A.2: Sample 768 Sheet Resistance

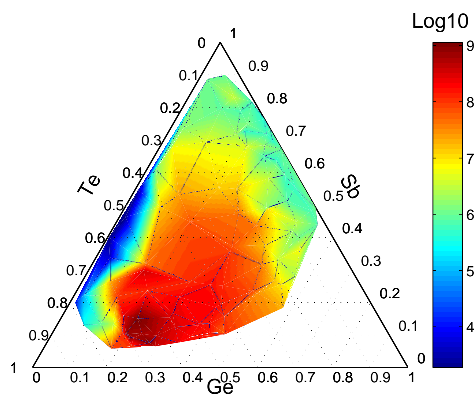

Figure A.3: Sample 792 as-deposited Sheet Resistance

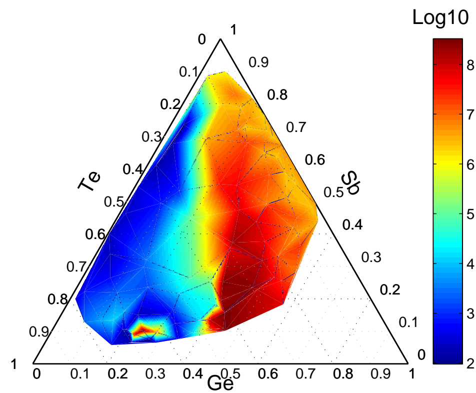

Figure A.4: Sample 792 after heating to 150°C

A.2 Refractive Index

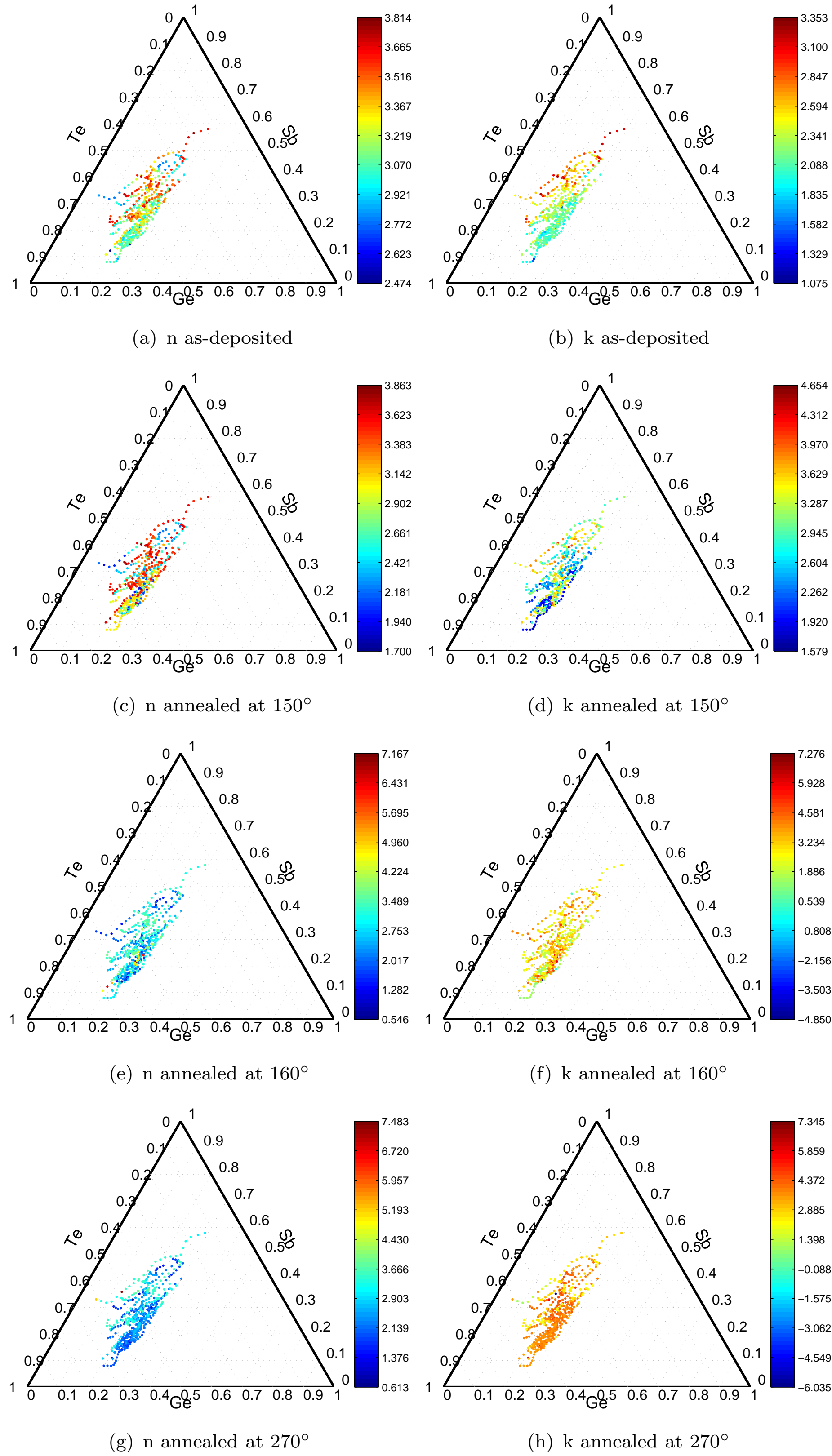

(a) n as-deposited

(b) k as-deposited

(c) n annealed at 150°

(d) k annealed at 150°

(e) n annealed at 160°

(f) k annealed at 160°

(g) n annealed at 270°

(h) k annealed at 270°

FIGURE A.5: Sample 781 refractive index, n, (532nm) and extinction coefficient, k, as a function of temperature

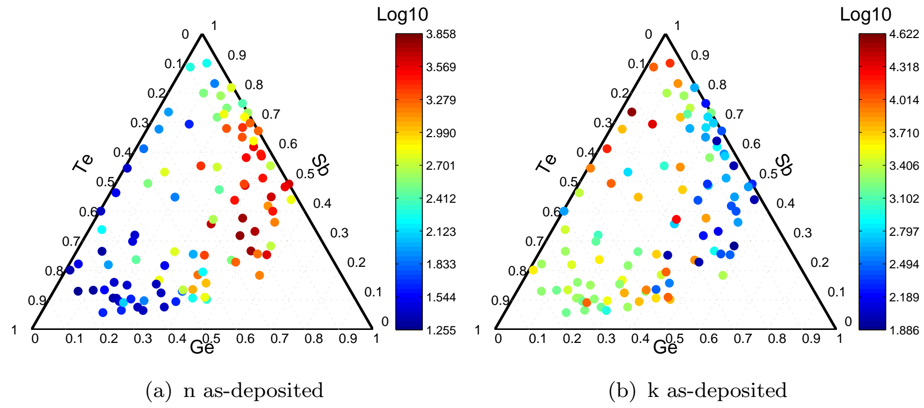

(a) n as-deposited (b) k as-deposited

FIGURE A.6: Sample 792 refractive index, n, (532nm) and extinction coefficient, k, as a function of temperature

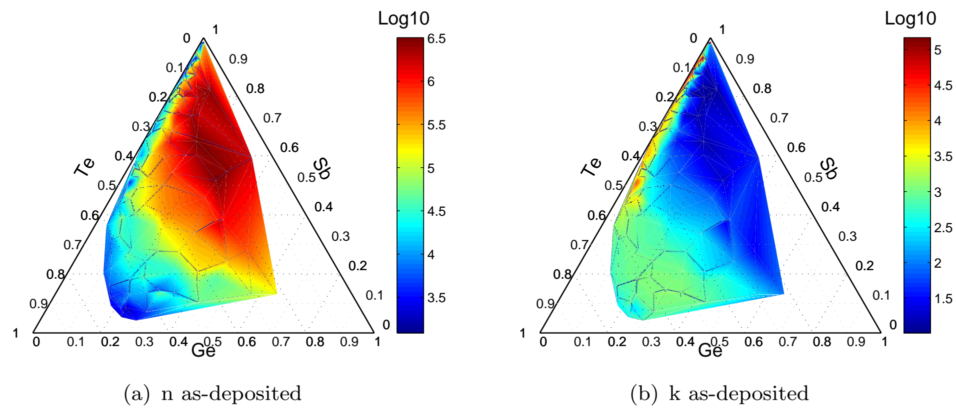

(a) n as-deposited (b) k as-deposited

FIGURE A.7: Sample 1306 refractive index, n, (532nm) and extinction coefficient, k, as a function of temperature assuming infinitely thick HEATED(633nm)

A.3 XRD Maps

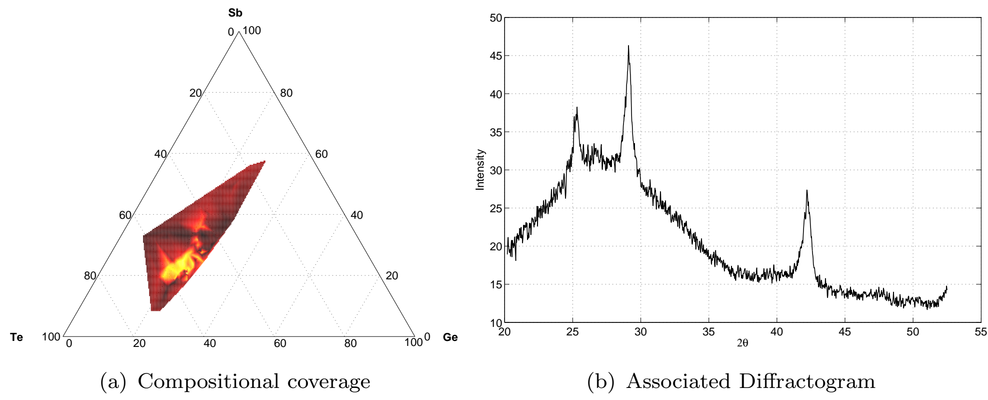

(a) Compositional coverage (b) Associated Diffractogram

FIGURE A.8: Observed as-deposited XRD Spectrum 1

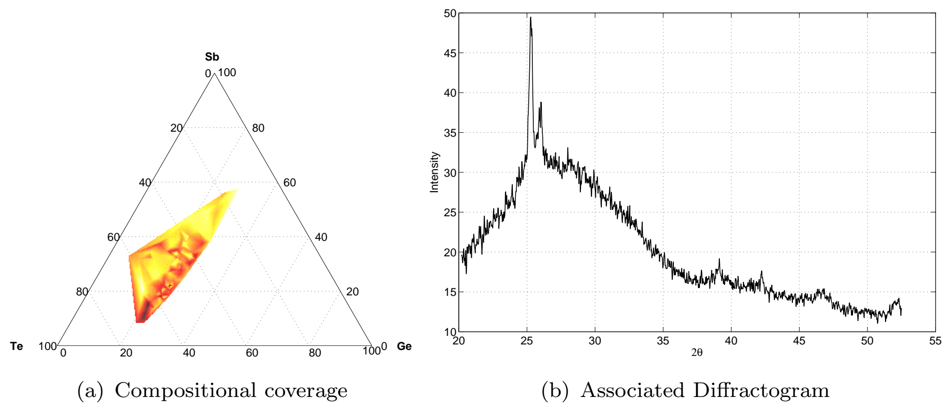

(a) Compositional coverage (b) Associated Diffractogram

FIGURE A.9: Observed as-deposited XRD Spectrum 2

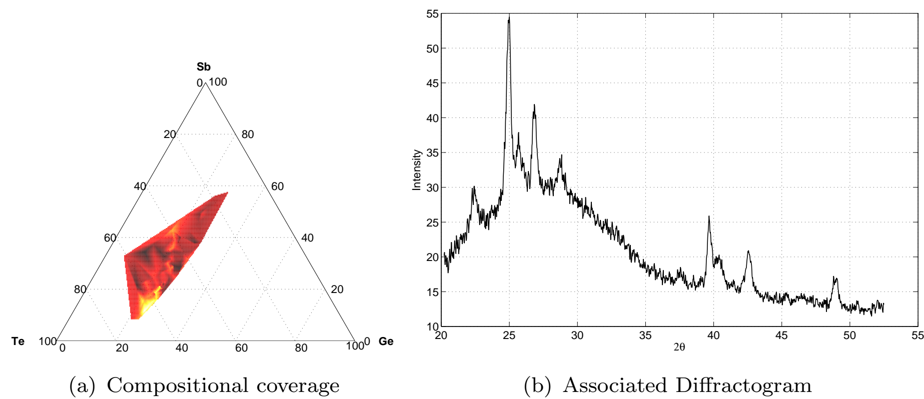

(a) Compositional coverage (b) Associated Diffractogram

FIGURE A.10: Observed as-deposited XRD Spectrum 3

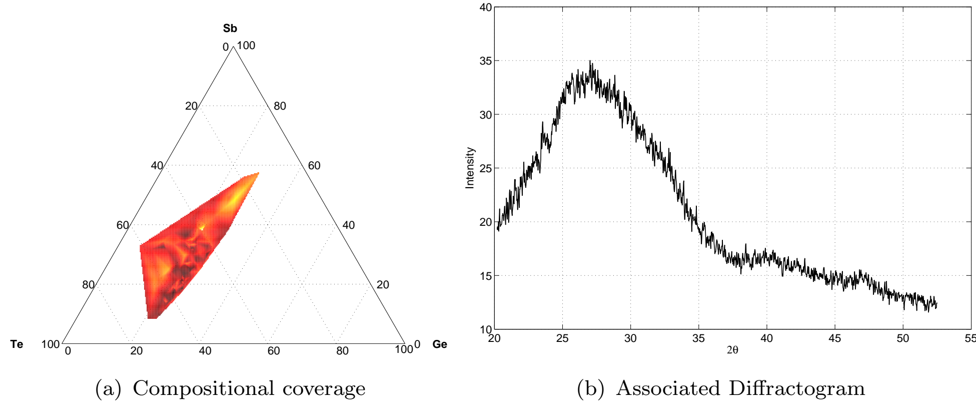

(a) Compositional coverage (b) Associated Diffractogram

FIGURE A.11: Observed as-deposited XRD Spectrum 4

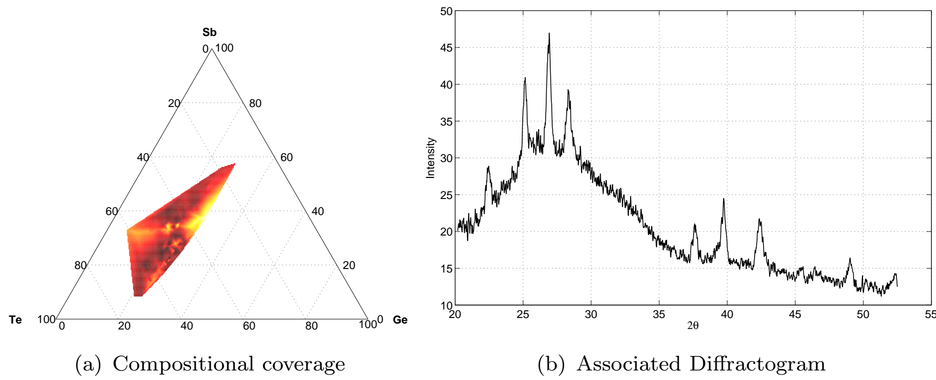

(a) Compositional coverage (b) Associated Diffractogram

FIGURE A.12: Observed as-deposited XRD Spectrum 5

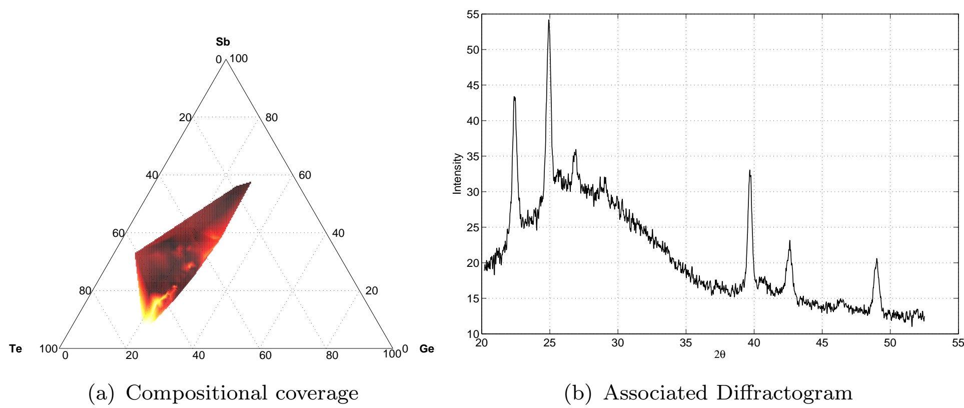

(a) Compositional coverage (b) Associated Diffractogram

FIGURE A.13: Observed as-deposited XRD Spectrum 6

Appendix B

High Temperature Four Point Probe Fabrication

A high temperature four point probe has been fabricated. The probe can be placed in a furnace and is capable of operation up to a temperature of $1000°C$. The probes are held in place via Dalfratex, silica ribbon. The probes are $0.5\mu m$ diameter but the point has been acheived by electro-chemically etching in a 0.6mol, 200ml, sodium hydroxide (KOH) solution. A diagram of the four point probe has been included in figure B.1.

A 7cm diamter, stainless steel ring, of thickness 0.5mm, is submerged in the solution. The tungsten probe to be etched is also submerged. A 15v AC supply is connected to the probe and the ring. The result is a gentle etching of the tip of the probe.

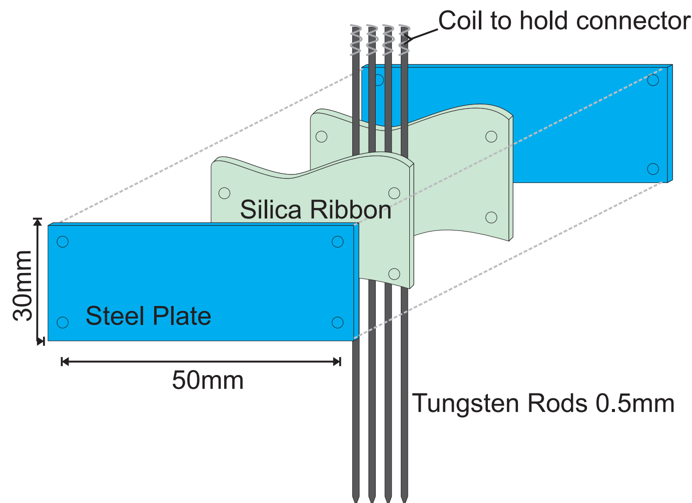

Figure B.1: Schematic of the high temperature four point probe

Bibliography

[1] R. P Feynman. Theres plenty of room at the bottom. In Horace D. Gilbert, editor, *Miniaturization*, pages 282–296. Reinhold, New York, 1961.

[2] Rainer. Waser. *Nanoelectronics and Information Technology: Advanced Electronic Materials and Novel Devices*. Wiley, 2005.

[3] Stanford R. Ovshinsky. Reversible electrical switching phenomena in disordered structures. *Physical Review Letters*, 21(20):1450, 1968.

[4] Stefan Lai and Tyler Lowrey. Oum - a 180 nm nonvolatile memory cell element technology for stand alone and embedded applications. Technical Digest - International Electron Devices Meeting, pages 803–806, Washington, DC, 2001. Institute of Electrical and Electronics Engineers Inc.

[5] H. Horii, J. Yi, J. Park, Y. Ha, I. Baek, S. Park, Y. Hwang, S. Lee, Y. Kim, K. Lee, U. In Chung, and J. Moon. A novel cell technology using n-doped gesbte films for phase change ram. 2003 Symposium on VLSI Technology. Digest of Technical Papers, pages 177–8, Kyoto, Japan, 2003. Japan Soc. Applied Phys.

[6] M. Lankhorst, B Ketelaars, and R Wolters. Low-cost and nanoscale non-volatile memory concept for future silicon chips. *Nature Materials*, 4(4):347–52, 2005.

[7] J. Tominaga, A. T. Nakano, and N. Atoda. An approach for recording and readout beyond the diffraction limit with an sb thin film. *Applied Physics Letters*, 73(15):2078–80, 1998.

[8] Hwang Inoh, Kim Jooho, Kim Hyunki, Park Insik, and Shin Dongho. Phase change materials in super-rens disk. *IEEE Transactions on Magnetics*, 41(2):1001–3, 2005.

[9] Kim Looho. Super-rens media using alternative recording systems. In *Optical nanotechnologies. Manipulation of surface and local plasmons*, pages 35–48. Springer-Verlag, 2003.

[10] Luping Shi, Towchong Chong, Pik Kee Tan, Xiang Hu, Jianming Li, Xiangshui Miao, Hongxing Yuan, and Haibiao Yao. Super-resolution near-field phase change

disk with sb70te30 mask layer. *Japanese Journal of Applied Physics, Part 1: Regular Papers and Short Notes and Review Papers*, 43(7 B):5001–5005, 2004.

[11] Simyon D Savransky. Analysis of us patents (1966-november 2004) in phase change memory. In *International Conference on Memory Technology and Design*, Hyeres Les Palmiers, France, 2005.

[12] Alexander V. Kolobov, Paul Fons, Anatoly I. Frenkel, Alexei L. Ankudinov, Junji Tominaga, and Tomoya Uruga. Understanding the phase-change mechanism of rewritable optical media. *Nature Materials*, 3(10):703–708, 2004.

[13] Wojciech WeLnic, Ariesto Pamungkas, Ralf Detemple, Christoph Steimer, Stefan Blugel, and Matthias Wuttig. Unravelling the interplay of local structure and physical properties in phase-change materials. *Nature Materials*, 5(1):56–62, 2006.

[14] Kim YoungKuk, K. Jeong, M. H. Cho, Hwang Uk, H. S. Jeong, and Kim Kinam. Changes in the electronic structures and optical band gap of ge2sb2te5 and n-doped ge2sb2te5 during phase transition. *Applied Physics Letters*, 90(17):171920–1, 2007.

[15] Matthius Wuttig. Rewritable dvds based on phase change materials. In Rainer Waser, editor, *Nanoelectronics and Information Technology*, volume 1, pages 643–656. Wiley-VCH, Aachen, 2nd edition, 2005.

[16] M. H. R. Lankhorst. Modelling glass transition temperatures of chalcogenide glasses. applied to phase-change optical recording materials. *Journal of Non-Crystalline Solids*, 297(2-3):210–19, 2002.

[17] Malcolm D. Ingram. *Electrical Properties of Glasses*, volume 9 of *Materials Science and Technology*. VCH, Verlagsgesellscaft mbH, glasses and amorpous materials edition, 1991.

[18] Joseph S. Hayden. Ecologically friendly optical glasses. *Optics & Photonics News*, pages 36–41, 2004.

[19] R. Asal and H. N. Rutt. Optical properties of laser ablated gallium lanthanum sulphide chalcogenide glass thin films prepared at different deposition laser energy densities. *Optical Materials*, 8(4):259–68, 1997.

[20] William B. Jensen. A note on the term "chalcogen". *Journal of Chemical Education*, 74:1063, 1997.

[21] Stephen R. Elliott. *Chalcogenide Glasses*, volume 9 of *Materials Science and Technology*. VCH, 1991.

[22] A M Rudnitskaya A D'Amico C Di Natale Yu. G. Vlasov, A V Legin. 'electronic tongue' - new analytical tool for liquid analysis on the basis of non-specific sensors and methods of pattern recognition. In *Sensors and Actuators, B: Chemical*, volume 65, pages 235–236, IMCS-7: 7th International Meeting on Chemical Sensors, Jul 27-Jul 30 1998, Beijing, China, 2000. Elsevier Science.

[23] J. Lucas and X. H. Zhang. The tellurium halide glasses. *Journal of Non-Crystalline Solids*, 125:1–16, 1990.

[24] A. K. Mairaj. *Optical Wavguide and Lasers in Improved Gallium Lanthanum Sulphide Glass*. PhD thesis, University of Southampton, 2003.

[25] A. Zakery and S. R. Elliott. Optical properties and applications of chalcogenide glasses: A review. *Journal of Non-Crystalline Solids*, 330:1–12, 2003.

[26] M. Asobe. Nonelinear optical properties of chalcogenide glass fibers and their appications to all optical switching. *Optical Fiber Technology Materials Devices and Systems*, 3:142–148, 1997.

[27] Merton C. Flemings Bernhard Ilschner Edward J. Kramer Subhash Mahajan K. H. Jurgen Buschow, Robert W. Cahn. *Encyclopedia of Materials: Science and Technology*. Elsevier Science Ltd, 2001.

[28] A Loireau-Lozac'H H Dexpert P Lagarde J.Flahaut S Benazeth, M Tuilier. An EXAFS structural approach of the gallium-lanthanum-sulfur glasses. *Journal of Non-Crystalline Solids*, 110:89–100, 1989.

[29] L. van Pieterson, M. H. R. Lankhorst, M. van Schijndel, A. E. T. Kuiper, and J. H. J. Roosen. Phase-change recording materials with a growth-dominated crystallization mechanism: a materials overview. *Journal of Applied Physics*, 97(8):83520–1, 2005.

[30] Peter M B Walker, editor. *Dictionary of Science and Technology*. Larousse, 1 edition, 1995.

[31] T M Hayes R A Street R J Nemanich, G A N Connell. Thermally induced effects in evaporated chalcogenide films. i. structure. *Physical Review B (Solid State)*, 18(12):6900–14, 1978.

[32] P.B. Klein P.C. Taylor T.P. Martin D.J. Treacy, U. Strom. Photostructural effects in glassy As2Se3 and As2S3. *Journal of Non-Crystalline Solids*, 35-36:1035–9, 1980.

[33] A. R. Silin. Light-induced ionic processes in optical oxide glasses. *Journal of non-crystalline solids*, 129:40–45, 1991.

[34] K. Tanaka H. Hamanaka and S. Iizima. Reversible photostructural change in melt-quenched As2S3 glass. *Solid State Communications*, 23(1):63–65, 1977.

[35] Paivi Riihola Andris Ozols Olli Salminen, Nina Nordman. Holographic recording and photocontraction of amorphous As2S3 films by 488.0 nm and 514.5 nm laser light illumination. *Optics Communications*, 116:310–315, 1995.

[36] A. Matsuda S. Iizima H. Hamanaka, K. Tanaka. Reversible photo-induced volume changes in evaporated As2S3 nd As4Se5Ge1 films. *Solid state communication*, 19:499–501, 1976.

[37] K.Tanaka H. Hisakuni. Optical fabrcation of microlenses in chalcogenide glass. *Optics Letters*, 20:958–960, 1995.

[38] T Grevatt HN Rutt RS Deol G Wylangowski DS Gill RW Eason, KE Youden. Pulsed-laser deposition of ga-la-s chalcogenide glass films for optical waveguide applications. *American Institute of Physics Second Conference on Laser Ablation: Mechanisms and Applications II*, page 583, 1993.

[39] D. Kozhuharova L. Tichy E. Cernoskova P.J.S. Ewen K. Petkov, R. Todorov. Changes in the physicochemical and optical properties of chalcogenide thin films from the systems as-s and as-s-tl. *Journal of Materials Science*, 39:961–968, 2004.

[40] A. Pirovano, A. L. Lacaita, A. Benvenuti, F. Pellizzer, and R. Bez. Electronic switching in phase-change memories. *IEEE Transactions on Electron Devices*, 51(3):452–9, 2004.

[41] Edward Arthur Davis N. F. Mott. *Electronic Processes in Non-Crystalline Materials*, volume 1. Clarendon Press, Oxford, 1979.

[42] B. T. Kolomiets. Vitreous semiconductors (ii). *Physica Status Solidi (b)*, 7:713, 1964.

[43] P. W. Anderson. Model for the electronic structure of amorphous semiconductors. *Physical Review Letters*, 34(15):953, 1975.

[44] R. A. Street and N. F. Mott. States in the gap in glassy semiconductors. *Physical Review Letters*, 35(19):1293, 1975.

[45] David Adler and Ellen J. Yoffa. Electronic structure of amorphous semiconductors. *Physical Review Letters*, 36(20):1197, 1976.

[46] Sir Nevill Mott. Electrons in glass. *Reviews of Modern Physics*, 50(2):203, 1978.

[47] John Park Manzur Gill, Tyler Lowrey. Ovonic unified memory - a high-performance nonvolatile memory technology for stand-alone memory and embedded applications. *Digest of Technical Papers - IEEE International Solid-State Circuits Conference*, 445-446:158–159, 2002.

[48] S. R. Ovshinsky. Localized states in the gap of amorphous semiconductors. *Physical Review Letters*, 36(24):1469–72, 1976.

[49] G. C. Vezzoli. Disappearance of the barrier offset voltage in the on-state characteristics of a chalcogenide threshold switch for short relaxations of holding voltage. *Journal of Applied Physics*, 50(9):5810–14, 1979.

[50] G. V. Bunton and R. M. Quilliam. Chalcogenide switching devices. *Marconi Review*, 35(184):24–41, 1972.

[51] Boris. Ushkov Robert. Fairman. *Semiconducting Chalcogenide Glass II: Properties of Chalcogenide Glasses*, volume 79. Elsevier, 2004.

[52] Daniel Lelmini and Yuegang Zhang. Analytical model for subthreshold conduction and threshold switching in chalcogenide-based memory devices. *J. Appl. Phys.*, 102:054517, 2007.

[53] L. Geppert. The new indelible memories. *IEEE Spectrum*, 40(3):48–54, March 2003.

[54] S. R. Ovshinsky. An history of the phase change technology. *Memoires Optiques et Systemes*, 127, 1994.

[55] Stefan Lai. Current status of the phase change memory and its future. *Intel publication*.

[56] R. Uttecht V. Kao O. Agrawal A. Pohm, C. Sie. Chalcogenide glass bistable resistivity (ovonic) memories. *IEEE Transactions on Magnetics*, 6:592– 592, 1970.

[57] S. R. Ovshinsky. Optically induced phase changes in amorphous materials. *Journal of Non-Crystalline Solids*, 141:200–203, 1992.

[58] R.G. Mani and S. Ramanathan. Observation of a uniform temperature dependence in the electrical resistance across the structural phase transition in thin film vanadium oxide (v o2). *Applied Physics Letters*, 91(6):062104, 2007.

[59] Nikolay Zheludev. All change, please. *Nat Photon*, 1(10):551–553, 2007.

[60] Erwin R. Meinders et Al. Determination of the crystallisation kinetics of fast-growth phase change materials for mark formation prediction. *Jpn. J. Appl Physics*, 42:809–812, 2003.

[61] Rubin K.A.; Barton R.W. Chen, M. Compound materials for reversible, phase-change optical data storage. *Applied Physics Letters*, 49:502–504, 1986.

[62] Hiroko Iwasaki et al. Completely erasable phase change optical disc II: Application of ag-in-sb-te mixed-phase system for rewritable compact disc compatible with cd-velocity and double cd-velocity. *Jpn. J. Appl. Phys.*, 32:5241–5247, 1993.

[63] Zhou Guo-Fu. Materials aspects in phase change optical recording. volume A304-A306 of *Mater. Sci. Eng. A, Struct. Mater., Prop. Microstruct. Process. (Switzerland)*, pages 73–80, Bangalore, India, 2001. Elsevier.

[64] J. H. Coombs, A. P. J. M. Jongenelis, W. van Es-Spiekman, and B. A. J. Jacobs. Laser-induced crystallization phenomena in gete-based alloys. i. characterization of nucleation and growth. *Journal of Applied Physics*, 78(8):4906–17, 1995.

[65] Richard Wright. Bbc future media and technology, 2007.

[66] Ultra density optical. http://www.plasmon.com/udo/index.html.

[67] Eugene Hecht. *Optics*. Addison Wesley, 1998.

[68] Christopher C. Davis Igor I. Smolyaninov, Yu-Ju Hung. Magnifying superlens in the visible frequency range. *Science*, 315(5819):1699–1701, March 2007.

[69] G. Binnig and H. Rohrer. Scanning tunnelling microscopy. *Helvetica Physica Acta*, 55(6):726–35, 1982.

[70] E. Betzig, J. K. Trautman, R. Wolfe, E. M. Gyorgy, P. L. Finn, M. H. Kryder, and C. H. Chang. Near-field magneto-optics and high density data storage. *Applied Physics Letters*, 61(2):142, 1992.

[71] K. Wang, D. Wamwangi, S. Ziegler, C. Steimer, and M. Wuttig. Influence of bi doping upon the phase change characteristics of ge2sb2te5. *Journal of Applied Physics*, 96(10):5557–5562, 2004.

[72] D. Wamwangi, W. Njoroge, and M. Wuttig. Crystallization kinetics of ge4sb1te5 films. *Thin Solid Films*, 408(1-2):310–15, 2002.

[73] Donald L. Smith. *Thin-Film Deposition: Principles and Practice*. McGraw Hill, 1995.

[74] Angstrom Sciences. Overview of sputtreing, 2003. Internet: http://www.angstromsciences.com/technology/sputtering.htm.

[75] H. Dieker and M. Wuttig. Influence of deposition parameters on the properties of sputtered ge2sb2te5 films. *Thin Solid Films*, 478(1-2):248–51, 2005.

[76] Andrew A Anderson D W Hewak Roger C Moore Sakellaris Mailis Nikolaos Vainos Andonis Hatziapostolou RW Eason, Devinder S Gill. Characterisation of compositional photosensitivity depndence by pulsed laser deposition. *ULF-LENS anual report 1994/95*, 1994.

[77] Carlos Zaldo Harvey N. Rutt Nikolaos A. Vainos Devinder S. Gill, Robert W. Eason. Characterisation of ga-la-s chalcogenide glass thin-film optical waveguides, fabricated by pulsed laser deposition. *Journal of Non-Crystalline Solids*, 191:321–326, 1995.

[78] H N Rutt R Asal, P E Rivers. A structural study of gallium lanthanum sulphide glass bulk and thin films by x-ray absorption fine structure spectroscopy. *Journal of Physics Condensed Matter*, 9:6217–6230, 1997.

[79] x. Iii-vs review, research, reviews, patents. *THE ADVANCED SEMICONDUCTOR MAGAZINE*, 19(7):42–44, 2006.

[80] Hideomi Koinuma and Ichiro Takeuchi. Combinatorial solid-state chemistry of inorganic materials. *Nature Materials*, 3(7):429–438, 2004.

[81] S. Guerin and B. E. Hayden. Physical vapor deposition method for the high-throughput synthesis of solid-state material libraries. *Journal of Combinatorial Chemistry*, 8(1):66–73, 2006. 1520-4766.

[82] Nicholas W. M. Ritchie. Nistmonte, 2006.

[83] John C. Russ. *Fundamentals of Energy Dispersive X-Ray Analysis*. Butterworths, London, 1984.

[84] Harland G. Tompkins. *A User's Guide to Ellipsometry*. Dover Publications, Mineola, New York, 2006.

[85] Joseph F. Keithley. *Low Level Measurements*. Keithley, Keithley Instruments Inc, 28775 Aurora Road, Cleveland, Ohio, 1998.

[86] Homer E. Kissinger. Reation kinetics in differential thermal analysis. *Analytical Chemistry*, 29:1702–1706, 1957.

[87] M. Zahra M.J. Starink, A. Determination of the transformation exponient s from experiments at constant heating rate. *Thermhimica Acta*, 298:179–189, 1997.

[88] A A Abu-Sehly A H Moharram, M Abu El-Oyoun. Calorimetric study of the chalcogenide se(72.5)Te(20)Sb(7.5). *Journal of Physics D: Applied Physics*, 34:2541–2546, 2001.

[89] R. Mehl W. Johnson. Reaction kinetics in processes of nucleation and growth. *Trans. Am. Inst. Mining Met. Engns.*, 135:416–458, 1939.

[90] M. Avrami. Kinetics of phase change. *Journal of chemical physics*, 7:1103–1112, 1939.

[91] M. Avrami. Kinetics of phase change. II transformation-time relations for random distribution of nuclei. *Journal of chemical physics*, 8:212, 1940.

[92] M. Avrami. Granulation, phase change, and microstructure kinetics of phase change. III. *Journal of chemical physics*, 9:177, 1941.

[93] T. Ozawa. *Bull. Chem. Soc. Japan*, 38:1881, 1965.

[94] F.C. Chalklin B. L. Worsnop. *X-Rays*. Methuens Monographs on Physical Subjects. Methuens, London, 3 edition, 1950.

[95] J. Feinleib, J. DeNeufville, S. C. Moss, and S. R. Ovshinsky. Rapid reversible light-induced crystallization of amorphous semiconductors. *Applied Physics Letters*, 18(6):254–7, 1971.

[96] A. W. Smith. Injection laser writing on chalcogenide films. *Applied Optics*, 13(4):795–798, 1974.

[97] R. Barton and K. A. Rubin. Laser-material interactions in phase change optical recording. Beam-Solid Interactions and Phase Transformations, pages 303–8, Boston, MA, USA, 1986. Mater. Res. Soc.

[98] R. J. von Gutfeld and P. Chaudhari. Laser writing and erasing on chalcogenide films. *Journal of Applied Physics*, 43(11):4688–93, 1972.

[99] N. Yamada, M. Takao, and M. Takenaga. Te-ge-sn-au phase change recording film for optical disk. volume 695 of *Proc. SPIE - Int. Soc. Opt. Eng. (USA)*, pages 79–85, San Diego, CA, USA, 1986.

[100] Kenichi Nishiuchi, Noboru Yamada, Nobuo Akahira, Mutsuo Takenaga, and Ryutaro Akutagawa. Laser diode beam exposure instrument for rapid quenching of thin-film materials. *Review of Scientific Instruments*, 63(6):3425, 1992.

[101] R. C. Ross, D. A. Strand, E. J. Bjornard, and J. P. DeNeufville. Crystallization rate and thermal stability of te-based alloy thin films for erasable optical recording. volume 70 of *Materials Research Society Symposia Proceedings*, pages 713–718, Palo Alto, CA, USA, 1986. Materials Research Soc, Pittsburgh, PA, USA.

[102] K. A. Rubin, R. W. Barton, M. Chen, V. B. Jipson, and D. Rugar. Phase transformation kinetics-the role of laser power and pulse width in the phase change cycling of te alloys. *Applied Physics Letters*, 50(21):1488–90, 1987.

[103] Cheng Lu and M. Mansuripur. Measurement of the thermal coefficients of erasable phase-change media. 1997 Optical Data Storage Topical Meeting ODS. Conference Digest (Cat. No.97TH8273), pages 96–7, Tucson, AZ, USA, 1997. IEEE.

[104] M. Mansuripur, J. K. Erwin, W. Bletscher, P. Khulbe, K. Sadeghi, Xun Xiaodong, A. Gupta, and S. B. Mendes. Static tester for characterization of phase-change, dye-polymer, and magneto-optical media for optical data storage. *Applied Optics*, 38(34):7095–104, 1999.

[105] Rongguang Liang, Chubing Peng, Kenichi Nagata, Kelly Daly-Flynn, and Masud Mansuripur. Optical characterization of multilayer stacks used as phase-change media of optical disk data storage. *Applied Optics*, 41(2):370–378, 2002.

[106] Kazuo Watabe, Pavel Polynkin, and Masud Mansuripur. Optical pump-and-probe test system for thermal characterization of thin metal and phase-change films. *Applied Optics*, 44(16):3167–3173, 2005.

[107] V. Weidenhof, N. Pirch, I. Friedrich, S. Ziegler, and M. Wuttig. Minimum time for laser induced amorphization of ge2sb2te5 films. *Journal of Applied Physics*, 88(2):657–64, 2000.

[108] Orazio. Svelto. *Principles of Lasers*. Kluwer, 4th edition, 1998.

[109] H.D. Wolpert. Autoranging/autofocus: a survey of systems. iii. *Photonics Spectra*, 21:133–142, 1987.

[110] V. Weidenhof, I. Friedrich, S. Ziegler, and M. Wuttig. Atomic force microscopy study of laser induced phase transitions in ge2sb2te5. 86(10):5879, 1999.

[111] K. D. Choquette, K. L. Lear, R. E. Leibenguth, and M. T. Asom. Vertical-cavity laser diode polarization switching and control. volume 40 of *IEEE Trans. Electron Devices (USA)*, pages 2117–18, Santa Barbara, CA, USA, 1993.

[112] J. Tominaga and N. Atoda. Study of the crystallization of gesbte films by raman spectroscopy. *Japanese Journal of Applied Physics, Part 2 (Letters)*, 38(3B):322–3, 1999.

[113] M. Chen, K. A. Rubin, and R. W. Barton. Compound materials for reversible, phase-change optical data storage. *Applied Physics Letters*, 49(9):502–4, 1986.

[114] L. Balde, B. Legendre, and A. Balkhi. Etude du diagramme d'equilibre entre phases du systeme ternaire germanium-etain-tellure. *Journal of Alloys and Compounds*, 216(2):285–293, 1995.

[115] P. Lebaudy, J. M. Saiter, J. Grenet, M. Belhadji, and C. Vautier. Identification of amorphous zones in the getesb system. *Materials Science Engineering A (Structural Materials: Properties, Microstructure and Processing)*, A132:273–6, 1991.

[116] Gautam Ghosh, Hans Leo Lukas, and Luc Delaey. Thermodynamic assessment of the sb-te system. *Zeitschrift fuer Metallkunde*, 80(10):731–736, 1989.

[117] N. Yamada, E. Ohno, K. Nishiuchi, N. Akahira, and M. Takao. Rapid-phase transitions of gete-sb2te3 pseudobinary amorphous thin films for an optical disk memory. *Journal of Applied Physics*, 69(5):2849–56, 1991.

[118] NK Abrikosov and GT Danilova-Dobryakova. An investigation of the structural diagram of sb 2 te 3-gete. *Neorganicheskie Materialy*, 1965.

[119] C. E. Wickersham, G. Bajor, and J. E. Greene. Impulse stimulated left double quote explosive right double quote crystallization of sputter deposited amorphous (in,ga)sb films. *Solid State Communications*, 27(1):17–20, 1978.

[120] N. Kaiser. Crystallization of amorphous antimony films. volume 116 of *Thin Solid Films (Switzerland)*, pages 259–65, Hajduszoboszlo, Hungary, 1984.

[121] A. Hirotsune, Y. Miyauchi, and M. Terao. High-density recording on a phase-change optical disk with suppression of material flow and recording-mark shape-deformation. *Japanese Journal of Applied Physics, Part 1 (Regular Papers, Short Notes)*, 35(1B):346–9, 1996.

[122] S. Privitera, E. Rimini, C. Bongiorno, A. Pirovano, and R. Bez. Effects of dopants on the amorphous-to-fcc transition in ge2sb2te5 thin films. *Nuclear Instruments and Methods in Physics Research, Section B: Beam Interactions with Materials and Atoms*, 257(1-2 SPEC ISS):352–354, 2007.

[123] R. Kojima, S. Okabayashi, T. Kashihara, K. Horai, T. Matsunaga, E. Ohno, N. Yamada, and T. Ohta. Nitrogen doping effect on phase change optical disks. volume 37 of *Jpn. J. Appl. Phys. 1, Regul. Pap. Short Notes Rev. Pap. (Japan)*, pages 2098–103, Yamagata, Japan, 1998. Publication Office, Japanese Journal Appl. Phys.

[124] Guo-Fu Zhou and Bernardus A. J. Jacobs. High performance media for phase change optical recording. *Japanese Journal of Applied Physics, Part 2: Letters*, 38(3B):1625–1628, 1999.

[125] N. Matsuzaki, K. Kurotsuchi, Y. Matsui, O. Tonomura, N. Yamamoto, Y. Fujisaki, N. Kitai, R. Takemura, K. Osada, S. Hanzawa, H. Moriya, T. Iwasaki, T. Kawahara, N. Takaura, M. Terao, M. Matsuoka, and M. Moniwa. Oxygen-doped gesbte

phase-change memory cells featuring 1.5-v/100-μa standard 0.13-μm cmos operations. International Electron Devices Meeting 2005 (IEEE Cat. No.05CH37703C), page 4 pp., Washington, DC, USA, 2005. IEEE.

[126] Qiao Baowei, Feng Jie, Lai Yunfeng, Ling Yun, Y. Lin, Tang Ting'ao, Cai Bingchu, and Chen Bomy. Effects of si doping on the structural and electrical properties of ge2sb2te5 films for phase change random access memory. *Applied Surface Science*, 252(24):8404–9, 2006.

[127] Ji-Lin Xia, Bo Liu, Zhi-Tang Song, Song-Lin Feng, and Bomy Chen. Electrical properties of ag-doped ge2sb2te5 films used for phase change random access memory. *Chinese Physics Letters*, 22(4):934–7, 2005.

[128] Lie Chao-Te, Kuo Po-Cheng, Hsu Wei-Chih, Wu Ting-Hao, Chen Po-Wei, and Chen Sheng-Chi. Ge2sb2te5 thin film doped with silver. volume 42 of *Jpn. J. Appl. Phys. 1, Regul. Pap. Short Notes Rev. Pap. (Japan)*, pages 1026–8, Waikoloa, HI, USA, 2003. Japan Soc. Appl. Phys.

[129] C. Yan-Fei, Peng Zhou, Yin-Yin Lin, Ting-Ao Tang, Liang-Yao Chen, Jing Li, Bao-Wei Qiao, Yun-Feng Lai, Jie Feng, Bing-Chu Cai, and Bomy Chen. Nitrogen and silicon co-doping of ge2sb2te5 thin films for improving phase change memory performance. *Chinese Physics Letters*, 24(3):781–3, 2007.

[130] R. Kojima and N. Yamada. Acceleration of crystallization speed by sn addition to ge-sb-te phase-change recording material. *Japanese Journal of Applied Physics, Part 1 (Regular Papers, Short Notes, Review Papers)*, 40(10):5930–7, 2001.

[131] Luping Shi Tow Chong Chong, Rong Zhao. Superlattice-like phase change random access memory. In *EPCOS/IMST*, Grenoble, France, 2006.

[132] Dr. Peter Haring Bolivar. Lateral design for phase change random access memory cells with low-current consumption. In *EPCOS*, Balzers, Liechtenstein, 2004.

[133] M. Laurenzis, A. Heinrici, P. H. Bolivar, H. Kurz, S. Krysta, and J. M. Schneider. Composition spread analysis of phase change dynamics in ge2sbyte1-x-y films embedded in an optical multilayer stack. *IEE Proceedings-Science, Measurement and Technology*, 151(6):394–7, 2004.

[134] Guangsheng Fu, Heju Xu, Shufang Wang, Wei Yu, Wei Sun, and Li Han. Epitaxial growth of zno films by helicon-wave-plasma-assisted sputtering. *Physica B: Condensed Matter*, 382(1-2):17–20, 2006.

[135] Fachinformationszentrum Karlsruhe. Inorganic crystal structure database, 2003-2006.

[136] N. Yamadaa and T. Matsunaga. Structure of laser-crystallized ge2sb2+xte5 sputtered thin films for use in optical memory. *Journal of Applied Physics*, 88(12):7020–8, 2000.

[137] Walter Kamande Njorge. *Phase Change Optical Recording Preparation and X-ray Characterisation of GeSbTe and AgInSbTe films*. PhD thesis, Aachen, 2001.

[138] O. Yu Prikhodko, Sh Sh Sarsembinov, A. P. Ryaguzov, S. Ya Maksimova, and V. Zh Ushanov. Atomic structure and short- and medium-range order parameters in amorphous chalcogenide films prepared by different methods. *Journal of Non-Crystalline Solids*, 353(18-21):2057–61, 2007.

[139] An Sung Hyuck, Li Xuezhe, and Kim Youl. Optimum growth conditions of ge-sb-te alloy thin film investigated by ellipsometry. *Japanese Journal of Applied Physics, Part 1 (Regular Papers, Short Notes, Review Papers)*, 43(3):1006–12, 2004.

[140] M. Kuwahara, O. Suzuki, N. Taketoshi, Y. Yamakawa, T. Yagi, P. Fons, K. Tsutsumi, M. Suzuki, T. Fukaya, J. Tominaga, and T. Baba. Measurements of temperature dependence of optical and thermal properties of optical disk materials. *Japanese Journal of Applied Physics, Part 1 (Regular Papers, Short Notes, Review Papers)*, 45(2B):1419–21, 2006.

[141] H. E. Hall J. R. Hook. *Solid State Physics*. Wiley, 2 edition, 1991.

[142] S. R. Elliott. *The Physics and Chemistry of Solids*. Wiley, Chichester, 1998.

[143] Lin Su-Shia. The effect of thickness on the bi-ge-sb-te films for reversible phase-change optical recording. *Materials Science; Engineering B (Solid-State Materials for Advanced Technology)*, 129(1-3):116–20, 2006.

[144] Lee Chain-Ming, Yen Wen-Shin, Liu Ren-Haur, and Chin Tsung-Shune. Performance of ge-sb-bi-te-b recording media for phase-change optical disks. *Japanese Journal of Applied Physics, Part 1 (Regular Papers, Short Notes; Review Papers)*, 40(9A):5321–5, 2001.

[145] C. M. Lee, T. S. Chin, and E. Y. Huang. Optical properties and structure of tellurium-germanium- bismuth-antimony compounds with fast phase-change capability. *Journal of Applied Physics*, 89(6):3290–4, 2001.

[146] S. Fujimori, S. Yagi, H. Yamazaki, and N. Funakoshi. Crystallization process of sb-te alloy films for optical storage. *Journal of Applied Physics*, 64(3):1000–4, 1988.

[147] Martijn H. R. Lankhorst, Liesbeth Van Pieterson, Mark Van Schijndel, Ben A. J. Jacobs, and Jan C. N. Rijpers. Prospects of doped sb-te phase-change materials

for high-speed recording. *Japanese Journal of Applied Physics, Part 1: Regular Papers and Short Notes and Review Papers*, 42(2 B):863–868, 2003.

[148] V. B. Ufimtsev, V. B. Osvensky, V. T. Bublik, T. B. Sagalova, and O. E. Jouravlev. Structure, homogeneity and properties of thermoelectric materials based on ternary solid solutions of bismuth and antimony chalcogenides. *Advanced Performance Materials*, 4(2):189–97, 1997.

[149] J. Bicerano and S. R. Ovshinsky. Chemical bond approach to glass structure. volume 75 of *J. Non-Cryst. Solids (Netherlands)*, pages 169–76, Bloomfields Hills, MI, USA, 1985.

[150] T. Matsunaga and N. Yamada. Crystallographic studies on high-speed phase-change materials used for rewritable optical recording disks. *Japanese Journal of Applied Physics, Part 1 (Regular Papers, Short Notes; Review Papers)*, 43(7B):4704–12, 2004.

[151] T. Matsunaga, Y. Umetani, and N. Yamada. Structural study of a $ag_{.4}in_{3.7}sb_{76.4}te_{16.5}$ quadruple compound utilized for phase-change optical disks. *Physical Review B (Condensed Matter and Materials Physics)*, 64(18):184116–1, 2001.

[152] W.Doring R. Becker. *Annalen der Physik*, 416(719), 1935.

[153] P. K. Khulbe, E. M. Wright, and M. Mansuripur. Crystallization behavior of as-deposited, melt quenched, and primed amorphous states of ge2sb2.3te5 films. *Journal of Applied Physics*, 88(7):3926–33, 2000.

[154] J. Alistair Kerr. *CRC Handbook of Chemistry and Physics*. CRC Press, 85 edition, 2001.

[155] M. M. El-Samanoudy. Effect of composition and deposition parameters on optical properties of ge25sb15bis films. *Thin Solid Films*, 423(2):201–211, 2002.

[156] Sacharia Albin, James D. Satira, David L. Livingston, and Thomas A. Shull. Stimulated electronic transition concept for an erasable optical memory. *Japanese Journal of Applied Physics Part 1: Regular Papers Short Notes*, 31(2B):715–719, 1992.

[157] N. Kato, T. Fukano, Y. Takeda, A. Takeichi, T. Motohiro, and S. Kawai. Ges2/metal thin film bilayered structures as write-once-type optical recording materials. *Journal of Applied Physics*, 100(11):113115–1, 2006.

[158] D. W. Pohl, R. Badertscher, M. A. Muller, and P. Wachter. Laser-induced phase transition in the surface of sms crystals. *Applied Optics*, 13(1):95–7, 1974.

[159] Y.D. West, T. SCHWEIZER, D. J. BRADY, and D. W. HEWAK. Gallium lanthanum sulphide fibers for infrared transmiss ion. *Fiber and Integrated Optics*, 19:229–250, 2000.

[160] M. Guittard A.M. Loireau Lozac'h and J. Flahaut. Glasses formed by rare earth sulphides L2S3 with gallium sulphide Ga2S3. *Material Research Bulletin*, 11:1489–1496, 1976.

[161] Heath Bagshaw Angela B. Seddon Ruihua Li, David Furniss. Decisive role of oxide content in the formation and crystallization of gallium-lanthanum-sulfide glasses. *Journal of Materials Research*, 14:2621–2627, 1999.

[162] A.M Loireau-Lozac'h J. Flahaut, M. Guittard. Rare earth sulphide and oxysulphide glasses. *Glass Technology*, 24:149–155, 1983.

[163] Brady DJ-Hewak DW West YD, Schweizer T. Gallium lanthanum sulphide fibers for infrared transmission. *FIBER AND INTEGRATED OPTICS*, 19:229–250, 2000.

[164] D.J. Brady. *GALLIUM LANTHANUM SULPHIDE BASED GLASSES FOR MID-INFRARED OPTICAL FIBRES*. PhD thesis, Faculty of engineering and applied science, department of electronics and computer science, 1999.

[165] A. Vancu J. Tauc, R. Grigorovici. Optical properties and electronic structure of amorphous germanium. *physica status solidi (b)*, 15(2):627–637, 1966.

[166] Lee Bong-Sub, J. R. Abelson, S. G. Bishop, Kang Dae-Hwan, Cheong Byung-ki, and Kim Ki-Bum. Investigation of the optical and electronic properties of ge2sb2te5 phase change material in its amorphous, cubic, and hexagonal phases. *Journal of Applied Physics*, 97(9):93509–1, 2005.

[167] R. Swanepoel. Determination of the thickness and optical constants of amorphous silicon. *Journal of Physics E: Scientific Instruments*, 16(12):1214–1222, 1983.

[168] Chung-Che Huang. *Development of germanium based sulphide glass by chemical vapour deposition*. PhD thesis, University of Southampton, 2005.

[169] M. Guittard, A. M. Loireau-Lozac'h, H. F. Berguer, S. Barnier, and J. Flahaut. Glasses in the la2s3-la2o3-ga2o3-ga2s3 system. *Journal of Solid State Chemistry*, 62(2):191–8, 1986.

[170] Norman B. Colthup. Infrared spectroscopy. In Robert A. Meyers, editor, *Encyclopedia of Physical Science and Technology*, pages 793–816. Elsevier Science Ltd, 2004.

[171] L. Criante, D. E. Lucchetta, and F. Simoni. Characterization of nano-pdlc as optical data storage materials. *Molecular Crystals and Liquid Crystals*, 453:155–63, 2006.